Magnetic Bead-based DNA Extraction and Purification Microfluidic Chip

Sayyed Mohamad Azimi

A thesis submitted for the degree

of

Doctor of Philosophy (PhD)

Brunel University

School of Engineering and Design

March 2010

Abstract

A magnetic bead-based DNA extraction and purification device has been designed to be used for extraction of the target DNA molecules from whole blood sample. Mixing and separation steps are performed using functionalised superparamagnetic beads suspended in the cell lysis buffer in a circular chamber that is sandwiched between two electromagnets. Non-uniform nature of the magnetic field causes temporal and spatial distribution of the beads within the chamber. This process efficiently mixes the lysis buffer and whole blood in order to extract DNA from target cells. Functionalized surface of the magnetic beads then attract the exposed DNA molecules. Finally, DNA-attached magnetic beads are attracted to the bottom of the chamber by activating the bottom electrode. DNA molecules are extracted from the magnetic beads by washing and re-suspension processes.

The numerical simulation approach has been adopted in order to design the magnetic field source. The performance of the magnetic field source has been investigated against different physical and geometrical parameters and optimised dimensions are obtained with two different magnetic field sources; integrated internal source and external source. A new magnetic field pattern has been introduced in order to efficiently control the bulk of magnetic beads inside the mixing chamber by dynamic shifting of magnetic field regions from the centre of the coils to the outer edge of the coils and vice versa. A Matlab code has been developed to simulate beads trajectories inside the designed extraction chip in order to investigate the efficiency of the magnetic mixing. A preliminary target molecule capturing simulation has also been performed using the simulated bead trajectories to evaluate the DNA-capturing efficiency of the designed extraction chip.

The performance of the designed extraction chip has been tested by conducting a series of biological experiments. Different magnetic bead-based extraction kits have been used in a series of preliminary experiments in order to extract a more automation friendly extraction protocol. The efficiency of the designed device has been evaluated using the spiked bacterial DNA and non-pathogenic bacterial cell cultures (*B. subtilis*, Gram positive bacteria and *E. coli*, Gram negative bacteria) into the blood sample. Excellent DNA yields and recovery rates are obtained with the designed extraction chip through a simple and fast extraction protocol.

Declaration

I declare that no part of the work referred to in this thesis has been submitted in support of an application for another degree or qualification in this or any other university or other institution of learning.

Dedication

To my parents for their Love and Support

Acknowledgements

First of all, thank God the almighty for providing me this opportunity and granting me the capability to proceed successfully.

This thesis would not have been completed without help and support I received from a number of people inside and outside the School of Engineering and Design. Perhaps it might be impossible to recall everybody, but a few people stand out in the writer's memory to whom these acknowledgements are confined.

Particularly, I would like to thank my first supervisor, *Professor Wamadeva Balachandran*, for his initial support in approving my bursary granted by Commercialisation Office at Brunel University. I would also like to thank him for his continued guidance and help throughout my PhD research.

I would like to thank my second supervisor, *Dr. Predrag Slijepcevic*, for his help and discussions on the biological aspects of my research.

I am indebted to many of my colleagues for their helps and supports. I would like to thank *Dr. Jeremy C. Ahern* for his valued technical discussions, which have always been helpful to me. I am also grateful for his assistance in fabrication of different experimental devices. I would also like to thank *Dr. Gavin Nixon* from LGC for his help during biological evaluation experiments performed in this project.

Mr. *Massoud Zolgharni* and *Dr. Reza Bahmanyar* have been both valued friends and colleagues. Technical discussions with both have always been helpful to me.

I would like to thank Brunel Commercialisation Office and in particular, *Mr. Adrian Simon* for his helps and support during my research and approving my overseas bursary payments.

I would like to express my deep sense of gratitude to my parents for their love and constant affectionate support. Without their support my life would have been more difficult.

Acronyms and Symbols

Acronyms

µ-TAS	Micro Total Analysis Systems
2D	Two dimension
3D	Three Dimension
AC	Alternate Current
CCD	Capillary Electrophoresis
CD	Charge-Couple Device
CE	Compact Disc
CFD	Computational Fluids Dynamics
CMOS	Complementary Metal-Oxide-Semiconductor
DC	Direct Current
DEP	Dielectrophoresis
DNA	Deoxyribonucleic Acid
EHD	Electro-Hydro-Dynamic
FDM	Finite Different Modelling
FEM	Finite Element Modelling
FVM	Finite Volume Modelling
GMR	Giant Magnetoresistance
LAMP	Loop Mediated Isothermal Amplification
LCD	Liquid Cristal Display
LGC	Laboratory of Government Chemists
LOAC	Lab-On-A-Chip
MAP	Magnetophoresis
MEMS	Microelectromechanical Systems
MHD	Magneto-Hydro-Dynamic
NRL	Naval Research Laboratory
N-S	Navier Stocks
PCR	Polymerase Chain Reaction
PDE	Partial Differential Equations
PDMS	Polydimethylsiloxane
PMMA	Poly(methyl methacrylate)
POC	Point of Care
PZT	Piezoelectric
Re	Reynolds Number
RNA	Ribonucleic Acid
SAR	Separate and Recombine
SAW	Surface Acoustic Wave
SDS	Sodium Dodecyl Sulphate
SHM	Staggered Herringbone Mixer
SNP	Single Nucleotide Polymorphism

SPE	Solid Phase Extraction
STD	Sexually Transmitted Diseases
UV	Ultra Violet

Symbols

A	Magnetic potential
A_c	Spiral conductor cross-section area
A_k	Key-type electrode cross-section area
A_s	Spacing cross-section area
B	Magnetic flux density
B_f	Body force
D	Diffusion coefficient
d_{Bead}	Magnetic bead diameter
d_{ch}	Chamber depth
d_{in}	Coil internal diameter
d_{out}	Coil internal diameter
du/dy	Velocity gradient
f	Frequency
F_0	Magnetophoresis force coefficient
F_d	Drag force
f_f	Frictional coefficient
F_g	Gravity force
F_m	Magnetophoresis force
H	Magnetic field intensity
h	Distance between magnetic field source and magnetic particle
I	Electric current
I_c	Current passing through circular spiral
I_k	Current passing through key-type electrode
I_s	Current passing through spiral coil
J	Electric current density
J_D	Diffusion flux
K	Boltzmann's constant
L	Characteristic Length
M	Internal magnetization
m_{eff}	Effective magnetic moment
P	Pressure
Q	Thermal energy
R	Ohmic resistance
S	Spacing between conductors
t_c	Conductor thickness
t_k	Key-type electrode thickness
t_s	Winding depth

T_{ss}	Steady state temperature
U	Dipole energy
u_m	Steady-state velocity of particle
V	Characteristic Velocity of fluid
W_c	Conductor width
W_k	Key-type electrode width
W_S	Winding width
α_0	Temperature coefficient of material
χ_m	Magnetic susceptibility
φ	Concentration of particles
Ψ	Scalar potential
μ	Fluid Dynamic Viscosity
μ_0	Permeability of free space
μ_r	Relative permeability
μ_{rB}	Relative magnetic permeability of particle
ν	Kinematic viscosity
ρ	Fluid density
ρ_0	Resistivity at reference temperature
σ	The ratio of winding width to winding depth
τ	Shear Stress

List of Figures

Chapter 1

Chapter 2

Chapter 3

Chapter 4

Chapter 5

Chapter 6

Chapter 7

List of Tables

Chapter 3

Chapter 4

Chapter 5

Chapter 6

Chapter 7

Contents

CHAPTER 1

GENERAL INTRODUCTION

1.1 Introduction

Over the past decade, miniaturisation has been the major trend in analytical chemistry and medical science with the scope to benefits from such scaling down factors [1-3]. The major motivation of the miniaturisation idea was inspired by the electronic industry that shifted from vacuum tubes to transistors and microelectronic chips. Such miniaturisation offers low cost, small size, high speed and operational simplicity compared to existing expensive, large size and time consuming laboratory based analysis techniques. In the standard method, the sample need to be collected from the site and sent to the specialised laboratories for analysis, which is a cost intensive and time consuming process. The next step is to perform the standard procedure, consuming large volumes of the reagents and using large and expensive instrumentations operated by a qualified person.

Development of miniaturised laboratory analysis techniques is mainly the result of achievements in the field of microfabrication technology and microfluidics. The advent of micro-electro-mechanical-systems (MEMS) has created the potential to integrate electrical and mechanical components in the same platform using standard fabrication techniques of semiconductor industry with almost the same equipments

and materials. The range of MEMS applications is growing very fast toward the implementation of micro-sensors and micro-actuators in Micro-Total-Analysis-Systems (μ-TAS) and Lab-on-a-Chip platforms (LOAC).

On the other hand, implementation of the laboratory-based analytical techniques in the LOAC platforms requires fluid handling process in micro-scales. This requirement has led to the development of the micropumps, microvalves, micro-filter, micro-separators and micromixers under microfluidics platforms. In fact, microfluidics enables the realisation of chemical and biological reactions in miniaturised integrated micromachined systems.

The revolutionary idea of the lab-on-a-chip may have the greatest impact on the modern society's health and life through shrinking the laboratory-based analytical techniques to a low-cost, fast and automated integrated microchip-based analysis. The application area is very vast from agricultural tests to forensic and bio-defence as well as food industry, pharmaceutical and diagnostics applications. For example in the pharmaceutical industry, large quantities of enzymes are used for drug design experiments to see which will block an enzyme related to a disease state. These tests are expensive and performed one at a time. These tests can be done in parallel and consuming small quantities of substances by using lab-on-a-chip systems.

In the diagnostic sector, the application of lab-on-a-chip systems can be realised in automation of clinical diagnostic procedures to a miniaturised microchip. This will decrease the cost of the standard test by reducing the reagent consumption by order of 10^3-10^4 [2]. In this sector, the application of point-of-care (POC) diagnostic devices attracted enormous interest from both industry and academia in order to automate genetic diagnostic tests on an integrated microchip. Although diagnostic tests have wide applications in biotechnology and medicine such as agriculture and farming for detection of pathogens in food, the application of nucleic acid analysis in human whole blood is the subject of this research. The recent progress in the field of microfluidics such as integrated multiplexor [4], microfabricated reaction and separation systems [5] and integrated microfluidic DNA amplification [6] or miniature integrated LOAC system [7] proposes molecular detection in an integrated microfluidic device that will be commercially available within a few years. In this area, the application of these chips in detection of the sexually transmitted diseases (STDs) has the most immediate potential in the market.

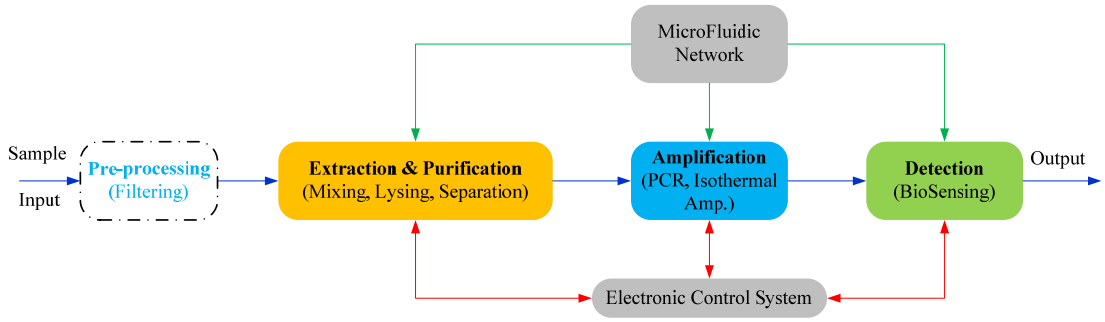

Figure 1.1. Block diagram of a typical POC diagnostic device with specific application in DNA chip.

1.2 Point of Care Diagnostic Devices

Figure 1.1 illustrates a block diagram of a LOAC diagnostic chip. A POC diagnostic device has three main functionalities as: sample preparation, amplification (only for DNA) and sample analysis or detection. However, an additional step might be necessary for pre-processing of the sample to increase the concentration of the target molecules such as filtering and pre-mixing (i.e. urine sample). Sample preparation is the first function of the chip where the real sample will be introduced into the chip together with the appropriate reagents. This can be done using a micropump(s) or other syringe-based systems. A pre-processing stage might be necessary before injecting the raw sample and reagents into the device such as warming up the reagents and/or pre-mixing of the reagents and the sample. After injecting the sample into the device, it needs to be processed, which might involve micromixing, heating and separation. In case of DNA extraction from whole blood, the sample preparation involves efficient mixing of whole blood and the lysis buffer in order to lyse the target cells and extract DNA molecules. Released DNA molecules then need to be separated from the rest of cell debris and bio-fluid.

Amplification is the next stage where the purified DNA molecule will be amplified to achieve the desired concentration, which is suitable for detection. This process can be fulfilled using thermal cycling PCR or isothermal amplification technique.

Final stage is the nucleic acid detection using a suitable biosensor device. The most common technique in nucleic acid detection involves the immobilization and hybridization process. Immobilization is the process of immobilising a known sequence of single strand DNA probe to the functionalised surface of the biosensor. By introducing the target DNA sequence, hybridisation takes place, if the target and

probe are complementary to each other. The next step is to detect the signal from hybridisation action. There are two main approaches to detect the hybridisation signal; labelled and label-free. In the first approach, target molecules will be labelled with specific tags and the signal can be generated from the interaction between the label and sensor. Electrochemical and magnetic biosensors are the example of label-based detection techniques. For example, the red-ox activity of the active label with the surface of the sensor in electrochemical sensors can be measured in the form of electric signal. The magnetic field of the magnetic bead tagged to the hybridised DNA molecule can change the resistance of the underlying GMR sensor and consequently, the signal can be measured as a variation in the sensor electric current. In the label-free detection techniques, the signal is mainly generated from the intrinsic properties of DNA molecules such as electric charge and mass variations. Occurrence of hybridisation can alter the total DNA mass on the surface of the sensor, which can be detected using quartz crystal microbalance sensor. Charge variation at the surface of the sensor can be detected using an underlying field effect sensor.

However, whilst there has been a great deal of work in the core areas, such as, miniaturisation of PCR for amplification of DNA and development of miniaturised DNA biosensors in microchip format, less effort has been exerted toward miniaturisation of DNA extraction/purification process. In fact, most of the currently demonstrated microfluidic or microarray devices pursue single functionality and use purified DNA or homogeneous samples at the input. On the other hand, practical applications in the clinical and environmental analysis require processing of the samples as complex and heterogeneous as whole blood or contaminated environmental fluids. Due to the complexity of the sample preparation, most available biochip systems still perform this initial step off-chip using traditional bench-top methods. As a result, rapid developments in the back-end detection platforms have shifted the bottleneck, impeding further progress in rapid analysis devices, to the front-end sample preparation where the real samples are used.

A problem with the currently available chaotic mixing in these platforms is that it usually requires the existence of moving parts, obstacles, grooves and twisted or three dimensional serpentine channels. The structure of these components tends to be complex, requiring complicated fabrication processes such as multi-layer stacking or

multi-step photolithography. Another problem with the existing DNA purification devices is that they are not suitable for integration in POC devices and are aimed toward laboratory-based bench-top purification processes. Therefore, the importance of fast, efficient and small-sized sample preparation and purification chip with the potential for integration in POC devices seems to be overlooked. Followings are some examples of the microchips and devices in such platforms.

1.2.1 DNA Detection

In the detection side, the research has conclusively resulted in many microchips capable of detecting target DNA in the sample. Since the redox-active molecule-based detection of hybridization is well established, two commercialized DNA chips are now being introduced onto the molecular diagnosis market. The first example of such a DNA chip, called the *eSensor™*, was developed by Motorola Life Sciences Inc [8] by using ferrocene as the active marker. This sensor was licensed to *OsmeTech PLC* for further commercialisation. Toshiba developed a CMOS-based DNA chip capable of detection single nucleotide polymorphisms (SNPs). This sensor was later licensed to *Antara BioSciences Inc* [9]. Recently *DNA Electronics Ltd* [10] developed another CMOS-based biosensor capable of detecting SNPs with the potential to be used in point of care diagnostic devices. This sensor is under validation process in collaboration with *Pfizer Ltd*. A magnetic-based DNA biosensor was developed by US-Naval Research Laboratory (NRL) using a giant magnetoresistive sensor (GMR) capable of detecting single magnetic bead used as the label [11]. This biosensor was later licensed to *Seahawk Biosystems Corporation* for further developments in clinical diagnostic applications. Although these DNA biosensors are fully functionalised as claimed, the inputs of such bio-chips are nothing but purified DNA sample.

1.2.2 DNA Amplification

Amplification has also grabbed significant attention with the scope to produce smaller, faster and automated amplification chips capable of performing multiplex PCR in one single cartridge. *Fluidigm* developed a PCR chip that can handle 48 PCR samples simultaneously using a digital array [12]. University of Utah, Centre of

Excellence for Biomedical Microfluidics, is developing a continuous flow PCR chip which is claimed to deliver 12 sec PCR cycles [13, 14].

1.2.3 DNA Extraction and Purification

In the purification platform, most work has been done on automation of the existing standard DNA purification protocols. *Qiagen QIAcube* is a fully automated robotic device developed to automate Qiagen spin-column kit [15]. This device can be used for purification of DNA, RNA and protein with the maximum of 12 samples per run. Although this device is fully automated, it has been designed for laboratory-based market and is not suitable for integration in POC devices. *Roche MagNA Pure*^{TM} is another robotic nucleic acid purification device which uses magnetic bead to isolate DNA from whole blood sample [16]. The total isolation time in this device takes up to 60min with 32 sample capacity. This device is designed for laboratory-based market and is not suitable for integration with POC devices.

1.2.4 Microfluidic Chips with Sample Preparation Capability

In addition to the above mentioned laboratory-based DNA extraction devices, there have been significant advances in development of integrated microfluidic chips for sample preparation in point-of-care diagnostic devices. The purpose of this section is to review the most important reported works on various types of the microfluidic extraction chips for application of the point of care diagnostic devices. This review covers both single functionality DNA purification chips and multi-functionality chips integrated with sample preparation chips.

Since the early development of the chip-based capillary electrophoresis (CE) by Harrison et al. [17], several researchers have developed microfluidic devices by integrating DNA amplification (PCR) with capillary electrophoresis (CE) followed by microarray-based florescent detection systems [18-22]. A list of microfluidic chips for clinical and forensic analysis using combined PCR and CE can be found in the review paper published by Elisabeth Verpoorte [23].

On the other hand, there are some reports on combined sample preparation, amplification and detection integrated on a single microfluidic chip. Although there are few reports on the extraction and purification of nucleic acid from whole blood

[24], the majority of the reported chips are designed to purify nucleic acids from serum and cells lysate [25, 26].

Since the aim of this work is to design a DNA extraction and purification device, the focus was given to review the reported microfluidic chips with sample preparation step. Although some reported microchips have used PCR-based thermal lysis to lyse the cells and extract the target DNA molecules, the majority of the reported chips have used solid-phase-extraction (SPE) technique to purify nucleic acids from various biological fluids. This technique includes: magnetic beads, silica columns/pillars, silica beads/particles, hybrid silica beads/sol-gel network and monoliths.

Thermal cycling PCR can be used for the cell lysis process. In this method, DNA extraction and purification steps are eliminated and the thermal cell lysis takes place in the first cycle of the PCR by starting the PCR at a higher temperature (95 °C). However, this method is limited to the purified cells cultures and cannot be used for a crude sample such as whole blood.

Waters et al. [19] reported a monolithic microchip device comprising a multiplex PCR chip integrated with electrophoresis sizing of the amplified products. Purified diluted E. coli cells culture was used as the input sample and the cells were lysed thermally by placing the entire microchip in a commercial thermal cycler.

El-Ali et al. [27] reported a microfabricated PCR thermal cycling chip integrated with sample pre-treatment chip. The sample pre-treatment process was performed using dielectrophoretic (DEP) capturing of the target cells from the bio-fluid. The performance of the device was tested on a sample containing yeast cells and heparin, which is a well known PCR inhibitor.

Yuen et al. [24] reported a microchip capable of blood sample preparation process and PCR amplification process in a silicon/glass microchamber. A series of 3.5 µm feature-size weir-type filters were fabricated inside the chamber using standard microfabrication technique in order to capture the white blood cells. The cells were lysed thermally by starting the PCR at higher temperature (5 min at 95 °C). The performance of the device was tested using small volumes of human blood (<3 µl) and a typical cell capturing efficiency ratio of 6.67% was achieved with the device. It was also noticed that higher cell capturing ratio can inhibit the PCR process due to the release of proteins from the lysed cells. Another filter-based sample processing

chip was reported by Hui et al. [28]. In this work, two different filters were designed to capture white blood cells and viral cells subsequently. The chips were fabricated using silicon/glass fabrication technology. No quantitative result was reported and the performance of the device was evaluated using the standard PCR and gel electrophoresis.

In a different approach for thermal cell lysis, Lee et al. [29] reported a microchip comprising a PCR unit integrated with DNA extraction capability. In their work, a laser diode was used to increase the temperature of the carboxyl-terminated magnetic beads. Consequently, higher temperature magnetic beads can burst the cell membrane with efficient external mechanical vibration. The efficiency of the device was investigated using various bacterial and viral cells cultures mixed in human serum. In a different work reported by the same group [30], a fully integrated, pathogen-specific DNA extraction device was fabricated on a polymer-based CD platform. Magnetic beads were used for dual purposes, cell capturing and cell lysing agent. The surface of the magnetic beads were modified with pathogen specific antibodies and thus could be used to collect and separate target cells. In addition, laser-induced magnetic beads can act as a micro-heater and thus lyse the attached cells. A vortex mixing step was generated by alternate spinning of the CD using an external device and accurate spin program. The same external spinning method was utilised for fluid handling as well. The efficiency of the device was investigated using different bacterial and viral cells cultures spiked into whole blood.

In a different bead-based DNA extraction approach, Chung et al. [31] reported a serpentine microchannel with immobilised beads inside the channel walls. An external laboratory-based bi-directional microfluidic driving system was used to perform the mixing of lysis buffer and blood with forward and backward flows. The same method was used to capture released DNA on immobilised beads. The DNA extraction efficiency of the device was tested using spiked bacterial cells culture into the blood sample and the efficiency of the device was investigated using PCR and gel electrophoresis (indicating very low DNA recovery levels).

In addition to the above mentioned DNA extraction methods, silica-based solid-phase-extraction (SPE) is the most widely used technique to extract nucleic acids from biofluids using three main steps; bind, wash and elute steps. Basically, nucleic acids adsorb to the silica surface in the presence of a chaotrope. Some combination

of intermolecular electrostatic forces, dehydration and intermolecular hydrogen bonding are involved in the adsorption of DNA on the silica surface [32]. The next step, which is washing process, is performed using ethanol or isopropanol to remove the species that inhibit PCR. Finally, captured nucleic acids on the surface of the silica are resuspended by eluting in a low-salt solution. The main reports in this category involve micro-engineered micropillars, silica beads and sol gels.

Micropillars can be microfabricated inside the channel to increase the surface to volume ratio, thus to increase the binding capacity of the device, in order to capture DNA molecules. In this method the surface of the silica micropillars acts as a binding site to capture DNA molecules. Although this is an efficient approach to increase the surface area, its application is restricted by the required complex and expensive fabrication process (reactive ion etching), which is not suitable for point of care diagnostic devices. On the other hand, the sample needs to be introduced into the device using a positive pressure or an external centrifugation step. In this case, the larger the surface area is, the longer the sampling process is.

Christel et al. [33] reported a micro-device containing micropillars, which yielded a 10-fold enhancement in the surface area in comparison with the standard channel. As the first represented microfluidic-based SPE device, an extraction efficiency of ~50% was reported for this device using a clean DNA sample. Cady et al. [34] reported a DNA purification device with similar micro-structured silicon-coated square-shaped pillars inside a silicon microfluidic channel. In their work, the total surface area was enhanced by 300-600% and cell lysate was used to investigate the efficiency of the device. On average, 10% of the bound DNA could be recovered using 50 µl of the elution buffer. A macro-scale-like elution volume of 250 µl was required to increase the recovery ratio, which is not suitable for the integration with other microfluidic chips in POC devices.

Since the application of micro-structured pillars are limited by complex and expensive microfabrication process, the most widely used solid supports for nucleic acids in a microfluidic chip are limited to silica beads and porous silica beads/sol-gel columns to create packed solid columns. In this method, a post-fabrication process is necessary to create the packed column inside the device. An external pressure source is necessary to introduce the sample into the device and to deliver the reagents necessary for the purification step. Due to the absence of internal cell-lysis and microfluidic mixing steps, this method is limited to samples containing free DNA

molecules, thus not suitable for processing of unlysed cells cultures and whole blood sample.

Sol-gel phase and hybrid sol-gel/silica beads network have been used for the purification of DNA from different biological samples. A sol-gel is a colloidal suspension (sol) that can form a solid network (gel) in a transition phase [35].

The first use of silica resin for the purification of DNA from biological samples inside a capillary channel was reported by Tian et al. [36]. An extraction efficiency of 70% was achieved using direct extraction of the DNA from white blood cells (lysed outside of the device). Wolfe et al. [37] used the same method in a microfabricated microchip and investigated the efficiency of the device using different silica and silica beads/sol-gel matrices for DNA purification process. A 25 μl aliquot of λ-phage DNA in guanidine stock solution was used as the input sample.

A microfluidic DNA purification device was reported by Breadmore et al. [38] using hybrid silica beads/sol-gel structure in a straight channel. In this method, hybrid structure tends to be more stable during the experiment and the device was tested by different biological samples including free DNA sample and diluted frozen blood sample. In the latter experiment, the lysis process was performed outside of the chip using diluted lysed blood sample (100 times dilution).

Wu et al. [39] reported another DNA purification device using hybrid compact silica beads in sol-gel matrix. The device was tested using different biological samples and a typical DNA extraction efficiency of 85% was achieved using free DNA sample. The efficiency of the device was tested using lysed blood sample as well and a typical efficiency of 68% was reported. However, blockage of sol-gel pores was also observed as the result of the presence of the components in the lysed blood.

As an alternative to the standard column materials, organic monoliths with rigid and porous structure provided with pores ranging from nano to micrometer have also been used for DNA purification in microfluidic chips [40, 41, 42, 43, 44]. These monolith structures offer large surface area, high mass-transfer ratio and controllable pore size. Wen et al. [41] reported a DNA purification device in a capillary using a monolith structure. The efficiency of the device for DNA purification was tested using free DNA sample and low volume (<100 nl) diluted lysed blood sample and an extraction efficiency of 85% was achieved using free DNA sample. However, the application of this device was limited to a very low volume lysed blood due to the

chip blockage as the result of the presence of the components in the blood sample. In order to overcome the monolith blockage problem, a novel two-stage DNA purification device was developed comprising a reversed-phase column for protein capture in series with a monolith column for DNA purification process [42]. In this method, 80% of the proteins from a 10 μl blood were successfully captured in the protein capturing stage and a typical DNA extraction efficiency of 69% was achieved using the monolith. The blood sample was pre-processed outside of the device to lyse white blood cells.

Chaotropic-based sample loading followed by an organic solvent wash in the solid-phase extraction techniques may reduce the efficiency of the amplification process. This is because both chaotropic sample and organic solvent are well-known PCR inhibitors. Therefore, a novel aqueous-based pH-induced nucleic acid capture and release technique was developed by Landers group [45, 46] by using a chitosan phase in the extraction process. Beads coated with chitosan, bind DNA molecules at pH 5 and release them at pH 9. The hydrophilic surface of the beads can increase the DNA binding capacity by reducing the non-specific binding of proteins. The efficiency of the device was tested using free DNA sample and small-volume (0.2 μl) lysed blood sample (10-fold dilution using lysis buffer) with typical efficiencies of 67% and 63% respectively.

The majority of the above reviewed works have focused on the solid-phase extraction of nucleic acid with the aim to isolate DNA/RNA molecules from the cell lysate, serum or lysed blood. However, there are a number of integrated microfluidic devices with the ability to perform on-chip cell lysis and purification from various bio-fluids. Hong et al. [47] reported an integrated microfluidic device for extraction and purification of the nucleic acids from bacterial cells in a nano-litre-scale processor. In this device, cells and lysis buffer were introduced into the chip and complete lysis was achieved after several minutes using on-chip rotary mixer. Cell lysate was then flushed over an affinity column packed with oligo-dT polymer magnetic beads. After a washing process, captured DNA/mRNA molecules were eluted in the elution buffer. The capacity of the device was limited to the maximum sample volume of 1.6 nl, which is not suitable for blood-based point-of-care diagnostic devices.

Legendre et al. [48] reported a microfluidic device comprising an integrated online DNA purification and PCR in a valveless glass micro-device. The purification chip was made of silica beads/sol-gel hybrid bed to capture DNA released from various biological fluids. The efficiency of the device was tested using free DNA sample as well as whole blood sample. However, the blood sample was diluted over 120-fold and the lysis process was performed outside of the chip. This microchip was further developed by Easley et al. [49] comprising sequential DNA purification, PCR and electrophoretic separation and detection of target DNA. However, the lysis process was still performed off-chip and nano litre-volume of the diluted lysate was introduced into the chip.

The only integrated microfluidic chip that contains all the necessary steps from sample-in to result-out was reported by Liu et al. [50, 51]. The reported bio-chip consists of sample preparation, amplification and microarray-based detection system. In the sample preparation stage, immune-magnetic beads were used to capture target cells. Cavitation microstreaming was implemented to facilitate cell capturing process from whole blood sample. An external magnet was used to concentrate and separate captured cells inside the PCR chamber during washing process. Cell lysis and DNA extraction was performed using thermal lysis at the first PCR cycle. The efficiency of the device was tested using spiked E. coli cells into the rabbit blood sample. A typical cell capture efficiency of 40% was achieved using Dynabeads. The duration for sample preparation process was reported as long as 50 minutes, which is a very long process and is not suitable for a point-of-care diagnostic device.

As described earlier in this section, all of the reported sample processing microchips can be divided in three main groups as follows:

- Thermal lysis and extraction chips using integrated PCR
- Solid-phase extraction using magnetic bead
- Solid-phase extraction (SPE) method using micropillars, silica beads and silica monolith

Thermal cell lysis is the simplest method to lyse and extract DNA from target cells. In this case, the sample processing step can be simplified to target cell capturing and separation process. However, this method is limited to purified cells cultures and cannot be used with more complicated bio-fluids such as blood. Another problem with this technique is the sensitivity of PCR to large sample volume. Cell debris

released from lysis process contains components that can inhibit PCR process [24]. Therefore, this technique is limited to a very small sample volume.

The next group of purification devices have used magnetic beads to selectively capture and separate target cells from bio-fluid. The lysis step in majority of them takes place using thermal cell-lysis either during PCR [50, 51] or by laser-inducing of the same magnetic beads [29, 30]. Since the lysis step takes place inside the PCR chip, the application of this technique is limited to small sample volumes. Another problem with this method is the fact that immune-magnetic beads are highly selective and are designed to bind to the specific cells. Therefore, different magnetic beads with different coatings are necessary for different target cells. Another disadvantage of this method is that the magnetic beads cannot capture free target DNA/RNA molecules existing within the serum.

The most efficient nucleic acids purification chips were developed based on the application of SPE matrices. The efficiency of these chips was comparable to the standard magnetic bead-based and column-based commercial extraction kits. However, all of the reported works based on this technique have used serum lysate, free DNA, cells lysate and/or lysed blood in diluted format as the input sample. Despite their excellent nucleic acids capturing efficiency, there are some major limitations with using this technique within point-of-care diagnostic devices. First of all, these chips are more suitable for nucleic acids purification and the extraction step needs to be performed off-chip using standard bench-top techniques. This is because of small pore sizes in highly packed SPE matrices. Crude samples such as blood and high concentrated cells lysate contain large bio-molecules such as proteins and peptides that might block the pores and reduce the efficiency of the device. Another problem with this technique is related to fluid resistivity of the SPE matrices. Although, more compact silica network can increase the efficiency of the device, it also increases the fluid resistivity, thus increasing the total sampling time. Large volume of the buffer necessary to elute captured DNA molecules from compact silica network is another disadvantage of these chips.

Therefore, none of the above reviewed works has successfully developed a fully functional sample processing bio-chip capable of extraction and purification of nucleic acids from a crude and heterogeneous sample such as whole blood. However, SPE systems are more suitable for POC applications when detecting minimal

residual disease and infectious agents with low copy number in the sample. However, design of SPE systems need to undergo fundamental evaluation to be suitable for both DNA extraction and purification process with increased capacity, high efficiency and low elution volumes. In this work, solid-phase extraction method was employed to design a microfluidic DNA extraction and purification device. However, the structure of the immobilised SPE systems was changed to a suspended magnetic beads format to be more suitable for cell lysis and extraction of DNA molecules from whole blood. In this method, an active and efficient magnetic mixing pattern was implemented to statistically increase the efficiency of cell-lysis and DNA capturing. Detail of the designed magnetic mixer can be found in *Chapter 5* and *Chapter 6*.

1.3 Aims and Objectives of the Research

The main aim of this research is to design a fast and simple DNA extraction and purification system to address the need for such a system in a point-of-care diagnostic device. The desired characteristics of such a system are fast processing, low cost, high yield and quality. Fast and low cost diagnostic test are the most important motivations behind the idea of point of care diagnostic chips that can compete with the traditional assays. In the existing bench-top robotic extraction/purification devices, this process takes up to an hour. Adding up this time with the amplification and detection time, it is not desirable for a point-of-care diagnostic testing.

The next important parameter is the yield of purified DNA molecule. It is very unlikely that a chip-based purification can compete with a spin-column purification method, which is the gold standard. A reasonable yield sufficient for the amplification process is the minimum requirement for such devices. The last parameter which is more important in the amplification process is the purity of the harvested DNA molecules. This is important because PCR is very sensitive to impurities that might inhibit the amplification process. Nevertheless, some isothermal amplification techniques such as LAMP (Loop-mediated Isothermal Amplification) are less sensitive to the purity of the DNA.

In order to design an optimised nucleic acid extraction and purification chip, most of the available literature has been reviewed and particular attention has been given to adapt the most suitable DNA extraction technique. The two most common DNA isolation methods are spin-column and magnetic bead-based protocols. Various kits are available in the market from different suppliers such as *Qiagen, Invitrogen, AGOWA, Bilatec* and *Promega*. The most common steps in the nucleic acid extraction and purification process are the incubation of sample in the lysis buffer, binding process, washing process and the elution step. Some kits have specific temperature requirements during incubation and other kits are not sensitive to the temperature. Despite the efficiency of reagents on lysing the target cells and loss of DNA during the washing process, efficient mixing of sample and magnetic beads is the key-factor in the yield of the magnetic bead-based kits. The other important factor is the potential of magnetic beads to specifically separate the purified target DNA molecules from the cell debris and the rest of the lysed blood. To achieve this, an on-chip clamping and heating mechanism is necessary. Therefore, based on these requirements and easier automation potential, magnetic bead-based purification protocol was selected in this research. The specific objectives of this research are summarised as follows:

- Design of suitable microfluidic environment to perform the nucleic acid extraction and purification steps (the options are: continuous mode using microchannel and static mode using microchamber).

- Using numerical simulation techniques to investigate time varying magnetic field based mixing of sample (whole blood) and lysis buffer containing suspended superparamagnetic beads to ensure efficient mixing and binding of released DNA molecules to the beads.

- Carrying out experimental investigation of switching magnetic field to determine optimised frequency of mixing.

- Carrying out experimental investigation of magnetic field clamping and washing to determine optimised DC current and required flow rate to minimise loss of magnetic beads.

- Designing and developing incubation temperature control circuit using the same current carrying conductors used for switching magnetic field.

- Selection of a suitable magnetic bead-based DNA extraction kit and adapting the bench-top protocol for the designed microfluidic environment.

- Designing and fabricating microfluidic DNA extraction and purification microchips and experimentally investigating the DNA extraction efficiency using whole blood.

1.4 Contribution to knowledge

The following contributions to knowledge are claimed:

- Design of a magnetic bead-based DNA extraction system using microfluidic microchamber and time varying magnetic field.
- Design, development and optimisation of suitable internal and external magnetic field sources to achieve maximum mixing efficiency of DNA molecules and magnetic beads.
- Development of a numerical model suitable for further investigation and optimisation of the designed DNA extraction system.
- Determination of the optimised switching frequency and current using numerical analysis and experimental validations.
- Development of an on-chip temperature control system and magnetic bead clamping process using the same current carrying conductors used for switching magnetic field.
- Introduction and development of a novel dynamic switching magnetic field to increase the efficiency of the magnetic mixing and magnetic clamping using quadrupolic and solenoidal field patterns.
- Adaption of the manual DNA extraction protocol to the automated friendly chip-based extraction protocol with shorter processing time.
- Biological validation of the DNA extraction efficiency using designed DNA extraction microchips and non-pathogenic bacterial samples.

1.5 Thesis Structure

The main body of the thesis comprises eight chapters and two appendixes containing the Author’s list of publications and a schematic diagram of the designed power

supply. Each chapter starts with a brief introduction and ends with concise summary of the work done in the chapter.

Chapter 2 reviews the most important reported works on various micromixing devices. Generally, the reported mixers have been categorised in two main groups as passive and active micromixing platforms. In passive mixers, the driving force is entirely geometrical and the mixing takes place mainly by diffusion in various schemes by using multi-lamination techniques. In some other passive mixers the mixing takes place through chaotic advection by modifying the channel geometry or implementation of various types of grooved obstacles. Active mixers are further categorised based on their actuation force as micro-stirrers, acoustic, electrokinetic and magnetic-based actuations. At the end of the chapter, a mixing device is introduced based on the magnetic actuation and magnetic beads.

Chapter 3 gives a brief description of the magnetic materials and response of different magnetic materials exposed to an external magnetic field. In this chapter, the strength of magnetic force induced on a magnetic bead was calculated mathematically. This calculation is the base of the magnetic force calculations in the numerical simulations performed in *Chapter 4* and *Chapter 5*.

In *Chapter 4*, a commercial simulation package is employed to perform numerical investigations on different aspects of the magnetic coils in order to design a suitable actuation mechanism for the mixing unit. At the beginning of this chapter, the simulation package has been introduced and the accuracy and methodology of the magnetic simulation has been studied using a series of evaluation simulations. Where possible, the magnetic modelling was performed in three-dimensional simulation mode. 2D simulation mode was used in some simulations, which have axial symmetries. In this mode, the accuracy of the simulation can be improved by increasing the total number of elements in the mesh-generation process. Various types of conductor geometries have been investigated to be used for magnetic actuation in internal coil arrangements. After selection of coil geometry, optimisation process was performed by studying the effect of different geometrical variables such as conductor thickness and coil external diameter. The optimisation process was applied to the external coil arrangements as well by studying the effect of coil thickness and coil external diameter as the key-factors. Finally, the effect of inter-coils mutual effect was investigated in two coil arrangement scenarios as the lateral

and cross mutual effects between in-plane coils and face-to-face coils. This study led to the introduction of a novel dynamic magnetic field switching technique, which, can be used to improve the efficiency of the magnetic bead mixing in the chamber.

In *Chapter 5*, the optimised coils in *Chapter 4* are used to study the bead trajectories using a developed *Matlab* code linked with *COMSOL* multiphysics. This code was applied to both internal and external coil arrangements and two sizes of magnetic beads. The result of this study confirmed the concentric movement pattern of magnetic beads resulting in a clump of beads collected at the centre of the chamber. A surface coverage study was performed to estimate the surface coverage factor, which gives the information about the efficiency of the DNA collection process using resulted beads trajectories.

Chapter 6 is devoted to a series of experiments to validate the results of numerical simulations provided in *Chapter 4* and *Chapter 5*. A series of magnetic coil bobbins were fabricated and wound to perform the magnetic field strength measurements and thermal analysis using a temperature sensor. The thermal activity of the coils were measured in DC and AC mode of supplied current representing the switching mode during mixing and constant current mode during magnetic clamping mode. The effect of embedded heatsink was also investigated on the ratio of heat generations in the coils. A brief account of the fabrication process is provided for the microfabricated microchamber, supplementary docking station, capillary test-rig and the electronic power/control unit. The capillary test-rig was used to investigate the behaviour of the magnetic beads inside a capillary tube representing a section of the microchamber. This experiment resulted in adjustment of the frequency of the switching magnetic field. The effect of dynamic magnetic field switching was also investigated using quadrupolic and solenoidal field patterns. A 25µl PMMA/PDMS chamber was used to investigate the filling performance and investigate the efficiency of magnetic clamping force inside the chamber.

Chapter 7 provides the results of the experimental evaluations of the designed DNA extraction device using real biological samples. In order to achieve this, bacterial DNA sample and cell cultures were spiked into the blood sample and the efficiency of the cell lysing and DNA binding was investigated using microfluidic microchamber and external magnetic coils. A pre-optimisation process was also performed in order to adapt the manual bench-top extraction protocol to a more

suitable automated chip-based extraction protocol. The adaption process was carried out using three different magnetic bead-based extraction kits and a standard column-based extraction kit was used for bench-marking purpose. Selected modified extraction protocol was used to investigate the efficiency of the extraction device. The extracted DNA samples were analysed using UV spectrophotometry and quantitative real-time PCR assay to obtain the quality, yield and recovery rate of the extracted sample.

Chapter 8 gives an overall conclusion on the work performed in this thesis and provides some suggestions for future research, which may potentially improve the performance of the extraction/purification process and increase the reliability of the proposed system for use in the point-of-care diagnostic devices.

CHAPTER 2

PASSIVE AND ACTIVE MICROMIXERS - A SURVEY

2.1 Introduction

In the past two decades, tremendous effort has been devoted to miniaturization in analytical chemistry and life science. Miniaturization of bio/chemical reactions is attractive for its potentials and advantages such as lower sample and reagent consumption, fast reaction time, lower cost, high throughput and automation possibility. The process of miniaturization involves microfabrication and employing microfluidics in general and micropumps, microvalves, biosensors and micromixers as supplementary parts. The applications of microfluidic are well studied from micro arrays and DNA sequencing to sample preparation and cell separation as well as DNA/protein detection. Because of its wide application area and fundamental role, microfluidics has attracted major interest from both industry and academia. The number of published literature is increasing rapidly in this area and many books are dedicated to microfluidics entirely [52-54].

Besides fluid handling and micropumps, micromixers are one of the most important parts of the miniaturized microfluidic devices; the so called lab-on-a-chip (LOC)

platform. Micromixers perform the key-role in such devices in mixing different biofluids and chemical reagents. This mixing is essential for the chemical reactions to extract the desired result for downstream applications. The application of mixing is widely employed from drug delivery and sequencing to nucleic acid synthesis and protein folding as well as enzyme reaction. Recently, some extensive reviews have been published on micromixers, which cover all major published reports on different types of the microfluidic mixings from early diffusion mixers to more recent chaotic mixers [55-59]. More systematic reviews on micromixers can be found in [60-63].

The purpose of this chapter is to critically review the microfluidic micromixing mechanisms with the scope to summarize different types of mixers published in literatures. Although various types of micromixers will be reviewed in this chapter, the application of micromixing in LOC platform is more interesting. In LOC platform, the focus is on point of care (POC) devises with the application of nucleic acid purification process. A mixing unit is an important part of a POC device where complex chemical and biological reactions take place to release DNA molecules from target cells. The freed DNA molecules then will be collected and separated using efficient mixing of collection agents inside the lysate. Therefore, the optimised mixing mechanism must be adopted based on this specific application.

2.2 Microfluidics

The term microfluidics describes the behaviour of fluid in sub-millimetre sizes and deals with control and manipulation of small volume fluids in such small dimensions. In fact, microfluidic systems need to be designed and work at intersection between multidisciplinary fields of physics, chemistry and engineering. The main reason to study the behaviour of fluid at micro-scale is that the dominant forces may differ from macro to micro-scales. In micro-scale, surface tension is a major factor that might change the behaviour of the fluid. In addition, the higher surface to volume ratio, higher mass-heat transfer ratio and low Reynolds number are other characteristic properties of microfluidic which needs to be fully understood and considered in design of any small-scale application. In this section, a brief introduction on microfluidics and its key-definitions is provided to describe the behaviour of fluid in small scale. This introduction will help to understand the concept of micromixing and its challenging research.

2.2.1 Basic Concepts and Definitions

One of the important properties of a fluid is defined as viscosity (μ) which can be described as the ratio of shear stress to velocity gradient. In other word viscosity describes the resistance of a fluid to any deformation caused by either external body immersed in fluid or between different layers inside the fluid. Viscosity is important because it acts as an opposing force in mixing of two liquids. Viscosity of a fluid might change by changing the temperature or pressure but if the viscosity of a fluid is constant at all shear rates at constant temperature and pressure; the fluid is called Newtonian Fluid. The relationship between the shear stress and viscosity and velocity in Newtonian fluid can be described as follows:

$$\tau = \mu \frac{du}{dy} \tag{2.1}$$

In which, τ is the shear stress, μ is the fluid dynamic viscosity coefficient and du/dy is velocity gradient. Water and most water-based fluid which are the fluid of interest in micromixing for POC devices are Newtonian fluids.

Another important characteristic of a fluid is the flow regime when the fluid is forced to move. In microfluidics, the flow regime is mainly laminar which can be described as parallel streamlines with no disturbance between the lines. Laminar flow is associated with high momentum diffusion and low momentum convection as well as independent velocity and pressure from time. On the other hand, turbulence flow regime can be described by chaotic and stochastic properties. Turbulent flow is defined by low momentum diffusion, high momentum convection and dependency of velocity and pressure to time and space. Whilst viscous force is the dominant force in laminar flow, inertial force plays the main role in turbulent flow. Therefore, the flow regime must be relative to viscous and inertial forces. This relationship is defined as Reynolds number as a dimensionless parameter and is given by the ratio of inertial force ($\rho V^2 L^2$) to viscous force (μVL) as follows.

$$Re = \frac{inertial\ force}{viscous\ force} = \frac{\rho V^2 L^2}{\mu VL} = \frac{VL}{\nu} \tag{2.2}$$

$$\nu = \frac{\mu}{\rho}, (\frac{m^2}{s})$$

Where, V is the characteristic velocity of fluid, L is characteristic length of the geometry, ρ is the fluid density, μ is the dynamic fluid viscosity and ν is the kinematic viscosity of the fluid.

Therefore, the flow regime can be identified by calculation of Reynolds number. In macro-scale, the dominant force is inertial force thus the flow regime is turbulent. On the other hand in micro-scale, fluid viscosity dominates and the flow is laminar. As a practical example, the water flow inside the pipe behaves laminar or turbulent at Reynolds numbers below 2300 and above 4000 respectively. In this example, the flow regime at Reynolds number between 2300<Re<4000 is transient which means partially laminar and partially turbulent. Therefore, the flow regime in micro-scale is completely laminar (Re<1), which makes the idea of mixing a very challenging topic at this low Reynolds number.

2.2.2 Equation of Fluid Dynamic (Navier-Stocks Equations)

Navier-stocks (N-S) equations are a non-linear set of differential equations which explain the motion of fluid in general. This equation is extracted by applying Newton's second low to fluid motion by assumption of continuum fluid and small fluid velocity compared to speed of light. The general form of these equations has no general solution and is used in computational fluid dynamics. The general form of N-S equations can be simplified by assumption of incompressible flow. This assumption explains that the divergence of velocity is zero ($\nabla . u = 0$) and the density of fluid is independent of pressure. Therefore, the simplified form of N-S equations can be written as follow:

$$\rho \frac{du}{dt} = -\nabla P + \rho B_f + \mu \nabla^2 u \tag{2.3}$$

Where, P is the pressure, u is the velocity, μ is the viscosity and B is the other body forces

In microfluidics, the fluid flow is called pressure-driven flow, which can be described by poiseuille law. This equation can be derived from N-S equations by applying boundary condition in microchannels. When a fluid is bounded by solid walls, the fluid velocity is zero at liquid-solid interface. This is because of molecular interactions between two phases which forces the fluid molecules to seek the

momentum and energy equilibrium of solid surface. This phenomenon is called no-slip condition and will be used as boundary condition at interface between fluid and solid surfaces. Therefore, the flow pattern by applying no-slip condition can be extracted from N-S equations, which is extracted as follow for two dimensional flows.

$$\frac{\partial P}{\partial x} = \mu \frac{\partial^2 u}{\partial y^2} \tag{2.4}$$

By applying the boundary condition and y=d/2:

$$u(y) = \frac{1}{2\mu}\frac{dP}{dx}\left(\frac{d^2}{4} - y^2\right) \tag{2.5}$$

In which, u is the velocity, μ is the dynamic viscosity and P is the pressure. This equation describes a parabolic pattern of fluid velocity with highest point placed at the centre of the channel (Figure 2.1).

2.3 Micromixing: Concepts and Limitations

The low Reynolds number, dominant viscous force and strong surface tension imply the non-turbulent behaviour of the fluid at small-scale fluids mixing concept. The flow regime is completely laminar, thus no mixing takes place at fluids interface. Nevertheless, in laminar flow pattern diffusion is the only phenomena that might help the mixing. In addition, a chaotic mixing pattern can be developed inside the fluid to enhance the mixing by various schemes.

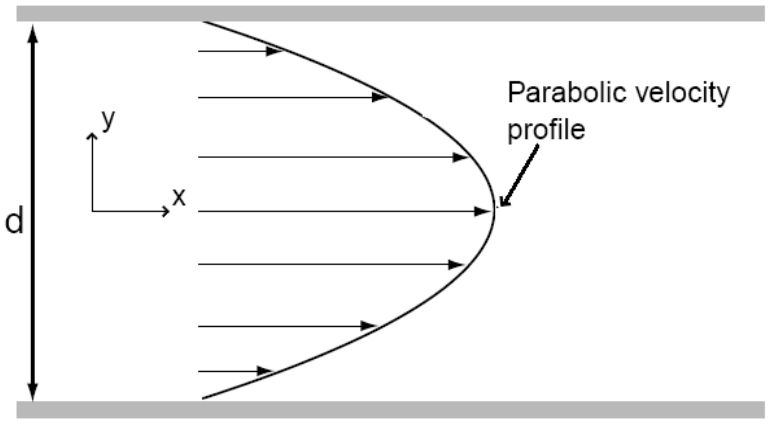

Figure 2.1. Velocity profile of a steady pressure-driven laminar flow with no-slip boundary conditions developed in a micro-channel.

In general, micromixers can be categorised as passive and active mixers. Passive mixers are the most developed type of mixers and tremendous efforts have been devoted by different research groups on this subject. The interesting part of passive mixing is that the mixing process mainly relies on diffusion and to some extent chaotic advection and no external source of energy is required. On the contrary, active mixing relies on external source of energy to perform the mixing. In this type, the mixing process is mainly based on chaotic advection. Therefore, in the following sections, the diffusion and chaotic advection phenomena are discussed briefly prior to reviewing passive and active mixers.

2.3.1 Diffusion

Diffusion is the process of statistic distribution of the given entities over space caused by random motion of those entities. In this distribution, the given entity moves from regions of higher chemical potential towards lower chemical potentials. In physics, diffusion can be realised as heat diffusion and molecular diffusion or Brownian motion which is the subject of this section. Brownian motion acts in the presence of non-uniform distribution of molecules or particles inside a fluid. Diffusion can be described mathematically by Fick's second law as follow:

$$\frac{\partial \phi}{\partial t} = D\frac{\partial^2 \phi}{\partial x^2} = D\nabla^2 \phi \tag{2.6}$$

Where, Φ is the concentration of particles or molecules, D is the diffusion coefficient and t is the time. By assumption of steady state diffusion which means the concentration of molecules will not change by time, the above equation can be simplified to Fick's first law:

$$J_D = -D\frac{\partial \phi}{\partial x} \tag{2.7}$$

Where, J_D is the diffusion flux and x is the position. This equation measures the amount of substance which flows through the unit area during short time intervals. An estimation of the average time of diffusion for the suspended particles inside the fluid over a given distance of L is given by:

$$\tau \cong \frac{L^2}{2D} \tag{2.8}$$

Where, τ is the time of diffusion and D is the diffusion coefficient or diffusivity and is defined as:

$$D = \frac{KT}{f_f} \tag{2.9}$$

Where, T is the absolute temperature, K is the Boltzmann's constant (1.35×10^{-23}) and f_f is frictional coefficient, which is the resistance force against diffusion. For a spherical particle with radius of r suspended in liquid with dynamic viscosity of μ, f_f can be defined as:

$$f_f = 6\pi r\mu \tag{2.10}$$

Equation (2.8) describes that the diffusion time is proportional to square of diffusion length and Eq. (2.9) shows the temperature dependency of diffusion coefficient. By increasing the temperature the fluid molecules, which have more energy, will be excited and increase the diffusion speed. Length dependency of diffusion time describes the limitation of diffusion mixing over longer distances. As an example, the diffusion time for a spherical particle with radius of $r = 1\mu m$ over a distance of $L = 100\mu m$ suspended in water can be estimated as long as $\tau \cong 13\ hours$, which is a very long diffusion time. The same average time can be calculated for a shorter diffusion length of $L = 10\mu m$, which reduces the diffusion time to $\tau \cong 7.93\ min$. Therefore, diffusion mixing over long distances seems to be unrealistic and is not desirable in bio-chemical analysis systems.

2.3.2 Chaotic Advection

Besides diffusion, advection is another form of mass transfer in fluid flows. Since advection acts at parallel direction to the main fluid flow, it is not functional at transversal mixing process. However, the so-called chaotic advection might enhance the mixing in microchannels significantly. Creation of heterogeneous mixture of homogeneous domains by creation of chaotic advection leads to a homogeneous mixture at molecular level by diffusion effect between adjacent domains [64]. Creation of chaotic advection in macro-scale can be performed by application of stirrers for example. In micro-scale channels, such techniques cannot be employed and chaotic advection is mainly created using special geometrical modifications or three-dimensional structures. Alternatively, an external force can be used to create chaotic advection in active micromixers.

2.4 Passive Micromixing Platform

The first type of micromixing device was based on passive mixing platform due to the simplicity of the concept. Passive mixers can be further categorised based on their arrangements of mixing phase to lamination, injection, droplet and chaotic advection categories. Figure 2.2 shows a schematic diagram of the different mixing schemes in passive micromixing platform.

2.4.1 Basic T-mixer and Y-mixer

As discussed earlier, mixing in micro-scale is based on diffusion phenomena. To achieve fast and efficient mixing, the mixing path needs to be decreased and contact surface at liquid-liquid interface need to be increased. The simplest diffusion mixing can be realised using a two inlet T or Y-shape channel [65, 66]. Two different streams of fluid enter from each inlet and join at the junction and create laminar flow through the channel. Since the mixing here takes place merely by diffusion, a very long mixing channel is necessary. Alternatively, mixing can take place in shorter channels by increasing the Reynolds number [67, 68]. Higher Reynolds numbers can be achieved at the very high fluid flow-rates. Figure 2.3 illustrates the concept of lamination mixing using T- and Y-mixers [60].

Wong at al [68] reported a chaotic mixing at Reynolds number of 500 in a T-mixer at velocity of 7.60 m/s and pressure of 7 bars. Although, a chaotic mixing can be created at this high velocity, it requires a very high supply pressure and high rigidity microchannels and strong bonding technique. Figure 2.4 illustrates this type of mixer at different applied pressures.

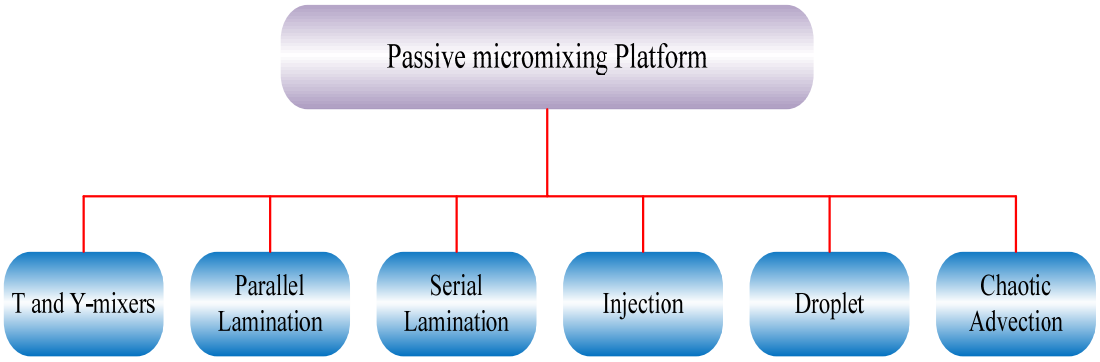

Figure 2.2. Schematic diagram of different mixing schemes in passive micromixing platform

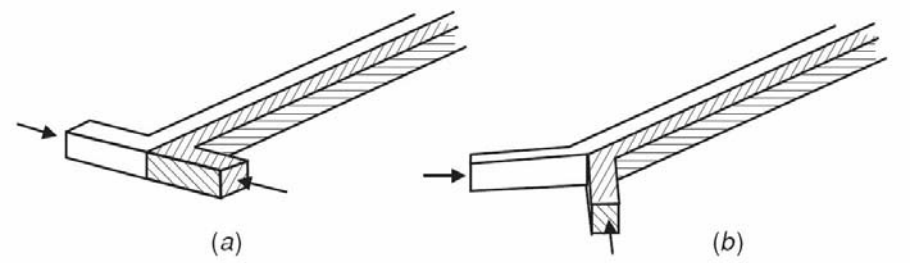

Figure 2.3. The concept of lamination mixing. a) T-mixer, b) Y-mixer. (Adopted from [60])

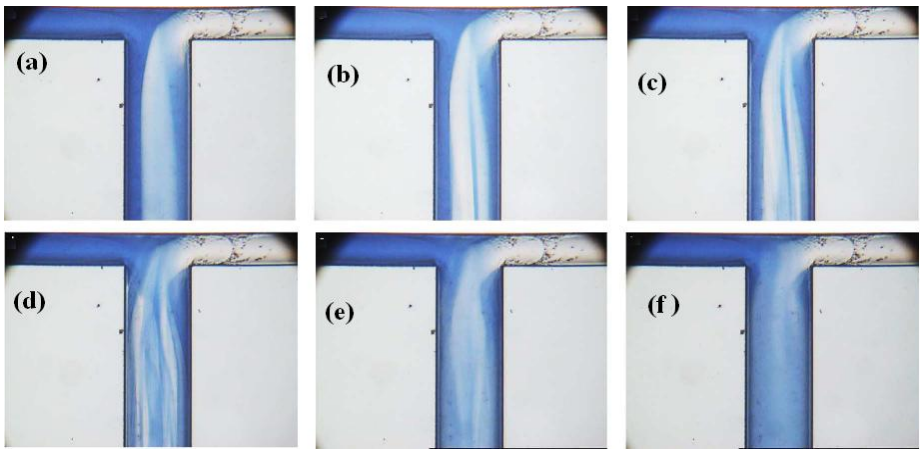

Figure 2.4. Chaotic mixing at high Reynolds number and high flow velocities at T-mixer at different pressures. (a) 1.12 bar; (b) 1.88 bar; (c) 2.11 bar; (d) 2.48 bar; (e) 2.77 bar, (f) 4.27 bar [60].

Another method to facilitate the diffusion mixing in T-mixer is to decrease the diffusion length. Hinsmann et al [69] reported a rapid diffusion mixer by reducing the diffusion length to 5μm in a channel with 10μm depth and 1mm width. In this work two inlet streams were redirected in which they laminate on top of each other. Diffusion can take place in 100ms in stopped-flow mode. The mixing performance can be enhanced by roughening the channel walls [70] or throttling the channel entrance [71]. Alternatively, the mixer can be further modified by implementation of obstacles inside the channel to create vortices and chaotic advection. This modified version of basic mixer will be discussed in chaotic advection mixing section.

A numerical simulation of mixing characteristic of a T-mixer with rectangular cross-section can be found in [72]. In this CFD simulation, the efficiency of mixing is investigated for three different flow regimes and various Reynolds numbers.

2.4.2 Parallel Lamination Micromixing Scheme

An effective method to improve the diffusion mixing is to increase the contact surface between two flows by creating multi-lamination flow configuration. In this

concept, instead of using long mixing path, two main flow streams will be divided to the number of sub-streams to increase the contact surfaces. Diffusion takes place at each narrow channel very quickly, in shorter mixing path [71-77]. Another method to increase the contact surface is by making interdigitated channel structure [78, 79]. The flow is usually driven by pressure, but can be generated using electrokinetic forces as well [80-82]. The concept of multi-lamination and reported parallel lamination mixers are illustrated in Figure 2.5 as well as reported interdigitated mixer.

Multi-lamination scheme can be used in a vortex mixer to enhance the mixing by creation of fast vortices in three-dimensional mixing pattern. In this type of mixing, a circular chamber [83, 84] is used with multiple inlets with a central outlet at top of the chamber. Hardt et al [85] numerically analysed a model of vortex mixer to investigate the performance of 3D vortex mixing. It was concluded that self-rotation effect takes place above the critical value of Reynolds number of 2.32. The result of simulation was confirmed by experimental analysis using microscopy analysis (Figure 2.6).

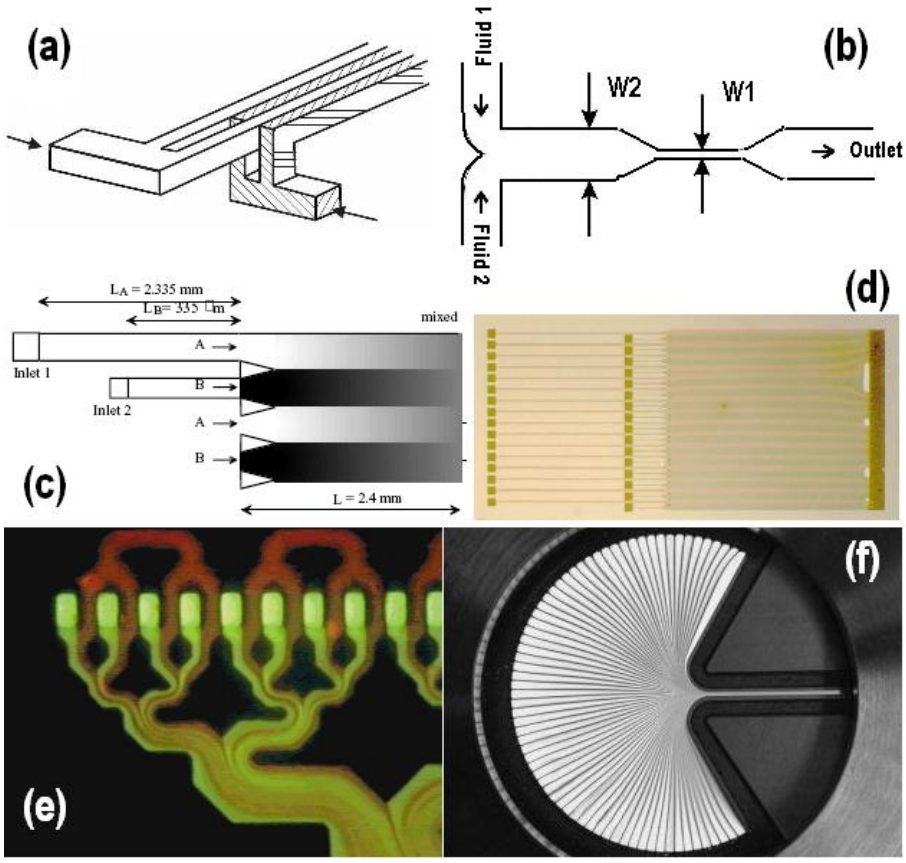

Figure 2.5. Multi-lamination mixing scheme; (a) the concept [60]; (b) the concept of narrow channel to increase the diffusion speed [73]; (c, d) principle of lateral mixing and mixing of green and red ink at P=7.8 kPa [76]; (e) microfabricated parallel mixer [77]; (f) interdigitated channel structure [79].

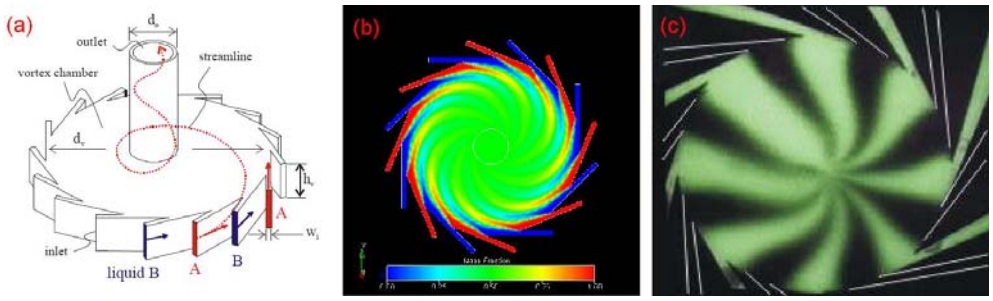

Figure 2.6. Vortex micro-mixers; (a) concept of the mixer, (b) cross-section view of vortex chamber showing mixing process (green indicates complete mixing), (c) a video capture of mixing dye at low velocity [83].

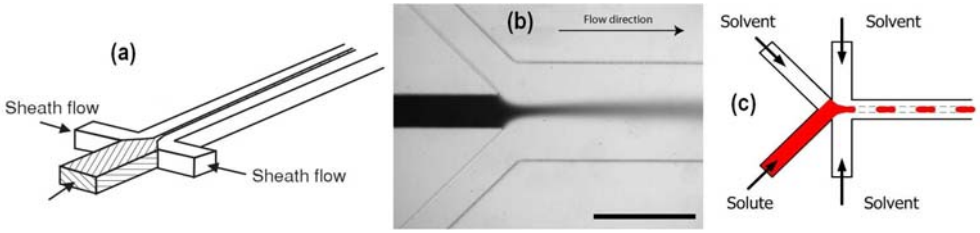

Figure 2.7 Parallel lamination mixing using hydrodynamic focusing. (a) The concept of hydrodynamic focusing technique [60]; (b) Image of blue food colouring stream in the middle inlet and two sheath water streams on sides [88]; (c) Segmented Hydrodynamic focusing [89].

Hydrodynamic focusing is another concept of multi-lamination mixing scheme which is used to reduce the diffusion length in order to accomplish the fast diffusion mixing. In this design, a relatively long channel is used with sample flow entering from the middle inlet which is sandwiched between two sheath solvent streams from side inlets (Figure 2.7a). Since the length of diffusion in this type of mixer can be reduced to a very narrow stream, the mixing process can take place in less than a second. A very narrow mixing channel of 10×10 μm was used by Knight et al [86] to investigate the performance of the mixing by hydrodynamic focusing technique. The width of sample flow in this method can be narrowed down by adjusting the pressure ratio of sheath flow and a complete mixing can be achieved in millisecond range [87]. This fast mixing is due to the very narrow diffusion length, which is a few micrometers in length, thus diffusion takes place instantly. A practical application of this type of mixer was used for cell infection (Figure 2.7b) by Walker et al [88]. A combination of hydrodynamic focusing and time-interleaved segmentation (Figure 2.7c) was reported by Nguyen et al [89] by adding another solvent inlet in the middle part. In this method the solute will be injected into the channel as a series of interleaved segments. Although hydrodynamic focusing reduces the transversal mixing path, segmentation technique reduces the axial mixing path, hence, improve the mixing efficiency.

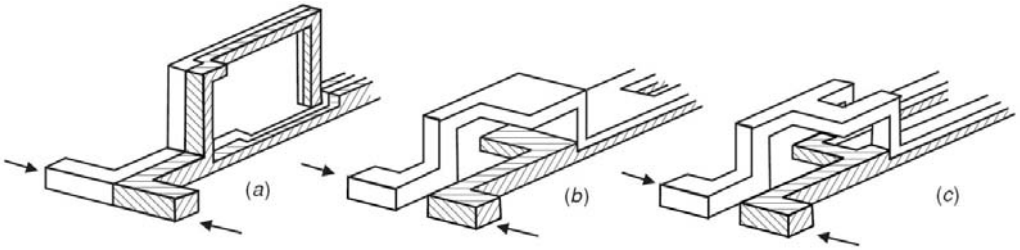

Figure 2.8. The concept of serial lamination scheme in various split and recombining configurations [60].

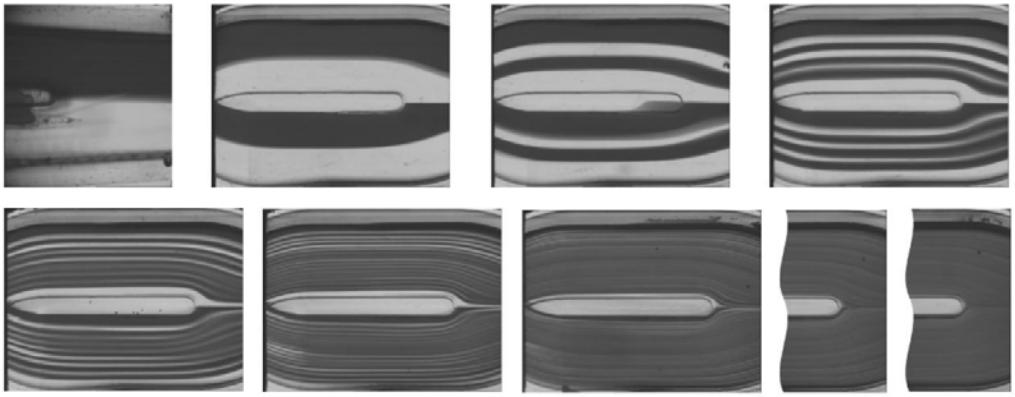

Figure 2.9. Optical inspection image of micromixing using multi-lamination technique in SAR mixer. The dark and light grey colours are blue dyed water and glycerol-water solution respectively [93].

2.4.3 Serial Lamination Micromixing Scheme

An alternative to parallel lamination technique to increase the contact surface between two liquids is called serial lamination technique. In this method, to increase the contact surface, fluid steams will be created inside the main channel instead of using parallel multi-channels. To create multi-fluid streams inside the channel, a so-called split and recombine (SAR) technique is employed. In this technique, the main fluid steams will be split and redirected by re-shaping the channel geometry with subsequent recombining the streams by further rejoining the split channels [90]. This process might take many times to increase the diffusion mixing by decreasing the diffusion length. The conceptual diagram of serial lamination technique using split and recombine technique is illustrated in Figure 2.8 for variation of SAR technique arrangements. The split and combining method could be achieved in various configurations such as, vertical splitting and then horizontal combining (a) or horizontal splitting and vertical combining (b, c).

Serial mixing was first reported by Branebjerg et al. [91] and Schwesinger et al. [92] to achieve fast diffusion mixing by application of multi-lamination flow streams.

Since then, different types of SAR mixers have been developed by various groups, but the concept remains the same [93-95]. The most interesting part of SAR mixers is that the multi-lamination pattern is achievable at low Reynolds number (<1) and low pressure (0.2-5 kPa) [91]. Figure 2.9 depicts the result of micromixing in SAR micromixer in a series of screen shots.

SAR mixing concept was further elaborated by application of electrokinetic driven multi-channels [94, 95]. In this modified version, multiple intersecting sub-channels will be used to laminate and change the flow pattern. He et al [94], used electro-osmosis flows in intersecting sub-channels to enhance mixing (Figure 2.10). In a different work reported by Melin et al [95], a pressure-driven flow was used in intersecting channel geometry to enhance mixing by changing the flow pattern (Figure 2.11). This design works only on plugs of two mixed liquids.

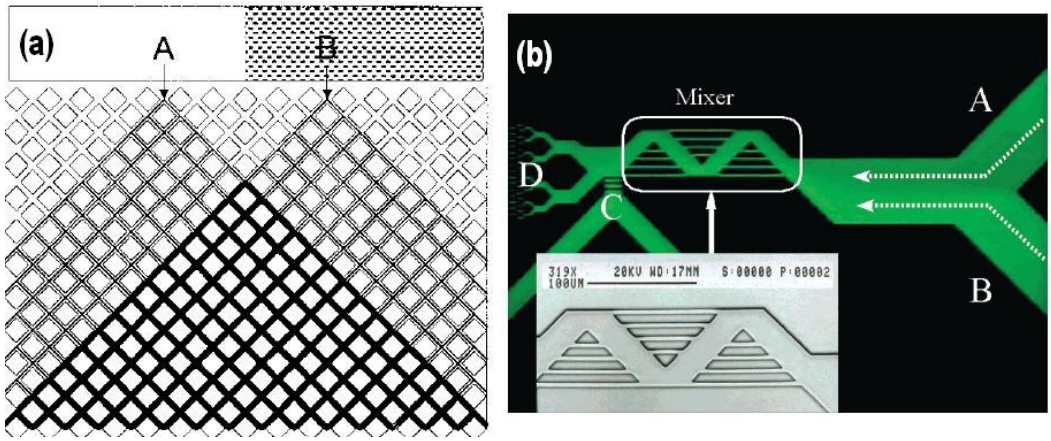

Figure 2.10. electro-osmosis-driven SAR mixer. (a) the concept of mixing using intersecting channels showing how the mixing might occur on two discrete streams (darkened colour shows the mixing region). (b) the actual microfabricated mixer and SEM image of that [94].

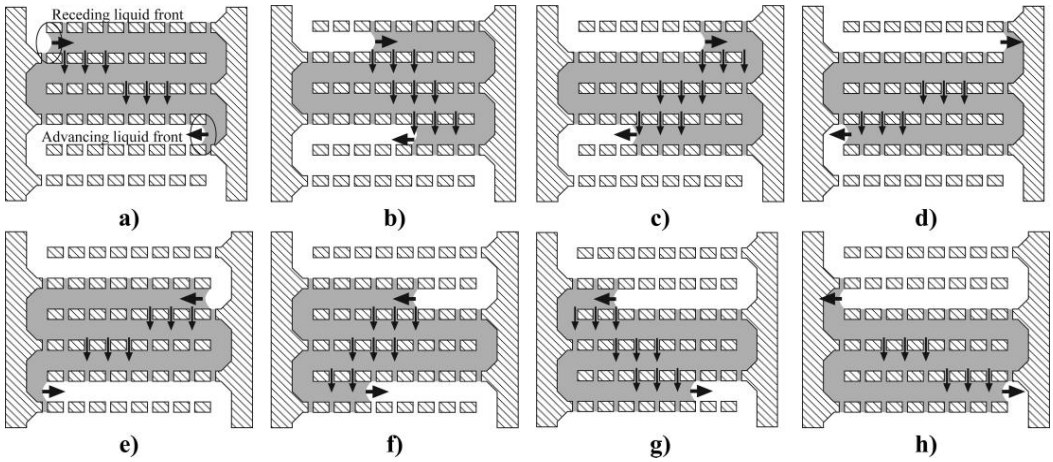

Figure 2.11. Schematic diagram of intersecting liquid plug showing the flow pattern inside the mixer at different times [95].

Fluids travelling inside a curved pipe or channel experience a radial pressure gradient as the result of interplay between inertial forces and centrifugal effects. These effects act along axial direction and radial direction along conduit's curvature respectively. Fluid flow with these characteristics is known as Dean Flow. Under appropriate conditions, Dean Flow pattern can be generated in microchannels to enhance the mixing by creating transversal flow field. A two-dimensional SAR micromixer was reported by Sudarsan and Ugaz [96] by generating multi-laminated flow pattern by characteristic application of Dean Flow. Figure 2.12 illustrates the creation of transversal flow under various Dean Numbers (a, b) which can be used to create multi-laminated flow pattern(c). Mixing efficiency using planar SAR mixer is illustrated in Figure 12d for various Reynolds and Dean Numbers after four recombination blocks.

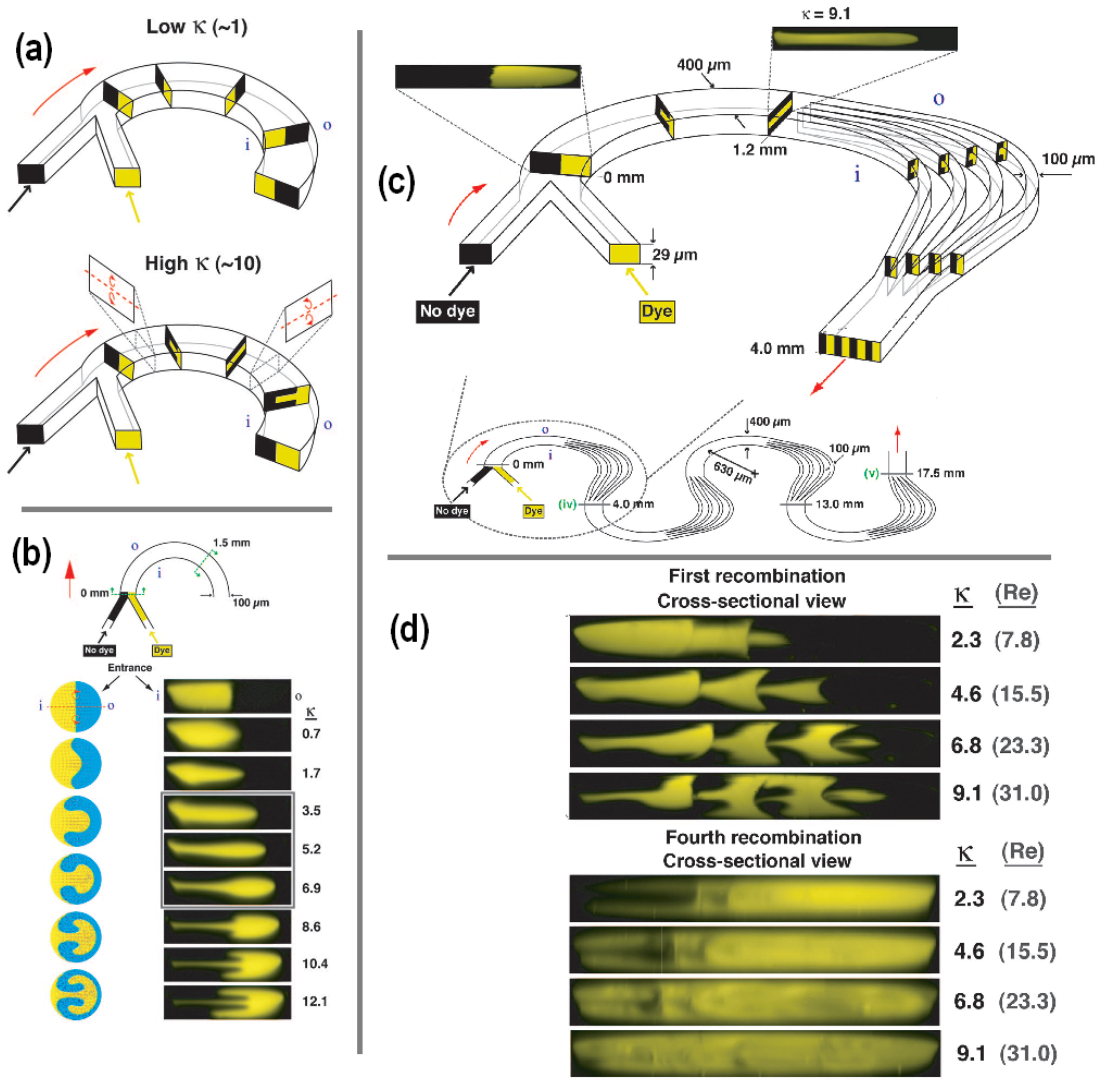

Figure 2.12. (a, b) Transversal flow pattern by Dean Flow phenomena in circular channel; (c) The concept of 2D SAR mixer by creation of multi-laminated flow pattern; (d) Result of mixing performance at the end of first and forth mixing blocks at different Reynolds and Dean numbers [96].

As a variation to Dean Flows, centrifugal effect can creates transversal flows in straight microchannels caused by Coriolis pseudo force [97, 98]. In this method, centrifugal force created by spanning the microchannel creates axial and transversal flows. By patterning the microchannel by split-and-recombine structures, force flow creates a multi-laminated flow pattern which can shorten the mixing time by up to two orders of magnitude.

Rapid expansion in channel cross-section in conventional T-mixer can decrease the diffusion length between segmented serial laminated fluids. Coleman et al [99] reported a micromixer based on symmetric sequential injection geometry and expansion chamber. In this work a sequence of two fluids will be injected using modified T-mixer with added inlet in the middle part of T-junction. At the end of the mixer, an expansion chamber is designed to increase the axial diffusive mixing by decreasing the diffusion length caused by sudden expansion of segments. The efficiency of mixing depends on the frequency of the injection and an efficient mixing of 99% was achieved in 2.3mm mixer length at a frequency of 10Hz (Figure 2.13).

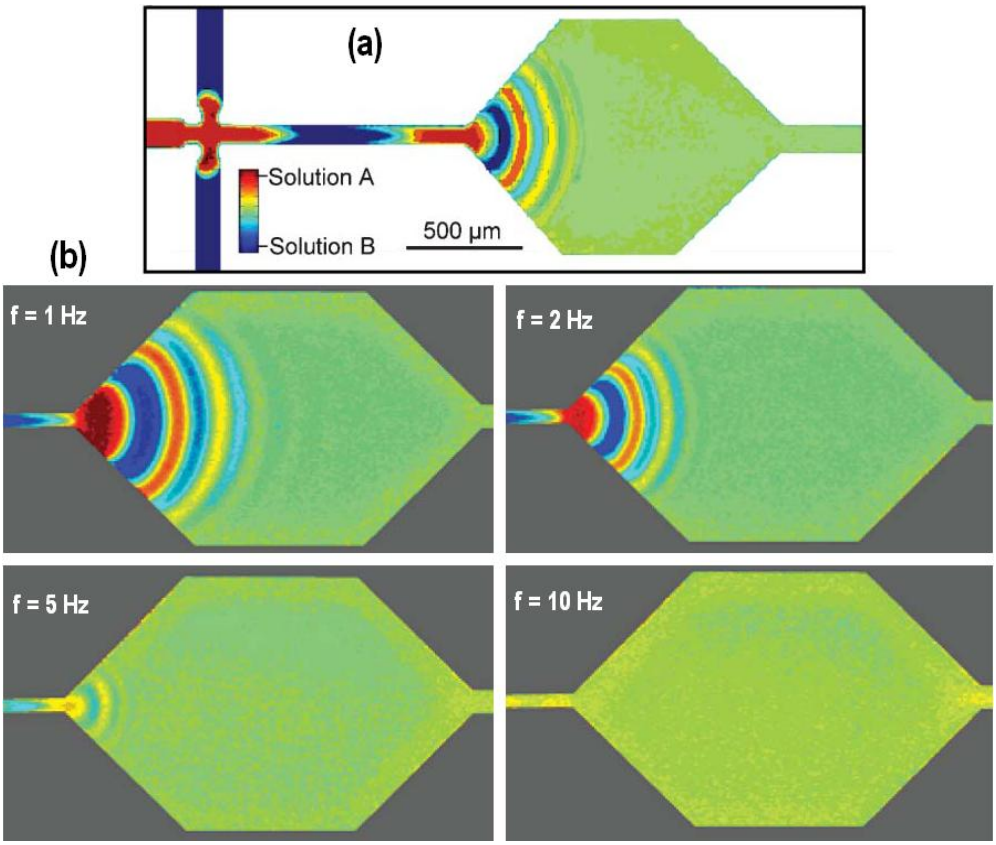

Figure 2.13. (a) Schematic of symmetrical sequential injection micromixer; (b) Fluorescence microscopy result of the mixer at different frequencies [99].

2.4.4 Injection-Based Lamination Micromixing Scheme

Injection technique can be used to create a matrix of small regional fluid lamination in SAR mixer. An array of micro-nozzles is used in this technique to inject micro-size droplets of one liquid on top of the other liquid. This injection technique creates a number of micro-plums inside the sample liquid which in fact increase the contact surface between two fluids and helps the diffusion to takes place faster.

An array of 400 nozzles was used in the work reported by Miyake et al [100] in a very thin micro-chamber to perform the lamination mixing by decreasing the diffusion length. A conceptual picture of micro-injection mixer with 400 nozzles is illustrated in Figure 2.14 showing the position of micro-nozzles and the micro-chamber. Micro-nozzles used in this work are positioned in rows, 10-100μm apart and a fast mixing time of 1.2sec was reported for the total injected volume of 0.5μl and the injection flow rate of 0.75μl/sec.

Obviously, this technique is limited to a very small-volume micromixing and might not be practical for larger-volume mixing requirements. Very similar mixing technique with different nozzle shapes and arrangements was reported by other groups as well [101-103].

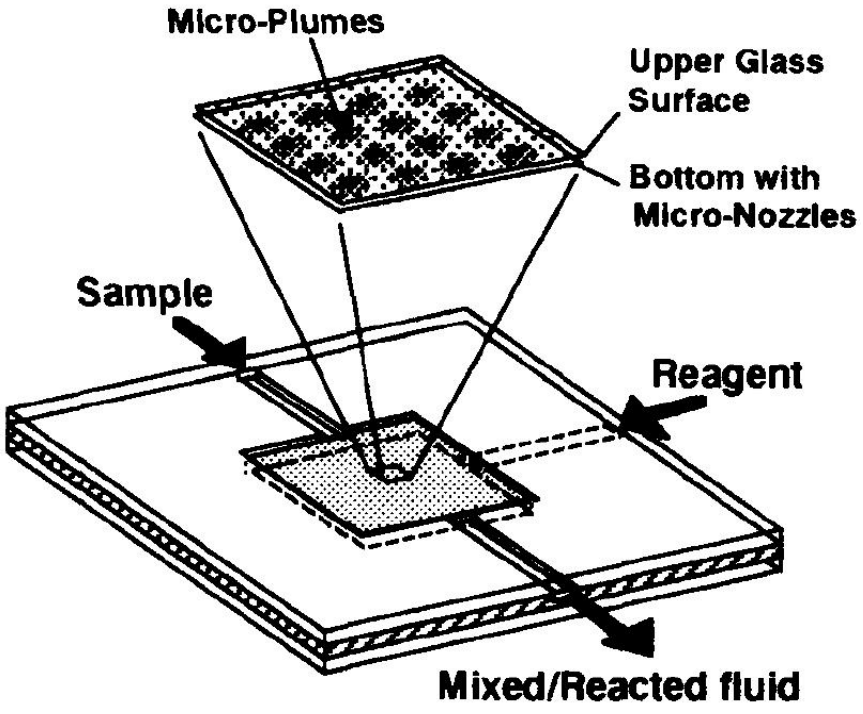

Figure 2.14. The concept of micro-injection technique employed to create regional small-volume diffusion mixing using array of micro-nozzles [100].

2.4.5 Droplet-Based Lamination Micromixing Scheme

Multi-lamination of two liquids can take place inside a droplet of nl/pl volume to achieve fast diffusion mixing. In this technique, a series of discrete droplets will be created from two liquids and will be forced to move inside the mixing path. The friction effect between channel wall and droplets together with droplet recirculation creates multi-layer streamlines inside the droplets during the drop's motion. This will consequently enhance the mixing by increasing the inter-layer diffusion of two liquids. As a variation of this technique, droplets may be manipulated individually using pressure [104], by application of thermo-capillary effect [105] or electrowetting actuation [106]. Alternatively, an immiscible phase effect such as oil-water can be employed to generate and carry droplets inside a carrier liquid such as oil [107, 108]. In this case, shear force between carrier liquid and droplet creates multi-laminated pattern of two liquids inside the drops. Figure 2.15 illustrates the concept and experimental result of this type of micromixing. Although the concept is multi-lamination diffusion mixing, the reported mixer was claimed to create chaotic advection inside the droplets by application of winding microfluidic channel.

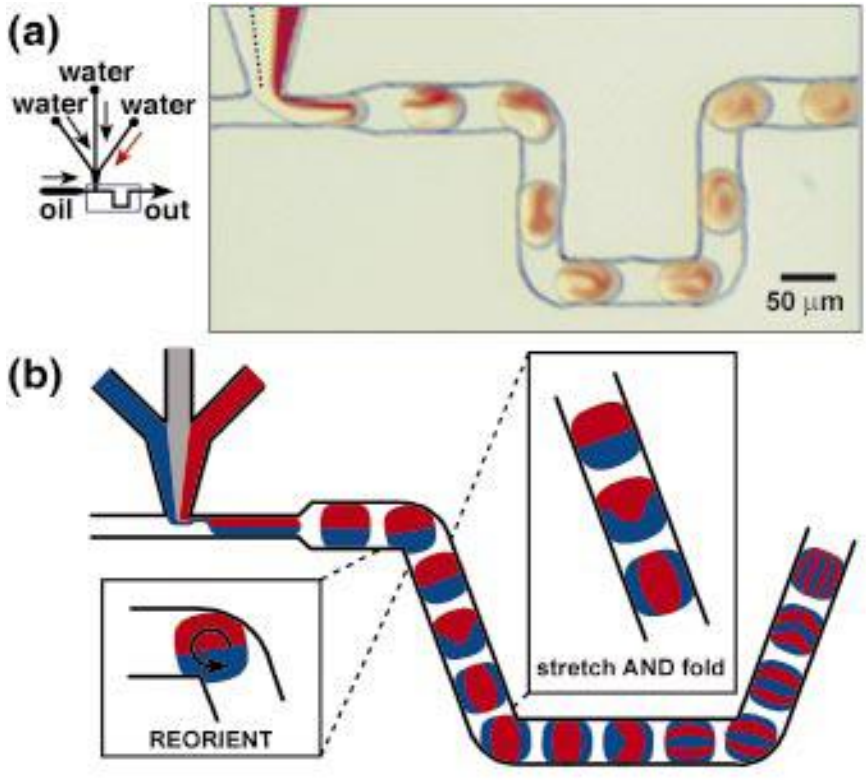

Figure 2.15. Droplet-based multi-lamination mixing. (a) Schematic of microfluidic network and a picture of experimental result of mixing of two dyed water samples. (b) Schematic diagram of creation of multi-layers inside the droplets [107].

2.4.5 Chaotic Advection Micromixing Scheme

As mentioned before, chaotic advection is another way of mass transfer in flows with low Reynolds number. The so-called chaotic advection can be created by creating some geometrical obstacles inside the mixing channel or by reshaping the channel itself. These geometrical modifications inside the channel can enhance the mixing by splitting, folding, stretching and breaking of the flow or creation of local eddies in higher Reynolds numbers [109, 110]. This method of creating chaotic advection is useful in passive micromixers where the idea is to perform the mixing without any external forces. Nevertheless, chaotic advection can be induced in the flow using external forces, which is the subject of active mixing platform and will be discussed in next section.

Employment of obstacle structures is among the simplest methods to create chaotic advection in the mixing channel. These obstacles can be placed inside the channel (Figure 2.16a) or can be created in the channel walls (Figure 2.16b).

A numerical simulation was performed by Wang et al [111] to investigate the effect of different arrangements of obstacles inside the mixing channel on mixing performance. Obstacles of 60μm in diameter were placed in the middle of the 300μm×100μm (width×depth) channel in different arrangements. The result of this simulation showed that obstacles cannot generate any eddies or recirculation at low Reynolds number. However, higher Reynolds numbers in asymmetric arrangement of obstacles can force one fluid to flow into another one. This transversal mass transfer at high Reynolds number can enhance the mixing significantly (Figure 2.16c).

The same concept was employed by Lin et al [112] in a 450pl microchamber and a number of seven 10μm diameter pillar-type obstacles were placed in the middle of the channel. The range of Reynolds number varies in different positions along the flow between 200 and 2000. A complete mixing was achieved in less than 50μs at this Reynolds number.

Effect of side-wall obstacles on mixing performance was investigated by Wong et al [70] by means of numerical simulation. A cross-shaped mixing unit was used in this simulation with outlet cross-section of 30μm×40μm comprising two 10μm×10μm

obstacles created in the channel walls. The use of cross-shaped mixing unit is preferred to standard T-shape mixer because of its larger contact surface by mixing middle fluid by two fluids from side-inlets. Nevertheless, a complete mixing of antibody (side-inlets) with enzymes (middle-inlet) was achieved in less than 1ms at the outlet channel in this simulation study (Figure 2.16d). The enhancement in mixing performance was thought to be the generation of eddies and lateral velocity components caused by side-wall obstacles.

Recently, Bhagat et al [113] reported a micromixer using diamond-shaped obstructions inside the mixing channel. The mixer was designed to work in low Reynolds number (0.02<Re<10). Complete mixing of fluorescein and water was achieved in 7mm long channel at Reynolds number of 0.1 (Figure 2.17).

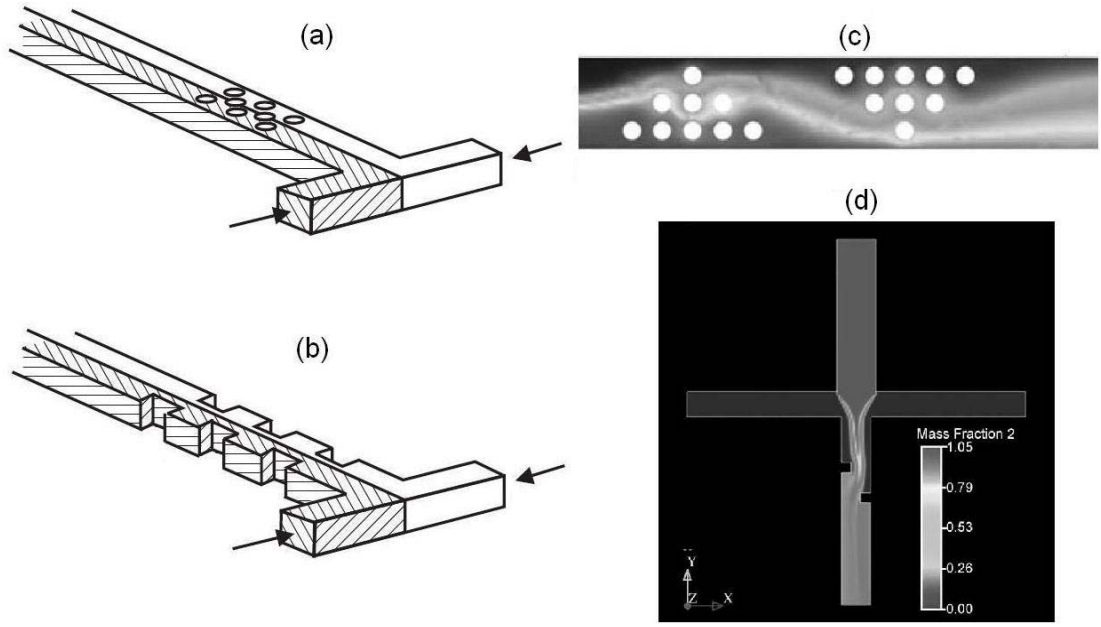

Figure 2.16. The concept of inducing chaotic advection in passive mixers by insertion of obstacles in the channel. (a) Obstacles created in the channel walls. (b) Obstacles created by placing 3Dstructures in the channel side-walls [60]. (c) Simulation result of chaotic mixing using asymmetric arrangement of obstacles [111]. (d) Creation of chaotic mixing in a cross-shaped mixing unit using two side-wall obstacles [70].

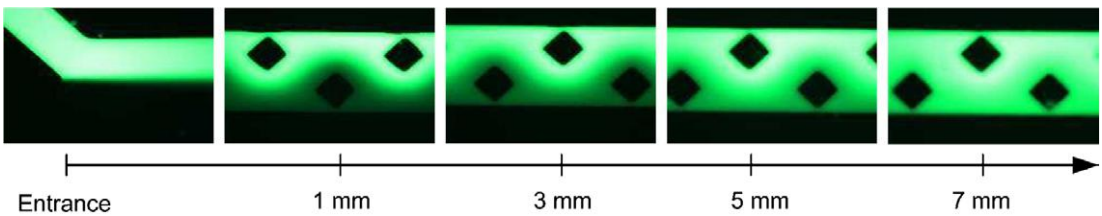

Figure 2.17. Passive micromixer using implemented diamond-shaped obstructions. Mixing efficiency of water (dark) and fluorescein at Re = 0.1 [113].

Recirculation can be generated at the relatively higher Reynolds numbers around the turns in a curved [114], sawtooth [115] or zigzagged [116] channels (Figure 2.18). This channel type has been investigated numerically in the work carried out by Mengeaud et al [116]. The simulation was performed in various Reynolds numbers ranging from 0.26 to 267 and various ratios of length of periodic steps to channel width (s/w). The simulation result showed that below a critical Reynolds number of 80, the flow profile is parabolic thus the mixing is entirely diffusion-based. Above this critical Reynolds number, a recirculation flow pattern was generated at channel turns causing transversal mass transfer between two fluids (Figure 2.18b). The efficient mixing will take place in an optimised s/w ratio. This s/w ratio was found to be 4, at Reynolds number of 267.

In the past reviewed chaotic advection micromixers, a relatively high Reynolds numbers were used to create eddies and recirculation. Although high Reynolds number might be necessary to achieve high flow rate micromixing in some microfluidic applications [117, 118], accurate microfabrication technique must be employed to acquire secure chip bonding and sealing.

Generation of chaotic advection at lower Reynolds number needs more sophisticated mixer design. Generally, a more complicated mixing path can be designed using twisted channels to increase the chaotic patterns at lower Reynolds numbers. In a work reported by Hong et al [119], an in-plane modified version of Tesla structures in 2D mode was designed to investigate the mixing performance numerically and experimentally. The mixing performance was improved significantly caused by Coanda effect in this structure (Figure 2.19). At lower Reynolds numbers, diffusion mixing is dominant but above Reynolds number of 5, a mixture of diffusion and convection contribute to the mixing performance.

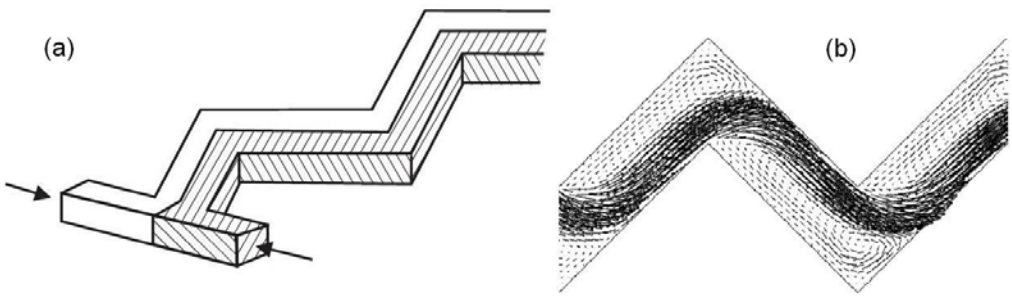

Figure 2.18. Chaotic mixing in a zig-zag-shaped microchannel. (a) The concept [60], (b) Velocity vectors showing recirculation at turns in Reynolds number of 267 and s/w ratio of 4 [116].

In a different work reported by Liu et al [120], a 3D serpentine channel resembling C-shaped repeating units was used to create chaotic mixing pattern (Figure 2.20a). The result showed that a uniform mixing was achieved at Reynolds numbers ranging from 6 to 70. The mixing performance was much faster than diffusion mixing or standard square-shaped channel. As a variation on this work, another three-dimensional serpentine channel was used in a work reported by Vijayendran et al [121] (Figure 2.20b). A very wide channel cross-section (1mm×0.3mm) was fabricated in L-shaped repeating units in total length of 30mm. The result indicated enhanced mixing by chaotic mixing pattern at tested Reynolds numbers of 1, 5 and 20.

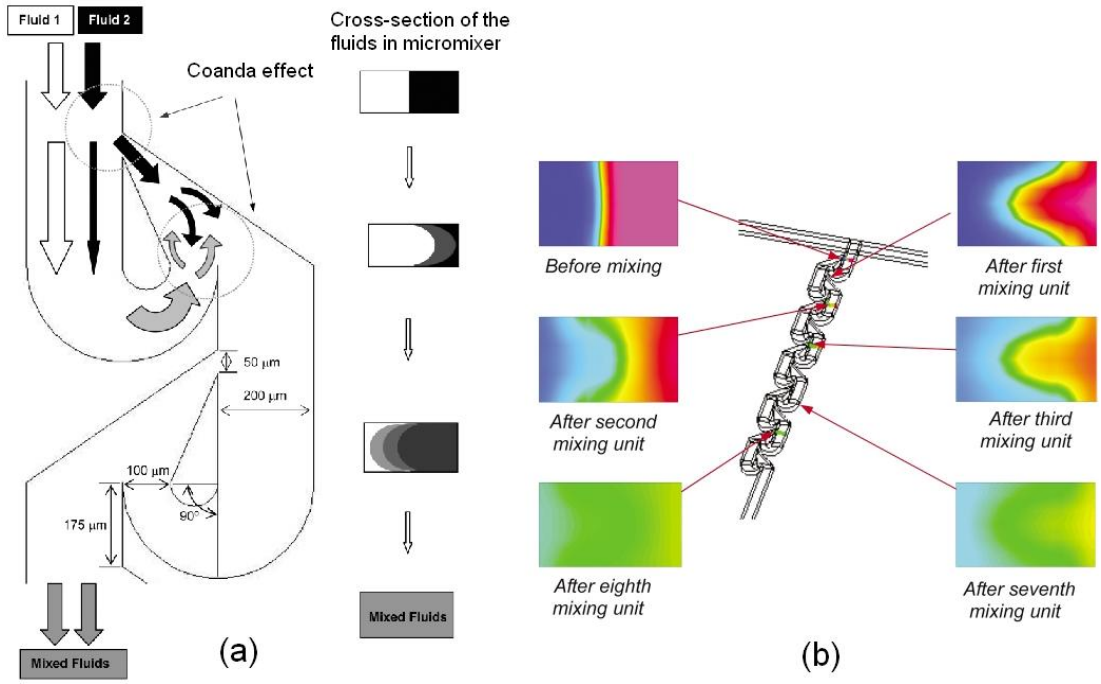

Figure 2.19. Application of modified Tesla structures to generate chaotic advection in the micromixer. (a) The concept of chaotic mixing; (b) mixing performance in different positions of 9-stage mixing unit [119].

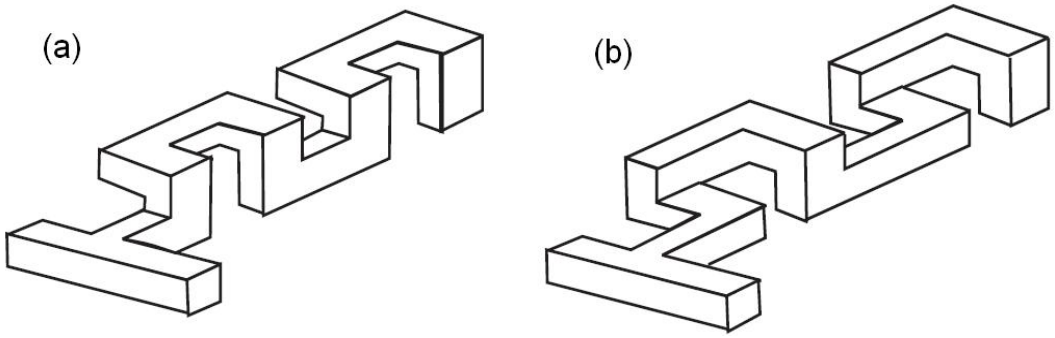

Figure 2.20. Various serpentine microchannel structures [60].

A more complicated design of mixing channel was reported by Chen and Meiners [122]. In this mixing scheme, the laminar flow was repeatedly folded by splitting, rotating and recombining in the mixing path. This will exponentially increase the flow concentration at the mixer, which leads to a fast and efficient diffusion mixing. An effective mixing was achieved at low Reynolds number (Re=0.1-2) in a very short mixing path (Figure 2.21).

A more geometrical complex micromixer was introduced by Park et al [123] using three-dimensional channel structure utilizing the theory of chaotic advection introduced in Ottino's book [124]. Based on this theory, the mixing channel was designed to enhance mixing by increasing stretching and folding through rotation as well as breakup process, which creates smaller blobs exponentially (Figure 2.22a). The result of mixing showed 70% mixing after passing through 4mm mixing channel. This mixer was tested at different Reynolds number of 1, 10 and 50 and the mixing efficiency was enhanced significantly.

Various twisted microchannel designs were used in a numerical simulation by Jen et al [64]. In this design three micromixers with inclined, oblique and wavelike channel geometry were used for investigations (Figure 2.22b-d). The channel walls were angled to produce a swaying fluid pattern which causes chaotic regime thus might creates chaotic advection. The result indicated that inclined-channel mixer produces better chaotic mixing. This type of mixer can produces a similar mixing efficiency compared to the standard T-mixer in shorter mixing path (31% shorter).

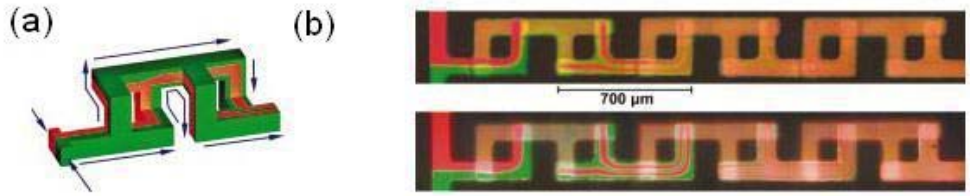

Figure 2.21. (a) The topological structure of the mixer; (b) The performance of a six-stage mixer at Reynolds number of 0.1 on two fluorescently labelled protein solutions (top) and in an aqueous 54% glycerol solution (bottom) [122].

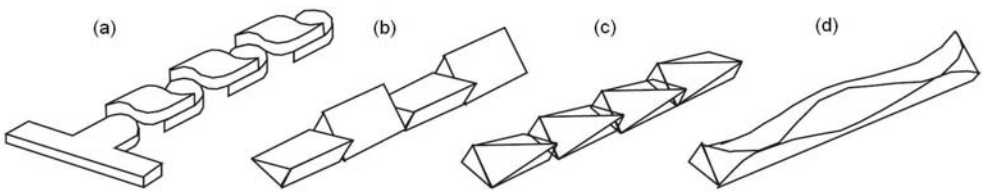

Figure 2.22. Various complex design of twisted micromixers to create chaotic advection. (a) 3D twisted microchannel, (b) Inclined mixer, (c) Oblique mixer, (d) Wavelike mixer [60].

A combination of chaotic advection and multi-lamination technique was used in a micromixer reported by Chang and Cho [125]. The 3D mixing path was patterned in two blocks of PDMS layer to create whirls and multi-lamination. The mixer was tested over a wide range of flow rates at various Reynolds numbers. This mixer can work efficiently in Reynolds number ranging from 0.26 to 26 at mixing length ranging from 2.8mm to 5.8mm.

As mentioned before, Dean Flow phenomena takes place in spiral and curved channels. Realisation of Dean Phenomena in planar spiral microchannel can be used in diffusion-based mixers to create multi-laminated flow pattern, which results in fast mixing of two fluids. Sunderan et al [126] reported a planar serpentine mixer which uses Dean Flow pattern to create multi-laminated flow pattern. Experimental results indicated efficient mixing of two coloured fluids at Reynolds numbers ranging from 0.02 to 18.6.

In a different work [96], it was shown that mixing efficiency can be further improved by combination of Dean Flow pattern in curved microchannels with abrupt change in cross-section of the channel. The effect of this change in the cross-section of the channel along the flow path can create expansion vortex effect that results in chaotic advection mixing of two fluids. Vortex can take place above certain Reynolds number caused by sudden expansion and pressure gradient. Combination of vortex effect in horizontal plane coupled with Dean Effects in vertical plane creates multi-vortex flow pattern which can increase the efficiency of mixing significantly. Figure 2.23b illustrate schematic diagram of the asymmetric serpentine micromixer incorporating Dean Effect and expansion vortex effect. The result of vortex effect using coloured dye streams is shown in Figure 2.23c at two different Dean Numbers. The result of mixing of fluorescein dyed fluids is illustrated in Figure 2.23d at different Reynolds numbers ($6.4<Re<32.2$) at various cross-sectional areas. A level of 80% mixing was achieved at 7.8mm length of channel at Reynolds number of 32.

Another method of creating chaotic advection is by creation of rips and grooves inside the microchannel [127-130]. In this method one fluid will be forced to move in lateral direction by a series of oblique rips or grooves. Subsequently, the force fluid circulates spatially repeatedly using multi-rips and grooves. This will create an effective chaotic advection mixing of two fluids inside the mixing channel. Application of ablated wells was first reported by Johnson et al [127] by creation of a

series of slanted wells in the channel using pulsed UV excimer laser. The channel was fabricated in width of 72µm and 28µm at top and bottom respectively with 31µm in depth. Four ablated wells were fabricated with 14 µm in depth. An electroosmotic-driven flow was used in this experiment and 75% mixing was achieved at low flow rates of 0.06 cm/s. the performance of mixing was tested at higher flow rate of 0.81 cm/s and a good mixing of 80% was achieved in 443µm channel length. This mixing performance requires 2.3cm diffusion mixing path in a similar standard T-mixer (Figure 2.24).

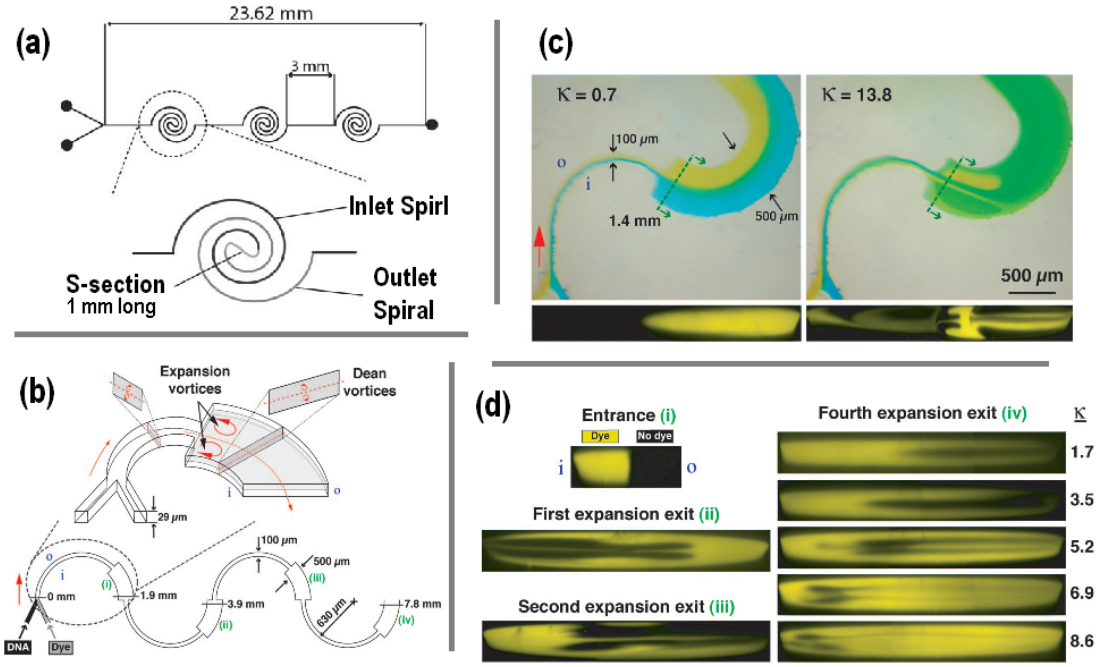

Figure 2.23. (a) Schematic of spiral mixer using Dean flow effect; (b) Schematic of serpentine mixer with abrupt cross-section expansions; (c) Creation of vortex at high Dean number; (d) Efficiency of mixing at different places marked in (a) for various Dean numbers [96, 126].

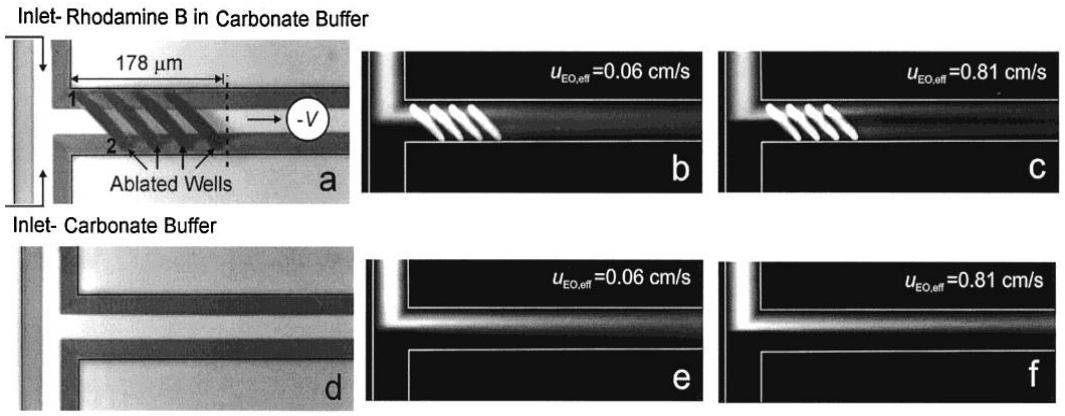

Figure 2.24. A Fluorescent microscopy image of mixing performance at two different flow rates (0.06 cm/s and 0.81 cm/s) in a T-shaped channel with four ablated wells (b, c) and standard T-shape channel without well (e and f) [127].

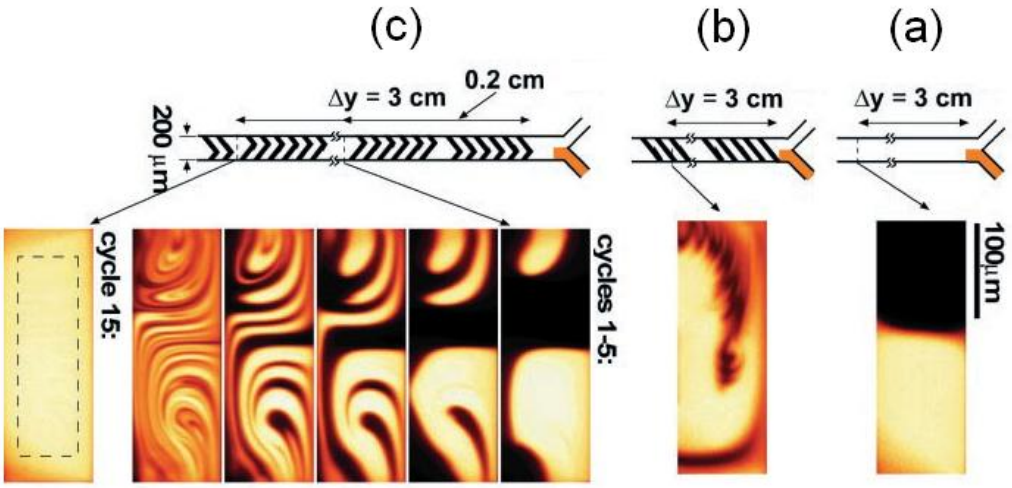

Figure 2.25. A comparison of mixing performance of three different micromixers at Reynolds number of 0.001 in mixing of 2 mM solution of Fluorscein-labelled polymer in water/glycerol mixtures (0 and 80% glycerol). (a) Y-mixer with no structure, (b) Y-mixer with straight ridges (c) Staggered herringbone structure mixer [128].

In a similar work, Stroock et al [128-130] reported a chaotic mixer by creating two different groove patterns in the mixing channel. The performance of these two groove patterns was tested in different Reynolds number and a very successful chaotic mixing was achieved in so-called staggered herringbone mixer (SHM) at Reynolds number ranging from 0.001 to 100 (Figure 2.25). In fact in staggered groove pattern, the alteration in the orientation of the herringbones between half cycles exchanges the positions of the rotation centre. This will induces a chaotic pattern subject to a repeated sequence of rotational and extensional local flows.

The generation of chaotic advection caused by helical flow pattern in microchannels with grooves was the subject of some numerical simulation studies. In these simulations, the effect of different groove pattern was investigated such as: single-sided straight ridge pattern [131], double-sided straight ridge pattern [132] and staggered herringbones structure [133]. The result of these simulations confirmed the occurrence of rotational flow pattern and subsequent chaotic advection in the mixing channel. The fabrication of different groove pattern including staggered herringbone structure on PDMS substrate was reported by Lim et al [134]. In this method a high brightness diode-pumped Nd-YAG laser was used for direct ablation on PDMS.

Application of patterning using heterogeneous surface charge was investigated by Biddis et al [135]. In this study, various charge patterns were investigated and it was indicated that mixing efficiency can be improved by creation of localised flow

circulation regions. Mixing efficiency was improved by 22% and 68% for the applied electric fields of 70 V/cm and 555 V/cm. Figure 2.26 shows the result of this study in comparison to the mixer without surface charge.

The concept of helical mixing in slanted grooves was further improved by implementation of parallel barrier structures in the channel [136]. The application of embedded barrier improves the mixing performance by changing the elliptical pattern to hyperbolic flow pattern in the barrier zone (Figure 2.27). The mixing channel is 240μm in width, 60 μm in depth and 21 mm in length with barrier cross-section of 40μm×30μm. A numerical study of mixing performance in barrier embedded micromixer was conducted by Kang et al [137] by focusing on effect of periodic and aperiodic sequence of mixing protocols. It was found that higher Reynolds numbers (Re≈30) results in larger rotation of fluid and faster mixing. A proper selection of aperiodic sequence will results in faster and more uniform mixing than a periodic sequence in a certain Reynolds number.

The most complicated design of chaotic mixer was reported by Bertsch et al [138] using miniaturised version of conventional large-scale static mixer used in food-processing industry. In this work, two types of mixers were tested and fabricated using integral micro-stereo-lithography process. This fabrication technique allows the manufacturing of more complex geometries in polymers. A cut-off view of these mixers is illustrated in Figure 2.28 with intersecting-elements-pattern in the mixing tube (a) and a series of parallel right/left-hand short helix elements in the tube (b).

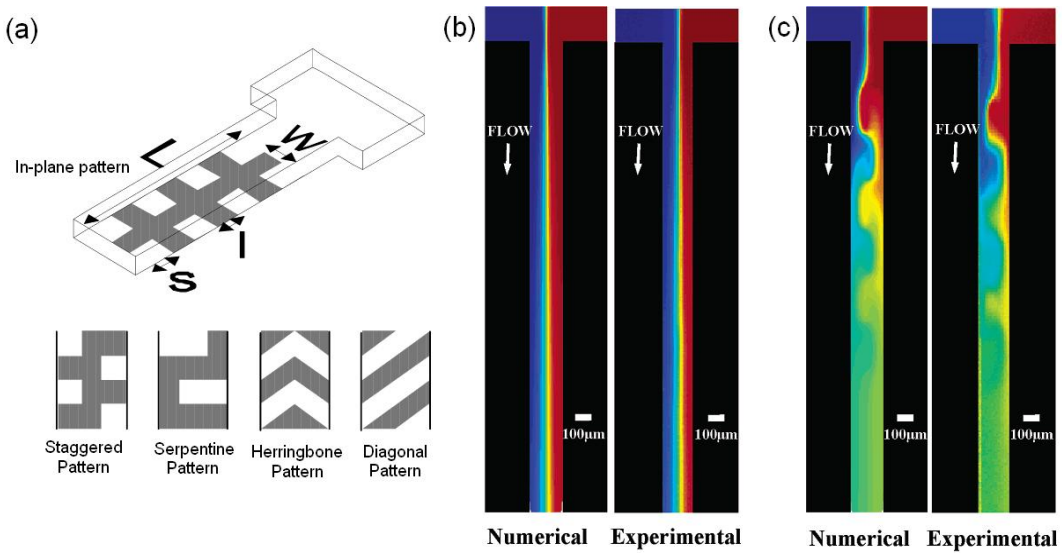

Figure 2.26. Chaotic mixing using surface charge. (a) Different surface charge patterns used for the study, (b) The mixing result without surface charge, (c) The mixing result in presence of surface charge with six patches staggered charge pattern and applied voltage of 280 V/cm [135].

These kinds of structures enhance the mixing by splitting, rearranging and combining the fluids in the intersecting-pattern mixer and rotational flow pattern in helical-channel mixer. The efficiency of mixing was investigated by numerical simulation of the 65000 uniformly distributed particles flow at Reynolds number of 12 (Figure 2.28c and d). This study indicated that both geometries perform efficient chaotic mixing at low Reynolds number. The intersecting-pattern tube creates more efficient chaotic mixing in comparison to helical-pattern mixing tube.

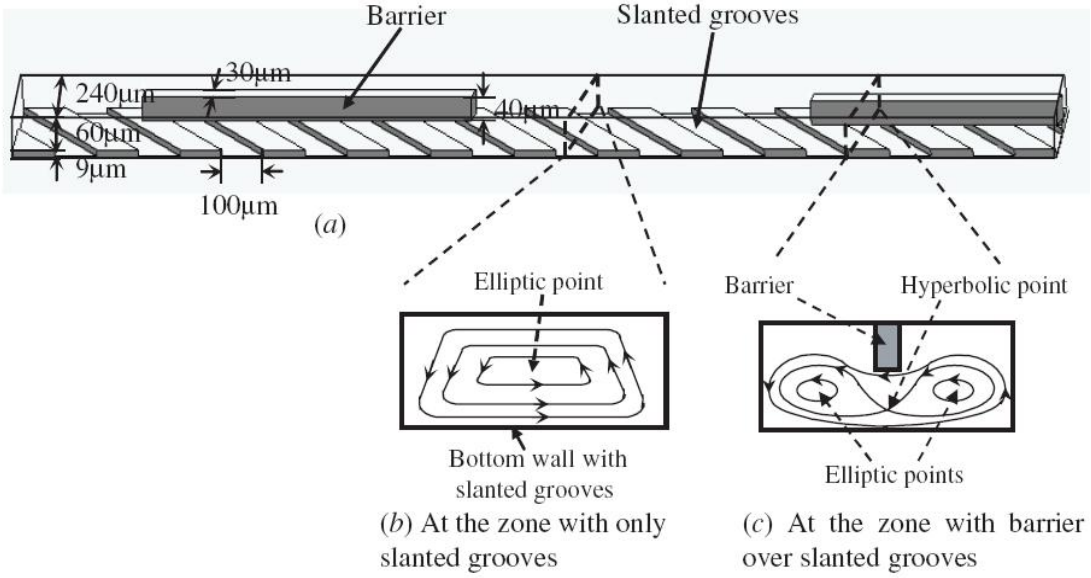

Figure 2.27. The concept of barrier embedded micromixer. (a) Schematic view, (b) Elliptic flow pattern, (c) Hyperbolic flow pattern [136].

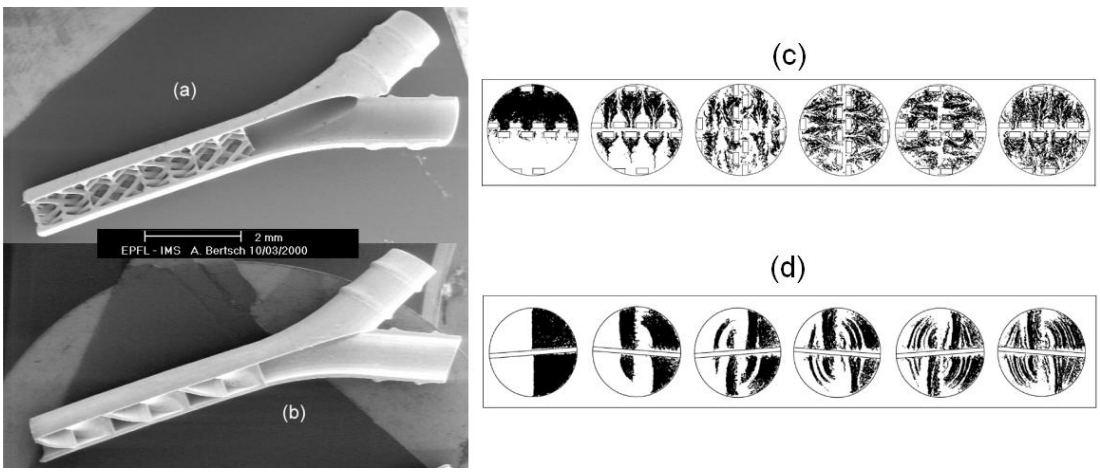

Figure 2.28. Helical mixing tubes. (a) Cut-off view of intersecting-elements-pattern mixing tube, (b) Cut-off view of helical-pattern mixing tube; (c) and (d) the simulation result of particle mixing at Reynolds number of 12 for mixing tubes of (a) and (b) respectively [138].

2.5 Active Micromixing Platform

The next micromixing platform relies on creation of chaotic regimes inside the mixer by application of an external source of energy. Since an external force will be used to generate the disturbance inside the mixer, the mixer geometry is less complex in comparison to passive mixers. Active micromixers can be categorised based on the source of external force used for creation of disturbance such as pressure, temperature, electrokinetic or magnetic. Figure 2.29 illustrate a schematic diagram of various types of active mixers based on their activation source.

2.5.1 Micromixing Using Miniaturised Micro-Stirrers

Stirring two liquids using impellers is the most common method of mixing in macro-scales. In this method, the mixing takes place by creation of turbulence caused by rotation of the stirrer. As discussed before, creation of turbulence in micro-scale is not possible due to the low Reynolds number. Nevertheless, application of stirring-bars in micro-scale might enhance the mixing by creating more interfacial areas and chaotic advection pattern through forced lateral and rotational flows. Analogous to the macro-scale solution, several miniaturised stirrers have been developed to perform mixing in micro-scales [139-141]. Lu et al [139] reported a micromixer based on micromachined magnetic bar, which can be activated externally by application of rotational magnetic field. Fast and successful mixing was achieved in PDMS-based mixing channel, mixing chamber and large mixing chamber using a 3×3 mixer array.

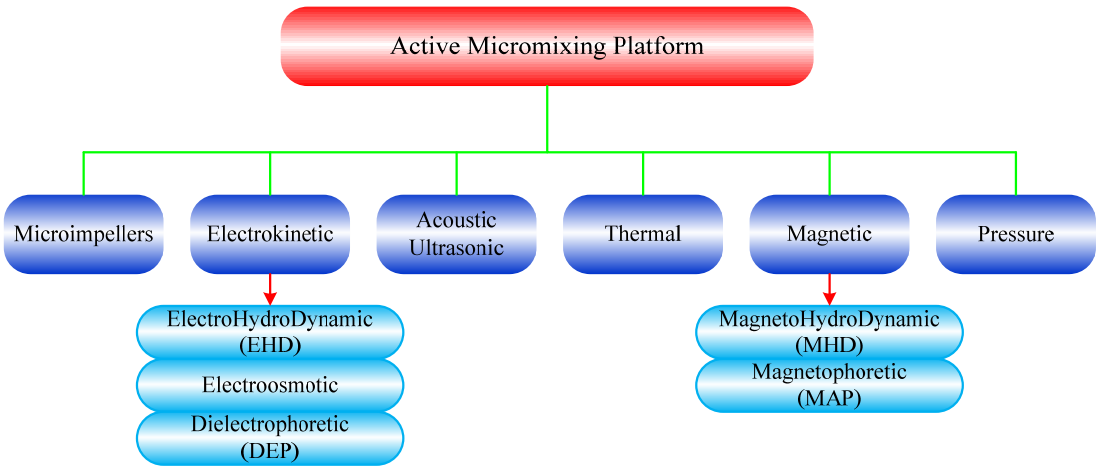

Figure 2.29. Classification of active micromixers based on external source of activation

This work was further improved by fabrication of a stir-bar monolithically integrated in parylene channel [140]. The diameter of the rotor and thickness of the stir-bar used in this experiment were 400µm and 16µm respectively. Figure 2.30 illustrate a picture of this micro-impeller (a) and the result of mixing of different food colour dyes in water is presented at the rotation speed of 150rpm (b). The application of magnetic-driven rotating-bar can be used for pumping the liquid inside the microchannels as well (c).

2.5.2 Micromixers Based on Pressure Field Disturbance

One of the simplest methods used for micromixing is the creation of disturbance in laminar flow pattern by applying pulsing flow pattern. In this method, two fluids will be injected into a T-mixer in which one fluid will be pushed into the mixer during a faction of time and will be stopped in order to push the other fluid in. the pressure applied by this switching pattern creates disturbance in segmented fluids inside the microchannel. Continuous switching flow pattern can be used to achieve full mixing of two fluids very quickly. Deshmukh et al [142, 143] used a Y-mixer to mix water and water/glucose by application of pressure-driven flow pattern. In this work an integrated micropump was used to create the pulsing flow pattern by switching on and off the micropump. The result of this experiment in different stages is illustrated in Figure 2.31.

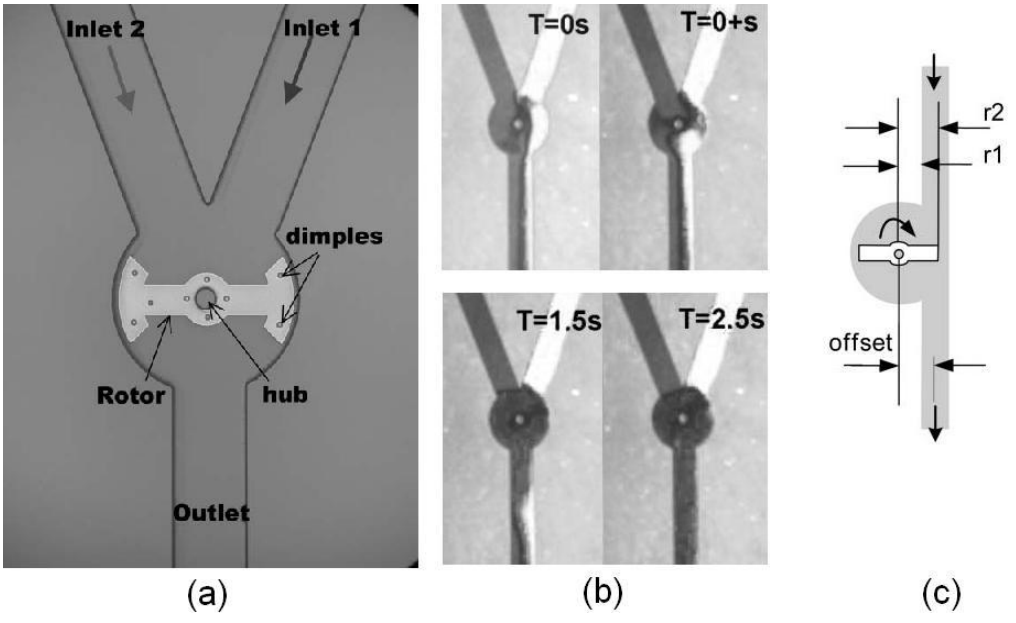

Figure 2.30. Micromixing using micro-impellers. (a) Optical image of the mixer; (b) Mixing performance of different coloured waters at different times; (c) the application of this device for pumping [140].

In a similar work, Fujii et al [144] used the same mixing concept of pressure flow pattern using an external micropump to perform mixing inside a Y-mixer.

Alternatively, pressure-driven flows can be applied smoothly using a sinusoidal flow pattern. In this method the pressure will be applied to one or both flows gradually from one or both inlets [145] or from multi inlets [146]. Glasgow and Aubry [145] investigated the performance of sinusoidal pressure field pattern on mixing inside a T-mixer with two inlets having 90 degree displacement and the outlet is across one inlet. A CFD simulation of aqueous solution at Reynolds number of 0.3 was performed in different pulsation phase shifts between two flows. The result of simulation indicated that applying pressure from one inlet will increase the interface area between two fluids and increase the mixing performance. The result showed an increase in the mixing efficiency by 83%. This was achieved by applying the pressure field to the perpendicular inlet.

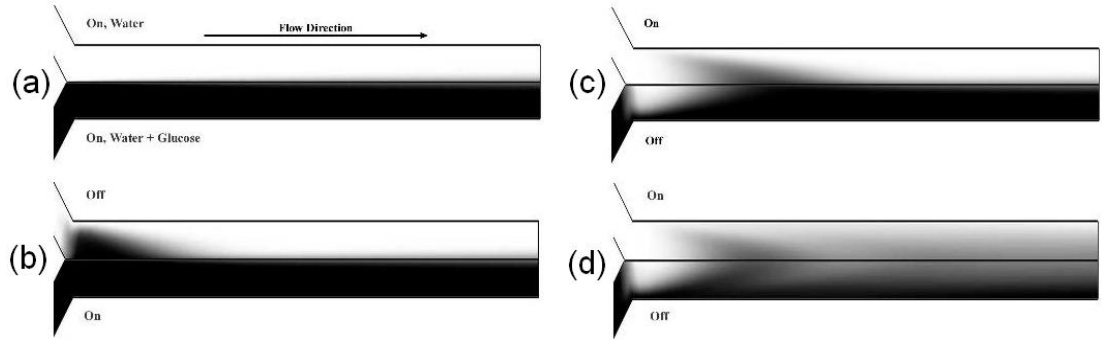

Figure 2.31. Pressure-field mixing. (a) Steady flow; (b) Top stream is stopped for 1/6 sec; (c) Bottom stream is stopped; (d) Switching flow pattern at frequency of 3Hz [142].

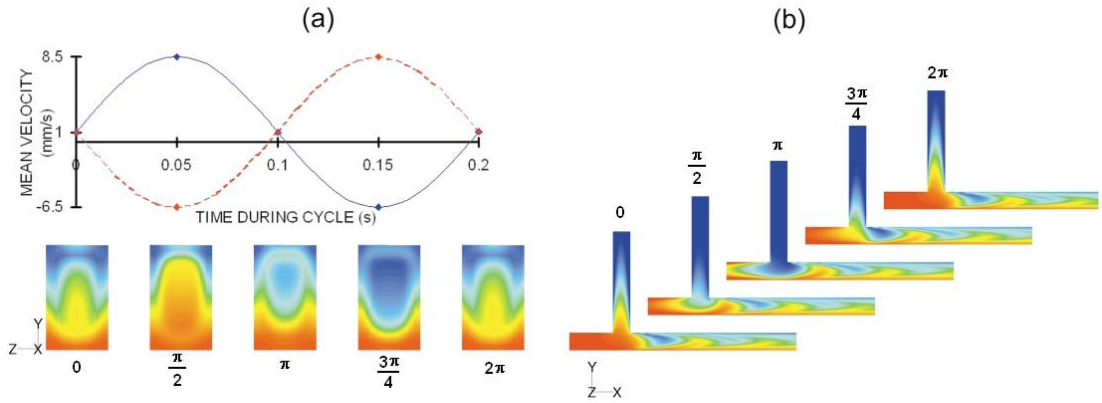

Figure 2.32. Numerical simulation result of mixing performance by applying sinusoidal pressure field to both inlets with 180° phase shift. (a) The snap-shots are taken from the outlet cross-section, 2mm down the channel; (b) Mixing profile across the channel at different times [145].

The mixing performance was decreased to 58% improvement by applying in-phase pressure flows to both inlets. However, out of phase sinusoidal pressure pattern with a phase shift of 90° and 180° result is much improved mixing performance by creating multi stretch and folding of two fluids in the channel. Figure 2.32 illustrate the CFD simulation result of this mixing method with 180° phase shift between two inlet flows.

This mixing concept was further elaborated by Niu and Lee [146] by increasing the number of inlets positioned across the mixing channel. In this work, a particle tracking simulation was performed in order to optimise the pulsation frequency and investigate creation of chaotic behaviour of the flow pattern inside the channel using Lyapunov exponents. It was indicated that the mixing performance is related to the pulsation frequency. In this work, the multi-pressure flow pattern was controlled by a computer-aid source-sink system. A further numerical modelling to characterise the performance of the pulsing-flow-pattern was presented by Okkels and Tabeling [147].

2.5.3 Acoustic-based External Disturbance Source

Acoustic wave is another source of energy that can be used as external source of disturbance in micromixers. The pioneering work on application of acoustic waves in microfluidic application was reported by Moroney et al [148]. In this work, the application of ultrasonic Lamb waves was used for pumping fluid in small-scales. The concept of acoustic actuation is based on mechanical displacement of some materials (quartz crystal) due to the applied voltage. Therefore, by applying an AC voltage to the material at resonant frequency of material, a continuous periodic mechanical distortion can be generated. This effect has found its way in design of active micropumps [148, 149]. However, this effect can be used in micromixers to create disturbance in the fluids to enhance mixing. Rife et al [149] reported an acoustic actuator using ultrasonic piezoelectric transducers that can be used for pumping and mixing by acoustic attenuation. Focused acoustic waves have been used to generate lateral movements in liquids using thin film piezoelectric transducers in circular sectors [150].

Yasuda [151] reported a high frequency acoustic micromixer to perform the mixing of red blood cells using piezoelectric zinc oxide thin film. The application of high frequency (3.5MHz) proved to be useful for mixing of biological samples. Biological

samples are very sensitive to the temperature induced by acoustic energy. In addition, ultrasonic waves around 50 kHz might generate cavitations in the water based biological solution, which is a harmful condition for biological samples. Therefore, a mega hertz range of ultrasound frequency is recommended for handling biological samples. A picture of Yasuda's ultrasound mixing chamber is illustrated in Figure 2.33 showing the performance of mixing by ultrasound irradiation.

Further application of acoustic mixing was reported by Yang et al [152, 153] using piezoelectric PZT ceramic at low frequencies (48 kHz and 60 kHz) for mixing of ethanol-water and uranine-water. The temperature rise was measured as 15°C during the activation of the mixer.

Acoustic streaming is another variation of acoustic micromixing. This technique benefits from the chaotic flow pattern created by cavitation microstreaming at lower band of acoustic waves (kHz-range). The surface of a trapped bubble in liquid acts as a vibrating membrane in the presence of acoustic field. The resonant frequency of vibration mainly depends on bubble size. The friction force generated at bubble-liquid interface creates a fluid flow around the interface, which is known as cavitation microstreaming.

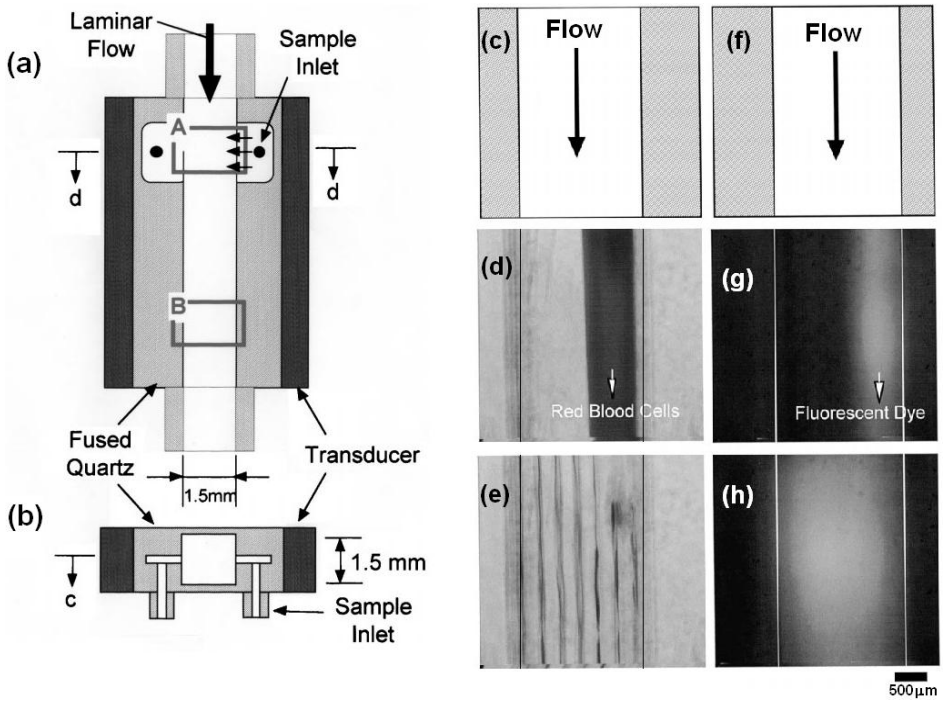

Figure 2.33. Acoustic mixer. (a,b) Schematic illustration of the mixing chamber at vertical and horizontal cross-section; (c,f) schematic of region B in (a); (d,g) Red blood cells and fluorescent dye before activation of the mixer; (e,h) Red blood cells and fluorescent dye during activation [151].

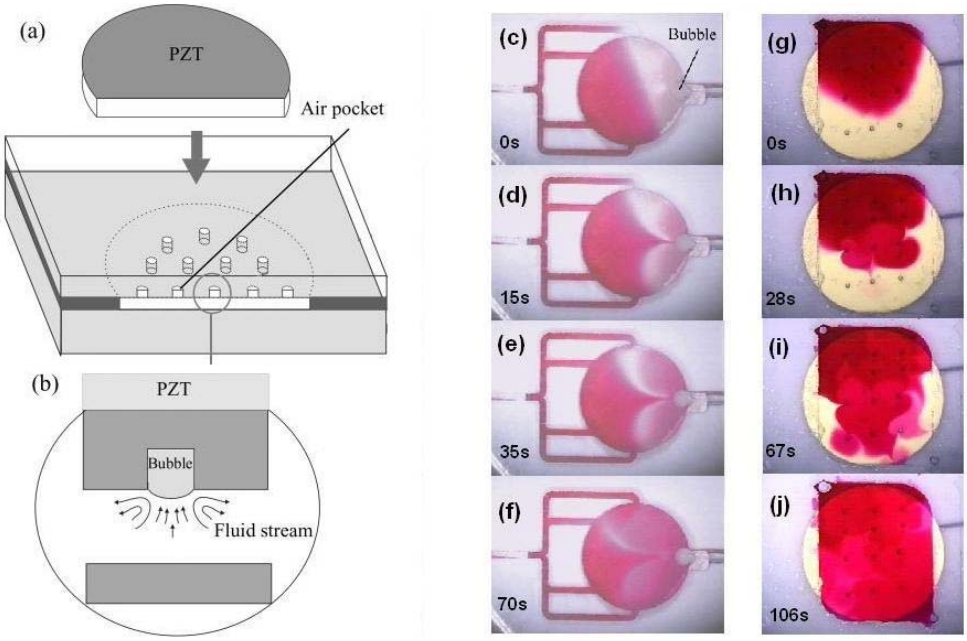

Figure 2.34. Micromixing based on cavitation microstreaming. (a) Schematic of mixer and bubble array; (b) Schematic of fluid stream induced by an air bubble; (c-e) and (g-j) The mixing performance of a single bubble and an array of 9 bubbles at different times (given on the pictures) [154].

A practical application of acoustic microstreaming in micromixing was reported by Liu et al [154, 155]. In this work, an integrated PZT transducer was used to activate an array of 9 air pockets, 2mm in diameter, inside the mixing chamber. The experimental result indicated a complete mixing of two liquids in less than 2 minutes (Figure 2.34). With no acoustic streaming, this mixing might take place in six hours by pure diffusion. In addition, it was found that higher voltage amplitude and use of square wave results in faster mixing performance

Acoustic stirring in higher frequencies can also be used in micromixing. Yaralioglu et al [156] reported an acoustic micromixer using an integrated piezoelectric transducer in a conventional Y-mixer made of PDMS. In their work, the transducer was made by deposited zinc oxide thin film on the surface of quartz substrate. The transducer was designed to operate at the frequency of 450MHz.

A mixer based on surface acoustic wave (SAW) using interdigitated transducers was reported by Tseng et al [157]. In this work the transducer was placed outside the mixing channel to alleviate heat generation inside the mixer. Acoustic energy generated by transducer excites longitudinal waves into the fluid through solid-liquid interface at a specific angel which depends on solid-liquid refraction characteristic. Application of concentrated SAW has also been used to perform mixing inside droplets by generating eddies and circulations [158].

Beside acoustic streaming and cavitation microstreaming, acoustic standing waves also have been used in micromixers [159]. While acoustic streaming is mainly a volume effect, acoustic standing wave is a radiation force which acts at the interface between two fluids. In addition, acoustic streaming propagates perpendicular to the fluid direction but acoustic standing waves radiate parallel to the flow direction. Therefore, a small density variation between two fluids is enough to cause the mixing at the liquid-liquid interface.

2.5.4 Micromixing Based on Thermal Disturbance

Thermal disturbance has been the subject of micromixing in some limited reports. The fact that diffusion coefficient is directly related to the temperature implies that increasing the temperature will decrease the diffusion time. The more interesting fact is that the viscosity of fluids is highly sensitive to the temperature. As an example, the variation in viscosity of water from 10°C to 80°C is nearly four times less. Therefore, the efficiency of mixing might be enhanced by increasing the fluid temperature.

Mao et al [160] reported an investigation of micromixing based on linear temperature gradient across the array of microchannels. In their work, the array of microfluidic channels were placed between a hot fluid source on one side and a cold fluid sink on the other side. This setup created a linear temperature gradient across the microchannels in which each channel was at a different temperature from 80°C to 8°C. The efficiency of mixing was investigated by measuring the quantum yield of semiconductor crystals. An important characteristic of these crystals is the temperature dependency of their fluorescence quantum yield. The experimental result indicated an order of magnitude change in the quantum yield of these particles over $70^{\circ C}$ variation in temperature.

In a different thermal mixer, Tsai and Lin [161] reported a micromixer based on thermal bubble agitation mechanism. In this work a nozzle-diffuser bubble actuated micropump was employed to generate the bubbles in various frequencies. The oscillatory flow generated by thermal bubbles of micropump can induce wavy interface to increase the surface contact between the fluids thus enhance the mixing. The optimised mixing was achieved at the frequency of 200Hz.

2.5.5 Micromixing Based on Electrokinetic Forces

The next group of micromixing lays blow the electrokinetic force as the external source of activation. Electrokinetic is the study of the motion of the selected entities subjected to the electric field. If this force is applied to the fluid, the term is called electro-hydrodynamic or electroosmotic forces. These types of forces have been widely utilised in design of micropumps. The application of electrokinetic forces to manipulate the suspended particles inside the fluid is called dielectrophoresis which has found it way in manipulation and separation of small particles in microfluidics. In this section, the stress is on application of these forces on microfluidic micromixing.

2.5.5.1 ElectroHydroDynamic (EHD) Micromixers

In the presence of electric charges in fluid subjected to an electric field, these charges will be dragged toward the opposite electrode through the fluid. This phenomenon has been employed to enhance the mixing of two fluids of different electrical properties [162, 163]. Moctar et al [162] reported an electrohydrodynamic mixer using a conventional T-mixer and an array of electrodes perpendicular to the channel and the fluid direction. Corn oil and doped-dyed corn oil with similar mechanical properties (viscosity and density) at Reynolds number of 0.02 were used for mixing. The effect of DC and AC (square wave and sinusoidal) electric field was studied on mixing performance. By applying the electric field of 4×10^5 V/m, a transversal flow will be generated at fluids interface, which destabilise the interface. This effect led to an instant mixing of two fluids in less than 0.1 second. The mixing is effective at both DC and AC electric field and only depends on the amplitude of the field. Figure 2.35 illustrate the result of EHD mixer on mixing of two corn oils at different applied electric fields. It is clearly shown in this picture that the performance of mixing is improved at stronger electric field.

In a similar concept, Tsouris et al [163] reported an EHD micromixer to perform the mixing of two miscible fluids such as alcohols in a T-mixer. The strength of applied electric field was up to 2×10^6 V/m in a channel with 450 μm in width. The experimental results indicated a very successful mixing of two liquids in 150 μm mixing length. This length for pure diffusion mixing was measured as 5000 μm.

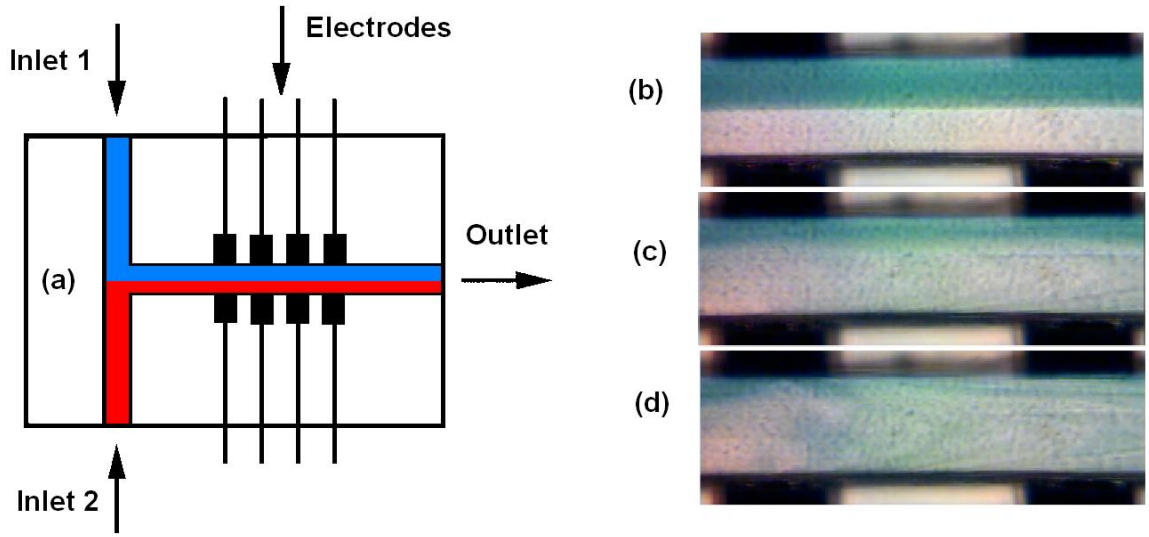

Figure 2.35. Electro-hydrodynamic mixing. (a) Schematic of setup configuration; (b-d) The performance of the mixing of two corn oil streams (pure and dyed) at (b) no field applied, (c) DC field of 4×10^5 V/m, (d) DC field of 6×10^5 V/m [162].

2.5.5.2 Electroosmotic Micromixers

The surfaces of most microfluidic materials such as glass, plastics and polymers reveal a net negative charge when interfaced with an aqueous solution. In the presence of these negative charges, an electric double layer will be created at the interface from positive charges (cations) presented in the solution. The depth of this layer is known as Debye length, which is the distance from the interface to where the electric potential energy is equal to the thermal energy. In the presence of an external electric field along the interface, positive charges presented in electric double layer will be dragged toward the cathode. The adjacent liquid to the double layer experience a net momentum and force the bulk of liquid to move toward the cathode. This phenomenon is called electroosmotic flow and is defined as the motion of bulk fluid at the solid-liquid interface due to the externally applied electric field. Although electroosmotic flow has widely been used in microfluidic micropumps, this section is more concern about the application of electroosmotic flow in design of active micromixers.

Lin et al [164, 165] reported an electroosmotic driven micromixer in a conventional T-mixer using switching DC field. The performance of the conventional switching mode was compared to the proposed pinched switching mode experimentally as well as using numerical simulation. In conventional mode, one inlet is connected to the applied voltage, but in pinched mode both inlets are connected to the applied voltage

(Figure 2.36a). The results indicated higher mixing performance of the pinched mode (97%) in comparison with the conventional mode (45-60%) at the distance of 1mm down the mixing channel. This is because the cyclic switching of the voltage drags the fluid into the channel and creates electrokinetic instability, hence, improve the mixing efficiency. In this work, optimised frequency of switching was investigated based on the magnitude of applied voltage. These optimal frequencies are 2Hz and 8Hz under low applied voltage of 60 V/cm and high applied voltage of 180 V/cm respectively. The results of simulation and experiments are illustrated in Figure 2.36b for optimal frequencies at different applied voltages.

Application of AC electroosmotic flow in micromixing was investigated by Sasaki et al [166]. In this work, AC voltage was applied to a pair of coplanar meandering electrodes laid parallel beneath the channel (Figure 2.37a). In this configuration, the tangential electric field creates two circular flow patterns inside the microchannel (Figure 2.37b).

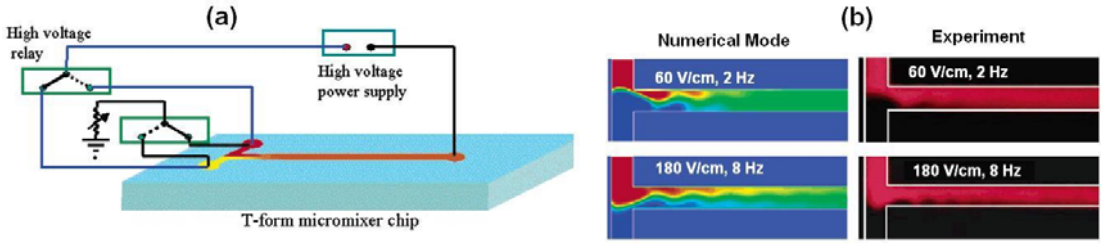

Figure 2.36. The electroosmotic mixer. (a) The concept of pinched mode switching mode; (b) The result of simulation and experiment at two different applied voltages under optimal frequencies [164].

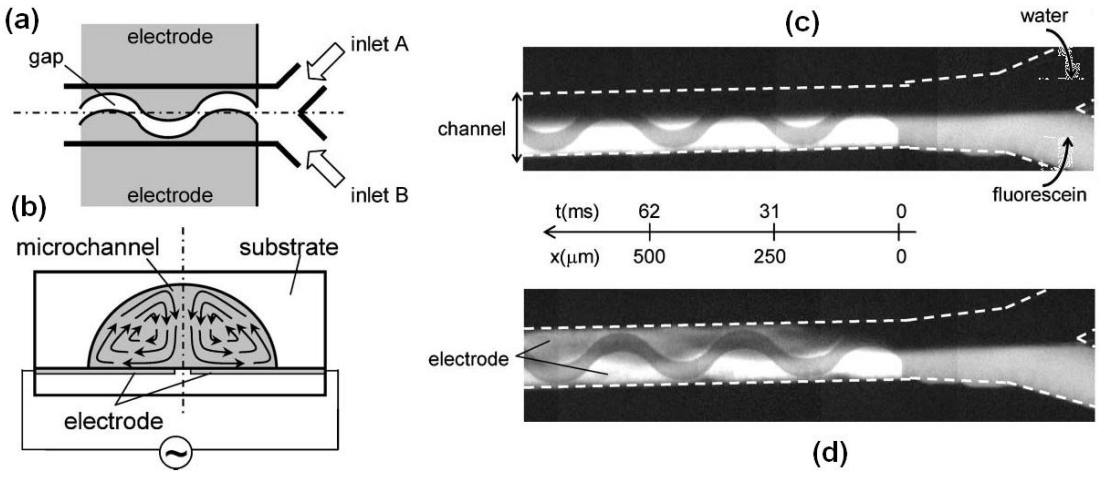

Figure 2.37. (a) Schematic of channel and meandering electrodes; (b) Cross-sectional view of flow circulation under AC electric potential; Fluorescence micrograph of mixing at (c) No applied voltage and (d) Applied voltage of 20 V (p-p) [166].

The meandering shape of electrodes creates an asymmetric circulation of two flows to cross the boundary between two fluids and hence, enhance mixing. A rapid dilution mixing was achieved in 0.18 sec at flow velocity of 12 mm/s inside the mixing channel, 120 mm in width. This performance is 20-fold faster than the performance of pure diffusion mixing in the same condition with no external force.

On a different electroosmotic mixing concept, Tang et al [167] reported a modulation-based flow pattern using periodic switching of electroosmotic flows between two inlets. This flow pattern will create a segmental pattern of two fluids inside the mixing channel and improve the mixing significantly. The result of simulation and experiment indicated a threshold frequency above which the modulation is not possible. This threshold frequency depends on the fluid flows and channel dimension. Figure 2.38 illustrate a schematic diagram of the mixer and simulation results at different dimensionless frequencies. Nevertheless, a reproducible and stable modulation of two fluids in the channel was achieved in frequencies ranging from 0.01 Hz to 1 Hz.

In a different approach Wu and Liu [168] reported an electroosmotic mixer based on temporal and spatial modulation of ζ-potential of channel surface. In this work, a conventional T-mixer was used and a series of asymmetric herringbone aluminium electrodes embedded at the middle of the channel. By controlling and varying the voltage of these embedded electrodes, the surface charge, hence, the ζ-potential of the surface was controlled by inducing positive or negative polarity. By activation of the external potential across the channel, a local flow circulation zone was generated as the result of interactions between different polarity double layers. The concept of this circulation flow pattern is demonstrated in Figure 2.39a.

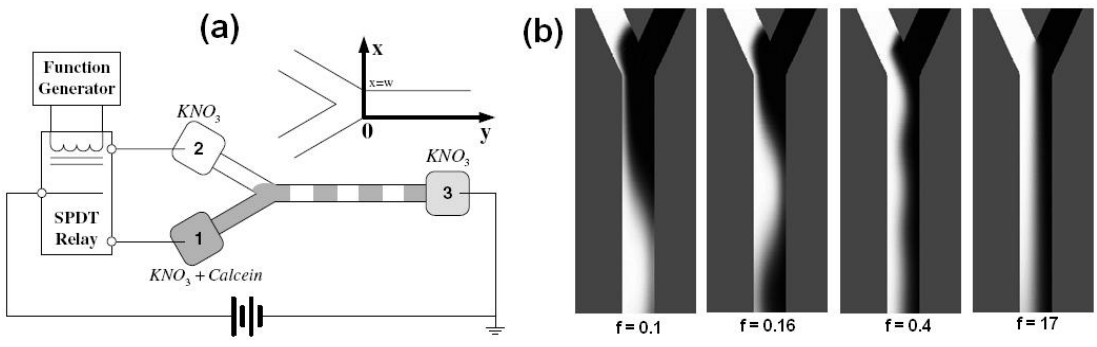

Figure 2.38. Modulation-based electroosmotic flow mixer. (a) Schematic diagram of the setup and the concept; (b) the result of simulation at different dimensionless frequencies [167].

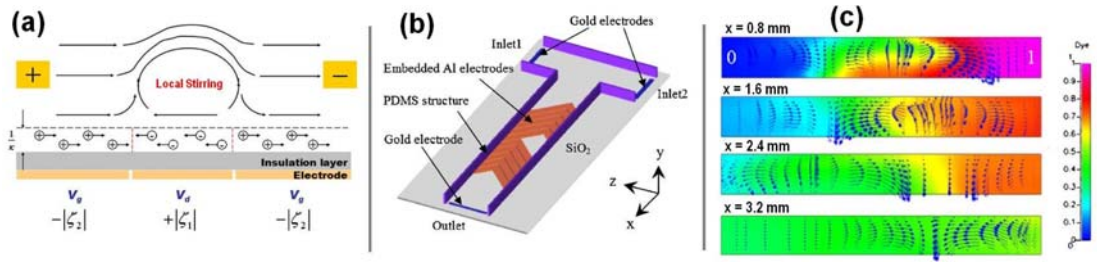

Figure 2.39. (a) Schematic of creation of circulation flow pattern; (b) Schematic of the mixer and electrode pattern; (c) The result of CFD simulation at different channel cross-sections [168].

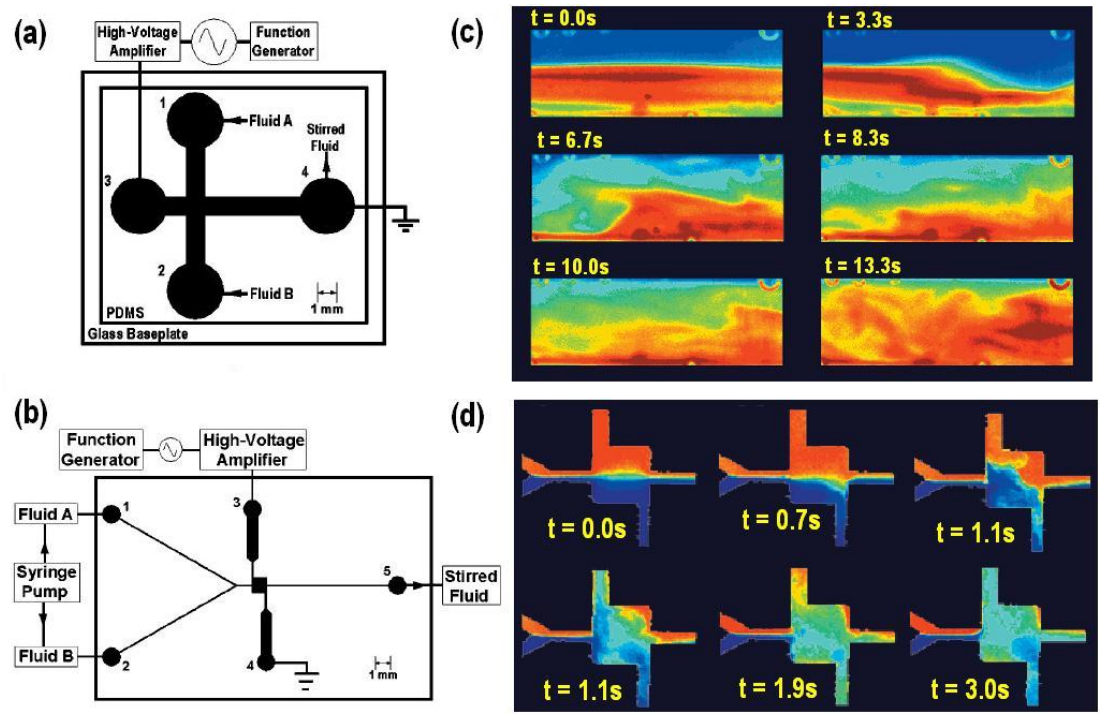

Figure 2.40. Ac electroosmotic mixer. (a and b) Schematic of mixing channel and chamber setup; (c and d) Time-step images of mixing performance for channel and chamber based mixing setups [170].

Nevertheless, creation of the local flow circulation results in rapid and homogeneous mixing of two fluids. Numerical and experimental results indicated an effective mixing ratio of 90% within 5 mm length of the microchannel (Figure 2.39c).

A two-dimensional numerical investigation of electroosmotic flows driven by a uniform electric field in a conduit with non-uniform distribution of ζ-potential was performed by Qian and Bau [169]. In this simulation, local ζ-potential values were induced and controlled by a series of embedded electrodes at top and bottom of the conduit. It was shown that by appropriate modulation of the ζ-potential, various flow patterns can be created inside the conduit. These flow patterns can efficiently mix two fluids by inducing chaotic advection patterns.

Another electroosmotic micromixer was reported by Oddy et al [170] by creating oscillating electroosmotic flow inside the mixing channel and mixing chamber using AC sinusoidal applied voltage. It was found that application of AC voltage creates electrokinetic instability by creation of rapid periodic stretch and folding inside the mixer. This instability can be used to stir the fluid streams with Reynolds numbers of order of unity. The mixing was successfully performed in both mixing channel (Figure 2.40c) and mixing chamber (Figure 2.40d) under pressure flow streams as well as electroosmotic flow streams. The time-scaled performance of the mixing was improved by almost two orders of magnitude in comparison to pure diffusion-based mixing.

2.5.5.3 Dielectrophoretic Micromixers

Dielectrophoresis (DEP) is the movement of polarisable particle/body subjected to a non-uniform electric field. Non-uniform nature of the electric field induces non-uniform distribution of electric dipoles on the particle/body, which induces a net electric force. If the polarisability of the particle is higher than the surrounding medium, the particle will be dragged toward higher field region (positive DEP). Otherwise, the particle will be repelled from higher field region under negative DEP force [171]. The application of dielectrophoresis in mixing of two fluids can be realised through stirring effect of suspended particles inside the fluids. In this method, stretch and folding of the particle trajectory create disturbance in the fluids interface as the result of friction forces in liquid-solid interface.

The application of dielectrophoresis activated micromixer was reported by Deval et al [172] and Lee et al [173]. In this work a time dependent Dielectrophoretic force was applied to a mixture of suspended polystyrene particles in DI water inside a patterned microchamber. The result of simulation and experiment indicated stretch and folding pattern will be created by activation of DEP force (Figure 2.41b).

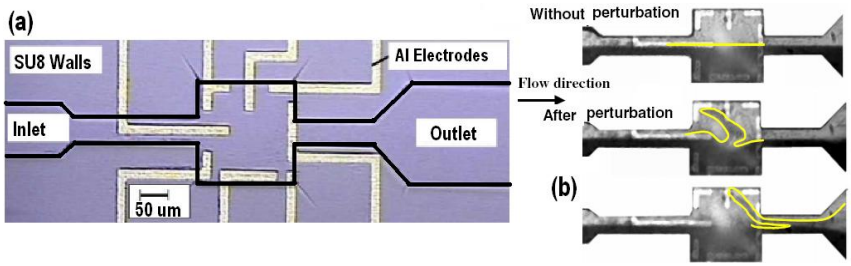

Figure 2.41. Dielectrophoretic micromixer. (a) Top view of the mixer and electrode pattern; (b) Stretch and folding of polystyrene particles [173].

This pattern creates chaotic particle trajectories which might enhance the mixing. Further evaluation of effectiveness of mixing by polystyrene particle was not supplied in this work.

2.5.6 Magnetic Micromixers

2.5.6.1 Magneto-Hydrodynamic (MHD) Micromixers

Charged particles inside an electrolyte will be dragged toward opposite field region in the presence of an electric field. Moving charges experience Lorentz force in the presence of magnetic field. Therefore, application of coupled magnetic and electric field can induce Lorentz force on charged particles inside an electrolyte solution. This effect, which is known as Magneto-hydrodynamic (MHD) effect, has been used in micromixers [174, 175].

Bau et al [174] reported a MHD mixer using alternating electric field applied to an array of deposited gold electrodes on the wall of a conduit. The conduit was filled with an electrolyte solution and subjected to a uniform magnetic field perpendicular to the surface of the electrodes. The interdigitated pattern of electrodes, generate electric currents in various directions, which in turn induces opposite Lorentz forces. Since the pattern of electrodes can be fabricated in different shapes and positioned in different orientations, the induced Lorentz force can creates a chaotic pattern of local currents, which creates eddies and enhances mixing. Figure 2.42 illustrate the schematic depiction of the MHD mixer and an experimental result of mixing of a dye stream in electrolyte solution.

Solomon and Mezic [175] reported a 3D vortex mixer derived by a weak time dependent 2D MHD flow. Generation of a pair of weak two-dimensional horizontal laminar vortex flow on top and bottom of a chamber results in generation of 3D vertical vortex flow caused by Ekman pumping mechanism. This method was studied numerically and experimentally and the results indicated that mixing is more efficient at resonant frequency. The mixing time in this mixer can take up to an hour for a typical vortex zone of 2.2cm×2.2cm.

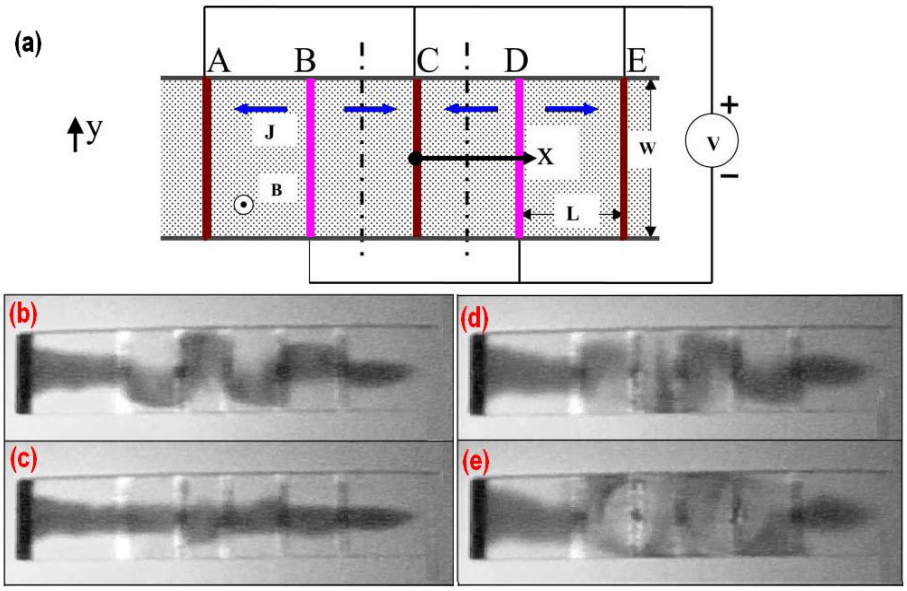

Figure 2.42. MHD micromixer. (a) Schematic diagram of the mixer and electrode pattern; (b-e) Deformation of dye stream under Lorentz force and mixing in solution [174].

2.5.6.2 Magnetophoretic (MAP) Micromixers

Magnetophoretic phenomena and its application to induce magnetic force on magnetic particles is the subject of the next chapter (*Chapter 3*) and will be discussed in more detail later. In this section the aim is to review micromixers that use magnetophoretic force as the external source of force to create disturbance in the mixing zone. The magnetophoresis force is analogous to dielectrophoresis force acting on magnetic dipoles. If a magnetically permeable body is exposed to a non-uniform magnetic field, the interaction between internal magnetisation of the body and external magnetic field creates a net force, which is towards the higher region of field strength. This force has been widely used in manipulation and separation of bio-molecules by application of small-size magnetic particles [176]. Since bio-fluids are inherently of non-magnetic nature, application of MAP force in micromixers is performed using suspended magnetic particles in the fluid. Therefore, the magnetic force is meant to perform the mixing by stirring the magnetic beads across the fluids interface. The spatial movement of magnetic beads inside the mixer drags the fluids from one side to the other side of the interface as a result of friction force.

Suzuki et al [177-180] reported a magnetic micromixer using a conventional T-mixer with serpentine mixing channel. Magnetic force was applied using embedded electrodes at the bottom of the channel. A chaotic mixing pattern of magnetic beads was created using specific switching combination of the electrodes by creating

efficient stretch and folding of material lines. Figure 2.43 illustrate the serpentine magnetic mixer and efficiency of the mixing by applying the magnetic force. A good mixing was reported in less than 10s at 1.3 mm mixing length by applying magnetic force of 1×10^{-12} N.

Another rotational magnetic field mixer was reported by Rong et al [181]. The nature of the magnetic force is usually one directional force, which leads to collection of magnetic particles at higher magnetic field region. Efficient mixing takes place by spatial mixing of magnetic beads inside the mixer. Therefore, in the absence of magnetic repulsive force, opposite directional attractive force need to be applied. This implies that to generate rotational magnetic field, at least three pairs of magnetic poles are required. In the work reported by Rong et al, a set of three magnetic poles was placed outside the mixing zone placed at the junction of a Y-shape mixing channel. It was shown that sequential activation of pole pairs can create a rotational force exerted on the magnetic particles. The magnetic coils are placed outside of the mixing zone and the magnetic field is introduced through implementation of magnetic tips. The strength of applied magnetic force was in order on 1×10^{-8} N. Application of this mixer is for mixing of cells and magnetic particles in order to collect the cells by active surface functionality of the particles. The concept of mixing sequence of this magnetic rotational field mixer is illustrated in Figure 2.44.

Magnetic bead tend to chain up and stick to each other inside the fluid when subjected to a DC or AC magnetic field. In fact if the strength of magnetic field is strong enough, a very compact and porous bulk of magnetic particles will be created inside the mixing channel. This effect has been used to enhance the mixing by creating dynamic porous structure inside the channel. When the flow passes through this magnetic porous structure, chaotic advection flow pattern forces two fluid streams to mix very quickly.

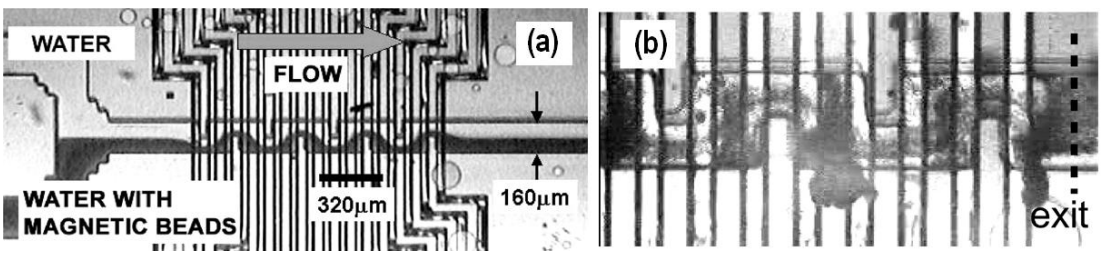

Figure 2.43. Magnetic micromixer; (a) The serpentine magnetic mixer showing no mixing when the magnetic field is not activated; (b) Performance of the mixing after activation of magnetic field disturbance [178].

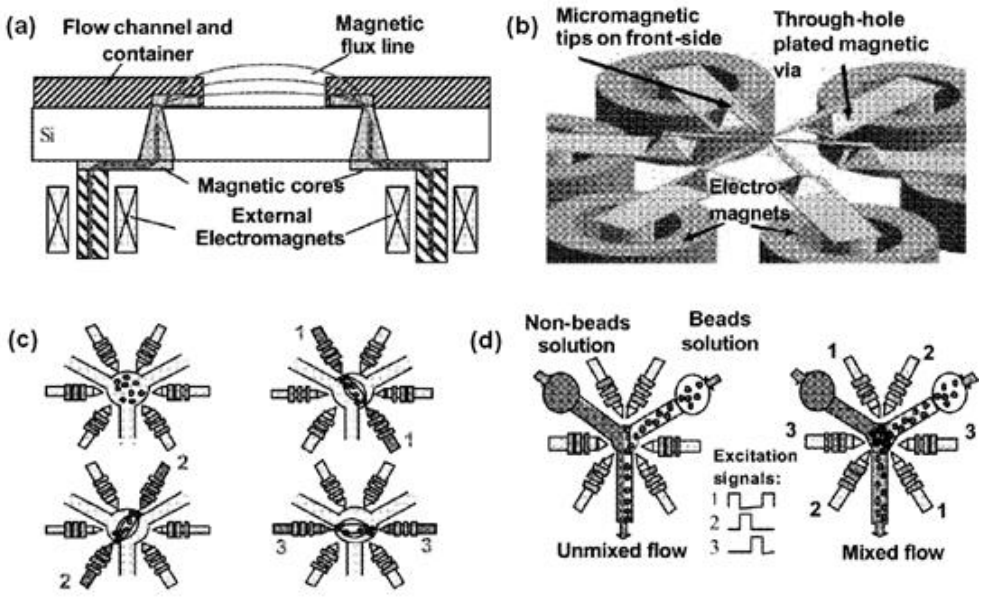

Figure 2.44. Magnetic rotational field mixer; (a) Cross-sectional and (b) 3D views of fabricated mixer; (c) The static working principle; (d) Dynamic working principle [181].

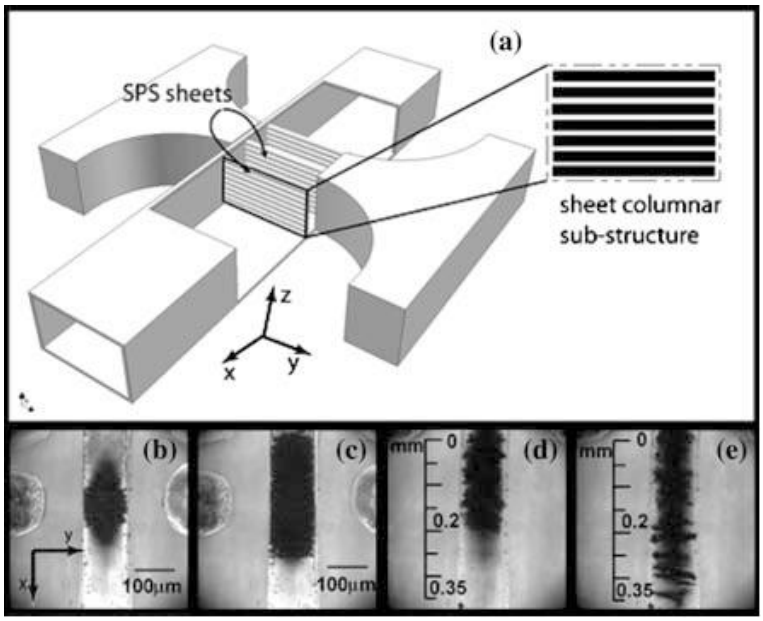

Figure 2.45. (a) Schematic view of magnetic supra-particle structure (SPS) in a microfluidic channel; (b) SPS at zero fluid velocity (u=0), f=100 Hz and B=5 mT. (c) SPS at u=0, f=5 Hz and B=5 mT. (d) SPS at u=0.4 cm/s, f=5 Hz and B=25 mT. (e) SPS at u=0.4 cm/s, f=5 Hz and B=20 mT [176].

Rida et al [176, 182, 183] used this magnetic structure to perform mixing inside a Y-shape mixer. The magnetic field was generated using an external electromagnet and was introduced to the side walls through embedded permalloy layer. Figure 2.45 illustrate schematic diagram of this magnetic mixer with integrated permalloy parts. An image of the magnetic clustering structure, so-called supra-particle structure (SPS) is shown in Figure 2.45b-e, which is shown at different magnetic field strength

and during perfusion of fluid. This mixing method is very similar to the concept of large conventional static mixers used by Bertsch et al [138] in design of chaotic helical mixer. The advantage of this method is the dynamic structure of the porous structure that can be agitated using DC and AC magnetic field. The efficiency of this mixer was tested using fluorescent and non-fluorescent streams and 70% and 95% mixing efficiency was achieved at flow rate of 5mm/s at DC and AC magnetic field modes respectively.

Shikida et al [184, 185] reported a droplet-based magnetic mixer using differential magnetic field generated by magnetic field modulation of a permanent magnet and integrated electromagnet. In this work the electromagnet was created using multi-layered aluminium foils to control the heat dissipation ratio.

The generation of strong magnetic field inside the mixer is the most challenging part of magnetic mixers [186]. This work was done by employing expensive multi-layered fabrication processes in conventional MEMS magnetic-based fabrication techniques. Lin et al [187] reported a particle-based magnetic gradient generator using micron-sized nickel particles implemented in the channel walls. Applied external magnetic field induces magnetic moment in the nickel particles. These particles can increase and concentrate the external magnetic field and generate higher magnetic gradient. It was shown that the magnetic force generated in the presence of these particles is 3.31 times greater in magnitude. Figure 2.46 illustrate the concept of embedded nickel particles in the side wall of cell separator.

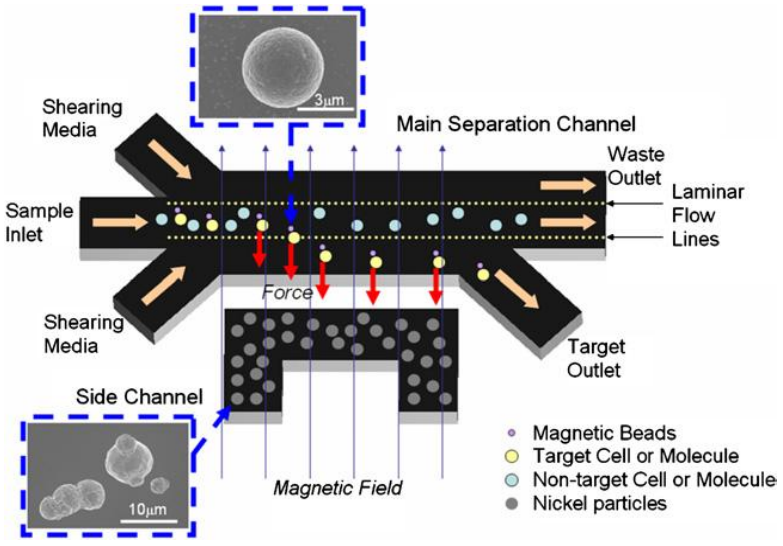

Figure 2.46. Schematic diagram of enhancing the magnetic gradient by application of embedded nickel particles (The picture describe the separation of magnetic bead attached to the cells) [187]

2.6 Conclusion and Discussion

As discussed in the previous chapter (*Chapter 1, Section 1.2.4*), the majority of the reported sample processing bio-chips have used solid-phase extraction system (SPE) to purify nucleic acids. Thermal lysis of the purified target cells was also used in some other bio-chips to perform the amplification step without the needs for DNA extraction and purification. However, the application of this method is limited to a very low cell concentration due to the presence of PCR inhibitors inside the cell membrane. In addition, a pre-processing step is necessary to capture and purify the target cells using a bench-top or chip-based protocol. Therefore, their application is not suitable for POC devices when detecting minimal residual disease and infectious agents with low copy number in the sample.

On the other hand, SPE systems are the most reliable and well-established techniques for nucleic acid extraction and purification process. This is because of the excellent bonding capacity between silica surface and nucleic acids. This unique bonding property has led to the development of many commercial laboratory-based nucleic acid extraction and purification kits [15, 16]. These kits can be divided into two main groups; column-based extraction kits and magnetic bead-based extraction kits. Compact and porous silica matrix is the base of all column-based extraction kits, which is the gold standard of nucleic acid extraction and purification. In this method, compact silica matrix increases the total bonding surface area, thus increasing the chance of DNA capturing. Due to this fact, tremendous effort has been devoted on the adaptation of the column-based DNA extraction technique to a microfluidic-based micro-chip format. The results of the reported works have shown that comparable results to that of the standard bench-top method were achieved using chip-based techniques [36, 39, 41, 42]. However, chip-blockage is the major issue with these chips using a heterogeneous sample such as whole blood, which contains various large-size molecules. Therefore, the application of the SPE columns remains limited to the purified DNA sample or diluted cell-lysate.

Another well-established solid-phase extraction technique is the silica-coated magnetic bead suspended in lysis buffer. Although the efficiency of this technique is not as good as column-based extraction, this technique can easily be adapted and used to extract and purify DNA molecules from whole blood in micro-chip format.

The efficiency of the DNA capturing in this method mainly depends on the efficiency of mixing the magnetic beads within the sample. The larger aspect ratio together with an efficient mixing pattern can increase the efficiency of the DNA capturing in a microfluidic system. Therefore, the purpose of this work is to design and develop a DNA extraction device to be used with an adapted standard magnetic bead-based DNA extraction protocol.

The standard process involves the extraction of DNA molecules from lysis of pathogenic viral and bacterial cells inside a heterogeneous medium such as whole blood. The lysis process takes place by introducing the lysis buffer into the blood sample followed by an enzymatic incubation step at the designed temperature. The incubation conditions, such as temperature and pH, are necessary for the lysis buffer to effectively lyse the cell membrane. After complete lysis process, released DNA molecules need to be captured on the surface of the suspended magnetic beads. Finally, a washing process is necessary in order to purify the captured DNA molecules from the rest of fluid containing cell debris, proteins and other potent PCR inhibitors. Therefore, there are three main steps that need to be considered in designing the DNA extraction device in this work. These steps are efficient cell lysis, efficient DNA binding and efficient DNA purification.

The purpose of this chapter was to review and study different reported microfluidic mixers in order to adapt the most suitable mixing platform to be used with the selected magnetic bead-based extraction protocol. In the passive mixing platforms, where the mixing entirely relies on diffusion and chaotic advection created by geometrical modification, the fabrication is limited to geometrical complexity of the mixer itself. Since the efficiency of these mixers is mainly based on the diffusion, and this is done by decreasing the characteristic length of the diffusion, the majority of these mixers have small channel depth. This is particularly problematic when using suspension fluids such as magnetic beads/lysis buffer, which might result in channel blockage. However, the application of passive multi-lamination mixers is more efficient when using non-suspension fluids. Various types of passive mixers have already been used in micro-chips using SPE systems [34, 42, 45].

From various types of the reported active mixers, the application of electrokinetic mixers is limited to the fluids with particular physical and chemical properties. For example, MHD mixers only work with electrolyte solutions, EHD mixers work with

highly conductive fluids, electroosmotic mixers work with high pH fluids and polarisable particles are necessary in dielectrophoretic mixers. In addition, the implementation of various electrode patterns is essential in all of the electrokinetic mixers, which adds an extra cost and complexity to the manufacturing process.

In the active mixing platform, the piezoelectric mixers and the magnetic mixers can be used for the efficient mixing of the magnetic beads within the blood/lysis buffer. The implementation of a piezoelectric mixer in a fully integrated POC device was first reported by Liu et al. [50, 51]. However, this mixer was used to capture the target cells on the surface of the immune-magnetic beads. Magnetic mixing platform can also be used in this work due to the presence of magnetic beads in the fluid [188-191].

Chung et al. [31] reported a magnetic bead-based DNA extraction device using immobilised magnetic beads on the channel walls and the solution flowing back and forth. The efficiency of the device was compared with the free bead sample and an 88-fold improvement was observed with the immobilised beads extraction technique. The probability of collision between the beads and the DNA is low due to the existence of other large molecules in the blood. In the presence of an external perturbation, the relative locations of the beads and DNA molecules remain unchanged. On the other hand, the probability of collision increases dramatically when the beads are immobilised. This is mainly because of the changes in the relative locations of the beads and DNA molecules. This fact implies that in order to increase the efficiency of DNA extraction, either magnetic beads or the fluid need to be immobilised.

2.6.1 Introduction of a Novel Magnetic Micromixer for Extraction of DNA from Whole Blood

Based on the above discussion, piezoelectric micromixers seem not to be suitable for the efficient mixing of the magnetic beads and the solution. Therefore, the only method that can selectively agitate the magnetic beads inside the immobilised solution is through the application of switching magnetic field.

The application of non-uniform external magnetic force generates effective spatial and temporal mixing of magnetic beads in the fluid to collect suspended DNAs. The non-magnetic nature of the bio-fluid and biological entities eliminates the effect of

magnetic force on these entities. Attached DNA molecules to the magnetic beads can be harvested through the application of DC magnetic field by clamping the beads at the bottom of the mixing unit. Despite most chemical reactions, in this work the generated heat resulted from joule heating of the electromagnets can be used for the enzymatic incubation process and helps to lyse the cells membranes. In addition, the viscosity of fluid decreases by increasing the temperature, which improves the spatial movement of the magnetic beads inside the mixer. Although the spatial-temporal movement of the magnetic beads inside the mixer might help efficient mixing of the whole blood and lysis buffer, this process can take place entirely by diffusion. This may be realised by creating the maximum contact surface and minimum diffusion length in the mixer.

Figure 2.47 depicts a schematic diagram of the proposed magnetic mixer/separator in a cross-sectional view. Since the blood/lysis buffer mixture needs to be incubated at a certain temperature, the static mixing concept is introduced through the application of micro-chamber. To decrease the diffusion length, two fluids need to be laminated on top of each other, which can be created by introducing two fluids to the opposite inlets at T-junction at the perimeter of the mixing chamber. This will create maximum contact surface between the fluids, thus decreasing the diffusion time. In this scenario, the diffusion time can be estimated based on Equation (2.8). Given the characteristic value of diffusion coefficient for liquids as $D = 1 \times 10^{-9} m^2 s^{-1}$, the average diffusion time of $\tau = 22.5s$ can be calculated for a typical diffusion length of $L = 150\mu m$. This diffusion time is negligible in comparison with the total incubation time (5-10 minutes). It worth mentioning that diffusion time decreases as the temperature increases during the incubation.

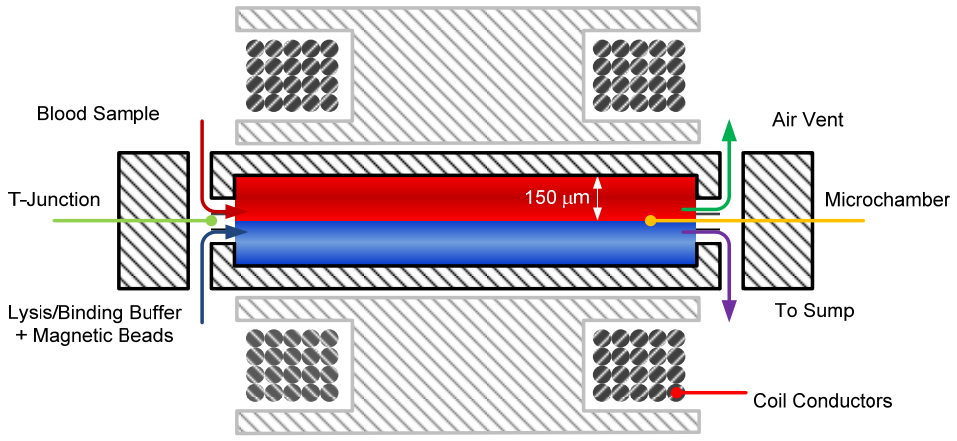

Figure 2.47. Schematic of proposed magnetic mixer using two external electromagnets placed on top and bottom of mixing chamber.

In the following chapters (*Chapter 4* - *Chapter 7*), the detail of the operating characteristics of this proposed micromixing chamber is described. Both simulation and experimental work that were concluded are reported and critically appraised.

CHAPTER 3

MAGNETOPHORESIS

3.1 Introduction

Magnetic particles have been the subject of research for a long time. Nowadays, their application has been widely spread in biotechnology from biosensors to magnetic separators and bio-manipulation. The non-magnetic nature of biological entities, make it very powerful candidate to employ magnetic particles to selectively separate/manipulate the molecule of interest from the mixture of different molecules. This work can be done by employing right surface coating on magnetic particles. By application of non-uniform magnetic field, these magnetic particles can be mixed in biofluids and capture the target molecule. These beads then can be separated magnetically from the rest of the fluid to downstream biological activities.

Different magnetic particles in various sizes and coatings are commercially available from different vendors. Whilst, they have different magnetic properties and fabrication technologies, all of them are based on application of small magnetic particles as single or multi cores inside a polymeric body. The magnetic core of this particles, make it easy to induce a net magnetic moment by applying an external magnetic field. The key-point here is the pattern of external magnetic field. The term 'Magnetophoresis' is an analogue to dielectrophoresis which describe the net force

applied on a non-conductive material under the influence of non-uniform electric field. Therefore, magnetophoresis describes the magnetic force applied on a magnetised body under the influence of non-uniform magnetic field.

In this chapter, a brief review of magnetic field and magnetic materials is given and finally applied force on a magnetic particle in non-uniform magnetic field is calculated mathematically.

3.2 Magnetic Field and Magnetic Materials

Unlike electric field, which can be generated by even a single electric charge, magnetic field is completely different and cannot be generated by a single magnetic charge. This is because there is no single magnetic charge. Therefore, magnetic field lines have no origin and end. Instead, magnetic field lines are always in close loops. In fact the origin of magnetic field is related to movement of electric charges. For example, electric current in a copper wire which is a collective motion of electrons, creates magnetic field. In more detail example, the spinning movement of electrons around nucleus creates magnetic field [192, 193].

Magnetic dipole can be realised when the magnetic field lines have sense of direction. This can happen in a solenoid, when magnetic field lines enter from top or bottom, depending on the electric current direction, and leave from other end of solenoid. In this case the south pole is where the lines enter the solenoid and the north pole is the other side. The solenoid is an example of electromagnet which means the magnet is created using forced electric current. The natural source of magnetic field can be found in rare earth magnet. In this example, the origin of magnetic field is not the forced current; instead the source is the spin effect of electrons in the material [193].

Nevertheless, what is important in this work is the study of reaction of different materials to external magnetic field. Unlike different reactions of materials to electric field as conductors, dielectrics and semiconductors, the reaction of materials to the magnetic field is more close to the magnetic dielectric. This is because there is no net magnetic charge in analogue to electric charge. Therefore, all materials react to the external magnetic field by change of spin orientation at atomic level. The different

atomic level reaction of materials can be realised as different macro-size classifications for materials. These materials are described below.

3.2.1 Diamagnetism

Consider atoms in which the net field produced by motion of orbital electrons is cancelled out by net field generated by spin electrons. These atoms have no net magnetic field in the absence of external field and thus such a material has no permanent magnetic moment m_0. By applying external magnetic field, the orientation of orbital electron will change to oppose the external field. This produces an internal magnetic field, the same as external magnetic field and in opposite direction. Therefore, the external magnetic field generates no magnetic torque on this material. This effect in materials is called *Diamagnetism*. Although, there is a small difference between internal and external magnetic field, this effect is very small and can be ignored in most cases. Since this effect arises from the spin effect of electron in atoms, all materials show diamagnetism. Copper, Gold and Silicon are examples of diamagnetic materials [192].

3.2.2 Paramagnetism

In some materials, the magnetic field generated by electron spin and orbital motion do not cancel each other out. Therefore, the atom has a net magnetic moment. This effect though will be cancelled in random orientation of atoms in material and the net magnetic moment of material is zero. In the presence of external magnetic field, there is a small torque on each atomic moment which tends to aligns atomic moments with the external magnetic field. This alignment increases the value of magnetic flux density (B) inside the material. Since diamagnetic effect still is operating on orbital electrons, it might counteract with the above increase. If the result of interaction between these two effects is an increase in the internal magnetic field, the material is called *Paramagnetic*. Otherwise the material is still diamagnetic. Potassium, Tungsten and Oxygen are examples of paramagnetic materials [192].

3.2.3 Ferromagnetic, Ferrimagnetic and Anti-ferromagnetic Materials

Atomic moment in these materials is very strong, which cause the adjacent atoms to either co-align or counter-align. In *Ferromagnetic* materials, the strong magnetic moment of free spin electron cause relatively large dipole moment. Inter-atomic

forces between these atoms align them in a parallel manner over a large atomic region which is called *Domain*. These domains have different shapes and sizes ranging from one micrometer up to few centimetres. Depending on size and in ferromagnetic materials, these domains are aligned in different directions in which they cancel each other out. By applying external magnetic field, stronger domains in direction of external field tend to grow up by using neighbouring domains. This effect creates relatively strong internal moment compared to external field. Although, the opposing domains still are present, by increasing external field they shrink into the aligned domains. This will increase the magnetisation of bulk material until at certain point in which increase in external field has less effect on internal magnetisation of material. In this state the material is saturated, which means aligned domains have filled the bulk material. After removal of external magnetic field, the random alignments of domains does not create an overall cancelation of individual moments and there is a residual magnetic moment left in the material.

Therefore, the state of ferromagnetic materials is different after each exposure to an external magnetic field. This property of ferromagnetic material is called hysteresis which means the material has a memory of previously applied field. The hysteresis loop of these materials shows the magnetisation memory state of material as well as saturation point. Iron, Nickel and Cobalt are the only materials that show ferromagnetic behaviour in room temperature though they lose this property above Curie temperature. In addition, some alloy of these materials such as Alnico which is aluminium-nickel-cobalt alloy, exhibit ferromagnetic behaviour [192].

In contrary to co-alignment of atoms in ferromagnetic materials, adjacent atoms tend to counter-align and cancel each other's moment out in *Antiferromagnetic* materials. The overall internal magnetic moment is zero and will be affected by external field slightly. Although many oxides, sulphides and chlorides show antiferromagnetic behaviour, manganese oxide was the first antiferromagnetic discovered material. Antiferromagnetism is often present at below room temperature.

In some materials, the alignment of atoms is in a situation in which their moments oppose each other but does not fully cancel each other out. Therefore, in response to an external field they show large internal magnetic moment. These materials are called *Ferrimagnetic* and their magnetic moment is less than ferromagnetic materials. Since the conductivity of these materials is below the conductivity of

semiconductors they are suitable for high frequency alternating field application. The example of this material is Ferrites which are mostly used in high frequency transformer cores. Another important example from this group is iron oxide magnetite (Fe_3O_4). These materials also lose their magnetic characteristic above Curie temperature [192].

3.2.4 Superparamagnetism

Superparamagnetism is created by embedding small size ferromagnetic materials in non-ferromagnetic matrix. In this mixture, the magnetic domains in ferromagnetic materials are separated from each other in a way that there is no interaction between them. The size of ferromagnetic particle needs to be selected in such a way that the particle comprises a single domain. Theoretically, the size of single domain is calculated as 14nm in diameter. The width of domain wall is a function of magneto-crystalline anisotropy, the exchange energy and lattice spacing of the crystal structure [194]. By decreasing the size of domains down to 15nm, particles domain reduces to a single domain and the domain wall will disappear. Since there is no extension of domain in the presence of external field, domain will reach saturation level in lower strength of external field. Demagnetisation takes place very quickly by the same reason in single domain particles. Therefore, the residual magnetic moment is eliminated because of random orientation of bulk compound material. These materials are called superparamagnetic because their bulky behaviour is similar to paramagnetic materials below Curie temperature [192].

An important application of superparamagnetic material is in audio and video recording tapes. Another important application of superparamagnetism is in fabrication of magnetic beads which is the subject of this thesis. A very wide range of commercially available magnetic particles are designed to exhibit superparamagnetic behaviour. This is because in the presence of external field, ferromagnetic particles tend to aggregate due to residual induced field. Therefore, in biotechnological applications where magnetic particles are mixed in a bio-fluid and external magnetic field is used for mixing and manipulation, superparamagnetic behaviour of particles is a necessity. A summary of different magnetic materials based on spin and domain arrangement is shown in Figure 3.1. Table 3.1 shows some characteristics of magnetic materials.

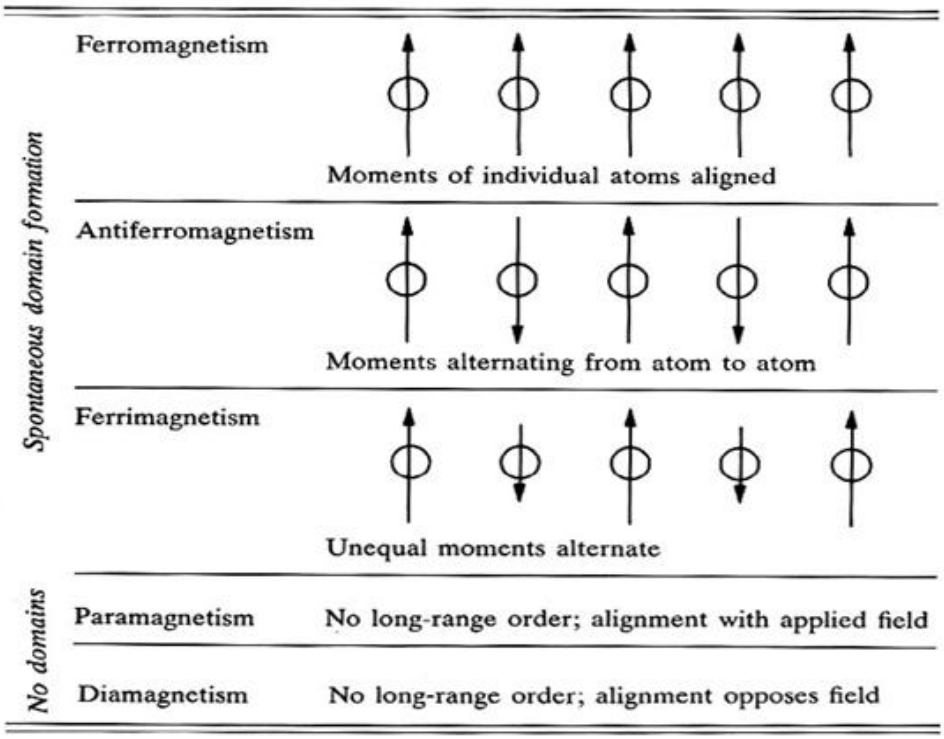

Figure 3.1 Schematic depictions of spin arrangements in different types of magnetic materials [195].

Table 3.1. Characteristics of magnetic materials (adopted from [192])

Classification	Magnetic Moments	*B* values	Comments
Diamagnetic	$m_{orb} + m_{spin} = 0$	$B_{int} < B$	No Domain
Paramagnetic	$m_{orb} + m_{spin} = small$	$B_{int} > B$	No Domain
Ferromagnetic	$\|m_{orb}\| \ll \|m_{spin}\|$	$B_{int} \gg B$	Multi Domains
Antiferromagnetic	$\|m_{orb}\| \ll \|m_{spin}\|$	$B_{int} = B$	Anti-Parallel Domains
Ferrimagnetic	$\|m_{orb}\| < \|m_{spin}\|$	$B_{int} > B$	Unequal Anti-parallel Domains
Superparamagnetic	$\|m_{orb}\| \ll \|m_{spin}\|$	$B_{int} > B$	Single Domain

Magnetic field intensity *H* is described as the external source of magnetic field and is measured in unit of [A/m]. On the other hand, internal magnetization *M* is defined as the magnetic dipole moment per unit volume and has a unit similar to magnetic field. The difference here is that the source of external magnetic field is electric current and the current source of internal magnetization is orbital electrons and electron spins [192]. The density of magnetic flux *B* which is measured in Tesla (T) can be defined for free space medium as a linear function of magnetic field as:

$$B = \mu_0 H \tag{3.1}$$

where μ_0 is the permeability of free space ($\mu_0 = 4\pi \times 10^{-7}\ N.A^{-2}$).

To find the actual relationship between magnetic field and magnetic flux density, internal magnetisation of material needs to be considered as well. The value of *B* in general is given as:

$$B = \mu_0(H + M) \tag{3.2}$$

This means that, the magnetic flux density is related to vector sum of internal and external magnetizations. Since the magnetisation of material is a function of external magnetic field *H*, the relationship between magnetization and external magnetic field can be explained by defining magnetic susceptibility of χ_m in linear isotropic media as follow:

$$M = \chi_m H \tag{3.3}$$

therefore:

$$B = \mu_0(H + \chi_m H) = \mu_0\mu_r H = \mu H \tag{3.4}$$

where

$$\mu_r = 1 + \chi_m \tag{3.5}$$

and

$$\mu = \mu_0\mu_r \tag{3.6}$$

In which μ_r is defined as relative permeability and μ is defined as permeability. Therefore, the relationship between *B* and *H* can be simplified to:

$$B = \mu H \tag{3.7}$$

3.3 Force on a Magnetized Particle in a Magnetic Field

Magnetic particles used in this work for extraction of DNA molecules from whole blood are designed to exhibit superparamagnetic behaviour. These particles are mixed with blood and other reagents and are exposed to a non-uniform magnetic field in order to create sufficient mixing to increase the chance of DNA-Particle bindings. Magnetic particles will be magnetised under external magnetic field and

will experience net magnetic force under non-uniform magnetic field. To investigate the performance of mixing and to optimise the designed pattern of applied magnetic field, the motion of magnetic particles need to be investigated. This investigation can be performed numerically using commercial simulation software. To be able to perform this simulation, calculation of net magnetic force on a magnetic particle in the presence of external field is essential. There are other forces influencing magnetic particles in a fluid such as gravity and hydrodynamic forces. Hydrodynamic force is applied to all cases in which there is motion of solid in fluid. This force together with gravity force will be investigated in detail in *Chapter 5*. Therefore, in this section the emphasis is to calculate the net magnetophoretic (MAP) force applied on magnetic particles.

Magnetic force applied on a magnetised particle under the influence of external field can be identified as two distinct sources. The main induced force is called 'imposed field', which is the direct result of external filed. The other applied force is called 'mutual particle', which is the result of other neighbouring magnetic particles [196]. In the latter case that magnetic particles are placed very close to each other, their internal magnetic field might be mutually influenced. This mutual interaction can be described in two ways; internal field of one particle induces an additional magnetic moment in other particle. In addition, the magnetic field of one particle can give rise to the inhomogeneity of the field pattern on other particles. Hence, the subject magnetic particle can experience an extra net magnetic force from neighbouring particles as well as external magnetic field source.

However, the mutual effect is very weak compared to the external field effect and decreases very quickly by inverse square distance from the surface of the particle. Therefore, this effect can be considered if particles are very closely packed in which their weak magnetic field can mutually interact. In particle laden fluid when the concentration of magnetic particles is very low, by assumption of uniform distribution of particles in the medium, the distance between particles is large enough to ignore mutual interaction. The threshold concentration depends on many parameters such as particle size and magnetic susceptibility. Nevertheless, for micron-size magnetic particles, in concentrations equal or less than 10^{15} particles/m^3 the mutual effect can reasonably be ignored [197]. At this concentration the spatial distance between two neighbouring particles is 10μm. With regard to small particle

size, this distance is large enough to ignore particle-particle mutual interactions. In most commercial DNA purification kits, the concentration of magnetic bead is well below this threshold concentration. Therefore, in this chapter, the mutual particle-particle effect will be ignored and the force induced by external source of magnetic field will be numerically calculated.

There are two approaches to calculating the induced magnetic force on a single particle due to the external field; moment-energy [196] and thermodynamic [197] methods. In this chapter, induced effective magnetic moment on a particle is calculated, based on moment-energy approach, which leads to an expression for the induced magnetic force on a particle.

To obtain a generalised expression of magnetic force on magnetic particles, a homogeneous sphere with radius of R and net magnetic polarization of M_2 is suspended in a magnetically linear fluid with permeability of μ_1.The sphere and fluid is exposed under almost uniform magnetic field intensity of H_0. Figure 3.2 shows a schematic diagram of fluid and magnetic particle under external magnetic field. The relationship between B, H and M is defined by Equation (3.2), which can be rewritten as:

$$B = \mu_0(H + M) = \mu_0(H + \chi_m H) \tag{3.8}$$

The volume magnetisation M is a function of internal magnetisation plus linear or non-linear function of external field H. This general expression can be used for any of paramagnetic, diamagnetic or ferromagnetic particles. Here it is assumed that the particle magnetisation is parallel to external magnetic field direction and there is no electric current flow in the medium ($\nabla \times H = 0$). By these assumptions, the magnetostatics problem can be solved by definition of a scalar potential Ψ as follow [196]:

$$H = -\nabla\Psi \tag{3.9}$$

Which has an assumed solution for Ψ_1 and Ψ_2 inside and outside of the sphere as follow:

$$\Psi_1(r,\theta) = -H_0.r.\cos\theta + \frac{X.\cos\theta}{r^2}, \quad r > R \tag{3.10}$$

$$\Psi_2(r,\theta) = -Y.r.\cos\theta, \quad r < R \tag{3.11}$$

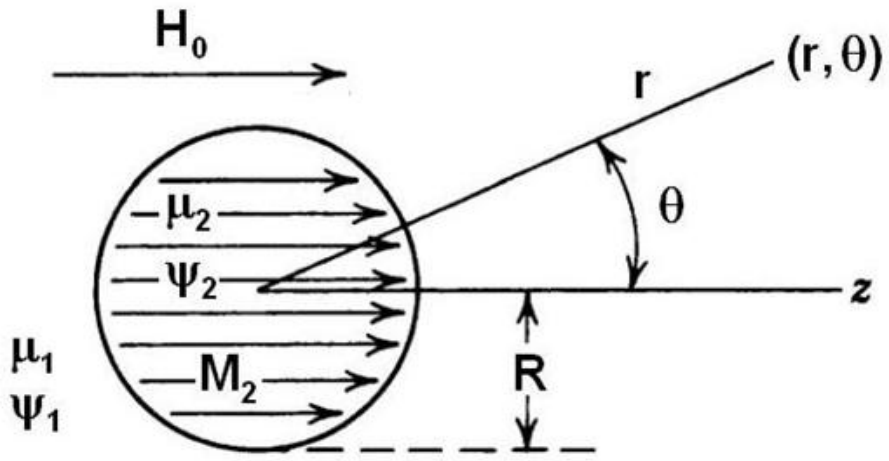

Figure 3.2. Sphere of radius *R* and permeability μ_2 immersed in a media of permeability μ_1 and subjected to a uniform magnetic field of magnitude H_0.

Where *X* and *Y* are constants and their value can be determined using two boundary conditions at the particle surface. In Equation (3.10), the first term is the contribution of external magnetic field and the second term is contribution of the dipole moment of magnetized sphere to magnetic potential outside the sphere. The first boundary condition is the continuity of magnetostatic potential at the boundary between particle and the fluid.

$$\Psi_1(r = R, \theta) = \Psi_2(r = R, \theta) \tag{3.12}$$

And the second boundary condition which defines the continuity of the magnetic flux density at particle-fluid interface.

$$\mu_1 H_{r1} = \mu_0 (H_{r2} + M_{r2}), \quad r = R \tag{3.13}$$

Where

$$H_{r1} = -\frac{\partial \Psi_1}{\partial r} \tag{3.14}$$

$$H_{r2} = -\frac{\partial \Psi_2}{\partial r} \tag{3.15}$$

H_{r1} and H_{r2} are the normal magnetic field intensity in fluid and sphere respectively. Therefore, by using the above boundary conditions in assumed solutions of Equation (3.10) and Equation (3.11), the coefficients X and Y can be determined as follow [196]:

$$X = \frac{\mu_0 - \mu_1}{\mu_0 + 2\mu_1} R^3 H_0 + \frac{\mu_0 R^3}{\mu_0 + 2\mu_1} M_2 \tag{3.16}$$

$$Y = \frac{3\mu_1}{\mu_0 + 2\mu_1} H_0 - \frac{\mu_0}{\mu_0 + 2\mu_1} M_2 \tag{3.17}$$

Where, *Y* describes the magnitude of uniform magnetic field H_2 inside the sphere. To extract the value of effective magnetic dipole moment of sphere (m_{eff}), dipole term in Equation (3.10) is compared with the magnetic potential of a dipole [198]:

$$\Psi_{dipole} = \frac{mR}{4\pi r^3} = \frac{m\cos\theta}{4\pi r^2} = \frac{Xcos\theta}{r^2} \tag{3.18}$$

The second term in Equation (3.10) gives the value of effective magnetic moment as:

$$m_{eff} = 4\pi X = 4\pi R^3 \left[\frac{\mu_0 - \mu_1}{\mu_0 + 2\mu_1} H_0 + \frac{\mu_0}{\mu_0 + 2\mu_1} M_2\right] \tag{3.19}$$

The first part explains the net effect of particle on fluid and the second term is the magnetisation of the magnetic sphere itself. This equation can be simplified in case of magnetic particle in free space in which $\mu_1 = \mu_0$.

$$m_{eff} = 4\pi R^3 \frac{\mu_0}{\mu_0 + 2\mu_1} M_2 \tag{3.20}$$

In a particle with radius of *R* and permeability of μ_2, which is magnetically linear, the magnetic moment can be defined as:

$$M_2 = \chi_2 H_2 \tag{3.21}$$

where χ_2 is the susceptibility of magnetic particle and is defined as:

$$\chi_2 = \frac{\mu_2}{\mu_0} - 1 \tag{3.22}$$

Therefore, by substituting the Equation (3.21) and Equation (3.22) in Equation (3.20), the effective magnetic moment can be rewritten as follow:

$$m_{eff} = 4\pi R^3 \frac{\mu_2 - \mu_1}{\mu_2 + 2\mu_1} H_0 = 3V \frac{\mu_2 - \mu_1}{\mu_2 + 2\mu_1} H_0 \tag{3.23}$$

Where, V is volume of the particle. Therefore, from Equation (3.23) and using the expression for the energy of dipole, the magnetic force induced on a particle can be calculated as follow:

$$U = -m.B = -\mu_1 m_{eff}.H_0 = -4\mu_1 \pi R^3 \frac{\mu_2 - \mu_1}{\mu_2 + 2\mu_1} H_0^2 \tag{3.24}$$

$$F_m = -\nabla U = \nabla(m.B) = \mu_1 \nabla\left(m_{eff}.H_0\right) = 2\pi\mu_1 R^3 \frac{\mu_2 - \mu_1}{\mu_2 + 2\mu_1} \nabla H_0^2 \tag{3.25}$$

Therefore

$$F_m = 2\pi\mu_1 R^3 \frac{\mu_2 - \mu_1}{\mu_2 + 2\mu_1} \nabla H_0^2 \tag{3.26}$$

Where F_m is the magnetophoresis force expression of a magnetic particle in non-uniform magnetic field H_0. From this equation the following conclusions can be extracted:

- Magnetic force is a function of particle volume
- Magnetic force is proportional to permeability of medium, μ_1.
- Since the term ∇H_0^2 can be written as $H_0.\nabla H_0$, magnetic force is directly proportional to magnetic field intensity and its gradient thereof.
- If the permeability of particle is bigger than that of fluid ($\mu_2 > \mu_1$), the magnetophoresis force is positive and particle will be attracted toward higher magnetic field intensity. In contrary, if the permeability of medium is bigger than that of particle ($\mu_2 < \mu_1$), the magnetophoresis force applied on particle will be negative. Therefore, the particle will be repelled from higher field intensity and will be attracted to lower field intensity.

Finally, assuming the medium is of non-magnetic nature ($\mu_0 = \mu_1$), the equation of magnetic force can be rewritten as follow:

$$F_m = 2\pi\mu_0 R^3 \frac{\mu_r - 1}{\mu_r + 2} \nabla H_0^2 \tag{3.27}$$

This assumption is valid in this work, since the fluid medium is a mixture of whole blood and biological reagents which are of non-magnetic nature. Therefore, Equation (3.27) can be used in this work to calculate the magnetic force induced in magnetic particles.

This magnetic force expression will be used in a magneto-hydrodynamic model of particle motion in fluid to simulate the particle trajectories inside the magnetic mixer. This particle trajectory study can be used to optimise the performance of the device.

3.4 Summary

In this chapter, a brief description of magnetic materials was given to understand the behaviour of different materials subjected to magnetic field. Among various materials, superparamagnetic materials are the core of most magnetic beads used in DNA purification kits. The most important property of this material is the fast demagnetisation effect, which is important to prevent permanent bead clustering effect during purification process.

The magnetic force induced in superparamagnetic beads was calculated based on moment-energy method under influence of non-uniform external magnetic field. This expression was simplified to Equation (3.27) with the assumption of non-magnetic nature of the fluids, which is valid in this work. This equation will be used for calculation of induced magnetic force inside the magnetic models in *Chapter 4*. In *Chapter 5*, the calculated magnetic force will be used in a bead trajectory simulation, using *Matlab* source codes, to study the behaviour of the magnetic beads under designed magnetic field patterns.

CHAPTER 4

ELECTROMAGNET DESIGN AND OPTIMIZATION

4.1 Introduction

The purpose of this chapter is to numerically design a magnetic bead-based mixer using internal/external electromagnets and superparamagnetic beads to be used for DNA extraction from whole blood. The idea is to apply non-uniform magnetic field to agitate magnetic beads in lysis buffer/whole blood mixture combined in a chamber. This action will efficiently cause the lysis buffer to lyse the target cells to release the DNA molecules. Subsequently, released DNA molecules will be collected by magnetic beads. The pattern of magnetic force applied to the beads must inherently possess unique properties to cause temporal and spatial distribution of beads within the chamber. Since the force applied on the magnetic bead is a function of magnetic field (H) and its gradient (∇H) thereof, key properties of the electromagnet are the magnetic field strength and its gradient inside the chamber. To achieve the desired magnetic field pattern, different possible coil geometries are simulated using COMSOL Multiphysics simulation package. Both internal and external coils are examined and their limitation is studied. Among various geometries, circular spiral coil exhibits the optimal force pattern inside the micro-chamber. Geometrical dimensions of internal and external coils are examined and optimised dimensions of the coil are concluded from simulation study.

4.2 Simulation Software

The concept of proposed DNA purification chip was previously introduced in *Chapter 2* (Section 2.6.3, Figure 2.47). The core of the DNA extractor is a magnetic mixer consists of two sets of current carrying conductors placed on top and bottom of the chamber. The efficiency of mixing highly depends on the magnetic field pattern generated by top and bottom conductors.

The most accurate method to solve the magnetic problem is to solve Maxwell's equations with appropriate boundary conditions. Unfortunately, there are very limited cases that these equations can be solved using the given boundary conditions. Due to the geometrical complexity of the magnetic coils in this work, there is no analytical solution to calculate the magnetic field generated by coils. It become worse, in case of calculating the magnetic force induced on magnetic particles. A solution to these magnetic problems is the application of numerical techniques to find an approximate solution for partial differential equations. Finite element method (FEM), finite volume method (FVM) and finite different method are three common techniques to solve partial differential equations numerically. In these methods, the geometry and the domain will be discriminated to finite elements, and the final solution is the sum of discrete solutions on each discrete element. Therefore the accuracy of the solution increases by increasing the number of discrete elements. Among different numerical techniques, finite element method (FEM), which is often the most accurate approximation technique, is more common technique in solid-based simulations and structural mechanics. On the other hand, FVM and FDM, which use slightly different descretization of the problem to large number of grids, have widely been used in computational fluid dynamics (CFD) modelling package.

There are many commercial simulation packages based on FEM modelling techniques for solution of partial differential equations such as: COMSOL Multiphysics, ANSYS and CFD-ACE+. In this work COMSOL Multiphysics was selected to model the magnetic problem because of its outstanding features. *COMSOL Multiphysics* is well-known finite element package that can be used for simulation of multiphysics problems. Versatility of COMSOL software in coupling different application modes brings the opportunity to simulate magnetic, fluidic and thermal behaviour of the model simultaneously and study their interactions at the same time. COMSOL uses *Maxwell's* equations in FEM approximation method to

solve magnetic problems. A unique feature to COMSOL Multiphysics is that, the underlying equations for electromagnetics are automatically available in all of the other application modes, thus the coupling is much easier between different application modes. Another important advantage of COMSOL is the COMSOL script and MATLAB export link, which can be used to incorporate the model with other products in those technical computing environments.

4.2.1 COMSOL Multiphysics

In this work, which involves different current carrying conductors, Electromagnetics Module was used. To simulate spiral coils in 3D mode, *Magnetostatics Application Mode (emqa)* in the *AC/DC Module* was used, which describes magnetostatics of conducting and magnetic materials. In this application mode, vector magnetic potentials in Cartesian coordinates (Ax, Ay and Az) are the dependent variables and electric current can be used as input in model's subdomain settings. To simulate non-circular patterns, either *Magnetostatics Application Mode* or *Electric and Induction Current Application Mode* can be used, which describes the quasi-statics of electromagnetic field system for conducting, magnetic and dielectric materials. In this mode, vector magnetic potentials in Cartesian coordinates (Ax, Ay and Az) and electric potential (V) are the dependent variables and electric current can be calculated from electric potential by the software. COMSOL uses electric potential to calculate electric current in order to calculate vector magnetic potentials. Subsequently, other magnetic parameters will be calculated from vector magnetic potentials.

In some cases, 3D application mode is not the most suitable mode for simulation of magnetic problems. In such cases, due to the geometrical complexities and subsequent mesh generation, large computing time and computer memory is necessary. In case of spiral conductors, 2D application mode can be used with some appropriate assumptions.

2D simulation, which considers structures axially symmetric around Z-axis with current in the angular direction, can be used only for circular geometries with application of *Azimuthal Induction Currents (emqa)* in *Magnetostatics Application Mode* or *Quasi-statics Application Mode*. Table 4.1 shows a summary of different

application modes used for simulation in this thesis. As it is shown in this table, a *Partial Differential Equation* (PDE) application mode is used to calculate magnetic force applied on magnetic beads inside the chamber. In addition, heat transfer module is used to calculate the thermal effect of the conductors.

4.3 Magnetic Field Calculation

In this section, a simple conductor geometry is used to investigate accuracy of 2D and 3D simulation in COMSOL Multiphysics. The magnetic field created by long current-carrying wire has a well-known analytical solution that can be found in any physics textbook. The magnetic field created by long current carrying wire is:

$$B = \frac{\mu_0 I_0}{2\pi r} \qquad (for\ r \geq R) \tag{4.1}$$

$$B = \left(\frac{\mu_0 I_0}{2\pi R^2}\right) r \qquad (for\ r < R) \tag{4.2}$$

Where, B is magnetic field in Tesla, I_0 is current passing through the wire in Ampere, r is the radius from the centre of the wire cross-section in meters, R is the radius of wire in meters and μ_0 is permeability of vacuum ($\mu_0 = 4\pi \times 10^{-7}\ T.m/A$).

Table 4.1. List of application modes used for simulations in this chapter.

COMSOL Module	COMSOL Sub-module	Application Mode	Space Dimension	Dependent Variables
AC/DC Module	Statics Magnetic	Magnetostatics (emqa)	3D	Ax, Ay, Az
AC/DC Module	Quasi-statics Magnetic	Induction Current (emqa)	3D	Ax, Ay, Az
AC/DC Module	Quasi-statics Electromagnetic	Electric and Induction Current (emqa)	3D	Ax, Ay, Az, V
AC/DC Module	Statics Magnetic	Azimuthal Induction Currents (emqa)	2D	Aphi
AC/DC Module	Quasi-statics Magnetic	Azimuthal Induction Currents (emqa)	2D	Aphi
COMSOL Multiphysics	PDE Modes	PDE, General forms	2D, 3D	User Defined
Heat Transfer Module	-	General Heat Transfer (htgh)	2D, 3D	T, J

To evaluate accuracy of simulation, the above current-carrying wire is simulated in COMSOL Multiphysics in 2D and 3D modes. In 2D simulation mode it is possible to apply infinite wire length but the space domain surrounding the wire is finite. Both space domain and wire length need to be assumed with a finite length in 3D mode. Detail of wire dimensions and simulation detail are given in Table 4.2. Figure 4.1 shows magnitude of magnetic field against radius (r) in a long current carrying wire calculated by standard equations, Equation (4.1) and Equation (4.2). Figure 4.2 and Figure 4.3 show a cross-sectional (left) and radial (right) plots of magnetic flux density simulated by COMSOL software in 2D and 3D modes respectively.

As it is shown in Figure 4.2 and Figure 4.3, both 2D and 3D modes accurately simulate the magnetic problem and their result is very close to the standard equations. 2D simulation gives slightly better result as it uses less assumption compared to 3D mode. In addition, 2D simulation mode has some more benefits as follows. Computation time in 2D mode is very low even with extra fine meshing. Very large space domain can be used, which increases the accuracy of simulation result. Whilst 2D mode offers very fast and simpler simulation condition, it is limited to geometrical symmetry. There are two geometrical symmetries available in COMSOL 2D mode, perpendicular symmetry and axial symmetry. Whilst perpendicular symmetry is suitable for geometries with one infinite dimension (i.e. long wires), axisymmetric symmetry is suitable for shapes with axial symmetry (i.e. circular coils).

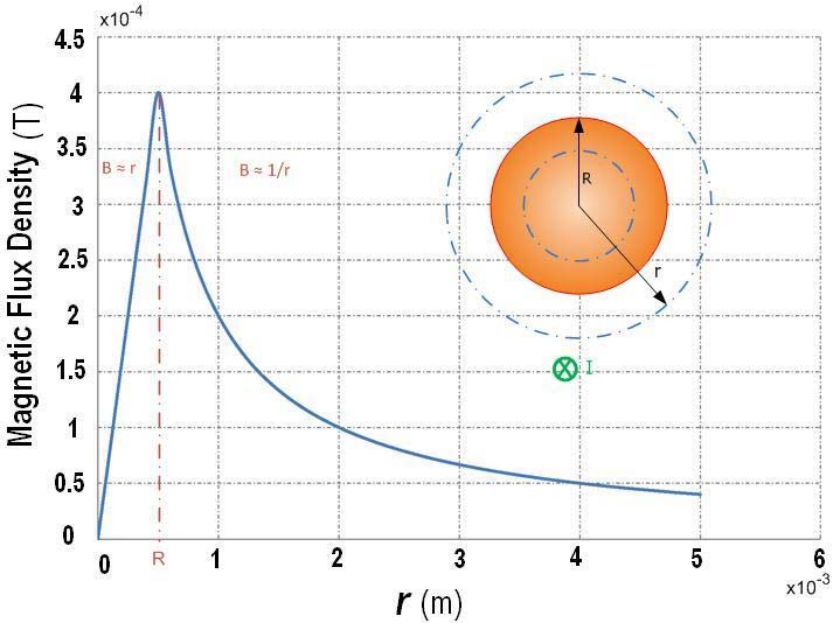

Figure 4.1. Magnetic flux density of a long current carrying conductor

Table 4.2. Details of simulation used in Figure 4.2 and Figure 4.3.

Application Mode	Space Dimension	Wire Dimensions (Length/Radius)	I(A)	Space Domain (XYZ)
Standard Equations	-	Infinite/0.5mm	1	Infinite
Magnetostatics (emqa)	3D	1cm/0.5mm	1	5cm/5cm/5cm
Perpendicular Induction Currents (emqa)	2D	Infinite/0.5mm	1	10cm/10cm/Infinite

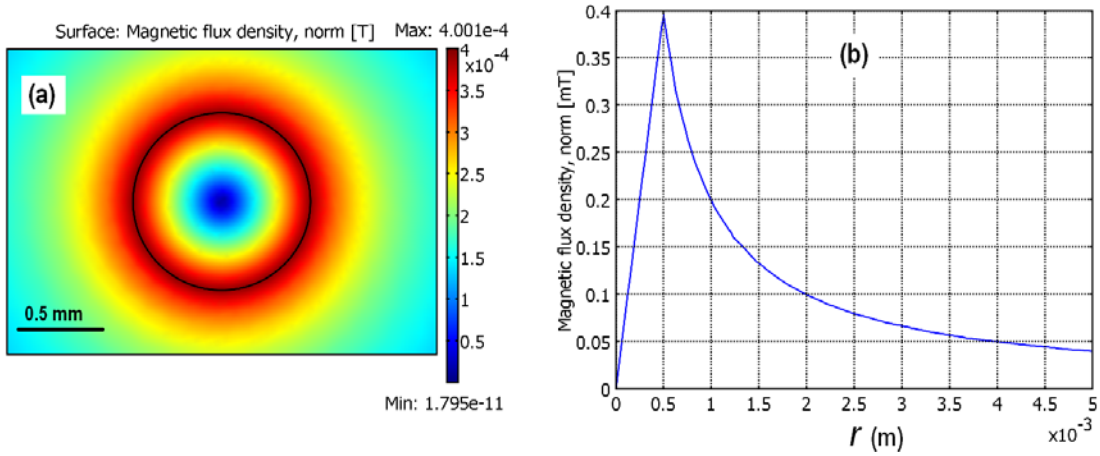

Figure 4.2. Simulation result of magnetic flux density of long wire in 2D mode. a) Cross-sectional plot of magnetic flux density. b) Radial plot of magnetic flux density.

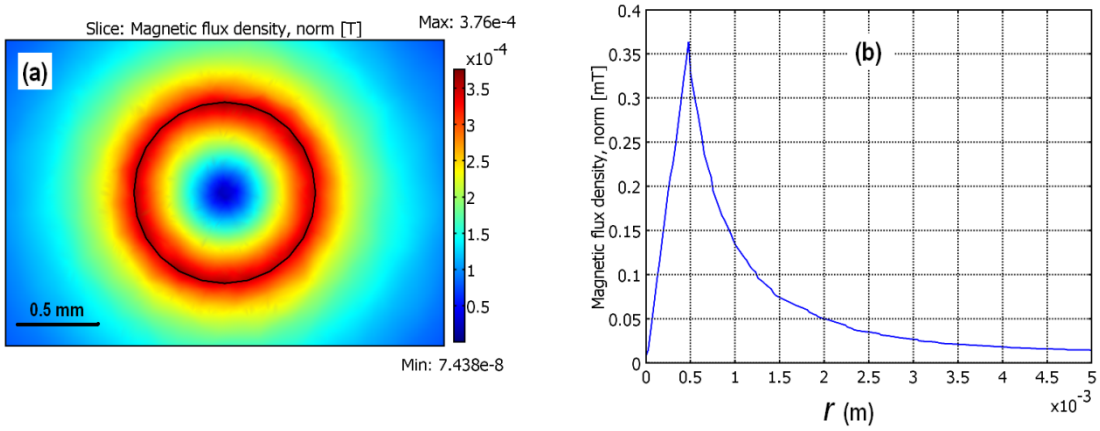

Figure 4.3. Simulation result of magnetic flux density of long wire in 3D mode. a) Cross-sectional plot of magnetic flux density. b) Radial plot of magnetic flux density.

4.4 Calculation of Magnetic Force Using PDE Mode

As described in Equation (3.27), the magnetic force applied on a magnetic bead exposed to a non-uniform magnetic field is a function of magnetic field strength *H* and magnetic field gradient of ∇H. COMSOL Multiphysics calculates different magnetic variables for a given geometry using appropriate boundary conditions. These variables are magnetic flux density *B*, magnetic field strength *H* and magnetic potential *A*. COMSOL initially calculates the magnetic potential *A* and then

recalculates other variables (*B* and *H*) by using first order derivative of dependent variable *A*. The problem with COMSOL is that the vector-elements cannot return second order derivatives of the dependent variables and the first order derivative is already used for calculation of *B* and *H*. Therefore, it is not possible to calculate magnetic force applied on magnetic beads directly in any magnetic module of COMSOL. This problem can be solved by application of partial differential equations (*PDE*) implemented in COMSOL. The method of magnetic force calculation using *PDE* Mode is described as follow:

1. Introduction of new set of variables in PDE mode
2. Solving the magnetic problem in magnetic module
3. Storing the solution
4. Update solver condition to evaluate initial value expression using stored solution in the solver manager
5. Set initial values in the subdomain setting for both applications (PDE and Magnetic application modes)
6. Update the magnetic solver with the new set of second derivatives extracted from PDE mode

Finally, the magnetic force can be calculated with defining force equation in the global expression of COMSOL. It is worth mentioning that application of PDE mode is limited to 3D application modes for simulation of spiral coils.

4.4.1 Calculation of Magnetic Force Applied on a Magnetic Particle

In this section, a typical magnetic force on a magnetic particle is calculated using COMSOL and the effect of various parameters on the strength of magnetic force is studied. Figure 4.4 depicts a simple setup that consist of a straight wire with circular cross-section and a magnetic particle placed above the wire at a distance of *h*. Magnetic force is calculated using the following expression:

$$F_m = F_0 H \nabla H = F_0 \nabla H^2 \tag{4.3}$$

$$F_0 = 2\pi\mu_0 R^3 \frac{\mu_r - 1}{\mu_r + 2} \tag{4.4}$$

Where, μ_0 is permeability of vacuum, μ_r and R are magnetic permeability and radius of magnetic particle respectively and H is magnetic field strength generated by current I. F_0 is constant coefficient, if the magnetic property of particle is known and will be calculated outside of COMSOL. Equation (4.3) describes applied magnetic force on a magnetic particle exposed to a non-uniform magnetic field H. There are many variables influencing the amplitude of magnetic force. Beside magnetic field strength H and its gradient ∇H, particle physical properties such as volume and magnetic permeability directly influence the strength of magnetic drag force. In addition, distance of particle from source of magnetic field shows a critical effect as well. These variables are listed below and are either investigated analytically or by means of simulation.

A. $\boldsymbol{\mu_{rB}}$: Relative magnetic permeability of particle
B. $\boldsymbol{R}$: Particle radius
C. $\boldsymbol{I}$: Electrical current passing through the source of magnetic field
D. $\boldsymbol{h}$: Distance between magnetic field source and the particle

4.4.1.1 Effect of Particle Physical & Magnetic Property on Magnetic Force

Figure 4.5 (a & b) shows variation of magnetic force coefficient (F_0) against different relative permeability of magnetic particle (μ_{rB}) and its radius (R) based on Equation (4.4). As displayed, amplitude of magnetic force shows direct dependency to the volume of particle. On the other hand, effect of particle relative permeability is not significant for $\mu_{rB} > 10$. Particles with higher relative permeability (contain more iron alloys) seem to exhibit ferromagnetic behaviour, thus tend to aggregate inside microfluidic channels. Relative permeability of particles ranging between $2 < \mu_{rB} < 20$ generates magnetic force coefficient of $25\% < F_0 < 75\%$. Therefore, optimization is a trade-off between magnetic force and aggregation probability. The higher the particle permeability, the greater is magnetic drag force and higher chance of aggregation. Figure 4.5 (c & d) shows the result of magnetic force variation against the particle distance from the wire (h) for different particle permeabilities (Figure 4.5c) and different particle sizes (Figure 4.5d). These graphs show that there is a close agreement between result of simulation and analytical calculation based on Equation (4.4). From magnetic point of view, the bigger the size of particle, the greater the influence of magnetic force.

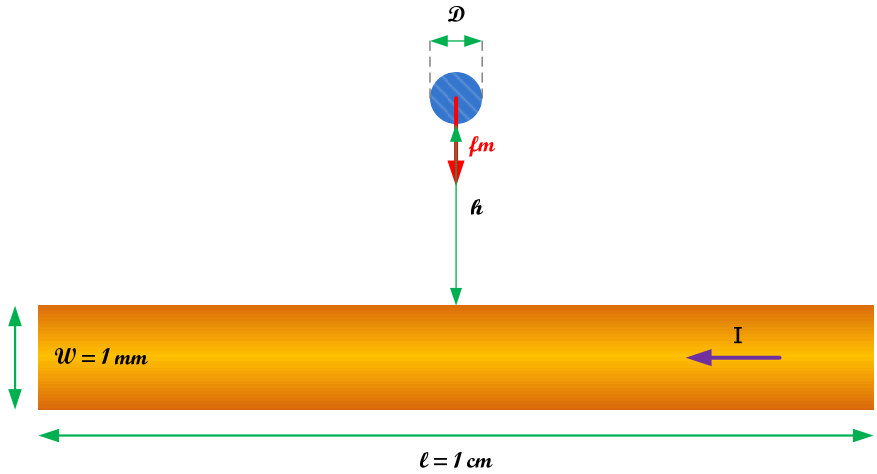

Figure 4.4. Schematic diagram of a long current carrying wire and a magnetic particle placed above the wire at the distance of *h*.

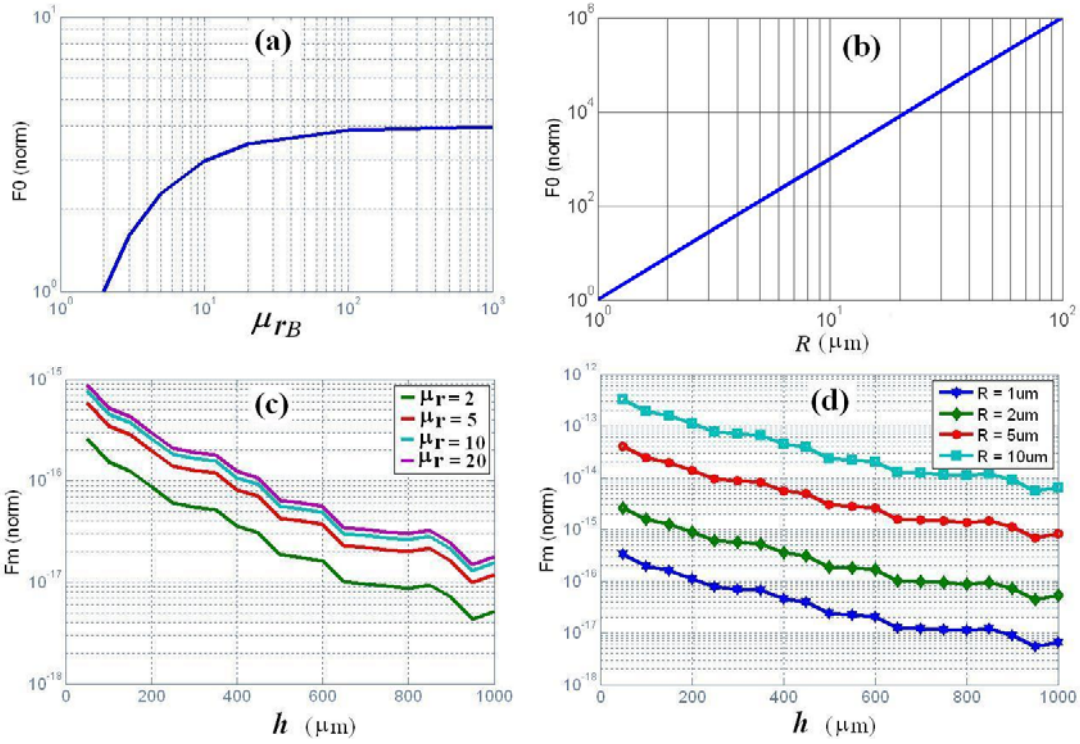

Figure 4.5. Effects of particle physical and magnetic property on magnetic force. a) Magnetic force against magnetic permeability of the particle. b) Magnetic force variation due to the particle radius ($\mu_{rB} = 2$). c) Magnetic force versus *h* for different relative permeabilities. d) Magnetic force versus *h* for different particle radius.

4.4.1.2 Effect of Electric Current *I* and Distance *h* on Magnetic Force

Figure 4.6 illustrates a surface plot of magnetic force applied on a typical magnetic particle, 2 μm in diameter and relative magnetic permeability of $\mu_{rB} = 2$. Figure 4.7 shows the simulation result of magnetic force applied on a magnetic particle for the arrangement in Figure 4.4 for two different currents given in Table 4.3. This result

shows that magnetic force responds to square of current I, and drops by inverse square of distance h (Figure 4.7). This is not surprising as Equation (4.3) shows that magnetic force is directly related to derivative of square of magnetic field:

$$F_m \propto \nabla H_0^2 \tag{4.5}$$

On the other hand, from Equation (4.1):

$$\begin{cases} B \equiv H \propto \dfrac{1}{r} \\ B \equiv H \propto I \end{cases} \tag{4.6}$$

By combining Equation (4.5) and Equation (4.6):

$$\begin{cases} F_m \propto \dfrac{1}{\mathrm{r}^2} \\ F_m \propto \mathrm{I}^2 \end{cases} \tag{4.7}$$

Therefore, to maximize the magnetic force on a selected magnetic particle, maximum electric current and minimum distance from source of magnetic field is necessary. Maximum electric current through a conductor is limited by the maximum temperature rise in the conductor as the result of joule heating. On the other hand minimum particle-magnet distance is mostly limited by fabrication technology.

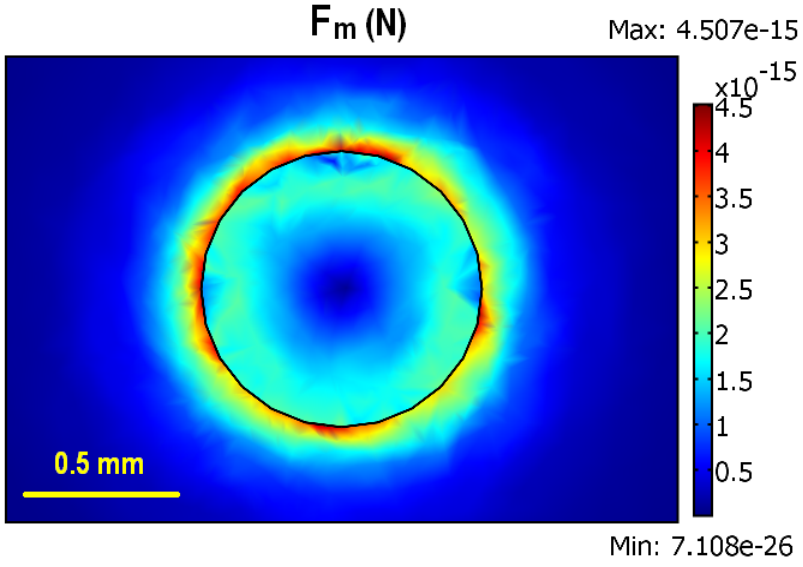

Figure 4.6. A cross-sectional plot of magnetic force pattern across a long wire generated by electric current of $I = 1\ A$. This force is applied on a magnetic particle with 2 μm in diameter and relative magnetic permeability of $\mu_{rB} = 2$.

Table 4.3. Detail of parameters used in simulation for Figure 4.6 and Figure 4.7

Particle Radius / Permeability	Particle Distance from Wire	Wire Length	Wire Diameter	Current
2 µm / 2	1 mm	1 cm	1 mm	1 A
2 µm / 2	1 mm	1 cm	1 mm	2 A

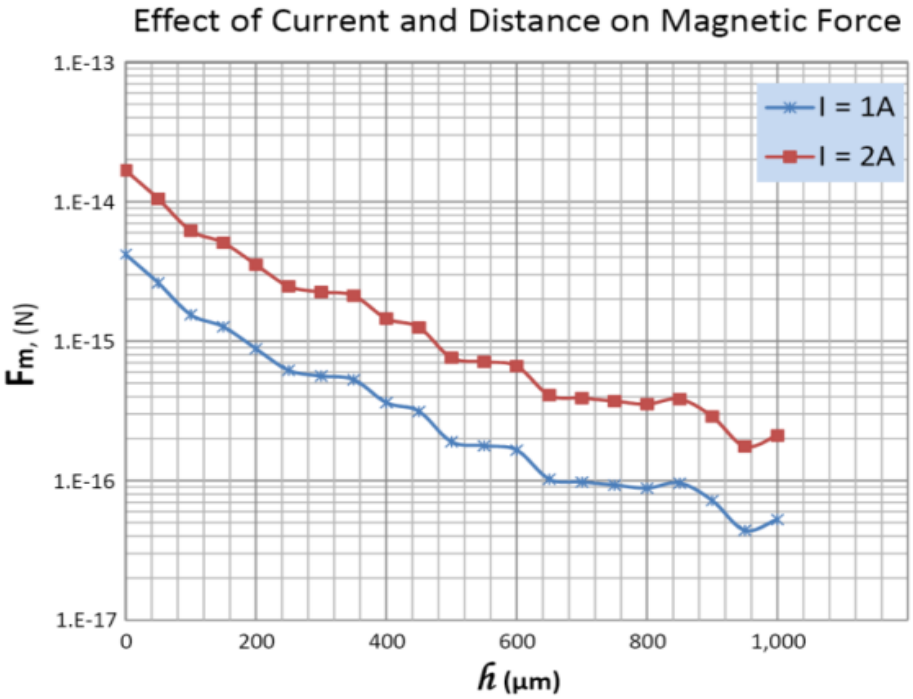

Figure 4.7. Effect of electric current variation on magnetic force applied to the magnetic particle

In the the above section (4.4.1), the effect of various geometrical and magnetic parameters were investigated using analytical and numerical analysis on strength of magnetic force applied on magnetic particles. The result of this study is summarised as follow:

- The magnitude of induced force is less sensitive to the magnetic permeability of the particles. In fact a relative permeability of $\mu_{rB} = 20$ produce 75% of the maximum force expected from permeability of the particle material.
- The relationship between the magnetic force and particle radius is in cubic order, which describes the importance of particle size on induced magnetic drag force.
- Magnetic force decreases by increasing the distance between particle and source of magnetic field by square law.
- Magnetic force increases by increasing the electric current of magnetic source by square law.

In order to increase the efficiency of the mixing, the mixer need to be optimised considering above parameters. Therefore, maximum current, minimum mixing depth and bigger magnetic particles are the key parameters that increase the mixing efficiency of the proposed mixer.

4.5 Electromagnet Design

The concept of the proposed magnetic mixer was introduced in *Chapter 2* (section 2.6.3 & Figure 2.47), using static magnetic mixing technique by application of a microchamber sandwiched between a pair of magnetic coils. The efficiency of proposed system on purification of DNA molecules highly depends on efficiency of the magnetic mixing of magnetic beads inside the microchamber. Chamber depth, magnetic property of magnetic beads and size of the beads, strength of magnetic field and physical property of the fluids (i.e. viscosity of the blood and buffers) are among the most important factors that directly influence the efficiency of the mixing. The effects of chamber depth (h), bead permeability (μ_{rB}) and size (R) as well as electric current (I) were investigated through numerical and analytical analysis. Some important factors such as magnetic bead and buffer properties are limited by the supplier of the DNA purification kits and might be variable form various suppliers. Therefore, these parameters are not considered in design of magnetic coils in this chapter. Instead, the emphasis in this work is to optimise the magnetic mixing unit through accurate design of magnetic field source with respect to the chamber geometry and fabrication simplicity. Hence, two important parameters that need to be considered in this design are the chamber depth and effective magnetic field pattern.

Chamber depth is the function of total chamber volume as well as penetration depth of magnetic field. Therefore, the optimisation process mainly depends on efficiency of magnetic field pattern, which leads to optimisation of chamber depth based on other parameters such as magnetic beads properties and buffer condition.

In design of magnetic field source, two different configurations are considered based on the fabrication point of view, microfabricated internal coils and miniaturised external coils. Besides different magnetic characteristics, these two configurations have significant impact on the final purification device. Although, internal coils are more compact and might have smaller size and dimensions, their implementation in the chamber walls increase the fabrication complexity and cost. This is not suitable

in a POC device with disposable cartridge type. On the other hand, in external coils configuration, the chamber design and fabrication is much simpler, which reduce the cost of final disposable cartridge. Another disadvantage in design of internal coil configuration is the limited heat dissipation ratio resulted from Joule heating of coil conductors. Thermal activity of external coils can be controlled by design of appropriate temperature control systems (i.e. heatsink or miniaturised fan). Nevertheless, both internal coil and external coil configurations are considered in this work, and their efficiency is investigated by means of numerical simulations.

4.6 Internal Coil Design

A schematic diagram of proposed magnetic mixer using internal coil configuration is illustrated in Figure 4.8. This mixing device comprises a circular four-port chamber made of PDMS sandwiched between a pair of conductors embedded on top and bottom of the chamber walls. Two insulation layers separate the actual mixing area from the conductor surfaces to eliminate any electrochemical activity between current carrying conductors and biofluids inside the chamber. The thickness of this insulation layer is in the order of a few micrometers.

Although with recent improvements in MEMS microfabrication technology it is possible to pattern various two-dimensional and three-dimensional multi-layered conductor geometries on plastic and glass, this process will increase the complexity of fabrication and increase the total costs. Therefore, in this work, the aim is to design a simple, low cost and effective conductor pattern using standard microfabrication technology. However, the first limitation is the maximum thickness of electrode patterning using metallic electroplating technique. In this method, the maximum thickness that can be electroplated is limited to less than 100 μm and more preferably 25μm. Therefore, in design of internal magnetic source in this work, the thickness of conductors was assumed to be less than 100 μm.

Generally, on-chip planar two-dimensional electrode-patterning can be categorised into two main groups based on their magnetic field patterns, multi-mutual and single-mutual inductors. In multi-mutual inductors, the conductors are mainly patterned in parallel directions in which the mutual effect between the magnetic flux of the neighbouring electrodes will add-up and leads to exponential increase in the total magnetic flux of the electrode pattern. The most common examples of this electrode

pattern are planar circular spiral and planar square spiral (Figure 4.9 a & b). On the other hand, in single mutual inductors, the magnetic fluxes of two neighbouring conductors are in opposite directions, and thus their mutual effect does not increase the total magnetic flux of the inductor. An example of this electrode pattern is planar serpentine electrodes (Figure 4.9c).

Since the main objective in design of electromagnet is to generate maximum magnetic field strength, spiral conductor geometry seems to be a better option compared to serpentine electrode pattern. Nevertheless, in this section, a simulation is carried out to investigate the performance of three common types of electrode pattern, circular spiral, square spiral and serpentine-shape electrodes.

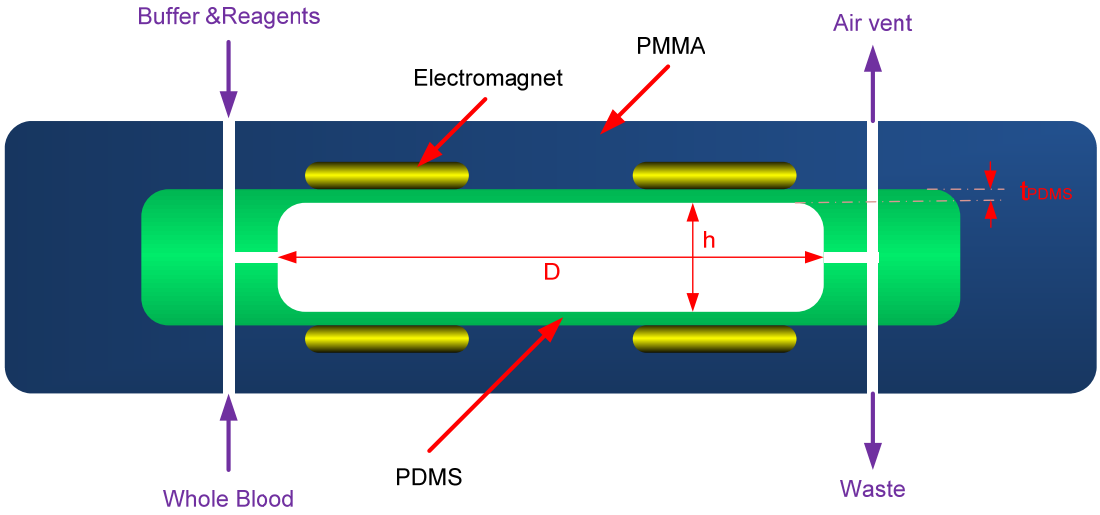

Figure 4.8. Basic schematic cross-sectional view of proposed DNA purification chip showing the position of coils and the chamber.

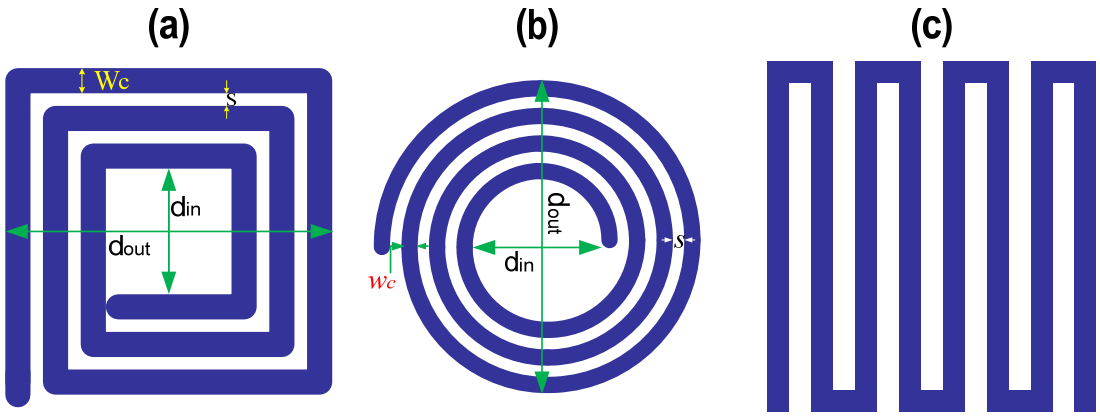

Figure 4.9. Three most common types of planar electrode patterns. a) Square spiral. b) Circular spiral. c) Serpentine electrode.

A comparison result of magnetic flux density between circular spiral and square spiral using COMSOL Multiphysics simulation is shown in Figure 4.10. These graphs are extracted across diametric lines from the middle of the spirals and above the surface of the conductors. To compare a circular spiral with a square spiral, their surface coverage needs to be identical. This indicates that both spirals can fit to identical volumes circular-shaped and square-shaped chambers with fixed chamber depth. An electric current density of $J = 1 \times 10^5\ A/m^2$ was applied to both spirals with 2 mm conductor thickness. With these assumptions, circular spiral generates stronger magnetic flux density compared to square spiral. The average increase in magnitude of circular spiral to square spiral is about $\approx 11\%$.

A similar magnetic field comparison between multi-mutual and single mutual inductors was carried out by design of three-dimensional models of square spiral and serpentine electrode in COMSOL. Geometrical details of this simulation are given in Figure 4.11. The outer diameter of both inductors is identical and a square-shape conductor cross-section of $W = 1\ mm$ is used for simulation with similar current density of $J = 1 \times 10^6\ A/m^2$. Figure 4.12 shows the result of this simulation for serpentine electrode and square spiral. The result is shown in surface plot mode for (Figure 4.12 a & b) and across the diametric line of A-A as shown in Figure 4.11 (Figure 4.12c). Simulation is repeated for different electrode surface coverage's in case of spiral coil (75%, 90% and 99%).

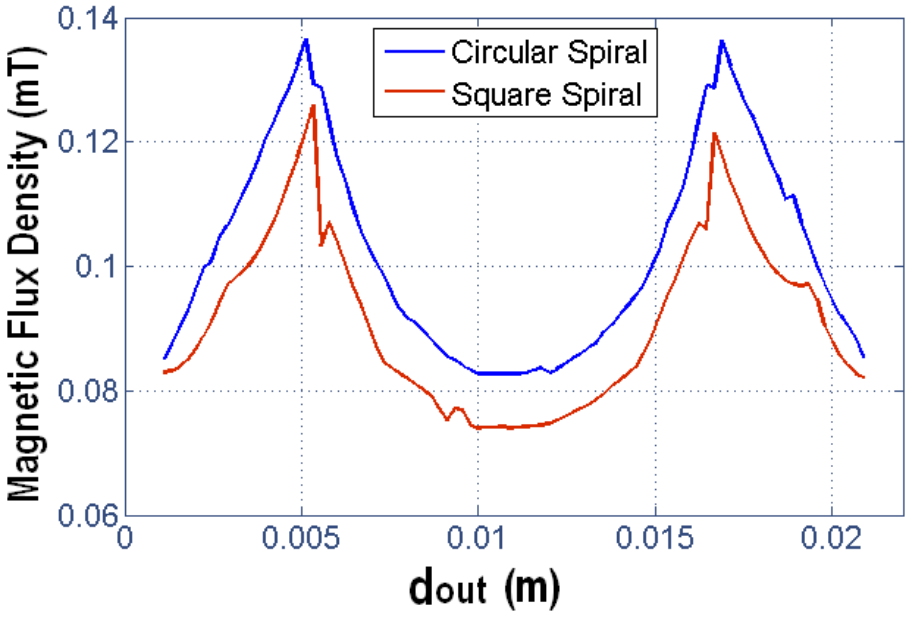

Figure 4.10. Magnetic flux density of circular and square spirals along diametric line.

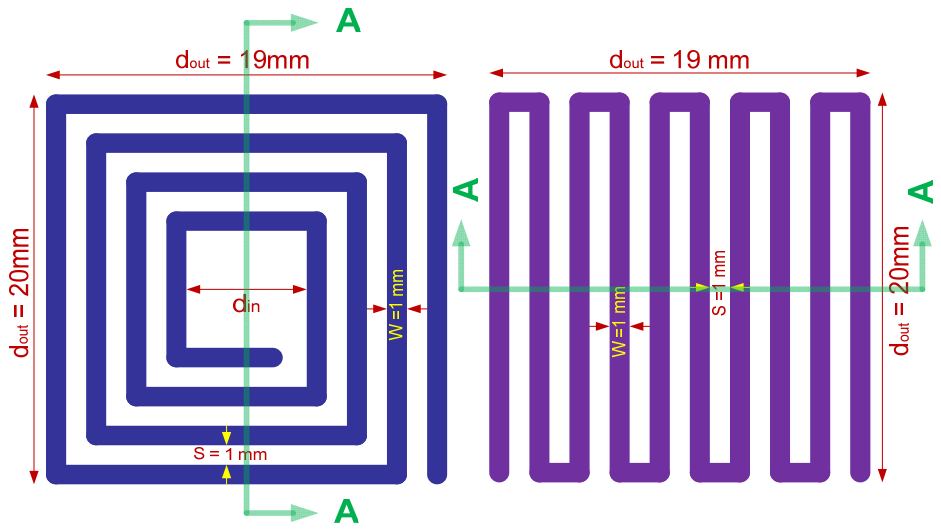

Figure 4.11. Detail of models used in simulation of Figure 4.12.

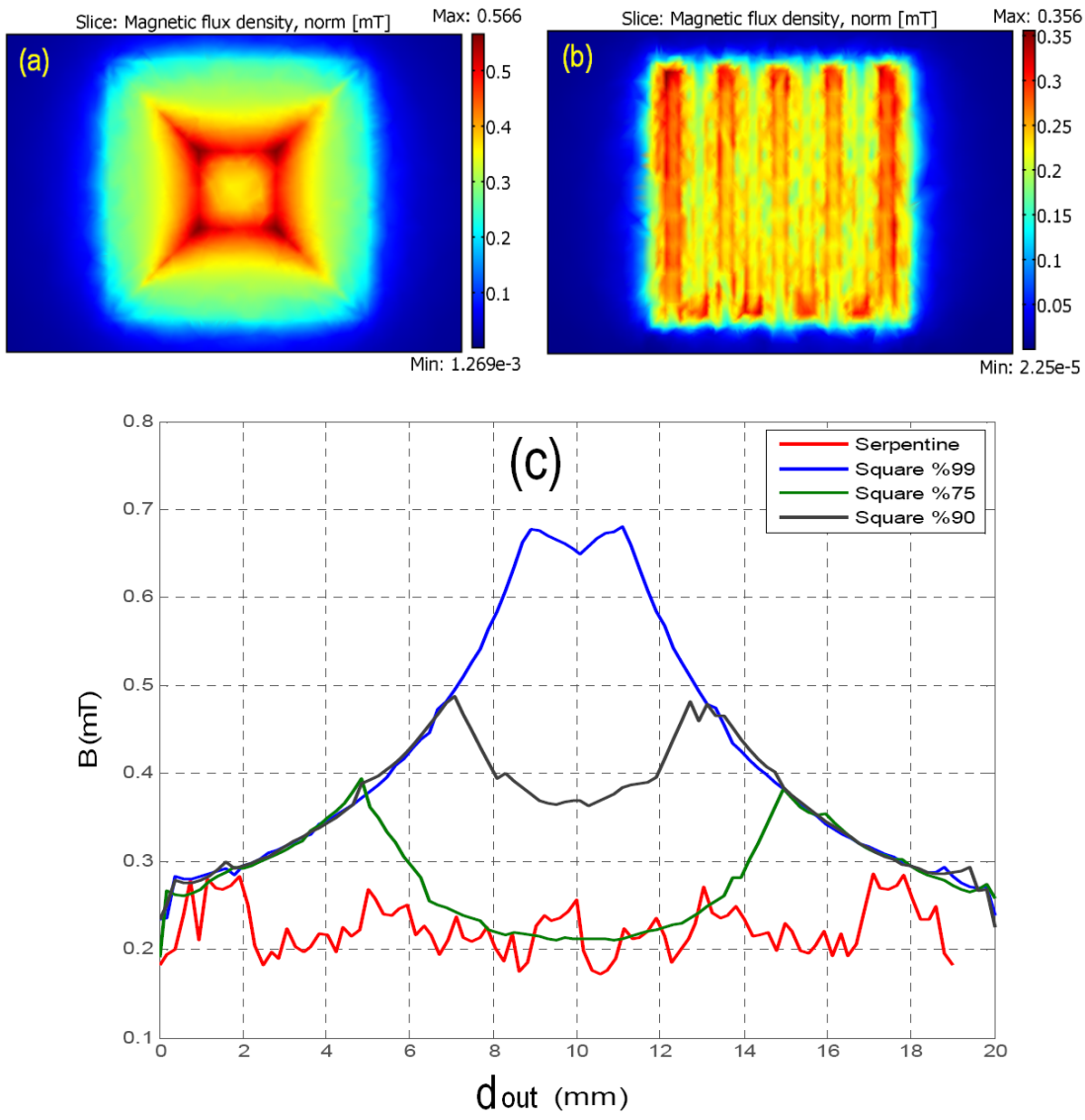

Figure 4.12. Plot of magnetic flux density generated by square shape spiral and serpentine electrode. Surface plots of magnetic flux density on top of (a) square spiral and (b) serpentine electrode. c) Diametric plots of magnetic flux density across the lines of A-A for serpentine electrode and square spiral with different electrode surface coverage (75%-green. 90%-black and 99%-blue).

As it is shown in these graphs, magnetic flux density generated by serpentine electrode is weaker than spiral coil. The advantage of serpentine electrode is the pattern of magnetic flux density, which has multi-peaks uniformly spread across the whole area. On the other hand, spiral coil has higher overall flux density and has a very high peak at inner edges of the coil. Another advantage of spiral coil is that the position of central peaks can be controlled by changing coil internal diameter (d_{in}). To fabricate spiral coil patterns, an additional layer is necessary to establish the electrical connectivity of the middle connector. This will increase the complexity and cost of fabrication compared to planar serpentine electrode. However, based on these simulations, planar circular spiral generates stronger magnetic field compared to square spiral and serpentine electrode. Therefore, from magnetic field point of view, circular spiral coil is a suitable choice to be used in internal-coil-configuration of the proposed magnetic mixer.

4.6.1 Key-type Electrode

As mentioned above, the most important disadvantage of circular spiral coil is the fabrication complexity regarding electric connection from the middle-end of the spiral. In order to overcome this problem, a modified version of spiral coil is introduced as illustrated in Figure 4.13. This modified version, which is called one turn coil or simply key-type electrode, generates the same magnetic field as the spiral coil, if the product of $Ampere \times Turn$ is a constant. In key-type electrode, the electrode patterning and the electric connections can be established in the same layer. In addition, the multi-turn electrode patterning is reduced to a single-turn electrode. Therefore, fabrication of key-type electrode is much simpler than circular spiral and serpentine electrode.

Another important advantage of the key-type electrode is the lower electric resistance compared to the spiral coil. This factor can be described based on the total cross-sectional difference between two coils. In key-type electrode, the total cross-section area is:

$$A_k = n.A_c + (n-1)A_s \tag{4.8}$$

Where, $A_k, A_c, A_s$and n are key-type electrode cross-section area, spiral conductor cross-section area, spacing cross-section area and number of turns respectively. Therefore, total cross-section area in key-type electrode is higher than spiral coil

by $(n-1)A_s$. Moreover, total wire length in key-type electrode is shorter than spiral coil. Shorter wire length and wider cross-section results in lower electric resistance hence, reduce Joule heating. Key-type electrode can handle higher current compared to spiral coil and therefore, generates stronger magnetic field and force.

Figure 4.14 shows a typical magnetic flux density for key-type and spiral coils at different heights from the surface (Z-values). In this simulation, spiral coil has n=4 turns with identical conductor width/thickness/spacing of $W_c = t_c = S = 1mm$ and is connected to a current source of $I_s = 1A$. On the other hand, key-type electrode is connected to a current source of $I_k = 4A$, to makes it as identical ($Ampere \times Turn$) as that of spiral coil. This result shows that with the identical condition, spiral coil and key-type electrodes create similar magnetic flux density pattern. At very close distances from the conductor surface, spiral coil generates a multi sharp, tooth-like pattern, which is due to the sharp edge of conductors. In general, key-type electrode makes a better choice to generate stronger magnetic force with higher electric current value.

Since key-type electrode represents a better magnetic field pattern compared to planar circular spiral coil, hereafter, this type of electrode is discussed in more detail to investigate effect of geometrical variations in magnetic force of internal coil configuration. Because the thickness of conductors in this configuration is limited to $t_k \leq 100\ \mu m$ (fabrication limitation), electrode width (W_k) and coil external diameter (d_{out}) are two parameters that will be used for optimisation process.

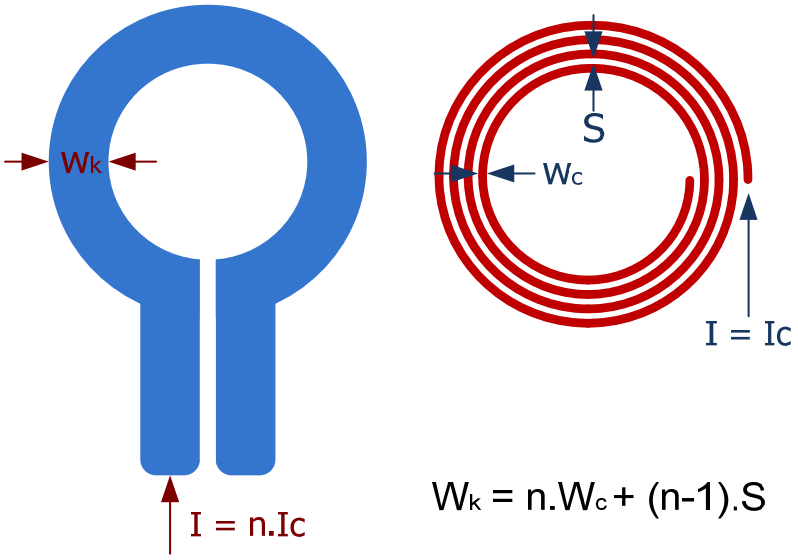

Figure 4.13. Schematic diagram of key-type electrode and planar spiral coil.

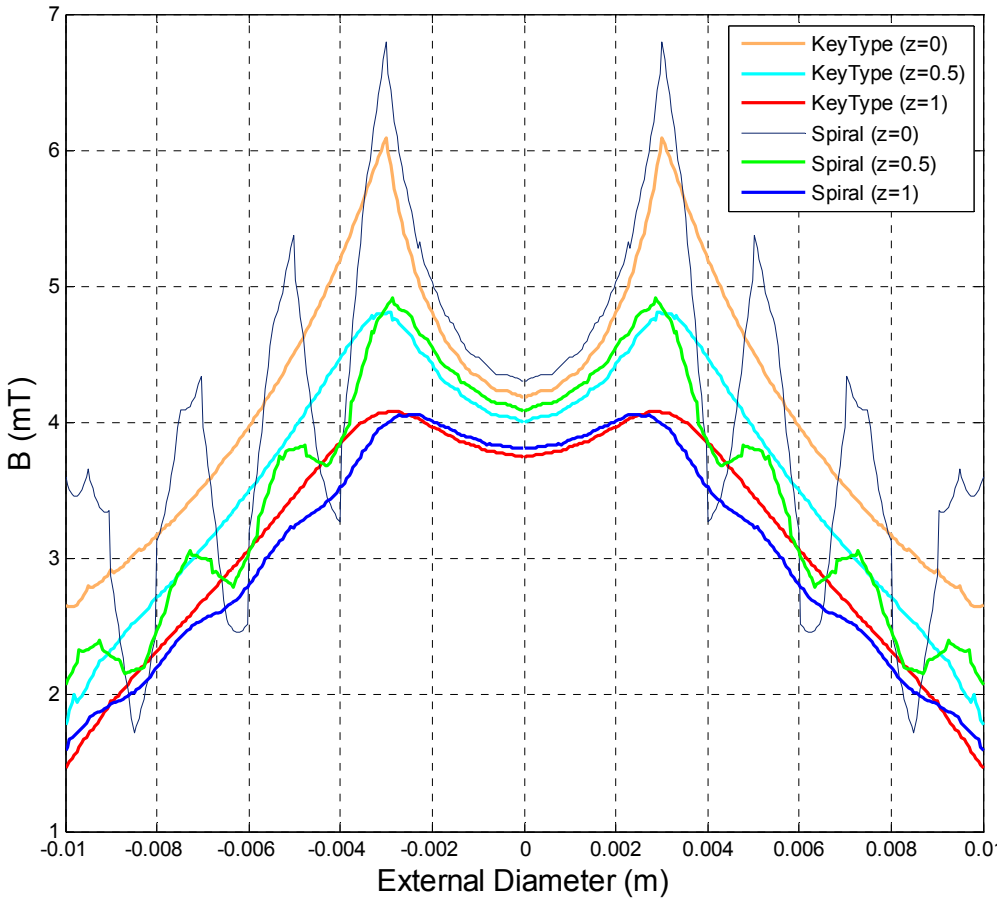

Figure 4.14. Comparison between magnetic flux density of key-type electrode and spiral coil

4.6.2 Effect of Electrode Width of Key-type Electrode, (W_k), on Magnetic Force

The effect of conductor width of key-type electrode on magnetic force was investigated using numerical simulation. This simulation was carried out by the assumption of fixed values of conductor thickness, $t_k = 100\ \mu m$, and the ratio of conductor width to total width of the electrode, $d_{out} / d_{in} = 2$. The value of magnetic force and magnetic field were calculated at fixed current density of $J = 2 \times 10^8$, and for a typical magnetic bead with diameter of $d_{bead} = 1\mu m$ and relative magnetic permeability of $\mu_r = 10$, placed at the inner edge of the electrode. This simulation was repeated for different conductor width (W_k) using the *K*-factor, which is defined as the ratio of conductor width to conductor thickness:

$$K = \frac{W_k}{t_k} \tag{4.9}$$

The value of *K*-factor for different electrodes used in this simulation is given in Table 4.4.

Table 4.4. The ratio of conductor width to conductor thickness.

***K*-factor**	**Conductor Width, W_k**	**Conductor Thickness, t_k**	**Coil Internal Diameter, d_{in}**	**Coil External Diameter, d_{out}**
0.25	25 μm	100 μm	50 μm	100 μm
0.5	50 μm	100 μm	100 μm	200 μm
1	100 μm	100 μm	200 μm	400 μm
2	200 μm	100 μm	400 μm	800 μm
4	400 μm	100 μm	800 μm	1600 μm
8	800 μm	100 μm	1600 μm	3200 μm

Figure 4.15 shows the variation of magnetic flux density, B (blue line), and magnetic force, F_m (red line), against different K-factors. As it was expected, the magnitude of magnetic flux density increases by increasing the conductor width (higher K-factors). Since the strength of magnetic force is directly related to the strength of magnetic field, H (Equation (4.3)), a proportional behaviour was expected for the graph of magnetic force. However, the result of magnetic force variation indicates an unexpected sharp peak of magnetic force at the point of $K = 1$. This graph can be explained in detail based on Equation (4.3) at different K-factors.

- $K < 1$: In this region, the value of conductor thickness is higher than the value of conductor width. This indicates that, the centre of higher magnetic flux density, at the edge of conductor, is shifted toward inner section of the conductor as illustrated in Figure 4.15 (b & c). As the result of this magnetic field shifting, the magnitude of magnetic force decreases at the conductor edge.

- $K = 1$: At this point, the width and thickness of conductor are equal. Based on Equation (4.3), magnetic force is a function of magnetic field intensity (H) and magnetic field gradient (∇H). On the other hand, graph of magnetic flux density shows that, the value of H is not maxima at this point. Therefore, at this critical value of $K = 1$ with square-shaped conductor cross-section, the product of $H.\nabla H$ is maxima.

- $K > 1$: Since the ratio of magnetic flux density is incremental in this region, the lower magnetic force ratio ($H.\nabla H$), indicates that the ratio of magnetic field gradient decreases by increasing the ratio of K-factor.

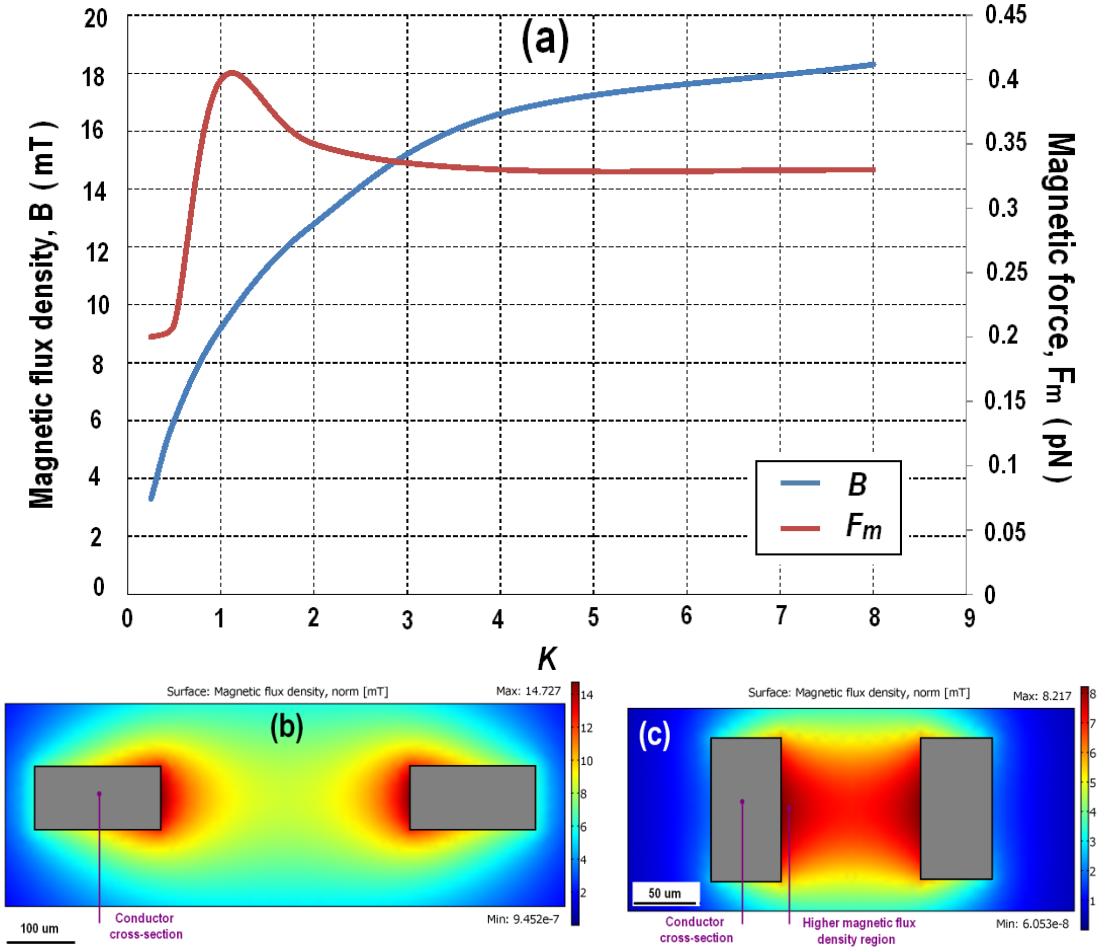

Figure 4.15. a) The variation of magnetic flux density (blue line) and magnetic force (red line) against conductor cross-section ratio (*K*). b, c) Cross-sectional plots of magnetic flux density in two different *K*-factors of *K*=2 (b) and *K*=0.5 (c)

4.6.3 Optimised Chamber depth (d_{ch}), Based on Coil External Diameter (d_{out}) in Key-type Electrode

In the previous section, the optimised cross-section of key-type electrode was investigated based on the maximum magnetic force generation. This maximum force was measured on the surface and at the inner edge of the conductor. In this section, the variation of the magnetic force will be at different distances from the surface of the conductor. Figure 4.16 illustrates a schematic of the chamber and key-type electrodes. For simplicity, the key-type electrode was modelled with a ring-shaped circular electrode. In this picture, t_k and W_k are the thickness and the width of the key-type electrode respectively. Inner and outer diameter of the electrode are shown with d_{in} and d_{out} respectively and the chamber depth is shown by d_{ch}. Since the thickness of the conductor is limited to the maximum thickness of $t_k = 100\ \mu m$, optimised coil external diameter $d_{out}$was investigated based on variation of the chamber depth d_{ch}.

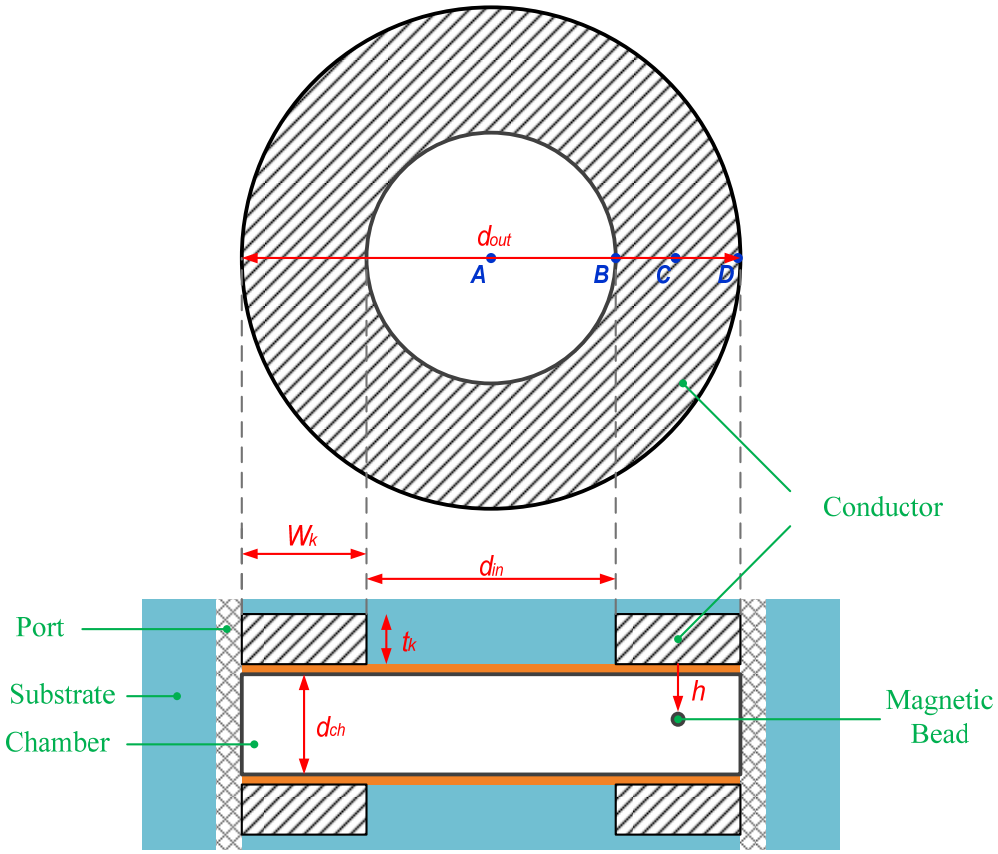

Figure 4.16. Schematic of the DNA purification chamber using integrated internal key-type electrodes (to reduce the simulation complexity, key-type electrodes are replaced by identical ring-shaped circular electrodes).

Figure 4.17 shows the simulation result of magnetic force variation against coil external diameter at different heights from the conductor surface (*h*). In this simulation, the force was calculated on a magnetic bead with diameter of $d_{Bead} = 1\mu m$ and relative magnetic permeability of $\mu_r = 10$ at fixed current density of $J_c = 2 \times 10^6\ A/m^2$. The conductor surface coverage was assumed to be 50% ($d_{out}/d_{in} = 2$) in all simulations. The force is plotted radially across the top surface of the coil along the *AD* line as shown in Figure 4.16. For easy comparison, all graphs have been normalized for coil external diameter. From these graphs it can be concluded that there are three different areas which respond differently to the dimension change. These areas are as follow:

1. Internal section of the coil: This area is not covered by conductors (d_{in}). Since the width of this area was assumed to be half the coil diameter, a quarter of whole coil surface and hence, one quarter of the magnetic beads will be covered by this area (assuming the beads are spread very uniformly across the surface). Generally, in this section magnetic force decreases with

increasing coil external diameter. Figure 4.18a shows the variation of magnetic force along a vertical line (point *A* in Figure 4.16) above different coils. Therefore, depending on the maximum height of the working chamber, optimum coil dimension will change. For instance, a 400 µm diameter coil, which has square conductor cross-section, is suitable for use with the chamber depth up to 50µm. For higher chamber depth the strength of magnetic force decreases sharply.

2. Conductor section: this area is fully covered by current carrying conductors and comprises three quarter of coil active area, and hence, covers majority of magnetic beads. Figure 4.18b shows variation of magnetic force along a vertical line at the middle of this area (point *C* in Figure 4.16). Once again, selection of optimized dimension for coil diameter depends on the actual depth of working chamber. For instance, a 400 µm diameter coil represent higher magnetic force for distances up to 20µm and for a chamber with depth of 100µm, the optimized coil diameter is $d_{out} = 1600\mu m$, which represent higher magnetic force compared to other coils arrangements.

3. Inner edge of coil: this area is the interface between the two previous sections. Since the majority of magnetic flux converges at this point, both magnetic field strength (*H*) and its gradient (∇H) thereof are very high at inner edge of the conductor. In fact, by increasing the coil external diameter, magnetic force at this point can be increased significantly.

Therefore, selection of an optimum external diameter for integrated internal coil mainly depends on the working chamber depth. The result of simulation, gives different optimised coil external diameter per chamber depth based on above three areas. However, the area covered by the conductor surface covers the majority of the magnetic beads population (75%). Therefore, this area was selected for optimisation of chamber depth and coil external diameter. Based on this assumption, the identified optimized coil diameters are extracted for different chamber depth, as illustrated in Figure 4.19. As shown in this figure, the strength of magnetic force decreases by increasing the chamber diameter (red solid line), which indicates that internal coil configuration is not a suitable choice for large-volume microchambers. Nevertheless, this information is just a guideline for estimation of optimized dimension and might slightly vary due to practical limitations.

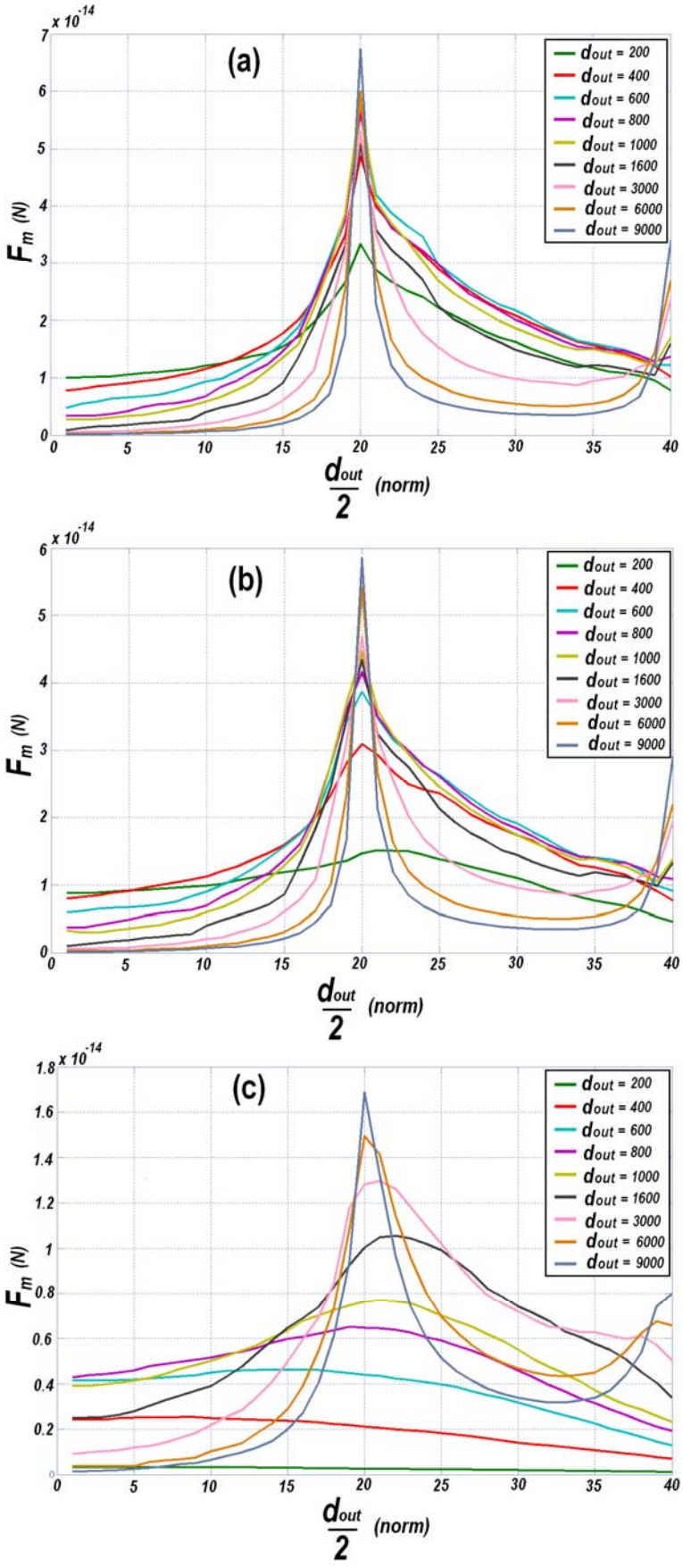

Figure 4.17. Radial plot of effect of coil outer diameter on magnetic force experienced by a magnetic particle at different heights above the coil surface. h=10μm (a), h=50μm (b) and h=150μm (c).

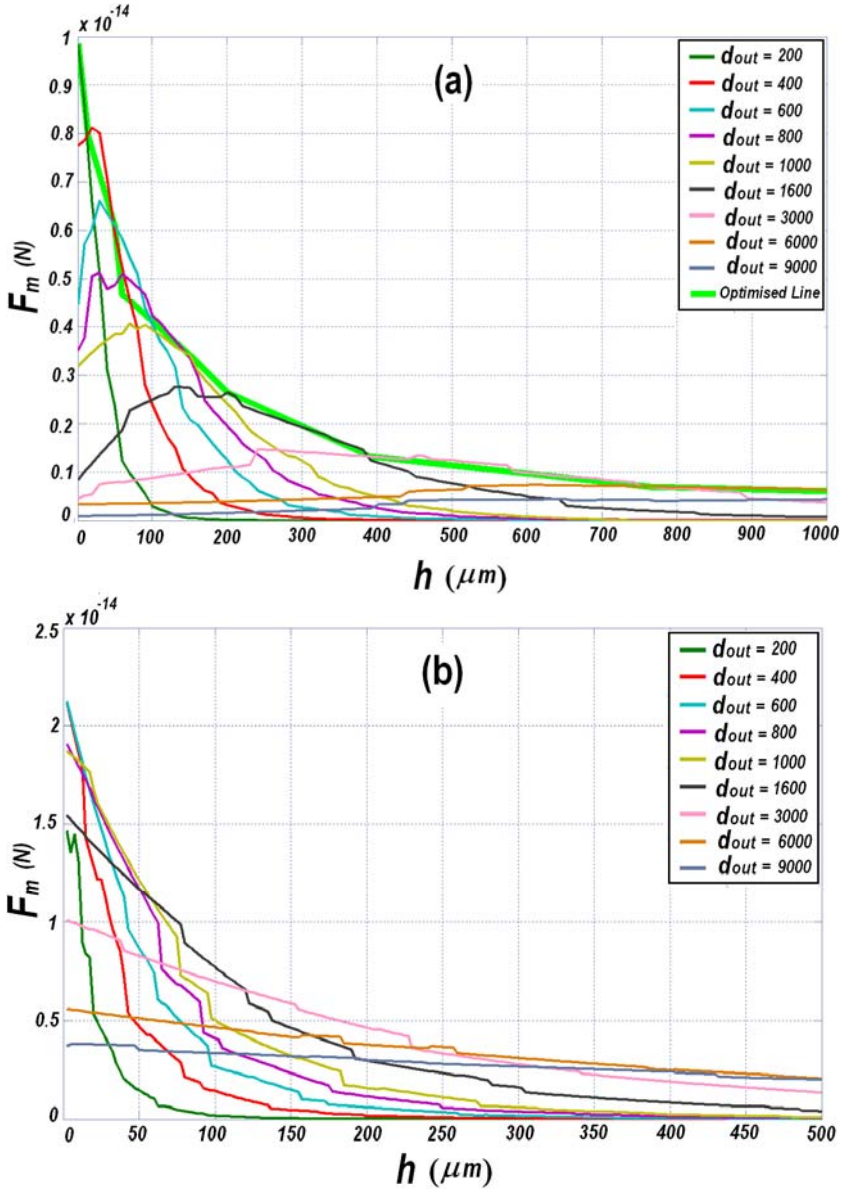

Figure 4.18. Vertical plot of magnetic force generated by different coils along perpendicular lines at the centre of coil (a) and middle of winding section (b).

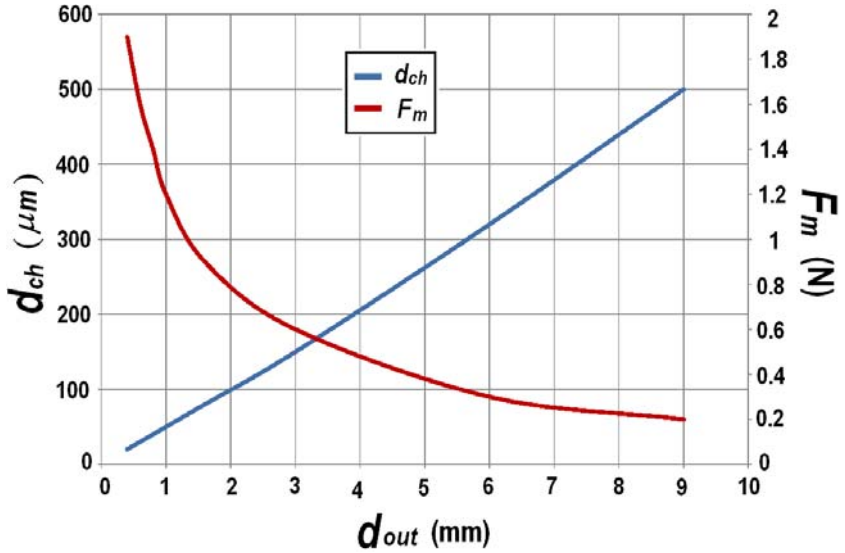

Figure 4.19. Optimised coil diameter in different chamber depth

4.6.4 Application of Magnetic Core in Internal Coil

The application of a magnetic core is another method to amplify the strength of magnetic field. The concept of magnetic amplification is illustrated in Figure 4.20a depicting the cross-sectional view of a circular spiral, embedded inside a ring-shaped magnetic material. The application of magnetic core is to create a low reluctance magnetic circuit for magnetic flux to pass through. This low reluctance circuit increases the magnetic flux density, thus generates higher magnetic force.

In this section, the application of magnetic core was investigated using numerical simulation techniques to evaluate the performance of integrated magnetic core on strength of magnetic field. To achieve this, the strength of magnetic flux density at the inner conductor edge of a circular spiral coil (Point A at Figure 4.20a) was measured and compared at three different scenarios, no core, full core and half core (Figure 4.20b-d).

Figure 4.20b shows a cross-sectional plot of magnetic flux density generated by planar circular spiral coil, which generates a maximum flux density of $B_{edge} = 0.645\ mT$ at the inner edge of the coil. A similar simulation was performed on the same coil by incorporating the magnetic coil with a full magnetic core (Figure 4.20c). The result indicated that, a 934 times amplification of magnetic flux density was achieved inside the magnetic core using a typical relative permeability of $\mu_r = 1000$. However, the magnetic flux density at the inner conductor edge was amplified 1.63 times ($B_{edge} = 1.05\ mT$). This ratio was measured as 1.42 times amplification ($B_{edge} = 0.91\ mT$) in half-core spiral coil (Figure 4.20d).

Variation of the magnetic flux density against relative permeability of the magnetic core is illustrated at Figure 4.21. This information is shown at two different points (A, B in Figure 4.13a) in full-core spiral configuration. These graphs indicate that the magnetic field of spiral coil is less sensitive to the permeability of the core, above a critical permeability of $\mu_r = 100$. Therefore, wide range of magnetic materials can be used as the core material (i.e. Nickel with typical permeability of 600).

From fabrication point of view, integration of magnetic core to the spiral coil increases the fabrication complexity and costs. On the other hand, application of magnetic core increases the magnetic field up to 63%. A similar amplification can be

achieved by doubling the conductor thickness using multi-layer fabrication. Therefore, application of magnetic core is not a suitable field amplification method in a low cost, disposable diagnostic chip.

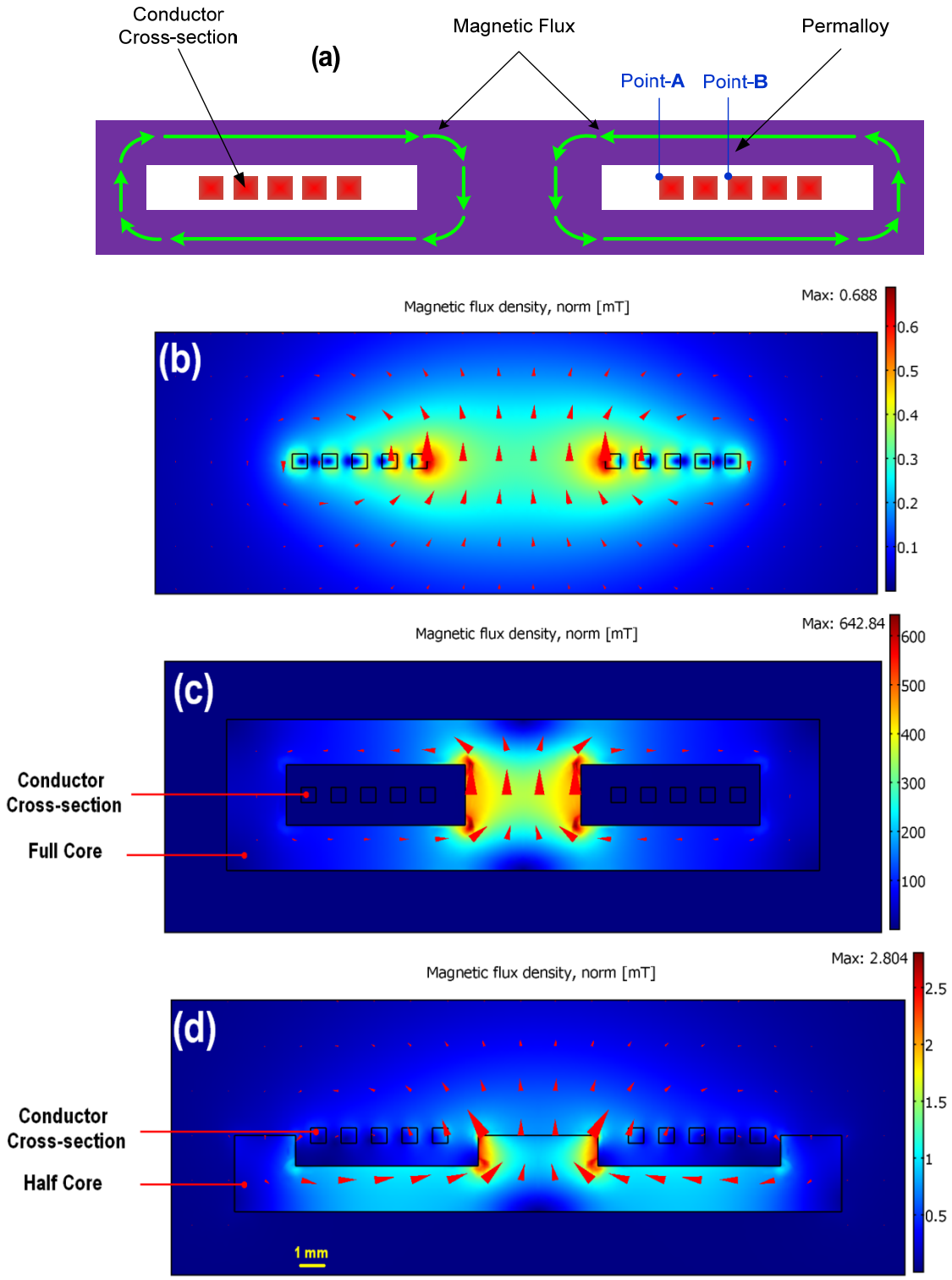

Figure 4.20. a) The concept of magnetic amplification using integrated magnetic core. Cross-sectional plots of magnetic field, generated by a circular spiral coil (a), full-core spiral (b) and half-core spiral (c).

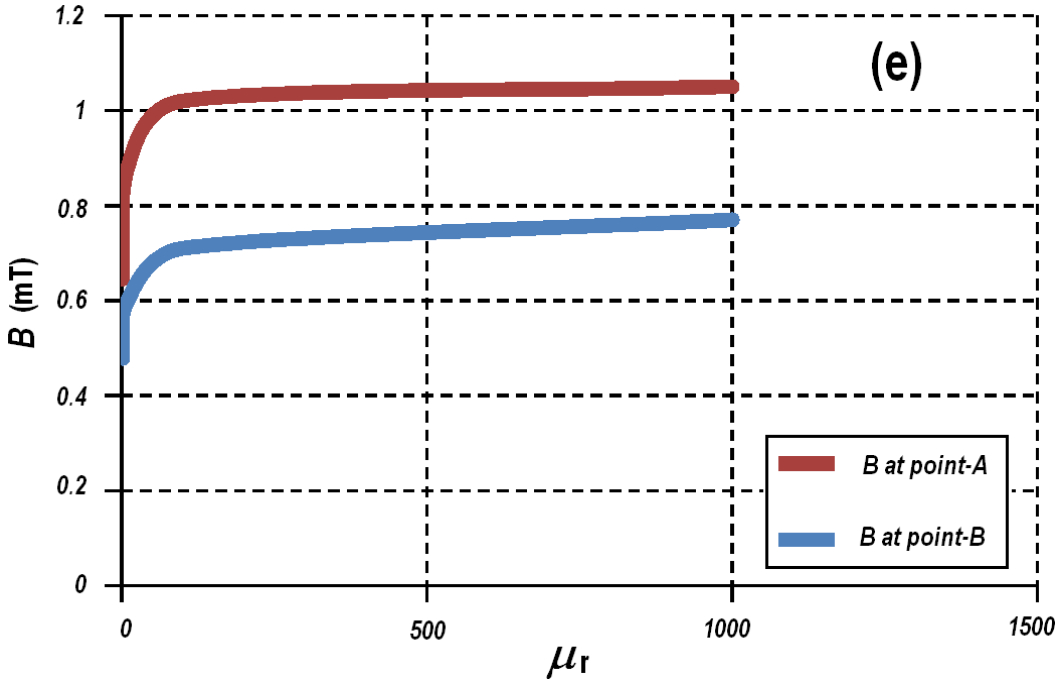

Figure 4.21. Variation of magnetic flux density against relative permeability of the core.

4.7 External Coil Design

As discussed in previous section, integrated internal coil is suitable for small-volume extraction chamber as the result of limited conductor thickness. Although a larger microchamber can be used by increasing the number of conductors in a series of key-type electrodes, it increases the ratio of inactive areas between electrodes. Another problem with internal coil configuration is the limited control over its thermal activity. This can be achieved using on-chip temperature controlling systems (i.e. Peltier elements), which add more cost on fabrication process.

External source of magnetic force is a solution to overcome these problems. Since external magnetic source can be fabricated using miniaturised solenoid coils, the strength of magnetic field can be controlled either by increasing the number of turns or increasing the electric current. The fact that the magnetic source is not embedded in the micro-chip reduces the fabrication complexity and cost significantly. Moreover, the thermal activity of external coil can be controlled by application of low-cost conductive and/or convective cooling systems (such as application of conductive heatsink or convective air-flow fans).

In this section, the application of the external magnetic source is investigated using numerical simulation techniques. As it was concluded from the previous section

(4.6), circular coils generate stronger magnetic field compared to other multi-mutual and single-mutual inductors. Therefore, in this section, a pair of miniaturised solenoid with circular windings is selected as the source of magnetic field. The concept of DNA extraction/purification chip with external magnetic coils is illustrated in Figure 4.22.

A numerical simulation was performed to extract the optimised geometrical dimensions. These parameters are the coil cross-section (A_s) and thickness (t_s). The actual winding cross-section (A_s) was assumed to be fully covered by the conductor surface. This assumption reduces the simulation complexity and computer process time in three-dimensional simulation mode.

4.7.1 Efficient Winding of External Coil

As mentioned above, the external coil can be fabricated by a winding a copper wire on a miniaturised bobbin. A cross-section of the actual winding area is shown in Figure 4.22 and is characterised by its winding width (W_s) and winding depth (t_s). In this section these parameters were used to extract the optimised winding cross-section (A_s) that produces maximum magnetic force.

Figure 4.23 shows the result of simulations for two different winding cross-sections. In these simulations, the winding cross-section was kept constant and the simulation was carried out for different thicknesses and width of winding section. This simulation is carried out for two different square cross-sections of $A_S = 25\mu m^2 \; and \; A_S = 4mm^2$. The magnetic force is calculated on a magnetic bead placed above the coil surface ($h = 500\ \mu m$) and the results are normalized for comparison purpose.

In this simulation, σ is defined as the ratio of winding width to winding thickness ($\sigma = W_s/t_s$). This result shows that the magnetic force is maximised when the winding cross-section is square-shaped. This means that the number of turns along the length of the coil must be equal to the number of turns along the width of the coil. In the other word, the product of ($Ampere \times turns$) is maximised, when $W_S = t_S$. Although both winding width and thickness were used as the variable parameters in this simulation, this result is in close agreement with the result of simulation extracted from internal coil configuration (section 4.6.1).

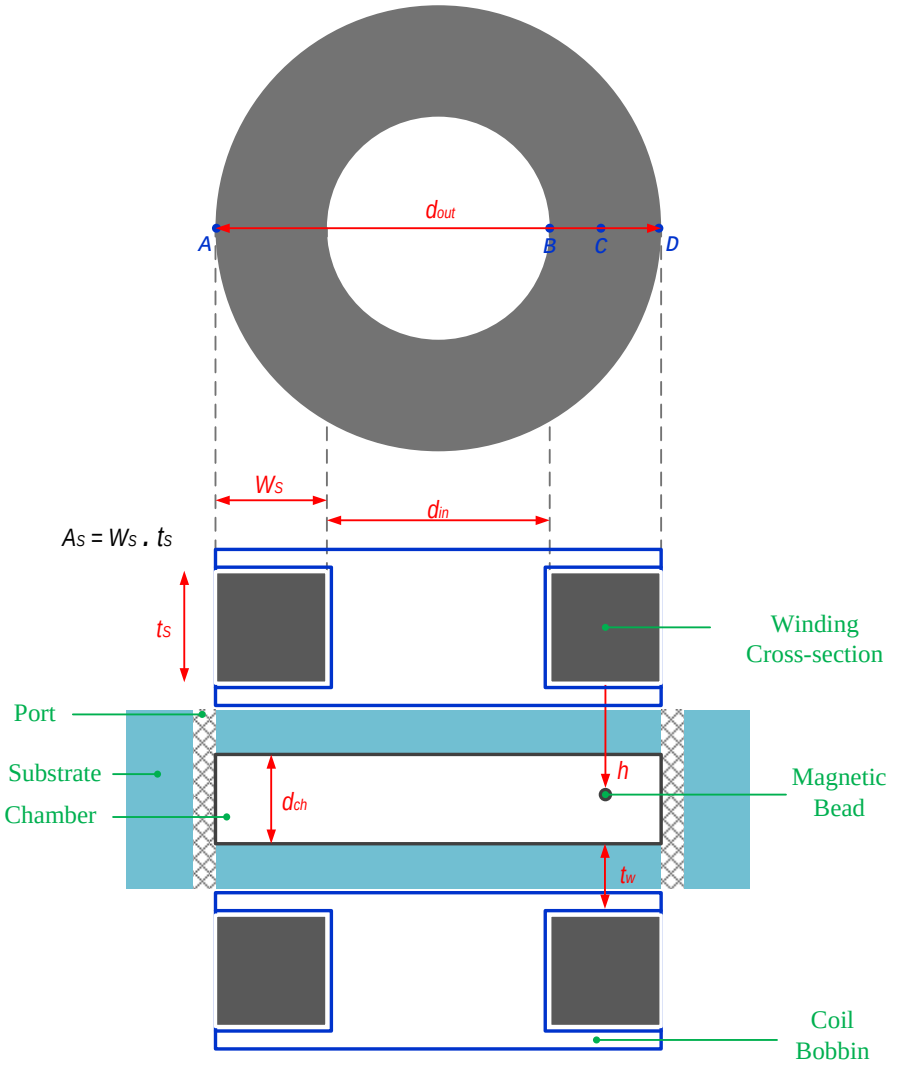

Figure 4.22. Schematic of DNA purification chip using external coil configuration.

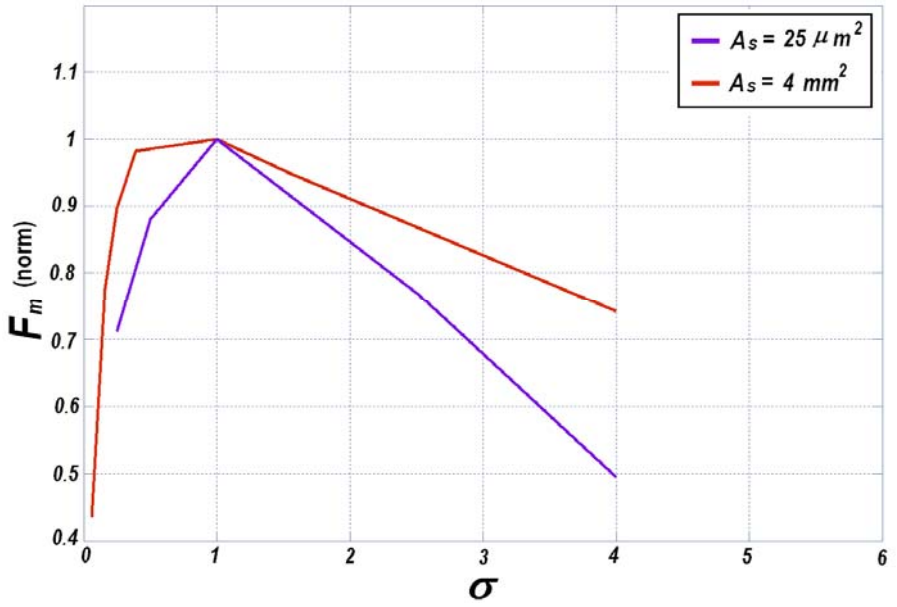

Figure 4.23. Variation of magnetic force against the ratio of conductor width to conductor thickness (σ) for different conductor cross-sections.

4.7.2 Effect of Coil Thickness on Fixed Width

From previous section it was concluded that a maximum magnetic force with a fixed conductor cross-section takes place with square-shape conductor section. However, this is the optimum condition in which the magnetic force is maximised with a fixed product of ($Ampere \times turns$). Any further increase in the supplied electric current or number of turns results in increase of the magnetic force strength. Increasing the number of turn can be realised by increasing the conductor cross section in the vertical and/or horizontal directions (along W_S or t_S). Among these two parameters, vertical expansion of the cross-section becomes the only option, when the horizontal expansion is not possible. For example, the outer diameter of the coil is limited by the overall chamber dimensions, which in turn, limits the horizontal expansion of the coil. Therefore, in this section, the effect of coil expansion in vertical direction (along t_S) was investigated with the fixed coil outer diameter assumption.

Figure 4.24 shows the result of simulation for variation of the magnetic force against different coil thicknesses. The outer diameter of the coil used in this simulation was, $d_{out} = 8\ mm$ and with fixed conductor width of, $W_s = 2\ mm$. The magnetic force was calculated on a magnetic bead with diameter of, $d_{Bead} = 1\mu m$ and relative magnetic permeability of, $\mu_r = 10$ at fixed current density of, $J_c = 2 \times 10^7$. The magnetic force was plotted across the coil diameter (A-D line in Figure 4.22) at different heights above the coil surface, $h = 500\ \mu m$ (Figure 4.24a) and $h = 1000\ \mu m$ (Figure 4.24b) and along a vertical line ($h = 0 - 2\ mm$) from the middle of the conductor, as shown by point-C in Figure 4.22. The variation of magnetic force was investigated for variation of conductor thickness ranging between $t_S = 0.5\ mm$ to $t_S = 24\ mm$.

This simulation shows that magnetic force increases significantly, by increasing the thickness of the conductor up to four times of its width. However, this effect will saturate afterward by further increase in the conductor thickness. This is because, the centre of the magnetic flux shifts from inner edge of the conductor toward middle of the coil (as discussed in section 4.6.2, Figure 4.15). The same concept is valid at different heights above the coil surface (Figure 4.24 a-c). The validation of this effect was investigated for different coil external diameters ($d_{out} = 8, 16, 32\ mm$) and the results are compared to each other, as illustrated in Figure 4.25. The simulation conditions were kept similar to the previous simulation, but the magnetic force was measured at inner tip of the conductors (point-B in Figure 4.22).

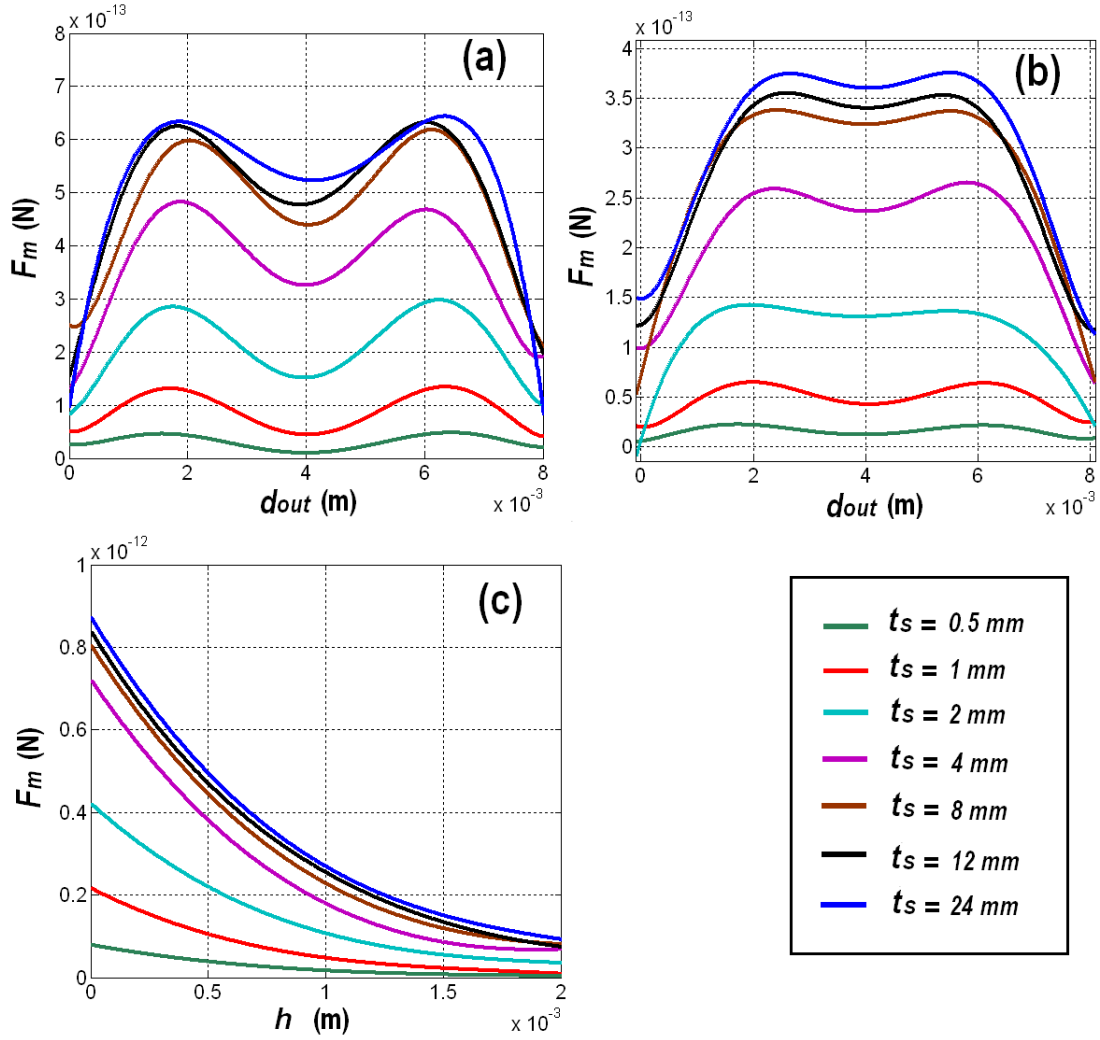

Figure 4.24. Variation of magnetic force against thickness of the conductor across a diametric line A-D (shown in Figure 4.22) at, (a) , (b) and, (c) along vertical line (point-C).

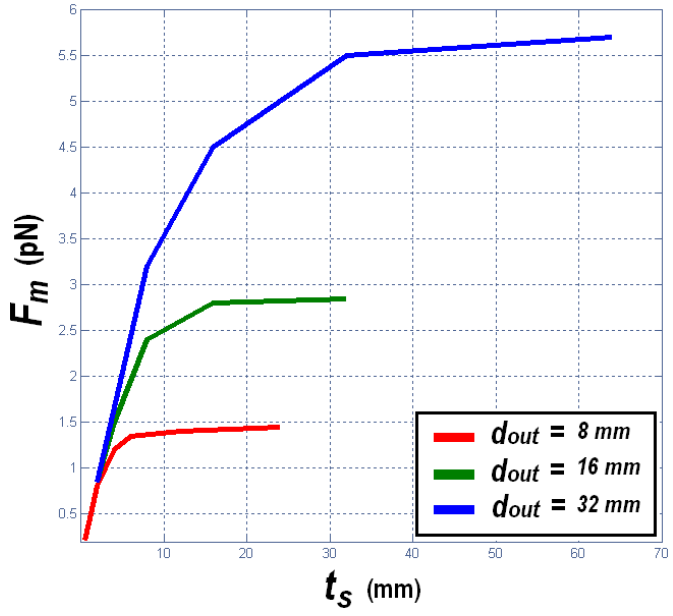

Figure 4.25. Effect of conductor thickness on magnitude of magnetic force, shown for different coil external diameters.

From graphs of Figure 4.25, it can be extracted that 95% of thickness effect takes place with increasing the thickness to four times of original square shape cross-section, therefore:

$$F_m(max) \cong 2 \times F_m(Sqr) \tag{4.10}$$

$$t_S(max) \cong 4 \times t_S(Sqr) \tag{4.11}$$

Where, $t_S(Sqr)$ and $F_m(Sqr)$ are the winding thickness and magnetic force generated by a coil with square shape winding cross-section respectively and $t_S(max)$ and $F_m(max)$ are, the maximum effective thickness and the maximum magnetic force generated by extending the winding depth. If the width of winding (W_S) is 50% of the coil radius:

$$W_t = \frac{r_{coil}}{2} = \frac{d_{out}}{4} \tag{4.12}$$

And because in square-shaped winding, $W_S = t_S$ then by comparing Equation (4.11) and Equation (4.12):

$$t_S(max) = d_{out} \tag{4.13}$$

Which means, the optimised thickness, for a coil with fixed width, is equal to the outer diameter of the coil. Further increase in thickness of winding will increase the magnetic force but in a very slow rate, which might not be reasonable due to the bigger dimension of the coil.

4.8 Final Chamber Coil Setup

Based on extracted information from simulation results, design of electromagnet and different coil arrangement can be optimised for internal and external coil arrangements. Regardless of coil position in the chamber, design of each electromagnet is application specific. There are many variables affecting the final coil design as follow:

- Chamber depth: Since the strength of magnetic force decreases by Inverse Square of depth, it is very important to calculate penetration depth of magnetic force based on chamber depth.
- Chamber volume: Based on the application, chamber volume might vary to accommodate required bio-fluid inside the chamber. Since the total volume

of the chamber is a function of chamber depth and width, coil arrangement must be optimized to cover the whole chamber area and specially the chamber depth.

- Magnetic Bead Property: There are many different magnetic beads commercially available for extraction of DNA or other bio-molecules. Characteristics of these beads vary from different manufacturers. These properties are the relative magnetic permeability (μ_{rB}) and size of the beads (d_{bead}). The magnetic property of beads will directly affect the amplitude of magnetic force they experience. Effect of dimension can be realized in the amplitude of magnetic and viscous forces experienced by the magnetic beads. In addition, if the size of bead is comparable to the chamber dimension, there might be a risk of bead clogging inside the chamber and microfluidic network due to the chaining effect of magnetic beads under the influence of magnetic field.
- Extraction protocols: Different commercially available extraction kits have different extraction protocols for buffers and sample to be used for optimum purification of target molecules. In other words, the ratio of target sample to chemical buffers differs in different kits. This will affect the total volume of the chamber, if there is a limitation of target sample to be used for extraction.
- Joule heating: Whilst magnetic force increases as the square of electric current, Joule heating increases in the same ratio. In some purification protocols, incubation at high temperature is one of the kit's requirements. In order to avoid overheating, which might damage the microchamber, the maximum allowed electric current must be considered in design of the magnetic coils. Joule heating is more important in internal coil design as the coil is embedded inside the chip and any temperature rise will be transferred to the chamber directly. In the case of external coil, there is a possibility to dissipate the heat by designing a suitable heatsink module.

In conclusion, design of electromagnet is a very complicated process, which has dependency on many variables. In other words, coil design for magnetic mixing is application specific. In the case of DNA extraction and purification, which is the subject of this work, the emphasis is to design an electromagnet based on total volume of the chamber, which is a function of minimum required sample and

extraction protocols. Chamber volume is a function of chamber depth and diameter. A chamber depth above $d_{ch} > 500\ \mu m$ increases the diffusion length, and thus requires long incubation time. Moreover, generation of efficient switching magnetic field becomes more challenging, across a chamber with higher depth ratio ($d_{ch} > 100\ \mu m$). Hereafter, in this work, the total volume of the chamber will be calculated based on the maximum chamber depth of $d_{ch} = 100\ \mu m$ and $d_{ch} = 300 - 500\ \mu m$ for internal and external coil arrangements.

4.9 Inter-coil Mutual Effects

In designing the magnetic mixer the main target is to perform efficient mixing and binding of DNA molecules to achieve highest yield. Efficiency of mixing increases by application of spatial magnetic force on magnetic beads. This requires a number of magnetic force generators on different sides of the chamber in order to drag the beads to different sides of the chamber. The higher the displacement of the beads, the higher the probability of collecting the target molecules. Since the magnetic force applied on the beads cannot be inverted to generate repulsing force, a minimum number of two coils are required to operate in opposite directions. Arrangement of coils is based on the chamber shape and geometry and total volume of the chamber. If the numbers of coils are more than one pair, these coils might have mutual effect on each other. This mutual effect happens, if their working cycle overlaps. In fact, the mutual effect needs to be investigated between every coil, which has overlapping working cycle with other coils. Based on the coil arrangements in this work, there are two types of mutual effects need to be investigated separately. These effects are as follow:

- Lateral mutual effect
- Cross mutual effect

4.9.1 Lateral Mutual Effect

This type of mutual effect is concerned with coils positioned in the same plane next to each other. This arrangement of coils is realised, when the chamber size is bigger than the coil and more than one coil is placed on each side of the chamber. This is necessary to cover the chamber surface with magnetic force pattern. To investigate the mutual magnetic effect, generated by in-plane coils, a model of four coil

arrangement was simulated using COMSOL Multiphysics, and the result was compared to a single coil, as illustrated in Figure 4.26. This simulation was carried out using ring-shaped circular conductors with outer diameter of $d_{out} = 8\ mm$ and equal conductor thickness/width of $t_{ring} = W_{ring} = 2mm$. An effective spacing of $S = 1\ mm$ was considered between coils in four-coil arrangement. The force was calculated on the magnetic beads with relative permeability of $\mu_r = 10$ and diameter of $d_{bead} = 1\mu m$ at current density of $J = 2 \times 10^7\ A/m^2$passing through the coils, in clockwise direction.

A plot of magnetic flux density on the surface of the coils, across the diagonal lines of A-A and B-B (as shown in Figure 4.26 c & d) are shown in Figure 4.26 (a & b). These graphs show that, the interaction between magnetic flux of two neighbouring coils reduces the peak of magnetic flux of both coils. This reduction ratio is higher at two adjacent edges of conductors (8%), and is lower at two distant edges (3.5%). More detail calculation was performed using evaluation of total magnetic energy density inside the subdomain. This calculation showed an average reduction ratio of 4.94% in total magnetic energy density of four-coil arrangement, compared to single core arrangement.

Another simulation was performed to investigate the effect of inter-coil mutual interactions on the strength of the magnetic force. The result of this simulation is shown in Figure 4.26 (c & d). These plots were captured on the surface of the coils. By similar calculation of average magnetic force between two above coils arrangements showed an average reduction ratio of 6.88% in four-coil arrangement compared to single coil arrangement.

This evaluation describes an overall mutual effect of in-plane coils assuming all coils are activated and have 100% overlap in working cycle. Obviously, any other working cycle results in fewer disturbances in magnetic flux and magnetic force. This conclusion is not unexpected as the majority of magnetic flux in a planar coil is concentrated on the coil surface at inner edge of the coil. The direction of this flux is perpendicular to the coil surface. Therefore, major parts of the magnetic flux generated by neighbouring coils are isolated from each other.

Further investigation of in-plane mutual effect was performed in the above four-coil arrangement by applying opposite-direction electric current to the neighbouring

coils. The result of this simulation is shown in Figure 4.27 with corresponding current directions of each coil. This result shows that, the average magnetic flux density and average magnetic force of each coil, in four-coil arrangement, increases by ≈6% compared to the single coil arrangement. This is because of positive mutual effect between magnetic flux of two neighbouring coils with opposite electric current directions. Therefore, in any in-plane multi-coil arrangement, which have overlapping working cycle, electric currents of the coils must be applied in opposite directions. This will increase the strength of magnetic force, as the result of positive mutual effect.

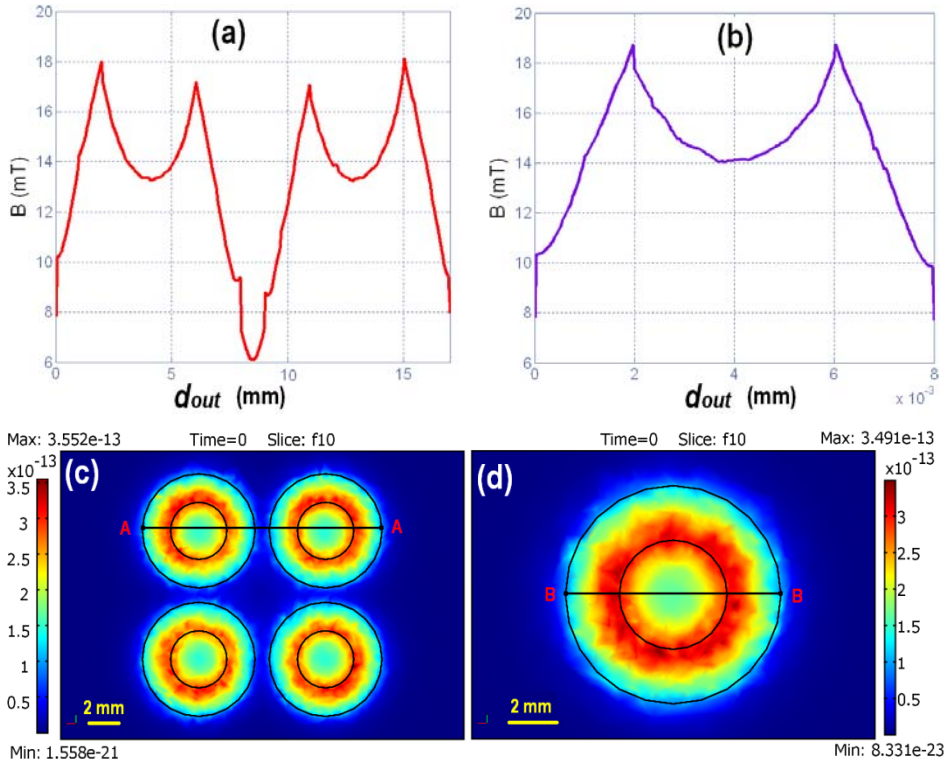

Figure 4.26. Mutual effect of neighbouring coils. (a, b) Plots of magnet flux density at the surface of the four-coil (a) and single coils (b) arrangements, across diametric lines of A-A and B-B. (c, d) Surface plots of magnetic force at the surface of the four-coil (c) and single coil (d) arrangements.

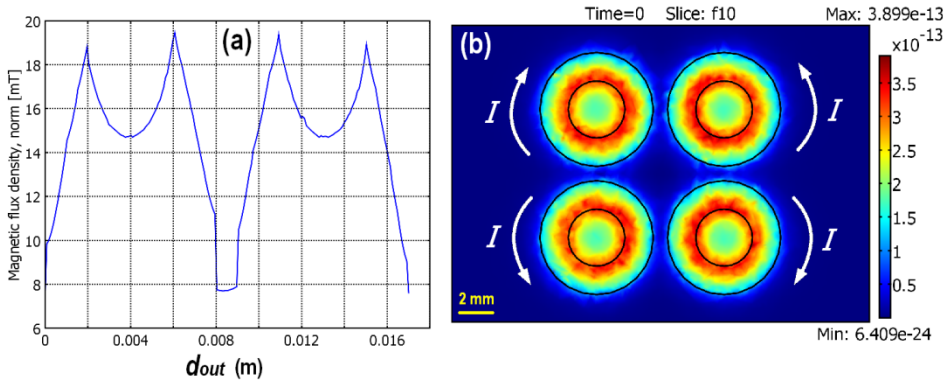

Figure 4.27. The effect of opposite-direction electric currents on the mutual effect of four-coil arrangement. a) Plot of magnetic flux density. b) Plot of magnetic force.

4.9.2 Cross Mutual Effect

Beside in-plane magnetic mutual effect between the coils, the other mutual effect can be realized between coil pairs on two opposite sides of the chamber. In fact these coils have been placed on opposite sides in order to create spatial magnetic mixing pattern. Usually, these two coils should not have an overlap in their activation time. Figure 4.28 shows a cross-section plot of magnetic flux density pattern for three different scenarios. These three scenarios are as follow:

1. No overlap: This pattern is the normal switching pattern of magnetic flux density when there is no overlap between two coils in their working cycle (Figure 4.28a). In this picture, the bottom coil is activated. The pattern of magnetic flux indicates that the magnitude of magnetic flux density is higher at the inner tip of winding section and gradually decreases to the middle section and external edge of the coil. This pattern of magnetic flux drags magnetic beads toward the higher field intensity, which is the inner edge of winding section.

2. Overlap with Parallel Electric Current: In this mode, both coils are activated and have an overlap in their working cycle. The polarity of electric current is in the same direction for both coils with identical current magnitude. This simulation result is shown in Figure 4.28b. This plot shows that in this mode magnetic flux of two face to face coils add up with each other in the middle section of the chamber and creates a stronger flux pattern. On the other hand, the amplitude of combined magnetic flux at outer section of the chamber will cancel-out. In fact this coil set up creates a bigger solenoid coil in which the concentration of magnetic flux is higher inside the solenoid. This field pattern is shown with arrows in Figure 4.29b, which resemble magnetic flux inside a solenoid.

3. Overlap with Opposite Currents: This mode is similar to the previous mode with different current directions. The result of simulation for this mode is shown in Figure 4.28c. This coil arrangement creates a field pattern similar to quadrupole magnet. Therefore, the magnetic flux density in the middle part of quadrupole is minimal, as the opposite fluxes cancel each other out. Instead the magnitude of flux is maxima at the vicinity of the poles, which in this arrangement is across the surface of winding section. An arrow plot of

magnetic flux density confirms this type of field pattern (Figure 4.29a). Therefore, the direction of magnetic beads, experiencing this field pattern, shifts from the inner edge of the coil toward the outer edge of the coil.

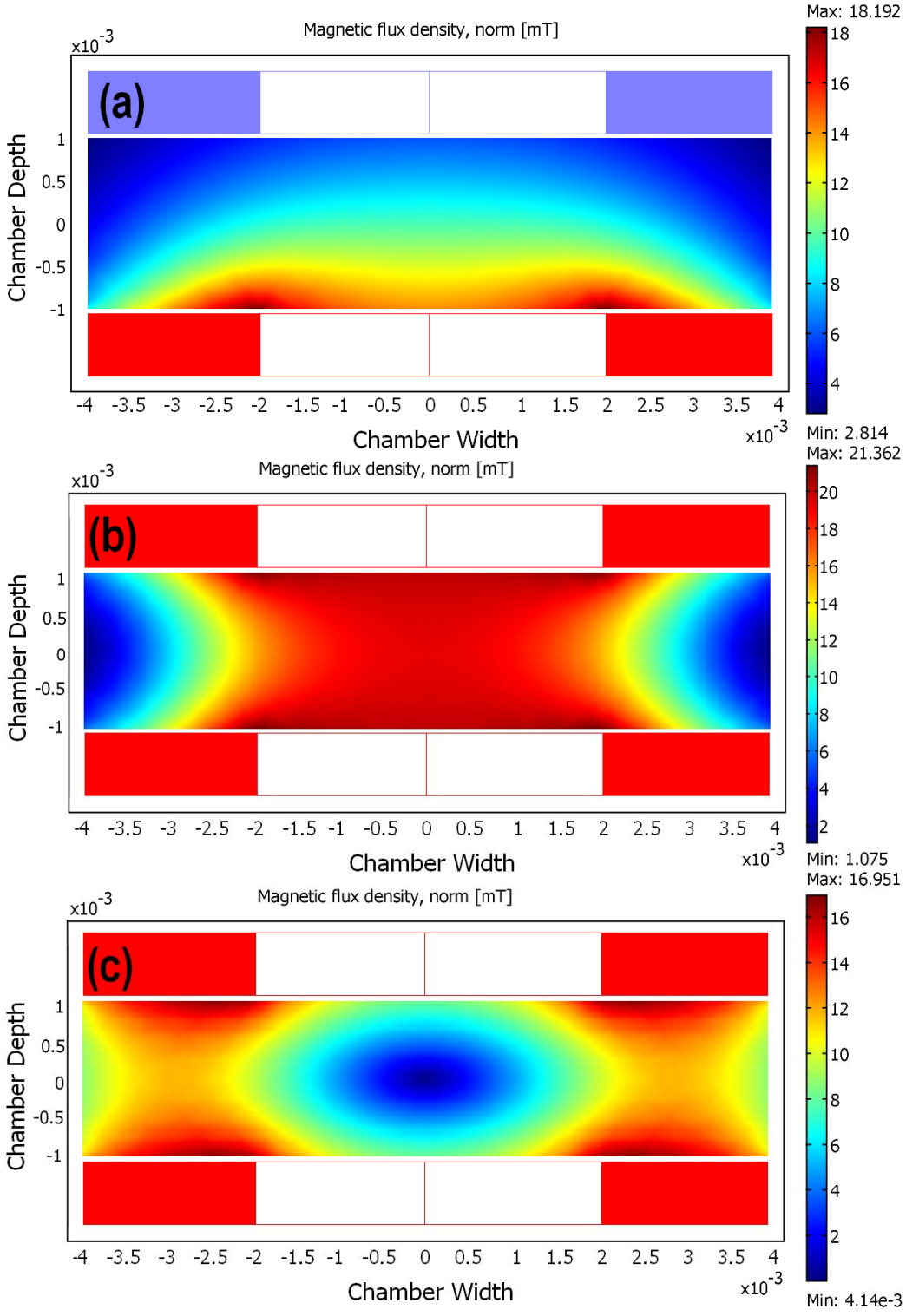

Figure 4.28. Cross-section plot of magnetic flux density of parallel coil arrangement in switching mode (a), overlapping cycle with parallel currents (b) and overlapping cycle with opposite-direction electric currents (c).

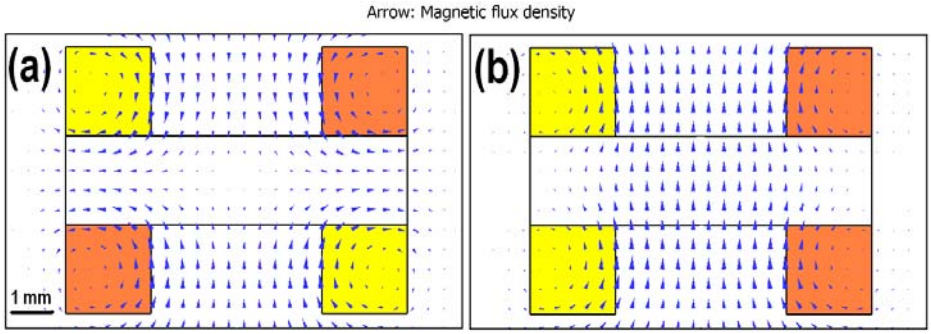

Figure 4.29. Arrow-plot of magnetic flux density showing the magnetic mutual effects. a) Quadrupolic coil arrangement. b) Solenoidal coil arrangement.

In conclusion, magnetic mutual effects have some advantages and disadvantages. On one side, the in-plane mutual effect between neighbouring coils disturbs the pattern of magnetic fluxes and hence reduces the magnitude of applied force. On the other side, application of cross mutual effect between two coils can be consider as an advantage in order to control the behaviour of magnetic beads inside the chamber. In fact, in normal switching magnetic force pattern, direction of bead-flow is toward the middle section of the coil. This is because magnetic beads tend to migrate to the areas with higher field intensity and gradient. Based on optimum conditions and the frequency of switching field, these beads might end up in the middle section very quickly. This will indicates the end of mixing period. Therefore, mixing time is limited to the position of beads inside the chamber and beads should collect target molecules during migration time from outer section toward middle section of the chamber. This type of mixing might be efficient in some cases with accurate force pattern design but is not efficient in every case. For instance, in DNA extraction process, DNA molecules need to be released from white blood cells using appropriate lysis buffer. Lysis process is not an instant chemical reaction and will take place in a couple of minutes (it depends on the extraction protocols). If the migration time of beads is less than lysis period, beads will pile up with no DNA attached at the middle part of chamber.

Therefore, with quadrupolic arrangement of coils there is a possibility to unpile the beads and return them to the beginning of migration track. In this case, the magnetic mixing and collection of target molecules can be repeated. This action can be repeated as much as necessary to achieve required efficiency.

In addition, application of solenoidal coil arrangement can be adopted to clamp magnetic beads. In most magnetic bead extraction processes, it is necessary to wash

cell debris off the beads and collect the target molecule. This will require an on-chip clamping process. Switching magnets can be used as clamping magnet with application of DC magnetic field. Solenoidal coil arrangement generates stronger clamping magnetic field pattern in comparison to single magnet strategy (using bottom coil).

Figure 4.30 shows a 3D simulation result of quadrupolic and solenoidal arrangements using COMSOL software. In these simulations two magnetic coils are placed at top and bottom of the chamber. The distance between coils is 2mm and coil's overall diameter is set to $d_{out} = 8mm$. Figure 4.30 (a & b) shows cross-section plot of magnetic force applied to a magnetic bead of 1µm in diameter and relative permeability of $\mu_r = 10$. Figure 4.24 (c & d) shows a surface plot of magnetic force at a height of 600µm above the coil surface. These surface plots of force clearly describe the difference between solenoidal pattern (c) and quadrupolic pattern (d). Solenoidal pattern is more concentrated on inner edge of the coil with higher intensity, and quadrupolic pattern is more spread on the winding surface and is less concentrated.

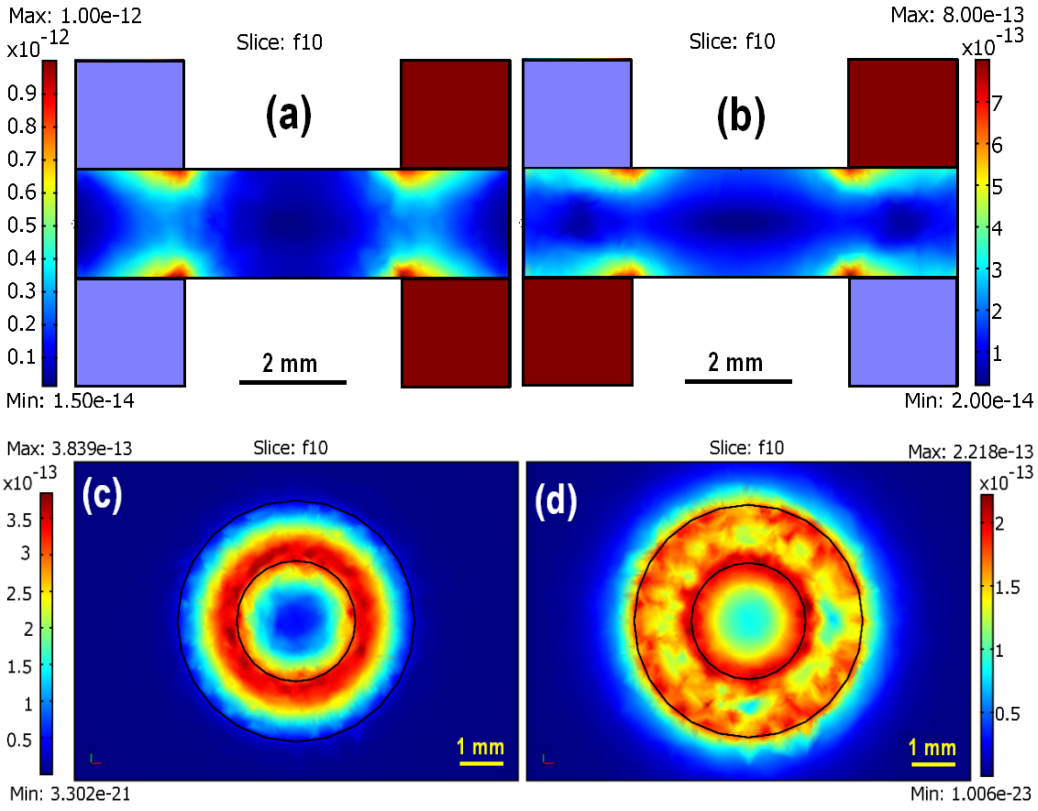

Figure 4.30. 3D simulation result of quadrupolic and solenoidal coil arrangements. (a, b) Cross-sectional plot of magnetic force for solenoidal (a) and quadrupolic (b) coil arrangement. (c, d) Surface magnetic force plot of solenoidal (c) and quadrupolic (d) coil arrangement at 0.6mm above the coil surface.

It is worth mentioning that, a hybrid force pattern can be generated using normal switching pattern, solenoidal and quadrupolic pattern. Hybrid pattern can be used in order to create a very versatile mixer, which offers more flexibility in movement of bead flow inside the chamber. This will increase the chance of collecting the target molecules. The application of different mixing patterns in magnetic mixing and clamping is presented in *Chapter 5* and *Chapter 6*.

4.10 Summary

In this chapter, a preliminary simulation study was performed to design a magnetic bead-based micro-mixer to be used for extraction and purification of DNA molecules from whole blood. Simulation was performed using commercial simulation software, COMSOL multiphysics. Different electromagnetic modules were used to accurately model this magnetic problem in 3D mode and where possible in 2D mode. PDE module in COMSOL was used to calculate magnetic force experienced by magnetic particles.

Various coil geometries were investigated to select the most appropriate coil arrangement for internal and external coil setup. Among different coils, key-type electrode seems to be the best candidate for internal coil setup. This is because of less fabrication complexity, higher cross-section ratio and lower electric resistance. Since the thickness of coil is limited by fabrication limitations, the optimised overall diameter of the coil is limited to a couple of millimetres with the chamber depth of up to 150µm. Therefore, internal coil setup is more suitable for small volume chambers. However, larger chamber can be used by adopting multi-key-type electrode pattern.

Spiral solenoid was selected to be used in external coil arrangement. A simulation study was carried out on different geometrical parameters of the external coil to investigate the effect of coil cylindrical height and outer diameter to achieve the desired strength of magnetic force. This study showed that the maximum magnetic force can be generated by a square-shape cross section of winding section. Further simulation on effect of cylindrical height showed that, the maximum effective height is equal to outer diameter of the coil.

A simulation study was carried out to investigate the mutual effect of neighbouring coils on each other. The result of in-plane coil arrangement showed small disturbance

and reduction in the magnetic field by supplying the electric current in parallel directions. This is because of negative mutual effect between neighbouring coils. However, by supplying the electric current in opposite directions, the strength of magnetic field increases, as the result of positive mutual interactions. On the other hand, the result of cross mutual effect opened a new advanced pattern of magnetic force, which can be used to increase the efficiency of mixing and clamping. Supplying the electric current in parallel directions, results in creation of solenoidal field pattern. This magnetic field pattern, concentrate the magnetic flux of both coils at the centre of the chamber. On the other hand, opposite-direction supplied current, shifts the centre of the magnetic field toward outer section of the chamber. Therefore, these two hybrid field patterns can be used to manipulate the bulk of magnetic beads more efficiently, inside the chamber.

Based on these preliminary studies, trajectories of beads were investigated to asses and quantify mixing efficiency. This is presented in *Chapter 5*.

CHAPTER 5

BEAD TRAJECTORIES AND OPTIMIZATION

5.1 Introduction

In the previous chapter, COMSOL multiphysics software was used to simulate the magnetic force pattern generated by different magnetic sources. Different geometrical parameters were studied and were optimised for integrated internal coil arrangement as well as external coil arrangement. Optimisation of internal coil was based on the practical limitation of the maximum conductor thickness, due to fabrication limitation. This limitation, limits the penetration depth of the magnetic force, and thus the chamber depth. Therefore, the application of internal coil arrangement is more suitable for small-volume mixing chamber. On the other hand, optimisation of external coil arrangement was investigated based on the larger distance between the coil surface and the microchamber. External coil arrangement has less physical limitation in order to generate sufficient magnetic force pattern inside the chamber, and therefore, is a better choice to be used for large-volume mixing chamber. However, in order to evaluate and compare the efficiency of internal and external coil arrangements, their maximum supplied electric current need to be extracted. Maximum current density can be calculated in a thermoelectric equilibrium. Therefore, based on maximum current density it is possible to evaluate

performance of internal and external coils in achieving efficient mixing. The efficiency of mixing can be evaluated using bead trajectory study. This study can be performed using Matlab software coupled with COMSOL. Therefore, a Matlab source-code was developed to evaluate the performance of designed magnetic coils and extract the optimised mixing frequency using bead trajectory simulation.

5.2 Internal Coil

As discussed in *Chapter 4*, internal coil is limited by thickness of conductor. This is because traditional metal deposition techniques such as sputtering and e-beam depositions are not suitable methods for making thick conductors. Electroplating of high-conductive material such as gold and copper can be used to fabricate thicker conductor patterns [199, 200]. By using electroplating, a conductor thickness of 10-100µm can be fabricated. Therefore, the maximum conductor thickness that can be used to design an internal coil is 100 μm. However, using electroplating technique, it is possible to fabricate multi-layers to achieve higher conductor thickness to withstand desired currents. This will complicate the fabrication process, which is not desirable.

As mentioned previously (section 4.62 *Chapter 4*), the optimised coil outer diameter depends on the depth of working chamber (this information was summarised in Figure 4.19). Based on this information, a chamber depth of $d_{ch} = 100\ \mu m$ was selected for bead trajectory study. A chamber depth of $d_{ch} < 100\ \mu m$, results in stronger magnetic force, but increases the risk of clumping the beads inside the chamber and microfluidic network. The strength of magnetic force decreases significantly, for a chamber depth of $d_{ch} > 100\ \mu m$. Based on the selected chamber depth and the graphs of Figure 4.19, a 2 mm in diameter key-type electrode ($t_k = 100\ \mu m, W_k = 0.5\ mm, d_{out} = 2\ mm$) was selected to be used in the bead trajectory study.

5.2.1 Internal Coil Maximum Current Density

Joule heating, also known as ohmic heating, describes the amount of heat generated by passage of an electric current through a conductor. It was first studied by J. P. Joule in 1841 and is explained by Joule's first law as follow:

$$Q \propto I^2.R \tag{5.1}$$

Where, Q is the released energy in the form of heat generated by current *I* passing through a conductor with ohmic resistance of *R*. In atomic level, joule heating is the result of released kinetic energy of electrons (in conductors), when they collide with atoms. As described in Joule's equation, the amount of heat is proportional to square of electric current. From Equation (4.7):

$$F_m \propto I^2 \tag{5.2}$$

by substituting Equation (5.2) into Equation (5.1):

$$F_m \propto Q \tag{5.3}$$

Which describes that amplitude of magnetic force is directly proportional to temperature rise in coil.

More accurate form of Joule's law describes that the amount of heat generated in a current carrying conductor is related to the time as well:

$$Q = I^2.R.t \tag{5.4}$$

This equation explains that the amount of heat will increase with time, but in reality temperature rise stops at an equilibrium point. Based on first law of thermodynamics, generated heat will be dissipated by means of conductive, convective transfers and radiation. The amount of heat dissipation depends on the steady-state temperature and thermal property of materials and the medium. In this work, COMSOL General Heat Transfer Module in coupled with Conductive Media DC Module was used to simulate this thermal problem. By solving this problem, steady-state temperature in conductors was calculated at equilibrium point for different current densities and the maximum current density was extracted based on designed coil geometry. This maximum current density was used thereafter to calculate the magnitude of magnetic force and bead trajectory studies.

A simple model of a ring-shape conductor, which represents the key-type electrode, was selected to investigate the thermal analysis. The electrode had a thickness of $t_k = 100\mu m$ and width of $W_k = 500\mu m$. Heat dissipation was assumed to be convective flux to surrounding air at temperature of $T_{Air} = 20℃$. Copper was used as the conductor material with temperature-dependent resistivity of:

$$\rho(T) = \rho_0(1 + \alpha_0(T - T_0)) \tag{5.5}$$

Where, ρ_0 is the resistivity at reference temperature and α_0 is the temperature coefficient of material. Physical property of copper used for this simulation is given in Table 5.1. Figure 5.1 shows heat transfer simulation result of the model for different current densities. This simulation was repeated and is shown for conductor cross-section of $t_k = 25\mu m$. The result shows that by decreasing the conductor thickness, capacity of conductor to handle electric current increases. By reducing the thickness, the relationship between conductor cross-section areas of two rings is as follow:

$$A_2 = \frac{1}{4} A_1 \tag{5.6}$$

Where, A_1 and A_2 are the cross-section area of conductors (measured in m^2) with thickness of $t_{k1} = 100\ \mu m$ and $t_{k2} = 25\ \mu m$ respectively. On the other hand, the electrical resistance, *R* of a conductor can be calculated as:

$$R = \rho \frac{l}{A} \tag{5.7}$$

Where, l is the length of conductor measured in (m), A is the conductor cross-section area measured in (m^2) and ρ is the electrical resistivity of the material measured in ($\Omega . m$). By comparing the electrical resistance of the two simulated electrodes using Equation (5.6) and Equation (5.7), the relationship between the ohmic resistances of two conductors can be extracted as:

$$R_2 = 4R_1 \tag{5.8}$$

Where, R_1 and R_2 are the electric resistance of conductors with thickness of $t_{k1} = 100\ \mu m$ and $t_{k2} = 25\ \mu m$ respectively.

By assumption of equal heat generation ratio and equal heat dissipation ratio, the relationship between current densities of the conductors, J_1 and J_2 can be extracted by substituting Equation (5.6) and Equation (5.7) in Equation (5.4).

$$if\ Q_1 = Q_2 \overset{I=JA}{\Longrightarrow} J_2 = 2J_1 \tag{5.9}$$

Table 5.1. Property of copper wire used for simulations.

Property of Material	Copper
Thermal Conductivity K (W/m.K)	400
Density ρ (Kg/m^3)	8700
Heat Capacity at Constant Pressure C_p (J/Kg.K)	385
Resistivity at Reference Temperature ρ_0 (Ω.m)	1.72×10^{-8}
Temperature Coefficient α (1/K)	0.0039

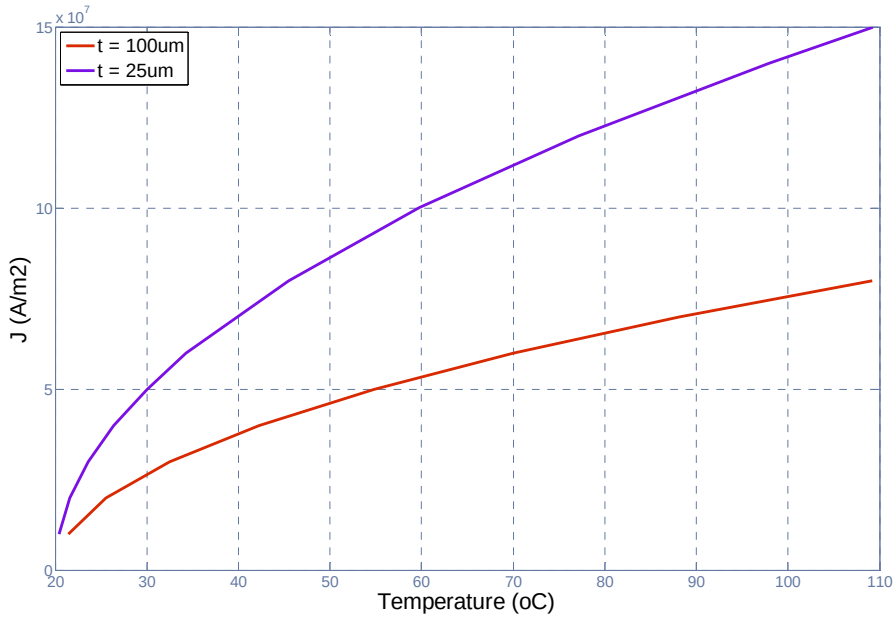

Figure 5.1. Steady state temperature graph for two different internal coil thicknesses.

The graphs of Figure 5.1 show a very close agreement between the above calculation and simulation result. Steady state temperature of 60°C occurs with current densities of $J_1 = 5.3 \times 10^7$ and $J_2 = 10.1 \times 10^7$ at the electrodes with thickness of $t_{k1} = 100\mu m$ and $t_{k2} = 25\mu m$ respectively.

A current density of $J = 5 \times 10^7 A/m^2$ was selected for simulation as the steady-state temperature at this current density was $T_{ss} = 56℃$. This temperature is necessary for the incubation of lysis/binding buffer and blood sample. The heat transfer between ring and the media is only through convective flow to surrounding air. The temperature will decrease by considering heat transfer between the conductor and surrounding materials, which will be used for microfabrication and selection of solid substrate.

In order to investigate the performance of magnetic mixing, beads trajectories inside the chamber need to be studied. This study cannot be performed using COMSOL

multiphysics, as this software has generally been designed to simulate the physics problems through finite element modelling. COMSOL script to some extent can be used for some preliminary post-processing. Bead trajectory study needs an accurate simulation by using proper programming software. The source code for this program will use the raw data from COMSOL simulation in order to perform the bead trajectory study. COMSOL multiphysics offers a solution to this problem via an internal link to Mathworks Matlab software. By using this link, all simulation result will be transferred to Matlab in order to perform required post-processing.

5.3 Motion of Magnetic Particles Inside Viscous Fluid

Further processes to investigate the path of magnetic bead inside the microchamber needs a proper physical model. This model describes the magneto-hydrodynamic behaviour of magnetic particles inside a fluid. Study of spherical particles inside viscous fluid is rather a complicated process, which involves hydrodynamic interactions in multiphase flow. The aim of this chapter is not to deeply investigate this matter. However, the objective is to build a simple model, which describes the behaviour of magnetic beads inside the chamber under influence of magnetic force. Therefore, this model can be used to evaluate the strength of magnetic force and extract the frequency of mixing. In order to build this simplified model, dominant forces on magnetic beads need to be extracted. Since this model involves motion of solid particles inside a liquid, this flow is considered as multiphase flow. Phase in general refers to any state of matter such as solid, liquid and gas. Figure 5.2 shows a schematic diagram of more common multiphase flows. As shown in this diagram, two-phase flow refers to liquid-liquid, liquid-gas, liquid-solid and gas-solid flows. An example of liquid-gas is bubbles inside the liquid or liquid drops in gas. A three phase flow is realized when the flow is a solid-liquid-gas mixture. In this study, solid magnetic particles are suspended inside the liquid; the problem is limited to liquid-solid two-phase flow. Another important aspect of multiphase flows is the coupling between different phases. For example in two phase flow, if only one phase has influence on other phase, the coupling is called one-way. If both flows have mutual interaction, then the flow is coupled two-way. Coupling may take place through mass, momentum and energy transfer between different phases. Mass coupling may take place through condensation or evaporation and energy coupling can take place trough heat transfer between phases [201]. Momentum coupling take place through

hydrodynamic interactions between different forces such as drag force. In more complicated description of the couplings, the flow might be considered as a four-way-coupled flow. This flow describes the interaction between different liquids and beads with counting the solid-solid interaction between magnetic beads. The interaction between beads can be described as particle-particle collision in two-phase flow regime.

Particle-particle interaction will take place, if the concentration of particles exceeds a certain number. The mutual effect between particles can be ignored for concentration below 10^{15} particle/m^3 [202]. Therefore, four-way coupling is not applicable in this study. Since the fluid is assumed to be static inside the chamber and the velocity of particles relative to liquid is very low, the flow regime can be considered at very low Reynolds's number (Re<<1). In this situation, the fluidic problem is reduced to two-phase flow with one-way coupling. This is because the motion of particles has no effect on the flow pattern. One-way coupling is valid here as only the fluid has effect on particle flow. This effect, which is known as drag force, is a function of fluid viscosity.

Another force acting on magnetic particles is the gravitational force. This force needs accurate consideration as it mainly depends on the mass property of both beads and fluid. Figure 5.3 shows a schematic diagram of forces acting on a magnetic particle inside a fluid.

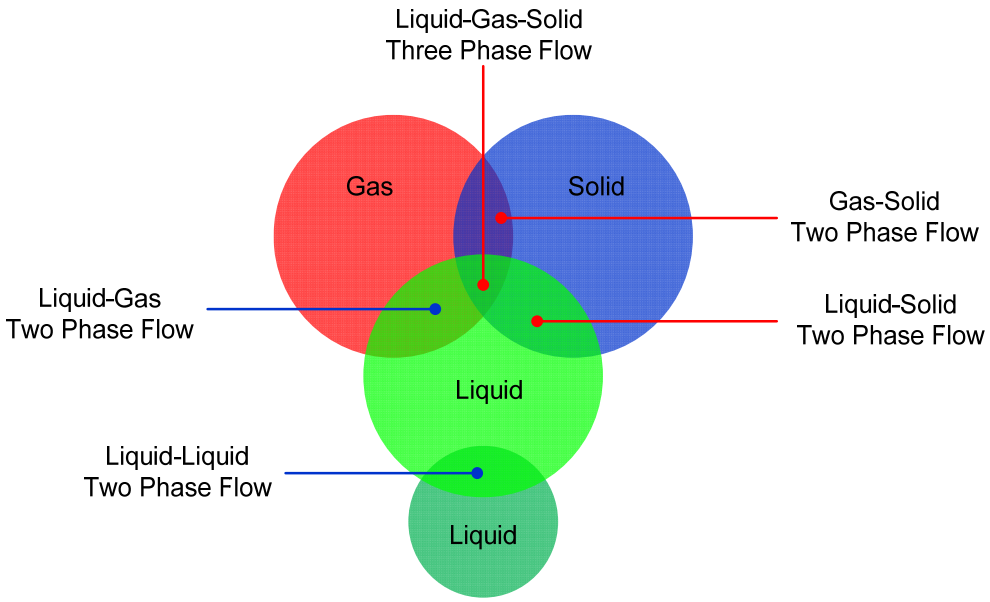

Figure 5.2. Schematic diagram of different phase flows.

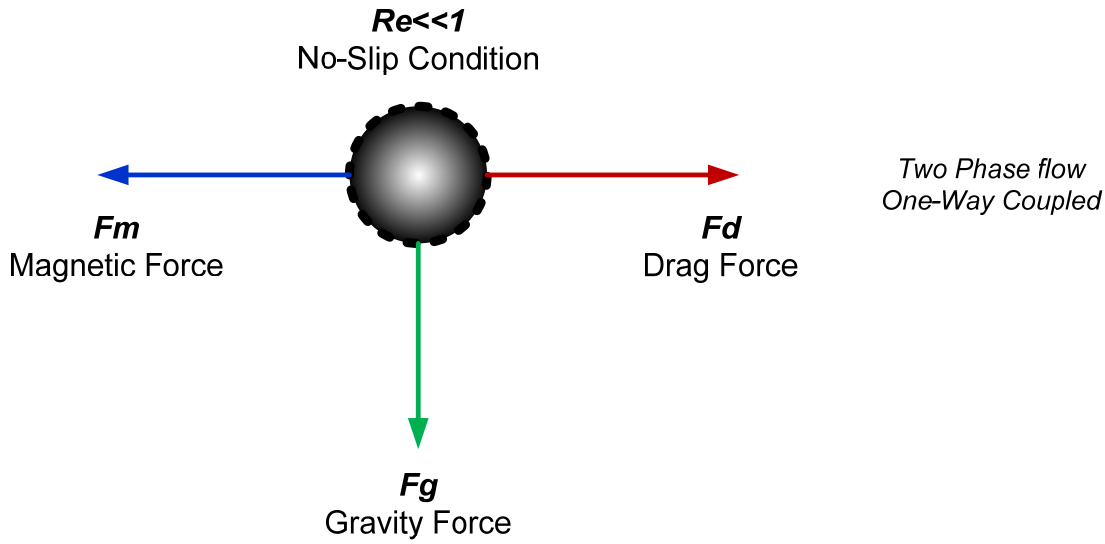

Figure 5.3. Schematic diagram of different forces acting on a magnetic particle inside a fluid.

5.3.1 Magnitude of Gravity Force

In general, magnetic beads are made of a mixture of iron oxide (Fe_2O_3 or γFe_3O_4) and polymers. The ratio of magnetic material varies from supplier to supplier and they are supplied in various shapes and diameters. Table 5.2 shows an example of three different magnetic beads and their properties. In this table, a typical gravity force applied on each bead is calculated. This calculation is based on suspension of beads in water. A typical magnetic force applied on each bead is given as well. Clearly the magnitude of magnetic force is much higher than gravity force. Practically, the bio-fluids of interest in this work, which contain whole blood, lysis and binding buffer, are more viscous than water. This indicates that the magnitude of gravity force on the magnetic beads can be less than that shown in Table 5.2. Hence, the effect of gravity force can be ignored in this work and the magneto-hydrodynamic model of magnetic beads inside the chamber can be simplified by a two-phase flow and one-way coupling. Dominant forces are induced magnetic force and opposing viscous drag force.

Table 5.2. Property of different magnetic particles and magnitude of gravity force on them.

Bead	Dynal M-280	Dynal MyOne	Spherotech CM-10
Diameter d_p (μm)	2.83	1.05	1.2-1.4
Average Density ρ_p (g/cm^3)	1.4	1.7	1.58
Gravity Force in water Fg (N)	4.744×10^{-14}	4.24×10^{-15}	6.67×10^{-15}
Average Magnetic Force F_m (N)	4×10^{-13}	2×10^{-14}	4×10^{-14}

5.3.2 Viscous Drag Force

The analytical expression of magnetic force acting on a magnetic particle under influence of a non-uniform magnetic field was calculated in *Chapter 3*. Another dominant force, which has effect on motion of magnetic particles inside the chamber, is viscous drag force. Drag force can be described as the resistance of fluid to movement of particle. This force is always relative and in opposite direction to particle movement. The magnitude of drag force depends on many parameters including particle and fluid properties. Relative flow condition for a spherical particle inside a fluid can be described by particle's Reynolds number:

$$Re_p = \frac{ud\rho}{\mu} \tag{5.10}$$

Where, ρ (kg/m^3) and μ (Pa.s) are density and viscosity of fluid, d (m) is diameter of spherical particle and u $(m/s)$is the velocity of particle relative to the fluid.

Fundamental governing law in this situation is the *Navier-Stokes* hydrodynamic equation of motion. This equation was solved by Stokes [203] for simplified case of creeping flow. Creeping flow describes the case of very low velocity relative flow of particles and fluid. The drag force extracted for this case is as follow:

$$F_d = 3\pi\mu du \tag{5.11}$$

Where, μ $(Pa.s)$ is the viscosity of fluid, $d(m)$ is the diameter of particle and u $(m/s$ is the velocity of particle relative to the fluid.

Drag force also known as *Stokes* law (Equation (5.10)), is valid at very low particle Reynolds number ($Re_p < 2$), which is the case in microfluidics [204]. Drag force is a mixture of skin friction force and pressure force. Friction force, which acts in a tangential direction parallel to the surface of the particle, constitutes two third of drag force. The remaining part comprises pressure force, which acts in a perpendicular direction to the surface. Primarily pressure force acts on front and back sides as other segments of this force cancel each other out. These segments of drag force can be written as follow.

$Skin\ Friction\ Force$: $2\pi\mu du$

$Pressure\ Force$: $\pi\mu du$

5.3.3 Equation of Motion of Magnetic Particle

As discussed above, magnetic force and viscous drag force are dominant forces in this study. The equation of magnetic bead's velocity can be extracted by solving *Newton's* second law of motion:

$$m_p \frac{\partial u}{\partial t} = F_m - 3\pi\mu d u \tag{5.12}$$

Where, m_p is mass of magnetic particle and F_m is the external magnetic force.

By applying magnetic force on magnetic particle, particle moves towards high intensity magnetic field. The moment particle starts to move, drag force acts on the particle. When the velocity of particle increases, drag force increases. At steady-state condition, there is no acceleration in the particle velocity and both magnetic force and drag force are equal and in opposite directions. Particle moves at constant velocity afterward. This terminal velocity can be extracted from Equation (5.12) as follow:

$$u_m = \frac{F_m}{3\pi\mu d} \tag{5.13}$$

Where, u_m is the steady-state velocity of particle.

Particle reaches this velocity in a fraction of time, which can be calculated as:

$$\tau = \frac{\rho_p d^2}{18\mu} \tag{5.14}$$

Where, ρ_p is the density of particle and τ is the particle relaxation time. Calculation of this time constant for *Dynal M-280* magnetic bead in water (data is given in Table 2) gives relaxation time of $\tau = 623 \times 10^{-9}\ s$, which is less than a micro second and can be ignored in this work. Therefore, the terminal velocity can be used directly for the simulation of magnetic particle tracking inside the chamber.

5.4 Particle Tracking Using Internal Coils

Maximum current density was calculated previously using thermal analysis in COMSOL multiphysics heat transfer module. A simplified magneto-hydrodynamic model was introduced in order to describe interactions between different forces

governing motion of magnetic particle inside the microchamber. Based on this model, terminal velocity of magnetic bead was extracted (Equation (5.13)). This equation can be used in a tracking program to study magnetic beads trajectories. The magnitude of magnetic force is not constant and will change when the particle moves. Therefore, in the simulation program, the velocity of magnetic bead was calculated in discrete time frames. In each time frame, the magnitude of magnetic force, hence velocity was assumed to be constant. In order to increase the accuracy of simulation, time frames were accurately selected. The time frame selection was based on trial and error, as the total numbers of frames depend on magnetic bead property, strength of magnetic force and viscosity of fluid.

Based on above assumption a Matlab code was developed in order to calculate particle motion in the chamber during mixing. This code uses partial differential equations created by COMSOL PDE Module and calculates the magnetic force. Magnetic field vector components of H_x, H_y and H_z were normally calculated by COMSOL AC/DC Module and their first derivatives, H_{xx}, H_{yy} and H_{zz} were calculated by COMSOL PDE Module. Therefore, magnetic force can be calculated as follow:

$$\boldsymbol{F_m} = 2\pi\mu_0 R^3 \frac{\mu_r - 1}{\mu_r + 2} \nabla \boldsymbol{H}^2 = \boldsymbol{K}.\nabla\left(H_x^2 + H_y^2 + H_z^2\right) \qquad (5.15)$$

$$= K.\left[\left(H_x.\frac{\partial H_x}{\partial x} + H_y\frac{\partial H_y}{\partial x} + H_z\frac{\partial H_z}{\partial x}\right)i + \left(H_x.\frac{\partial H_x}{\partial y} + H_y\frac{\partial H_y}{\partial y} + H_z\frac{\partial H_z}{\partial y}\right)j + \left(H_x.\frac{\partial H_x}{\partial z} + H_y\frac{\partial H_y}{\partial z} + H_z\frac{\partial H_z}{\partial z}\right)k\right]$$

$$\boldsymbol{K} = 2\pi\mu_0 R^3 \frac{\mu_r - 1}{\mu_r + 2}$$

After calculation of force vector on each particle, vector particle velocities u_x, u_y and u_z were calculated based on Equation (5.13) in different directions of x, y and z. Particle movement in three dimensions can be calculated for each time frame. Therefore, particle trajectories can be evaluated by integrating sum of discrete velocities using Euler integration method as follow:

$$r_p = \int u_m \, . dt = \frac{F_m}{3\pi\mu d} \tag{5.16}$$

5.4.1 Simulation Setup

Based on the above procedure, a pair of ring-type electrode representing the key-type electrode was used for simulation of internal coil configuration. These two rings were placed on top and bottom of a chamber of depth of $t_{ch} = 100\ \mu m$. The current density was adjusted to the maximum value of $J_{Ring} = 5 \times 10^7 A/m^2$, which creates the maximum temperature of $T_{ss} = 56℃$. Both coils were placed at a distance of 10 µm from the chamber surface, which resembles an insulation layer and/or chamber wall thickness. Two fluid viscosities of $\mu = 0.001\ Pa.S$ and $\mu = 0.002\ Pa.S$ were used in simulations. Detail of the geometry used in this simulation is given in Figure 5.4. Table 5.3 shows the parameters used for the simulations.

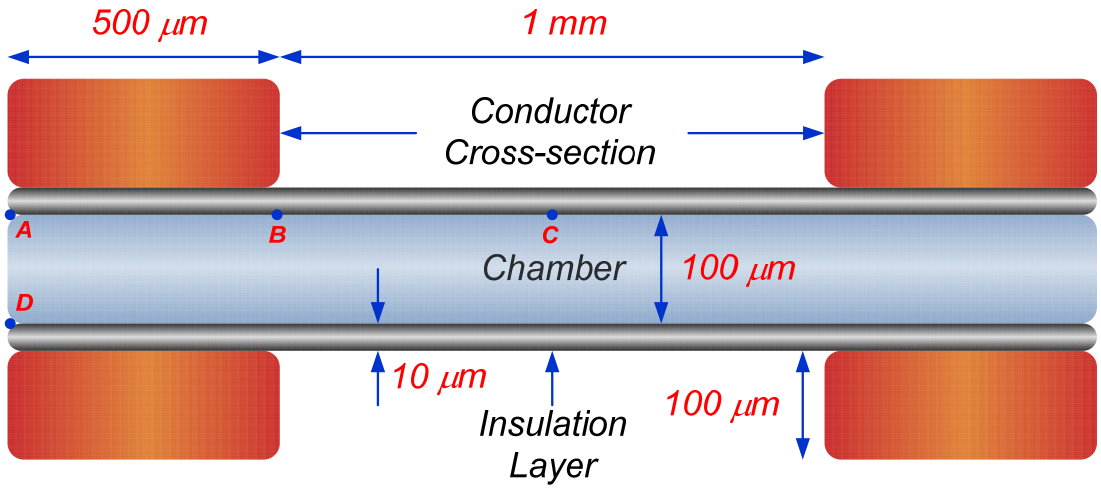

Figure 5.4. Schematic cross-sectional view of internal coil arrangement used in simulation.

Table 5.3**. The parameters used for the simulation.**

Ring Thickness, t_R	100 µm
Conductor Width, W_R	500 µm
Ring Internal/External Diameter, d_{in}/d_{out}	1mm/2mm
Total Current Density, J_R	5×10^7 A/m^2
Chamber Depth/Width/Volume, $t_{ch}/W_{ch}/V_{ch}$	100 µm/2mm/314nl
Beads Relative Permeability, μ_{rB}	10
Bead Diameter, d_{Bead}	1 µm/3 µm
Fluid Viscosity, µ	0.001/0.002 Pa.S

5.4.2 Particle Trajectory Using 1µm Diameter Beads

Figure 5.5a shows simulation results of bead trajectories performed using 1 µm beads. A set of eleven beads were placed on top of the chamber in a horizontal arrangement along radial line from centre of the chamber (as shown by A-C line in Figure 5.4). Coils were activated with an equal duty cycle of 20s, which gives a frequency of $f = 0.025Hz$. Figure 5.5b shows another simulation results that was carried out in the same conditions, but magnetic beads were placed in a vertical line perpendicular to coil surface at one end of the chamber (as shown by A-D line in Figure 5.4). Since the magnetic force pattern is uniformly distributed across any circular path inside the chamber, a 2D plane, perpendicular to the chamber and coils, was selected to study the behaviour of the magnetic beads. These simulations were performed for a total mixing time of $t = 5\ min$.

The results of horizontal particle arrangement study (Figure 5.5a), describe the efficiency of vertical component of magnetic force in movement of magnetic particles. As it was expected, particles close to the inner edge of the coil experience stronger magnetic force and move faster. Particles close to the centre and outer boundary of the chamber are placed in weaker magnetic force region and their respond is slower.

The results of vertical particle arrangement study (Figure 5.5b), describe the speed of particles toward the centre of the chamber. The movement pattern of the beads can be divided into two different groups, transient mode and steady-state mode. In transient mode, the bulk of magnetic beads will be divided to two streams and each bead stream moves toward one coil surface. This is because, the average magnetic force, experienced by magnetic beads, from each coil is not equal. Particles closer to the top or bottom coils, experience a net force toward those coils.

After transient mode, two magnetic bead streams are fully trapped by one coil. In the steady-state mode, magnetic beads follow a similar parallel movement pattern (zigzag) toward stronger magnetic field region at the inner edge of the coil. Durations of transient and steady-state modes depend on various parameters such as, the strength of magnetic field, particle size and magnetic property.

Since water viscosity was used in these simulations, the terminal velocity of magnetic beads reduces in higher viscous fluid, such as lysis buffer and whole blood

mixture. This can be solved by increasing the activation time of the coils (decreasing the frequency). However, lower frequencies increase the overall mixing time, which is not desirable. Another solution to overcome this problem is by increasing the size of magnetic beads. Another important factor that influences the mixing efficiency is the surface coverage. Despite transient mode, magnetic beads trajectories do not cover the chamber surface properly, at the given frequency of $f = 0.025\ Hz$. This problem can be solved either by decreasing switching frequency or increasing the size of magnetic beads. As mentioned above, lower switching frequencies are not desirable. Therefore, larger-size magnetic beads need to be used in the mixing chamber using internal coil arrangement.

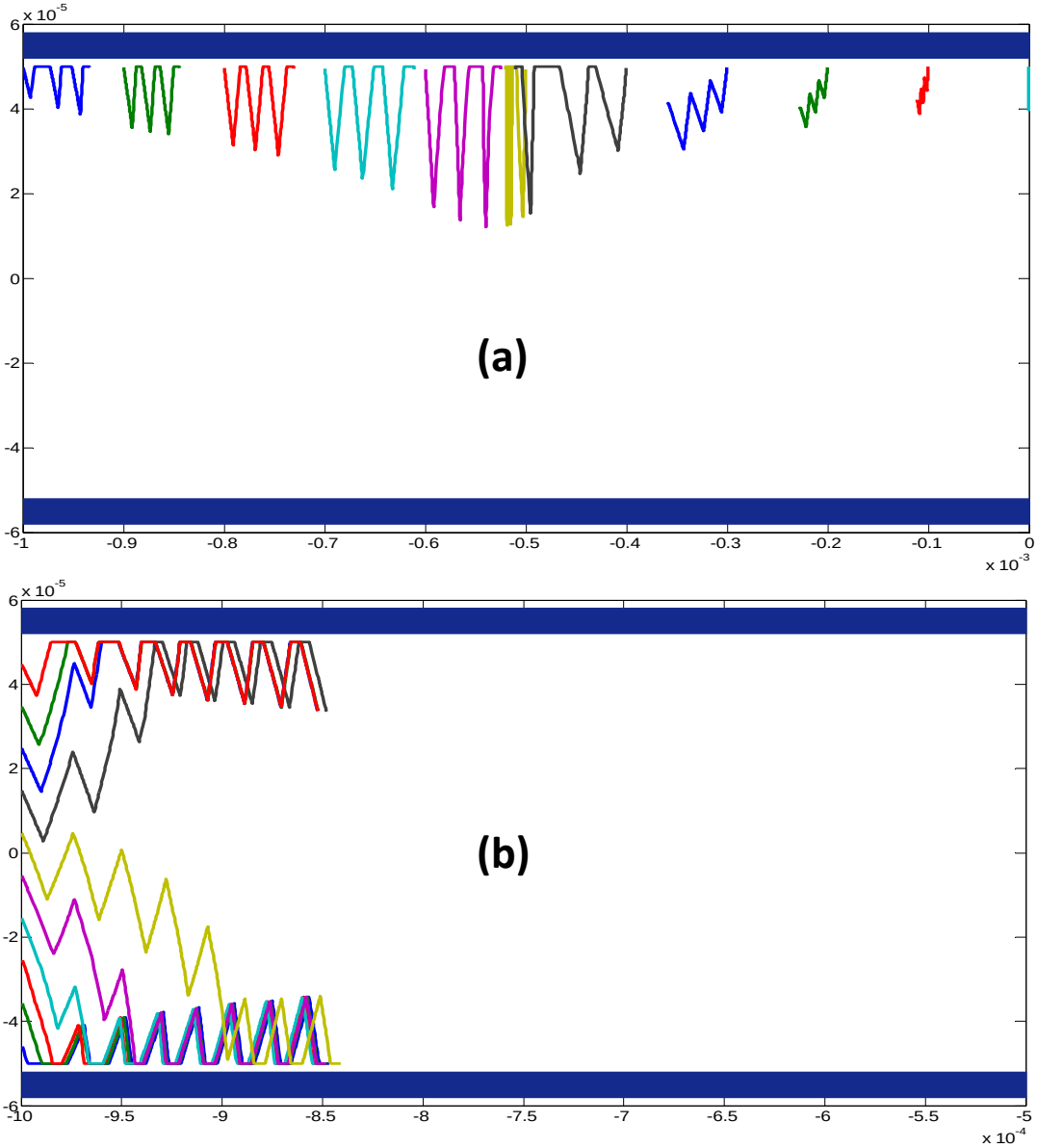

Figure 5.5. Simulation result of bead trajectories for beads of 1µm in diameter and relative permeability of $\mu_r = 10$ at switching frequency of $f = 0.025\ Hz$ and current density of $J = 5 \times 10^7\ A/m^2$. a) Vertical study. b) Horizontal study

5.4.3 Particle Trajectory Using 3µm in Diameter Beads

A similar set of simulations were performed using 3µm diameter magnetic beads to investigate the effect of bead size on particle trajectory. In these simulations, viscosity of fluid was doubled, which is more realistic value for Blood/Lysis buffer mixture. The results of these simulations are shown in Figure 5.6 in horizontal arrangement, (a) and vertical arrangement (b) for a total mixing time of $t = 3\ min$. A switching frequency of $f = 0.05\ Hz$ was extracted based on trial and error to achieve full coverage at the middle of mixing zone (point B, as shown in Figure 5.4). Despite faster respond of magnetic beads in this simulation setup, the overall behaviour of the beads is similar to the previous simulations. Duration of transient mode is decreased due to the increase in the strength of magnetic force. In the steady-state mode, both vertical and horizontal velocities of the beads are increased. The average vertical and horizontal velocities are $u_v = 5\ \mu m/sec$ and $u_H = 2.5\ \mu m/Sec$ respectively.

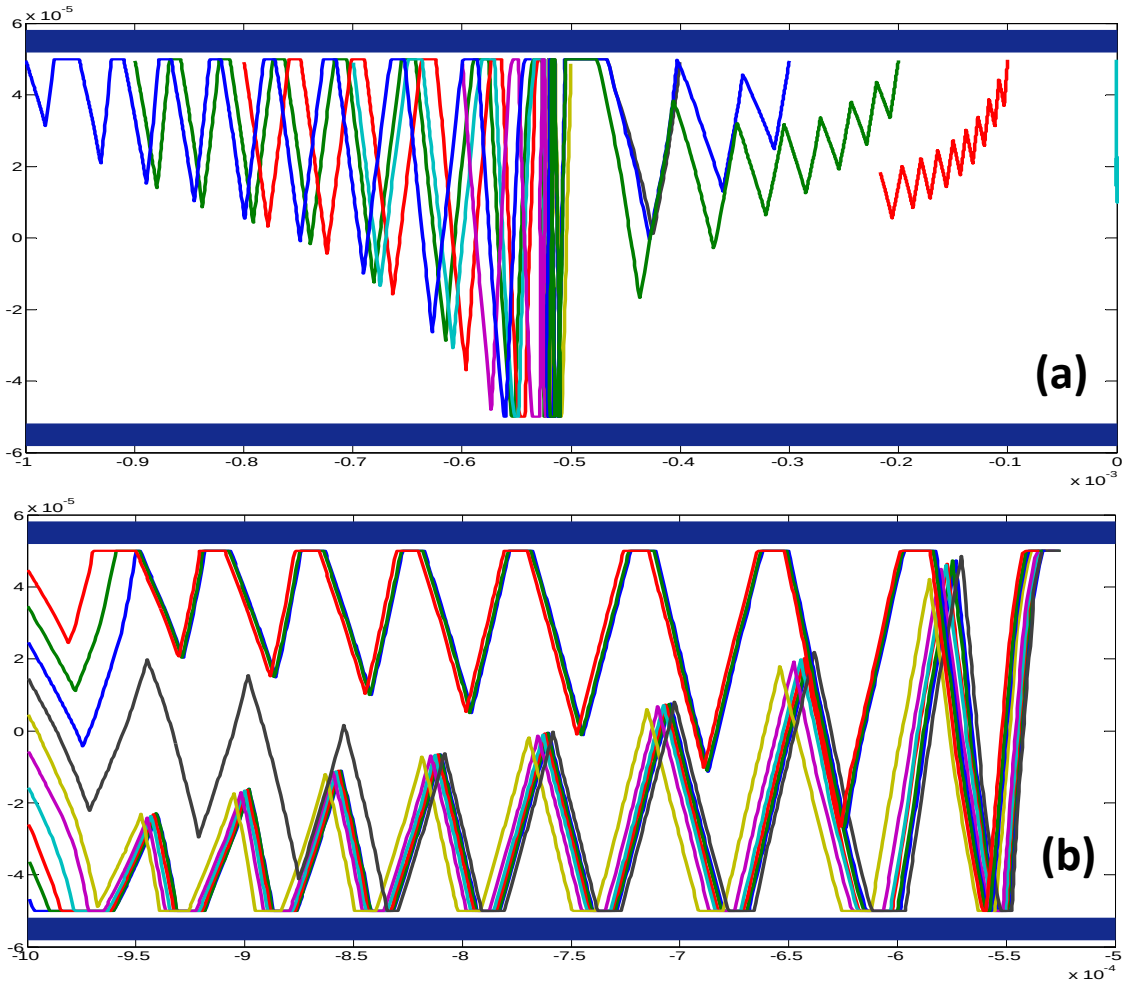

Figure 5.6. Simulation result of bead trajectories for beads of 3µm in diameter. a) Vertical study. b) Horizontal study

Horizontal velocity indicates that after 200 sec, all particles are collected at inner edge of the coil. The average vertical velocity can be used to extract the optimum frequency of mixing. Since magnetic beads within the chamber are acted upon by two coils, each stream of beads needs to travel at least half the chamber depth during activation time. In this case that the depth of travel is 50µm, the minimum activation time is 10 second. This activation time results in travelling distance of 50µm in vertical direction. Activation time of less than 10 second will increase the stretch and folding of magnetic beads in zigzag path, but reduces the efficiency of mixing by reducing the chamber coverage. Higher activation times might increase the surface coverage by cross mixing of two bulk of beads, but decrease the stretches and folding. Stretch and folding describe the number of times beads are attracted to each coil. The higher this number, the higher the chance of DNA/Bead binding.

In another simulation, a total number of 500 beads ($5 \times 10^{14}\ particles/m^3$) were placed inside the chamber in a uniform distribution to cover the whole surface area, from centre of the chamber to one end of the chamber. The horizontal and vertical distances between neighbouring beads were $20\ \mu m$ and $10\ \mu m$ respectively. Simulation time was set to three minutes and conditions were similar to the previous simulation. The result of particle trajectories is shown in Figure 5.7.

On the conductor surface, beads are divided into two groups. The numbers of beads attracted to the top electrode are more than the number of beads attracted to the bottom electrode. This is because the simulation was started by top electrode, and thus more beads end up at this electrode. In central part, beads show lower surface coverage as the magnetic force is weaker in this area. Colour intensity describes the total surface coverage and explains that bead density increases in the vicinity of inner edge of conductors. This is because beads tend to travel toward this point.

Figure 5.8 shows snapshot of beads' position in different times. A set of 20 beads in two columns are positioned at one end of the chamber. Positions of beads are captured from the start of simulation to the end at 30 second time intervals. Bead behaviour can be explained in four different stages as follow:

1. Initial position: this step is shown with blue dots and explains the primary uniform distribution of magnetic beads.

2. Transient mode: where the beads start to rearrange themselves into two different groups (red and green dots).
3. Steady state mode: in this mode all beads are divided into two groups (brown, magenta and cyan dots). Each group is attracted to one individual coil and beads will move in a parallel path to each other.
4. Clump mode: this mode takes place in the vicinity of inner edges of coils. In this mode two different bulk of magnetic beads merge together and bounce between two coils together (yellow dots).

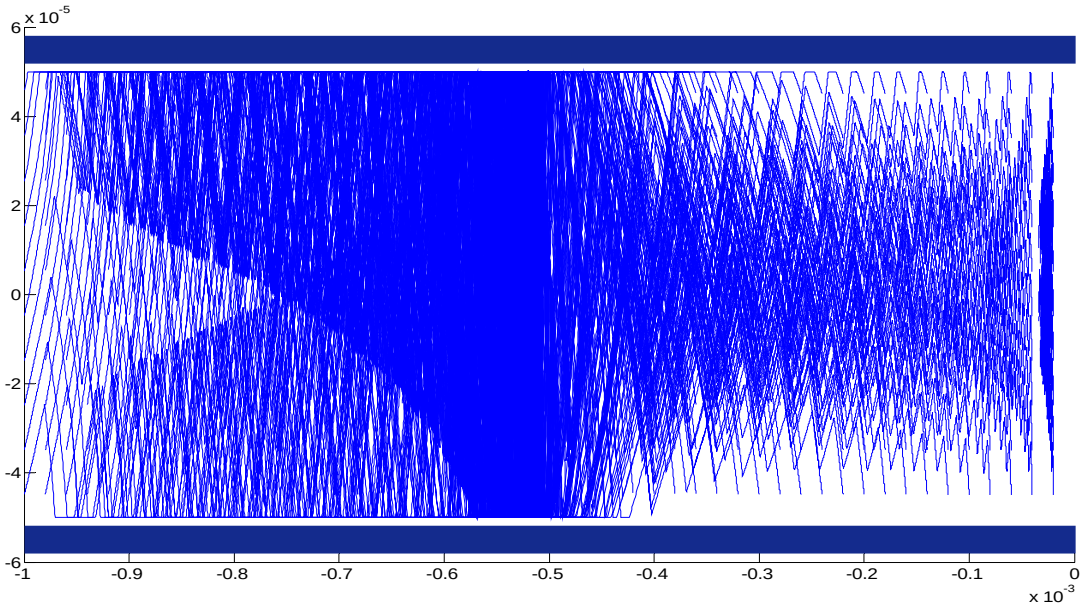

Figure 5.7. Cross-sectional view of bead trajectories for 500 beads in half-chamber for a period of 3 min and switching frequency of $f = 0.05\ Hz$. The colour intensity describes the surface coverage.

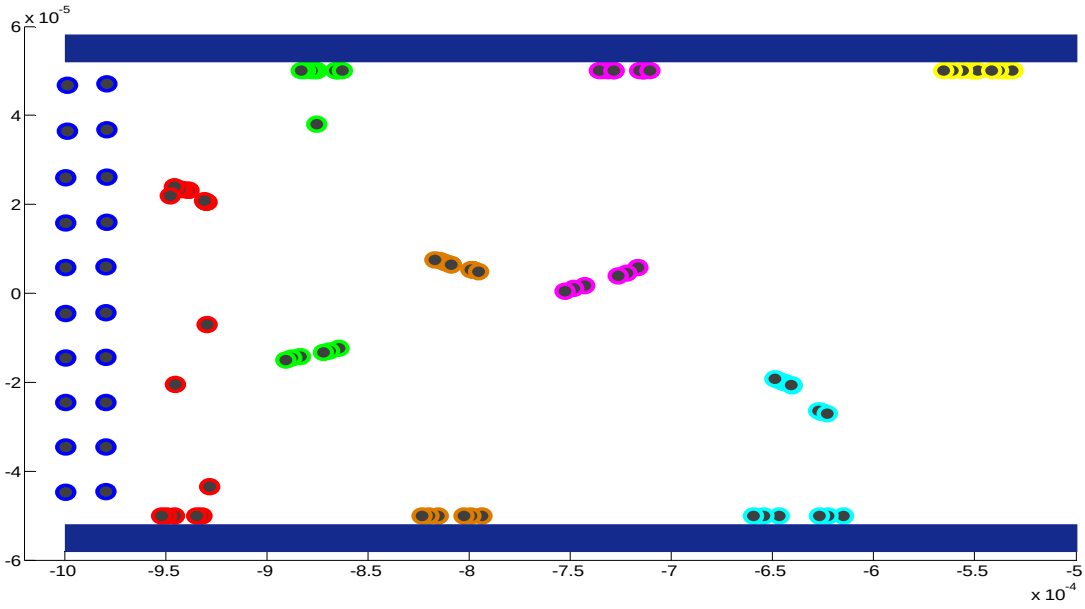

Figure 5.8. Snapshot of beads position at different time (30 sec intervals).

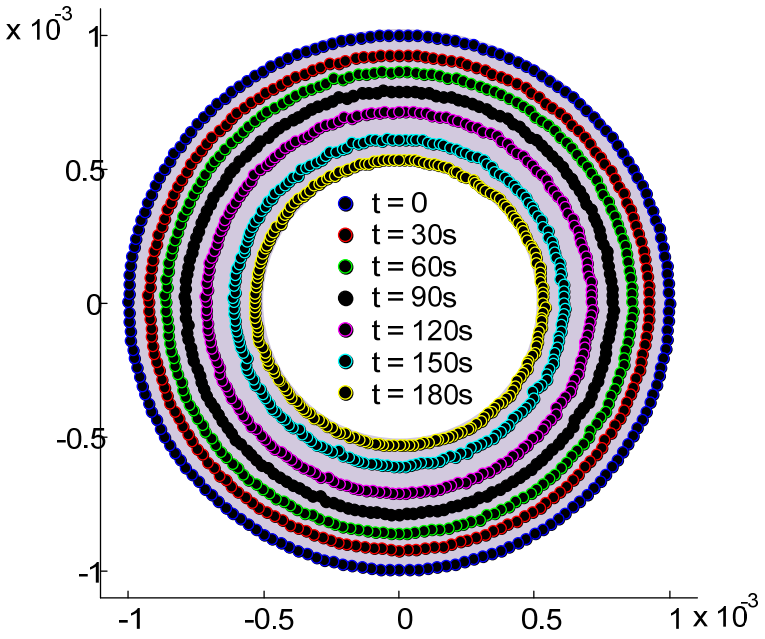

Figure 5.9. Surface plot of magnetic beads trajectories from outer section of the coil toward centre in different times (30 sec intervals).

Figure 5.9 shows a different view of beads' migration toward the centre captured from top of the chamber. A total number of 320 magnetic beads were placed at outer diameter of the chamber between two coils. Coils were activated in sequence with frequency of $f = 0.05Hz$. Positions of beads were captured in 30 sec time intervals and are shown in different colours. Pattern of movement is similar to a series of concentric circles. All magnetic beads were collected at inner edge of the coil in 180 second.

5.4.4 Evaluation of Surface Coverage Using Target Molecule Capturing

In order to evaluate the efficiency of mixing using the above simulations, a Matlab code was developed to investigate the surface covered by magnetic beads trajectories. By using this calculation it was possible to identify the number of target molecules that can be captured using the mixing pattern described above. To perform this calculation, total mixing surface was assumed to be covered by target molecules. In order to capture more accurate result, dimension of target molecules assumed to be negligible compared to dimension of beads. Magnetic bead captures target molecule, if they make physical contact along bead trajectory path. A number of 500 beads were uniformly distributed inside the chamber in a 2D cross-sectional plane. This plane was limited by conductor surface on top and bottom. The horizontal and vertical distances between neighbouring beads were 20 μm and 10 μm respectively.

Figure 5.10 shows the result of simulation inside the chamber working area. Blue dots describe the areas not covered by bead trajectories and therefore, no target molecule will be captured in these areas. As it is shown in this plot, majority of un-captured molecules appear on chamber outer diameter and in the central part. This is the area that magnetic force strength is weak and velocity of beads is minimal. On the other hand, capturing increases toward coil's inner edge, where all bead will be collected. This is because the natural direction of bead flow is toward this area. Calculation shows that surface coverage is, $CF = 87.54\%$ with this pattern of beads flow. In order to evaluate the effect of bead concentration on capturing efficiency, simulation was repeated with different numbers of beads and capturing efficiency was recorded (Figure 5.11). In these simulations, distribution of beads is not uniform and they are placed at one end of the chamber, where the magnetic force is minimal.

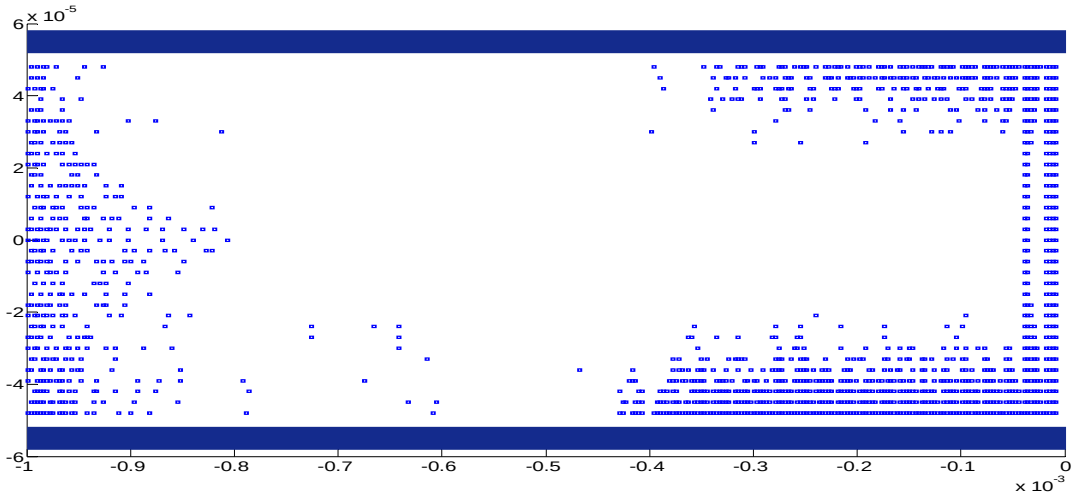

Figure 5.10. Simulation result of surface coverage by beads trajectories (blue dots show the areas not covered by beads).

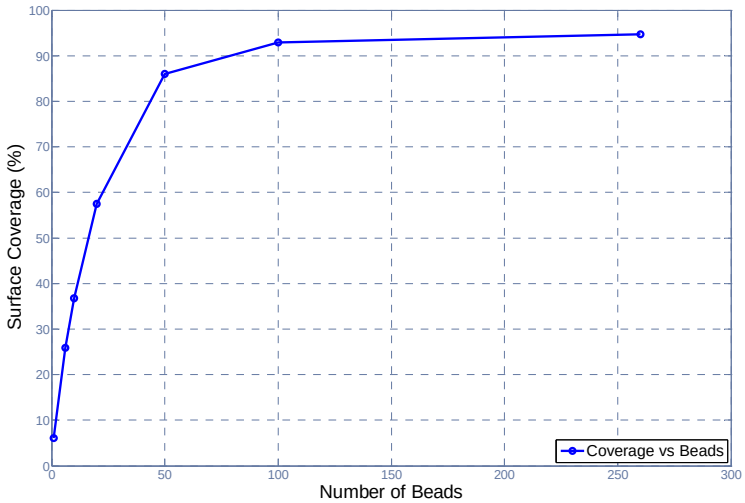

Figure 5.11. The relationship between surface coverage and number of beads if they are placed at one end of the chamber.

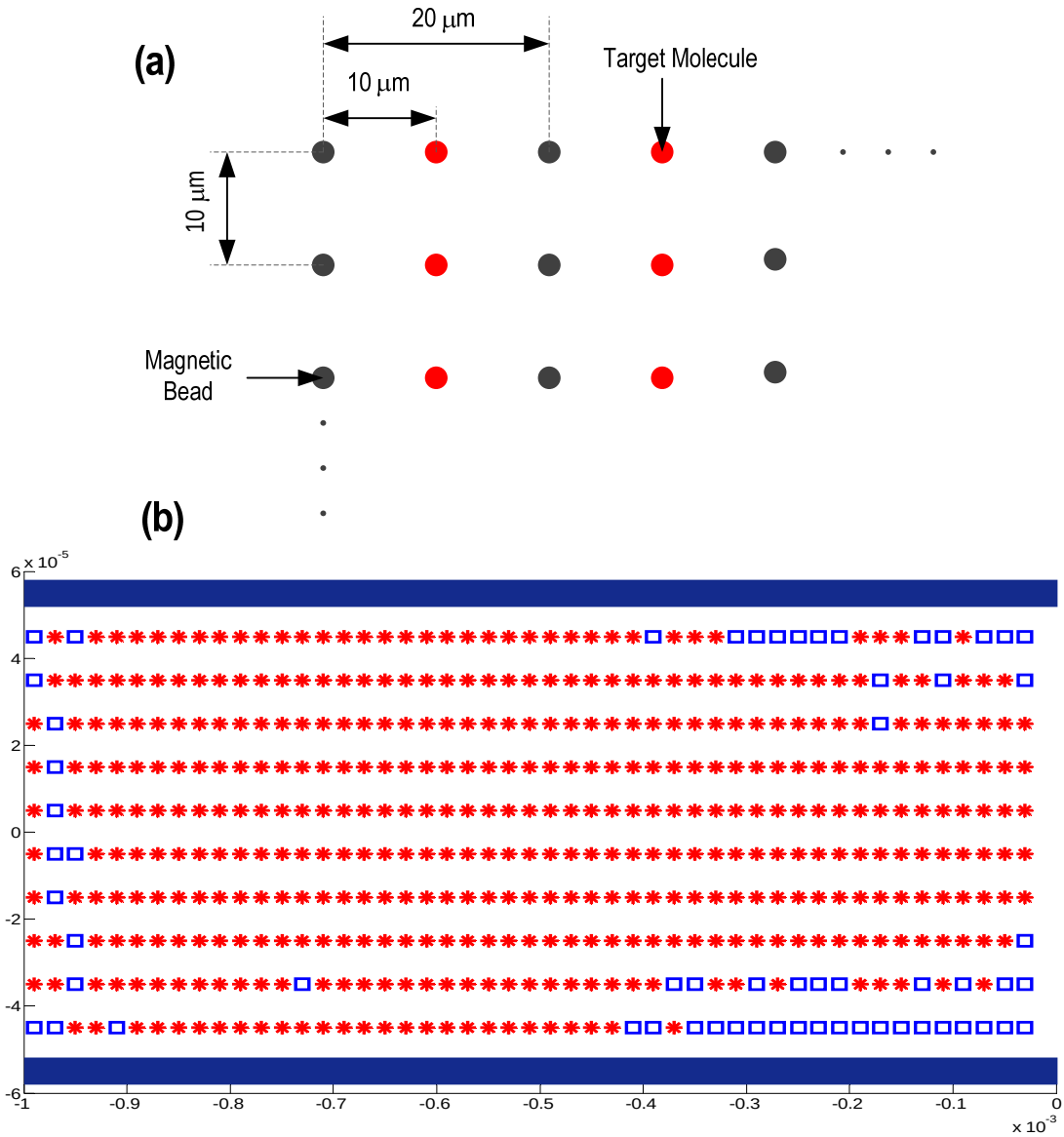

Figure 5.12. Target molecule capturing simulation. a) Detail of magnetic bead and target molecule distributions. b) The result of capturing simulation using a total number of 500 beads and 490 target molecules. Red dots show the captured molecules by beads and blue squares show uncaptured molecules.

The graph of Figure 5.11 shows that even with lower concentration of beads it is possible to achieve high surface coverage, if these beads are placed at the chamber outer diameter.

To evaluate the surface coverage efficiency, a total number of 500 beads and 490 target molecules were distributed uniformly inside the same surface area (Figure 5.12a). The result obtained shows that 429 target molecules were captured by magnetic beads (red stars) and 61 molecules (blue squares) were not captured (Figure 5.12). This gives the capturing efficiency of 87.55%, which is in close agreement with the result of total surface coverage calculated above.

5.5 External Coil

A stronger magnetic field can be generated using external arrangement of the magnetic coils. Although the distance between the chamber surface and coil actual surface is very long ($\approx 500\ \mu m$), the bigger product of $Ampere \times Turns$ generated by this coil arrangement can compensate the strength of magnetic field. The performance of the external coil was investigated in *Chapter 4* and optimised dimensions were given in section 4.7.2. Based on these calculations, it was shown that square-shapes cross-section generates the optimum magnetic force with constant cross-section area ($W_S = t_S$). In addition, it was concluded that the magnetic force is maxima, if the value of coil conductor thickness (t_S) is equal to the value of the coil outer diameter (d_{out}). Therefore, the optimised range of coil conductor thickness can be explained by the value of coil external diameter and by the assumption of, $d_{out} = 2d_{in}$.

$$\frac{d_{out}}{4} < t_S < d_{out} \tag{5.17}$$

This equation shows the relationship between the conductor thickness of the coil and the outer diameter of the coil. The outer diameter of the coil can be defined by the total volume of the chamber. In this work, a typical small-volume chamber was selected to perform the bead trajectory study. Figure 5.13 shows a schematic diagram of the chamber using external coil arrangement. The chamber was $d_{out} = 8\ mm$ in diameter and $d_{ch} = 300\ \mu m$ in depth. The total distance between the chamber and coil surface was assumed to be $t_w = 500\ \mu m$. This thickness comprises the thickness of chamber walls on the coil side and the thickness of coil bobbin on the chamber side. To perform the beads trajectory study using this coil arrangement, the maximum current density needs to be extracted using thermal analysis.

5.5.1 External Coil Maximum Current Density

To extract the maximum current density of external coils, a thermal model was created using heat-transfer module of COMSOL Multiphysics based on the above geometrical details (as shown in Figure 5.13). The simulation was performed using two different coil conductor thicknesses (2 mm and 8 mm). The result of thermal analysis is shown in Figure 5.14 for different coil thickness. In these simulations coil

surface were assumed to be in direct contact with air at room temperature. As mentioned previously, an optimum temperature of $T_{ss} = 55\ ^{\circ}C$ is necessary during incubation process in the purification protocol. Therefore, the maximum current densities for two mentioned coils at the above temperature can be extracted from the graphs of Figure 5.14.

$$t_S = 2\ mm \rightarrow J = 1.45 \times 10^7\ A/m^2$$

$$t_S = 8\ mm \rightarrow J = 1.15 \times 10^7\ A/m^2$$

Obviously, these current densities are much less than the current capacity of internal coil. This is because the ratio of heat dissipation in internal coil is much higher due to the larger coil surface to volume ratio.

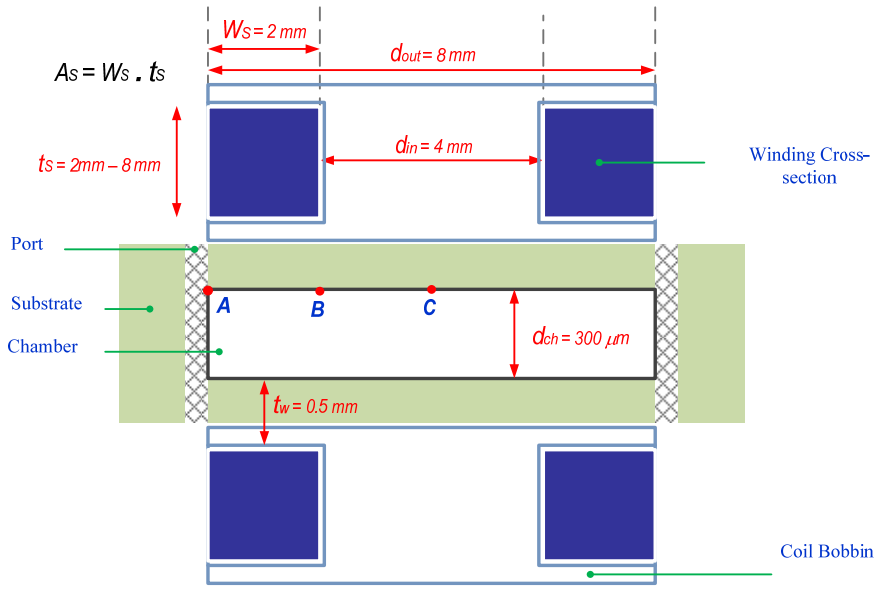

Figure 5.13. Schematic diagram of cross-section view of coil arrangement in external coil setup.

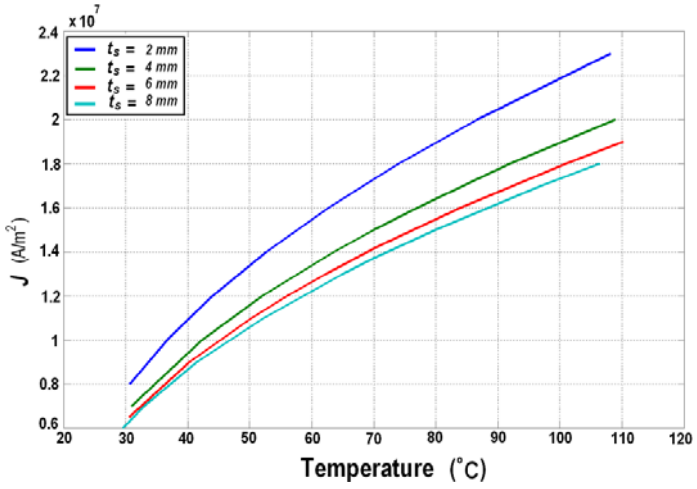

Figure 5.14. Steady-state thermal analysis on external coils for different coil thicknesses.

As discussed in *Chapter 4*, section 4.7.2, the magnitude of force generated by coil with 8 mm in thickness was twice as the magnitude of force generated by square cross-section coil. This conclusion was made by the assumption of equal current densities passing through the conductors. However, the result of thermal analysis indicated that the maximum current capacity of 8 mm thickness coil ($\boldsymbol{t_S = 8\ mm}$) is lower by a ratio of 20.7%. Since the strength of magnetic force is proportional to the square of electric current (Equation (4.7)), the relationship between the magnetic force of two above coils can be calculated as:

$$\boldsymbol{F_m(t_S = 8\ mm) \cong 1.26 F_m(t_S = 2\ mm)}$$

Which indicates that, the magnetic force generated by an 8 mm in thickness coil is 26% stronger than that of a 2 mm in thickness coil.

5.5.2 Particle Trajectory Using 3µm Diameter Beads

Based on maximum current density a simulation was carried out using Matlab software in order to investigate bead trajectories inside the chamber. Chamber and coil dimensions were selected as proposed in Figure 5.13 using the coil with conductor thickness of $t_S = 2\ mm$. Two-dimensional plots of some bead trajectories are shown in Figure 5.15a in half-chamber (across A-C line, as shown in Figure 5.13). Coil switching frequency and total activation time were kept similar to that of the internal coil simulations, $f = 0.05Hz$ and 180 second respectively.

Beads vertical and horizontal velocities show significant improvement compared to internal coils as the magnitude of magnetic force is much stronger here. However, the ratio of bead horizontal movement compared to the chamber size seems to be lower here. This is because the chamber diameter is four times bigger than the chamber used for internal coil arrangement. To collect all the beads in the inner edge of the chamber a mixing time of 720 second is necessary, which is four times longer than that of the internal coil arrangement.

Another simulation was carried out by increasing the thickness of coil to $t_S = 8\ mm$ to investigate the effect of coil thickness in improvement of magnetic bead trajectories. The results of this simulation are plotted in Figure 5.15b. The simulation was carried out for a period of 180 sec and current density of $J = 1.15 \times 10^7\ A/m^2$.

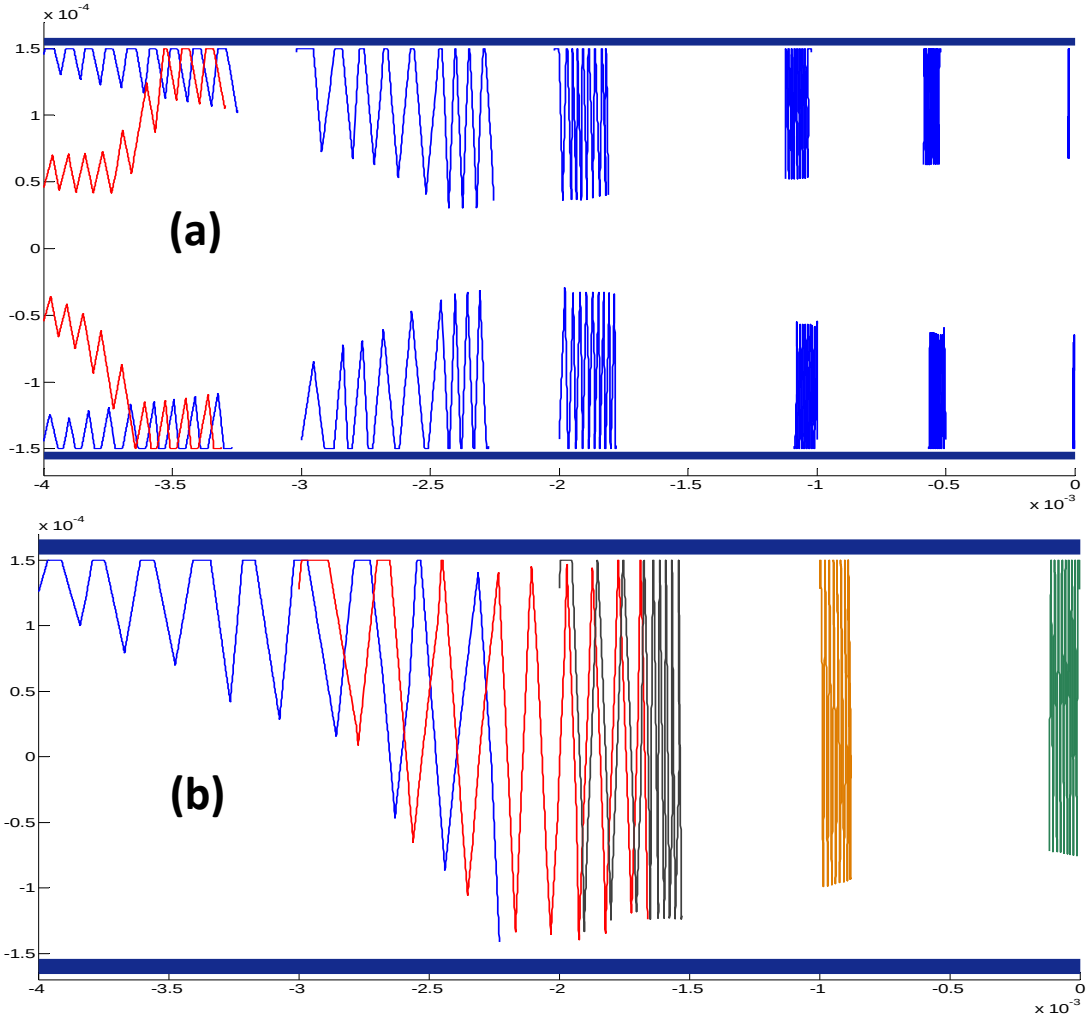

Figure 5.15. Bead trajectory simulations using external coil arrangement inside a 300µm deep chamber at switching frequency of $f = 0.05\ Hz$. a) $t_S = 2\ mm$ and $J = 1.45 \times 10^7$. b) $t_S = 8\ mm$ and $J = 1.15 \times 10^7$.

The results of these simulations show that the vertical and horizontal velocities of the magnetic beads are improved significantly using 8 mm in thickness coil. This is the result of increase in the strength of magnetic force due to the higher value of *Ampers×Turns* product.

Although the overall beads behaviour in these simulations is very similar to the internal coil arrangement, the ratios of vertical and horizontal velocities are changed significantly. The horizontal movement of particles is affected in two different ways. The ratio of horizontal velocity in the area covered by the surface of the coil conductors is increased significantly. On the other hand, the horizontal velocity of magnetic beads in the centre of the chamber is decreased.

In areas covered by actual coil conductor surface, the region of higher magnetic flux density shifts towards the centre of the coil as the result of increase in the thickness

of the coil compared to the thickness of internal coil. This will consequently increase the horizontal gradient and therefore, particle horizontal velocity in this section.

The lower horizontal velocity in the centre of the chamber can be explained considering magnetic flux density pattern of coils at different levels. Figure 5.16 shows magnetic flux density of external coil at different heights above the coil surface. In the vicinity of coil surface ($h = 50\ \mu m$), there are two peaks of high flux density above the coil inner edges, which gradually decrease toward the centre of the chamber. This gradient generates the horizontal factor of vector magnetic force. By moving away from the surface of the coil, the magnitude of flux density at these peaks decreases quicker than other areas. This will reduce the gradient of horizontal force in the central part. Therefore, at the height of $h = 650\ \mu m$, which is the centre of the chamber and the midpoint between two coils, the horizontal gradient is very low (as shown by Cyan-line in Figure 5.16). This low horizontal gradient explains the lower horizontal bead velocity in this area. However, the magnitude of vertical force is almost uniform in the whole surface at central part of the chamber. Another interesting information, which can be extracted from graphs of Figure 5.16 is that at a specific distance from the surface of the coil ($h = 1150\ \mu m$), the horizontal gradient will be inverted and shifts toward the center of the chamber. In this case, the peak of magnetic force is moved to the center and all magnetic beads will be collected at this point instead of coil inner edges.

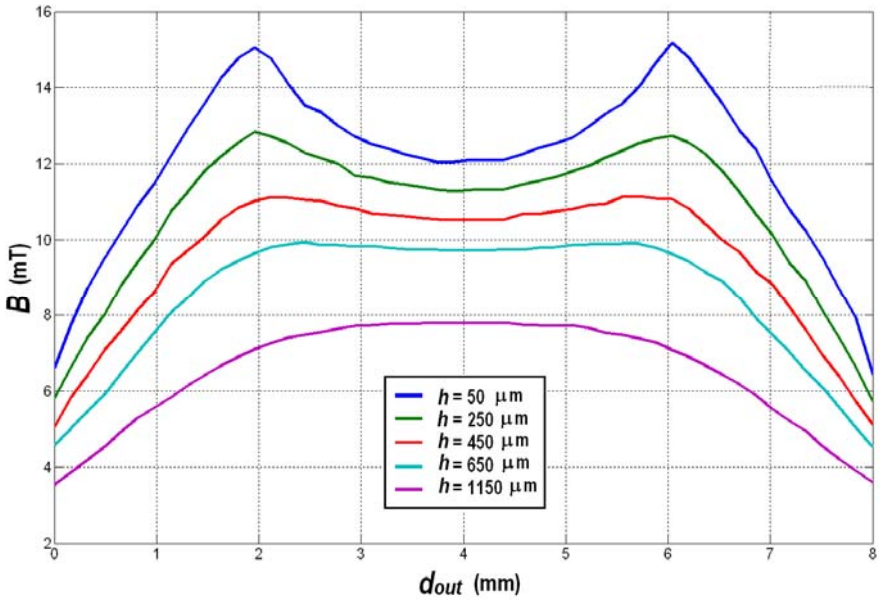

Figure 5.16. A plot of magnetic flux density of an external coil, at different heights above the coil surface. This graphs show the variation of magnetic field gradient against vertical heights (h).

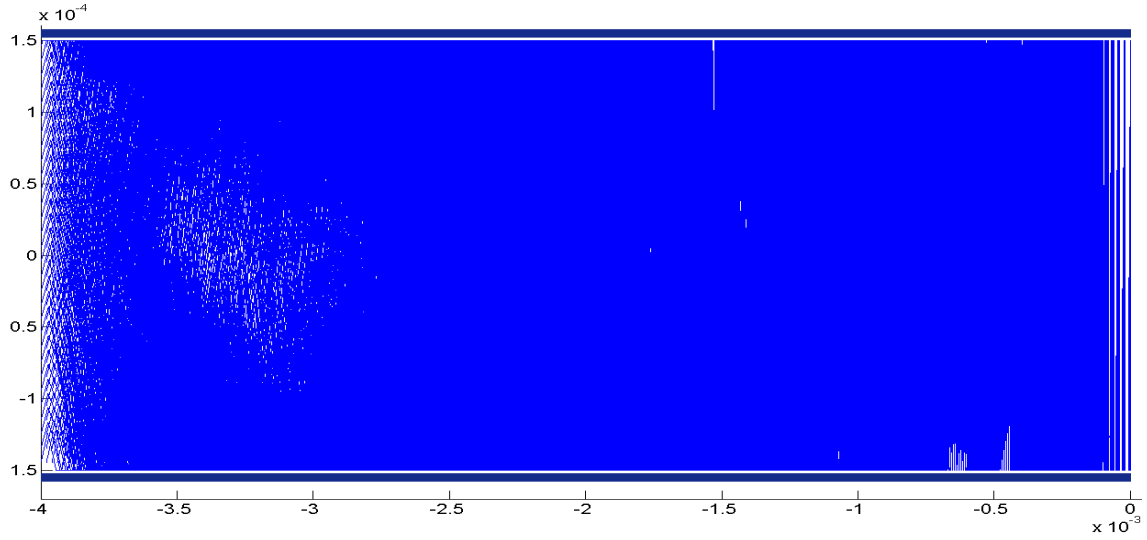

Figure 5.17. Cross-sectional view of bead trajectories for 6030 number of beads in half-chamber for period of 3 min.

5.5.3 Calculation of Surface Coverage Using External Coils

To calculate the surface coverage ratio with external coil arrangement, a total number of 6030 particles were placed uniformly inside one side of the chamber. This particle distribution gives a total density of $5 \times 10^{14} m^{-3}$. Whole chamber area was assumed to be fully covered by dimensionless target molecules. The bead trajectories are shown in Figure 5.17. Blue colour intensity shows the covered areas by bead trajectories and white colour intensity denote uncovered areas. The result of surface coverage calculation shows that 99% of the surface is covered and target molecules will be captured in these areas. This calculation was based on 180 second coil activation time, switching frequency of $f = 0.05\ Hz$ and maximum current density of $J = 1.15 \times 10^7$ using 2 mm thickness coils.

5.6 Summary & Discussion

The purpose of this chapter was to investigate the magnetic beads trajectories inside the proposed DNA Purification chip. This chip consists of at least a microchamber sandwiched between two magnetic coils in internal or external arrangements (as illustrated in Figure 5.4 and Figure 5.13). In order to investigate the efficiency of mixing DNA molecules and magnetic beads, a magneto-hydrodynamic model was introduced. This simplified model was based on two-phase-flow and one-way-coupling. In this model, magnitudes of different forces were discussed and it was concluded that gravity force of particle's mass can be ignored in comparison to

typical magnetic force. Therefore, magnetic force and fluid viscous drag force were the most effective force factors on particles. Particle trajectories were simulated based on maximum current capacity of coils in two different scenarios, internal and external coil arrangements. Current capacities were extracted based on thermal analysis. Internal coil represented higher current capacity due to the higher heat dissipation ratio from the surface of the coil. The optimal internal coil dimension of, $d_{out} = 2\ mm$ was selected to perform the beads trajectories study in a chamber with depth of,$d_{ch} = 100\ \mu m$. Since the thickness of external coil is not limited, coil dimension depends on the usage limitations. In this Chapter, typical 8mm in diameter coils were used for particle trajectory study. Since the magnitude of magnetic force is stronger with external coils, chamber depth was increased to 300 µm. Surface coverage was introduced as the ability of magnetic particles to cover the whole chamber area. The related simulation result shows the the percentage of target molecules that will be captured by magnetic beads during migration from their original place toward the chamber centre. Simulation results showed that surface coverage of internal and external coil arrangements were 87.55% and 99% respectively. While both coil arrangements represent sufficient magnetic force pattern to capture high yield of DNA molecules, some advantages and disadvantages of both scenarios are summarised as follows:

Internal coil advantages

- Small size and can be fully integrated
- High surface coverage and high DNA capturing ratio
- Simple fabrication process using key-type electrodes
- Higher current capacity due to the larger surface area
- Can be used for small scale purification process

Internal coil disadvantages

- More fabrication complexity in comparison to external chamber design
- The maximum chamber depth is in order of 100 µm, which increases the risk of bead coagulation and might result in chip blockage
- Application of large scale purification results in very wide chamber and complicates fabrication of electrodes
- Cannot be used for bigger particles due to the limited chamber depth

External coil advantages

- Can be used for larger volume chambers
- Higher magnetic force pattern can be achieved
- Beads can be mixed at higher frequencies
- Simple chamber fabrication process
- Higher surface coverage and DNA capturing
- Ability to be used for bigger magnetic particles which results in higher frequencies and stronger magnetic forces. This is because of bigger chamber depth, which decreases the risk of bead coagulation or clumping
- Maximum current density can be increased by increasing heat dissipation ratio. This can be achieved by designing an appropriate heatsink on coil bobbins.
- While the microfluidic chip must be disposable, external coils can be reutilised.

External coil disadvantages

- Although external coil generates very high magnetic force, the actual distance between coil surface and working chamber compromise this benefit to some extent.
- Larger chip and coil dimensions, in comparison to internal coil setup.

Most DNA extraction protocols use higher buffer/blood ratios. The actual volume of blood that can be used for extraction is typically between 20%-25% of the chamber total volume. Therefore, the maximum blood sample that can be used in internal-coil microchamber is limited to a few microliters. In majority of DNA purification processes, larger blood sample volumes increase the chance of capturing pathogenic DNA molecules. Therefore, external-coil microchamber, which is more flexible on the chamber size and volume, is more desirable. However, the application of internal-coil microchamber remains limited to some specific areas, which need smaller sample volumes and more compact chip sizes.

CHAPTER 6

EXPERIMENTAL VALIDATIONS

6.1 Introduction

Design of a magnetic mixer using internal and external coils was performed in *Chapter 4* and optimised coil and chamber dimensions were extracted using finite element numerical simulations in COMSOL Multiphysics. These optimised dimensions were used to evaluate the performance of magnetic mixing by means of bead trajectory study and subsequent target molecule capturing in *Chapter 5*. A preliminary electro-thermal model was built to estimate the maximum current density in both coil-arrangements. It was concluded that external coil arrangement exhibits better performance in magnetic mixing, bio-molecule capturing and minimises the risk of bead coagulations (clumping). Therefore, external coil arrangement was selected in order to perform real biological DNA extraction/purification tests. To perform the real-sample experiments, it is necessary to validate the accuracy of simulation carried out in previous chapters. This chapter is entirely dedicated to pre-experimental validations of simulation studies. Optimal conditions as a result of simulations and pre experimental validations will then be

used in the following *Chapter 7* in real biological DNA extraction/purification experiments. The actual parameters that were selected for validation are listed below:

- Magnetic Field Strength
- Coil Temperature
- Beads Trajectories
- AC and DC Electric Currents
- Frequency of Switching

In addition to above validation experiments, DC magnetic field required for in-chamber clamping of magnetic beads was also extracted. This is an important step during the washing process to hold the DNA-attached beads in the chamber, while flushing the cell debris, etc. Finally, a set of microfluidic studies were carried out to investigate the limitations of sample feeding into the microfabricated chamber and proper washing process.

6.2 Magnetic Field Measurements

6.2.1 Experiment Setup

Since the base for all previous simulations, in COMSOL Multiphysics, is the magnetic field strength, the first parameter that needs to be validated is the strength of magnetic field. This measurement was performed using a magnetometer. Figure 6.1 shows a photograph of the DC magnetometer (*Alphalab, Inc*.) that was used in this experiment. This magnetometer has the minimum resolution of 0.01 gauss (1 μT), which is 1/50 of the earth's magnetic field. The maximum range of this meter is 20,000 gauss (2 Tesla). This magnetometer has a universal Hall Effect sensor, which has 1.1 mm thickness and 4.3 mm width. A series of different size bobbins were made in order to wind external coils. These bobbins are shown in Figure 6.2, and their characteristic details are given in Table 6.1. The type of wire used for coil winding was copper wire, gauge 42 (SWG #42) with circular cross-section of 101.6μm. It is possible to use different wire gauges, but the higher the wire gauge is, the thicker the wire insulation and the higher the current supply should be.

Three different types of bobbin were made using PMMA and aluminium. The width of winding was kept at, $W_S = 2\,mm$, which gives an overall outer diameter of, $d_{out} = 8\,mm$. Different coil heights of, $t_S = 2\,mm$, $t_S = 4\,mm$ and $t_S = 6\,mm$

at the same coil outer diameter were fabricated and used for the tests. Since the coils were manually winded, different numbers of turns were achieved in the same bobbin dimension. The average number of turns counted on each coil is given in Table 6.1.

Figure 6.1. A photograph of the magnetometer used in the experiment to measure the magnetic flux density of external coils.

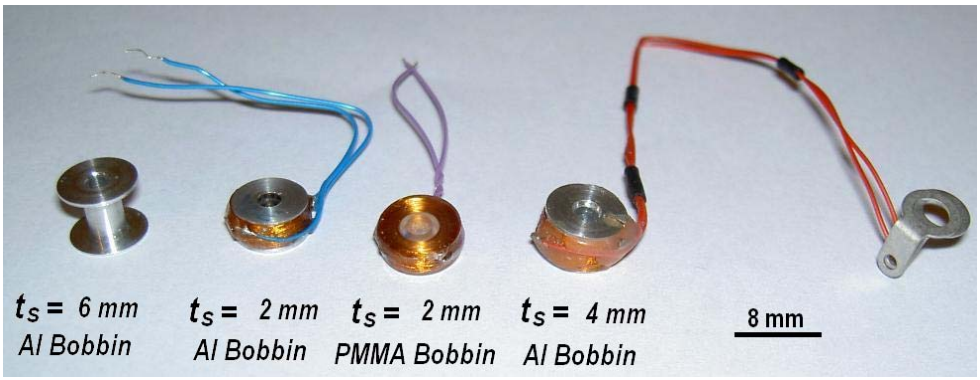

Figure 6.2. A photograph of different external coils.

Table 6.1. Characteristic information of different winded coils.

Coil Number	**2×2**	**2×4**	**2×6**
Coil Thickness (t_S)	2 mm	4 mm	6 mm
Coil Outer Diameter (d_{out})	8 mm	8 mm	8 mm
Winding Width (W_S)	2 mm	2 mm	2 mm
Electric Resistance (R_S)	15.4 Ω	32.7 Ω	49 Ω
Bobbin Cheek Thickness (t_{cheek})	500 µm	240 µm	250 µm
Bobbin Material	Al/PMMA	Al	Al
Average Number of Turns (n)	360	750	1100

Calculation shows that total conductor cross section in each bobbin are $2.83\ \mu m^2, 5.89\ \mu m^2\ and\ 8.64\ \mu m^2$ in 2×2, 2×4 and 2×6 bobbins respectively. The total conductor cross-section that was used in simulation was $4\ \mu m^2, 8\ \mu m^2\ and\ 12\ \mu m^2$ for the above coil bobbins. The difference between experimental and simulation is the actual dead-space in windings. A part of this dead-space arises from the insulation layer of the copper wire. The other part is the space between circular wire cross-sections. Consequently, these dead-spaces reduce the effective total cross-sections by 29.25%, 26.4% and 28% in 2×2, 2×4 and 2×6 coils respectively. The thickness of bobbin's cheek was narrowed down to 500 µm in PMMA bobbin and 250 µm in aluminium bobbins. Since the rigidity of PMMA is not as good as aluminium, a lower thickness is not suitable to hold the windings and might be deformed during winding.

6.2.2 Magnetic Flux Measurement

Based on practical limitation of coil winding, a corrected COMSOL magnetic model was prepared to simulate magnetic flux densities of coils 2×2 and 2×4. This model had exactly equal number of turns compared to winded coils, as given in Table 6.1. Since the magnetometer's Hall Effect sensor is covered by a protection rubber, this rubber thickness was accurately measured ($t_r \cong 500\mu m$) in order to calculate the actual distance of sensor from the surface of the coil. These distances were $h = 1\ mm$ and $h = 0.74\ mm$ for 2×2 and 2×4 coils respectively. The results of simulations and experimental measurements using magnetometer are shown in Figure 6.3. These graphs show the variation of magnetic flux density against variation of electric current passing through copper wire gauge 42 (SWG #42). This comparison shows that, beside inter-windings dead spaces, experimental result is in very close agreement with the simulation results.

6.3 Thermal Measurements

The next parameter that needs to be validated using experiment is the amount of heat generated in conductors due to Joule heating. In the previous chapter, steady state temperature of coil was calculated with an assumption of direct heat dissipation from the conductor surface to the air at room temperature. This assumption is not valid in practice, since the actual windings need to be winded on a bobbin. In this section aluminium and PMMA bobbins were used for thermal experiments. Physical and thermal characteristics of copper, aluminium and PMMA are given in Table 6.2.

Table 6.2. Properties of materials used in thermal simulation.

Property of Material	Copper	Aluminum	PMMA
Thermal Conductivity K (W/m.K)	400	160	0.19
Density ρ (Kg/m^3)	8700	2700	1190
Heat Capacity at Constant Pressure C_p (J/Kg.K)	385	900	1420
Resistivity at Reference Temperature ρ_0 (Ω.m)	1.72×10^{-8}	-	-
Temperature Coefficient α (1/K)	0.0039	-	-

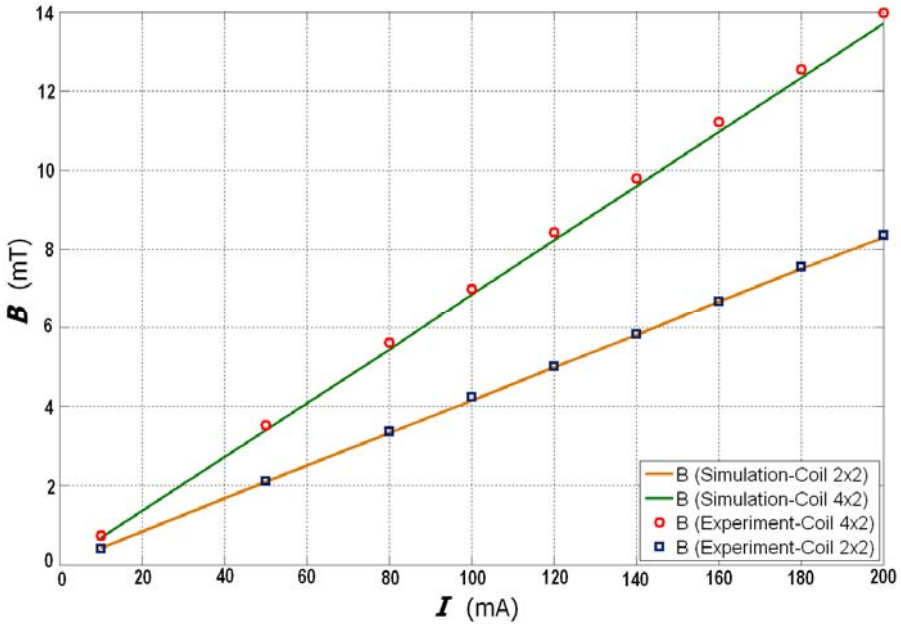

Figure 6.3. Result of simulation and experimental measurement of magnetic flux density.

6.3.1 Steady State Temperature in DC Current Mode

Based on practical limitation of coil winding, a corrected COMSOL model was created for (2×2) and (2×4) coils and steady-state temperature was recorded with different currents. This information is shown in Figure 6.4 (solid lines). The winded coils were used in order to repeat the same temperature recordings using a type *K* temperature sensor. These graphs are shown in Figure 6.4 for comparison (dashed lines). The experimental results are in close agreement with simulation results. In this experiment, coil (2×2) had a PMMA bobbin and coil (2×4) had an aluminium bobbin. Steady-state temperatures were recorded after 15 minutes activation time and between each reading the coil was allowed to cool down to room temperature (T_a = 20 °C). Based on this corrected model and experimental measurements, the maximum DC currents to be used in (2×2) and (2×4) coils are 107 mA and 84 mA respectively. These currents generate a steady state temperature of T_{ss} = 56 °C.

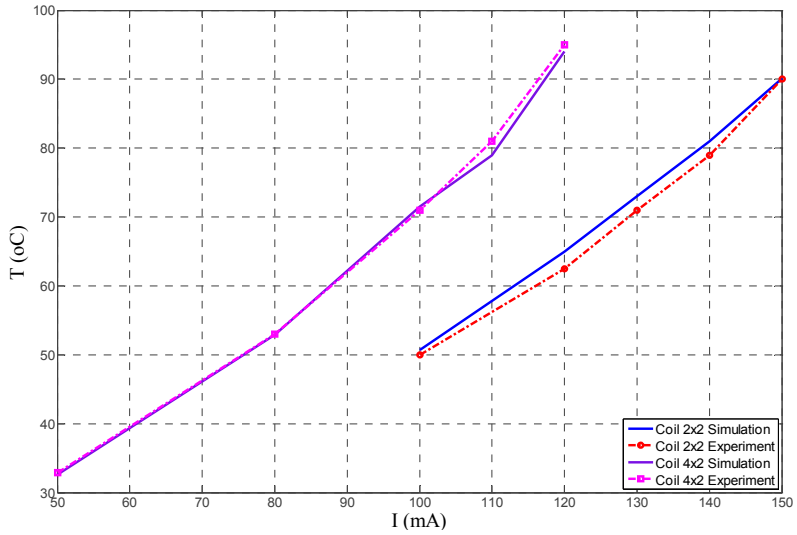

Figure 6.4. Steady state temperature comparison between simulation results and experimental measurements in DC current mode for different coils.

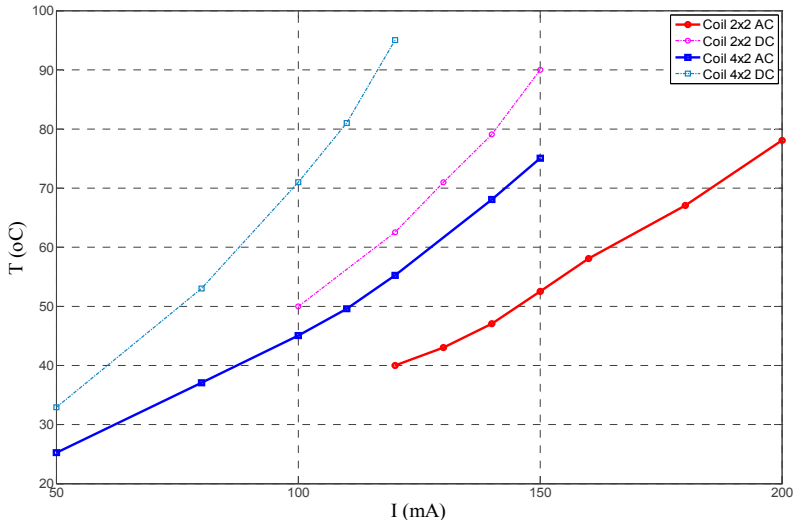

Figure 6.5. Steady state temperature comparison between simulation results and experimental measurement in AC ($f = 1\ Hz$) current mode for different coils.

6.3.2 Steady-State Temperature in AC Current Mode

In the above experiment, coils were activated using continuous DC current. Since these coils are designed to be used for mixing in AC switching current mode, it is worth looking at steady-state temperature in switching mode. Therefore, an experiment was conducted using the same coils under different switching currents and steady-state temperature was recorded. The frequency of switching was set to $f = 1Hz$ during measurements. This result is shown in Figure 6.5 (solid lines) in comparison with the graphs of temperature variations in DC currents mode (dashed lines). The maximum switching current increases to 155 mA and 120 mA for coils (2×2) and (2×4) respectively, to achieve temperature rise of $T_{ss} = 56℃$.

6.3.3 Effect of Additional Heatsink in Steady State Temperature

So far the steady state temperatures of magnetic coils were numerically calculated using simulations and this result was evaluated using handmade winded coils. Based on these results and required incubation temperature of $T_{ss} = 56℃$, the maximum switching currents were then extracted in different coils. With reference to earlier bead trajectory simulation results, these switching currents create enough magnetic force to perform desired mixing. In order to improve the efficiency of mixing, it is necessary to increase the frequency of mixing. The optimised frequency of mixing is a function of magnetic force strength and maximum current density. The maximum coil current is restricted by heat dissipation ratio from the surface of the coil. Therefore, it is necessary to investigate other options to improve the maximum current capacity of the coils.

In this section, the focus is to design a modified version of bobbin that performs more efficiently on dissipation of heat caused by joule heating in coils. This modified version of coils then perform better on AC current as well as DC current, where it seems to be the bottle-neck in clamping the beads inside the chamber. The most common methods of heat dissipations are through conductive cooling (e.g. application of appropriate heatsink) and/or convective cooling using forced fluid/gas flow (e.g. using a fan or oil cooling). In this section conductive cooling system was employed in order to investigate the efficiency of heat dissipation ratio. To investigate this, two modified version of aluminium bobbins were fabricated, which consisted of castellated heatsinks. These castellated heatsinks have the total-depth/teeth-depth ratios of 5 mm/2.5 mm and 6 mm/3.5 mm respectively. These heatsinks increase the total surface area by 3.3 and 4 times, larger than that of the normal bobbin type (see Figure 6.6a).

Figure 6.6 (b-g) shows a simulation result of the temperature distribution on different heatsink designs using coil (2×4) and coil (2×5). These simulations were carried out for two different DC currents of 100 mA (b, d and f) and 140 mA (c, e and g), and the results were compared with the normal bobbin type. This simulation shows that application of conductive cooling using embedded heatsink increases the heat dissipation ratio significantly. The average efficiency of heat dissipation is 0.22°C/mA and 0.17.5°C/mA for two heatsink bobbins of (2×4) and (2×5) respectively.

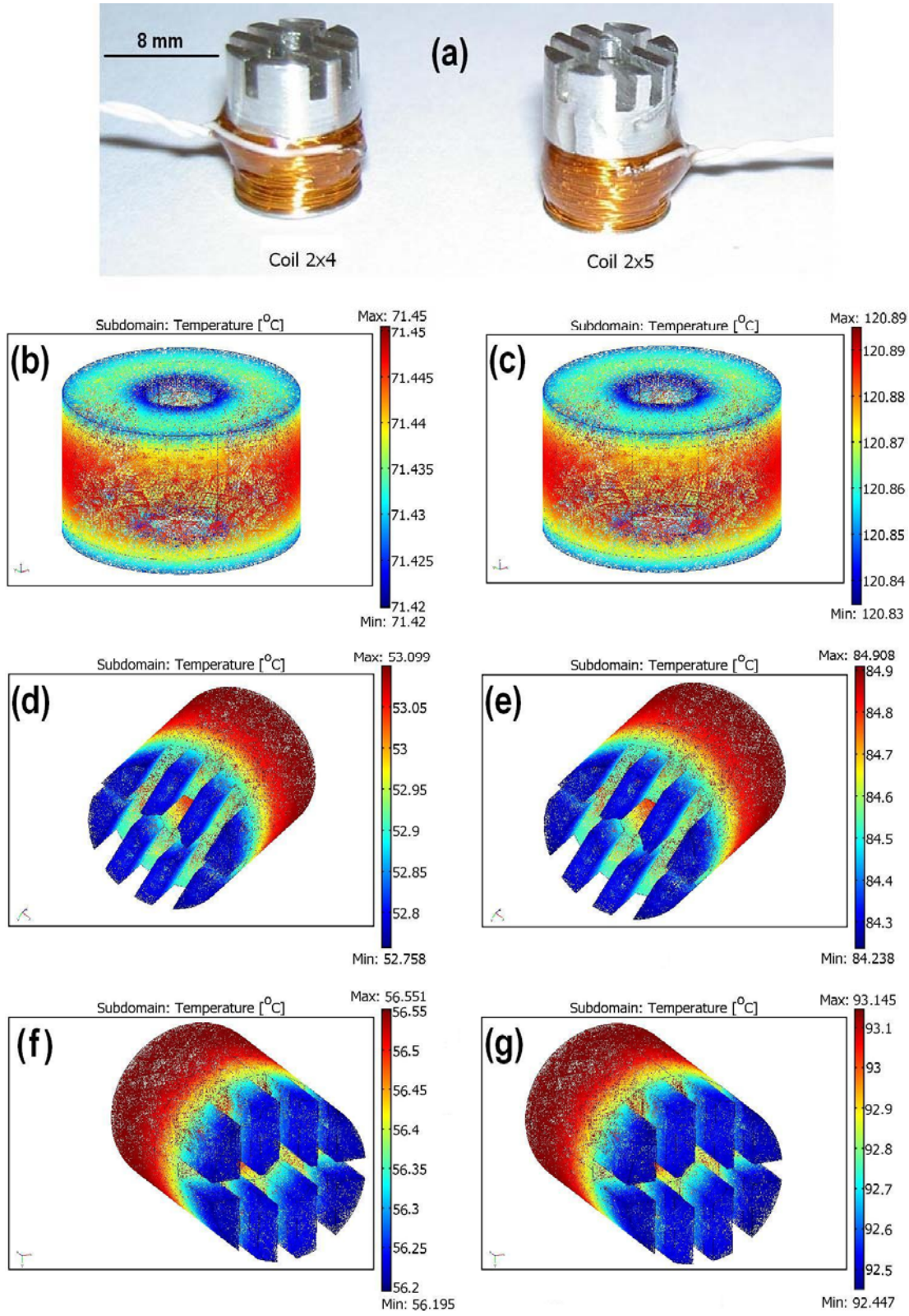

Figure 6.6. Simulation results of the temperature distribution on different heatsink coils, compared to the normal bobbin. a) A photograph of the fabricated winded heatsink coils. b) Normal bobbin (2×4), $I = 100\ mA$. c) Normal bobbin (2×4), $I = 140\ mA$. d) Heatsink bobbin (2×4), $I = 100\ mA$. e) Heatsink bobbin (2×4), $I = 140\ mA$. f) Heatsink bobbin (2×5), $I = 100\ mA$. g) Heatsink bobbin (2×5), $I = 140\ mA$.

Figure 6.7 shows a plot of experimental results carried out on two different heatsink coils. Characteristic details of these coils are given in Table 6.3. These graphs describe the variation of steady-state temperature in bobbins caused by Joule heating in AC and DC modes (solid lines). The efficiency of heatsink was compared with the normal bobbin shape (dashed lines). This experiment shows that the maximum DC current is increased to 105 mA and 100 mA for (2×4) and (2×5) heatsink coils respectively. The maximum switching currents are also increased to 155 mA and 145 mA for the above coils (dotted lines).

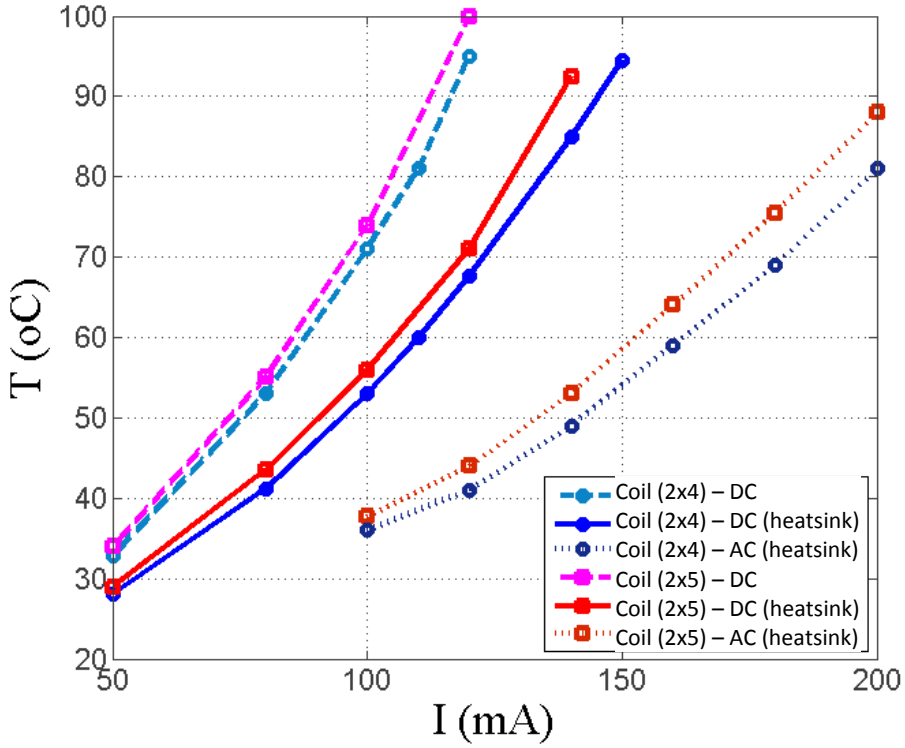

Figure 6.7. Experimental result of steady-state temperature measurements on different heatsink bobbins in AC and DC modes.

Table 6.3. Characteristic detail of different heatsink coils.

Coil Number	**2×4**	**2×5**
Coil Thickness (t_S)	4 mm	5 mm
Coil Outer Diameter (d_{out})	8 mm	8 mm
Winding Width (W_S)	2 mm	2 mm
Electric Resistance (R_S)	32.7 Ω	29 Ω
Bobbin Cheek Thickness (t_{cheek})	250 µm	250 µm
Bobbin Material	Al	Al
Number of Turns (n)	750	920
Heatsink Total Depth / Teeth Depth	5 mm / 2.5 mm	5 mm / 2.5 mm

Table 6.4. The values of maximum coil currents to maintain the steady-state temperature rise of 56°C.

Coil Number	DC Current (mA)	AC Current (mA)
Coil $(\mathbf{2 \times 2})$	107	155
coil $(\mathbf{2 \times 4})$	84	120
Heatsink Coil $(\mathbf{2 \times 4})$	105	155
Heatsink Coil $(\mathbf{2 \times 5})$	100	145

Since the efficiency of heatsink is a function of total surface area, it is not limited by geometrical shape and dimension. Therefore, design of heatsink can be modified to fit in the final DNA extractor device. Although the application of heatsink coil is desirable in switching mode, its more effective application is in DC current mode, which is used for clamping of the magnetic beads during washing process. In addition, DC current mode can be used to generate quadrupolic and solenoidal field patterns to increase the efficiency of the mixing.

Based on the above thermal measurements, the maximum electric currents were extracted for different coils at switching (AC) mode as well as continuous (DC) mode. This information is given in Table 6.4. These maximum currents were calculated based on the optimum temperature $T_{ss} = 56°C$, which is necessary for the incubation of blood/lysis buffer during extraction process. This temperature can be maintained by controlling the coil current using a thermocouple temperature sensor.

6.4 Fabrication and Experimental Setup

An experimental study need to be conducted in order to evaluate the efficiency of the magnetic force generated by external coils. This evaluation can divided into two different sections based on the application of AC and DC current modes as follows:

- Efficiency of magnetic mixing using bead trajectory study
- Bead harvesting efficiency using magnetic clamping of beads

In magnetic mixing study, it is necessary to have access inside the microchamber in order to capture response of beads to the viscous drag force and magnetic force. Due to the geometrical limitations, both top and bottom surfaces of the chamber are covered by magnetic coils. Therefore, to carry out this study, the only option is to model a portion of the cross-section of the chamber using a capillary microchannel. This will give enough access point across the diametric line of the microchannel and

coil. Since the magnetic force pattern is identical across concentric circular paths from the centre of the chamber and coil, this model gives accurate estimation of overall behaviour of the beads.

The magnetic bead harvesting study needs to be performed in full chamber due to the bulk effect of clumped beads and specific fluidic and geometrical influence on clamping efficiency. The access point in this study is from the top surface of the chamber. This is possible because during clamping process, only the bottom magnet is activated and the top magnet is switched off, thus can be removed.

A capillary test-rig was constructed to carry out preliminary bead trajectory experimental studies. An 8mm diameter (15 µl capacity) microfabricated microchamber with supplemental device docking station was made to be used for clamping experiments. A custom-designed power/control unit was designed and made to be used for activation of magnetic coils. The next section describes the experimental setup and detail of microfabrication of the chamber and other supplemental apparatus used in this study.

6.4.1 Microfluidic Chamber Fabrication

In order to investigate the magnetic clamping, a microchamber needs to be fabricated with appropriate microfluidic tubing and suitable docking station. The overall dimension and volume of the extraction chamber need to be designed based on each specific application. This variation in chamber size mostly will be reflected in chamber diameter rather than the depth. Due to the limitation in magnetic force penetration rate (field gradient), depth of the chamber is limited between 200 µm – 500 µm. Therefore, a small volume chamber was selected in this work to investigate the magnetic clamping efficiency. To reduce the dead-space, chamber diameter was set to 8 mm to fit in the active area of the same size magnetic coils (used for previous experiments and simulations).

A schematic diagram of the microchamber is depicted in Figure 6.8. The chamber was made form PMMA as core material, which possess high mechanical rigidity and is well known material used in microfluidic chips. PDMS, which is another well known bio-compatible material, was used to fabricate the internal surfaces of the microchamber. The chamber comprises three layers structure.

The middle part, which is in contact with bio-fluid, was made of PDMS that is sandwiched between two PMMA outer layers. PMMA was die-cut to accommodate the chamber and port vias. Since it is important to accommodate the external coils at the closest possible distance from the chamber, a 1mm sheet of PMMA was used for fabrication of outer layers. A recess was hot-embossed into the PMMA to provide an end-wall of approximately 250 μm thickness, and to form a cylindrical wall some 9 mm in diameter to accommodate the winded coils.

After embossing the two PMMA layers were micromilled (#73 drill) to create the porting. Four ports were initially designed for inlets and outlets. One port was designed for air vent, two ports for inlets (reagent and sample) and the last port for outlet. Two inlet and outlet port pairs were positioned at 180° angle around the circumference and were symmetrically positioned in a vertical line to create a T-shape junction.

A 12 mm diameter pitch circle was used for drilling the ports. A $300 \mp 15\ \mu m$ thick cast sheet of PDMS was then die-cut to fabricate the middle chamber layer. The necessary vias were made to link to the outer PMMA layers. It was initially intended to pressure-assemble and seal three layers by using two 1.6 mm diameter screws. This method failed to securely seal the device. Therefore, a thin layer of PMDS was coated on PMMA to act as a bonding agent.

The bonding of PDMS thin layer was made with an elastomer mix of 5:1 base/curing agent ratio, rather than usual 10:1 ratio. This new mixture ratio has lower viscosity and reduced cure time and most importantly improved bonding to PMMA. This PDMS mixture was left at room temperature for 1 hour before assembling the chip. After sealing, the sandwiched layers were placed between two aluminium blocks at 60 °C temperature for 1½ hour to cure the PDMS.

Port-way feeds were made from 6mm length stainless steel tubing set into 2.4mm×1mm polystyrene collars and drilled (#73) to form ferrules. The ferrules were then secured into the PMMA ports using epoxy resin. Finally, 100mm length, 250μm bore medical-grade PVC tubing was used to provide the microfluidic networks at inlets and outlets. A photograph of microfabricated microfluidic four-port chip is shown in Figure 6.9 with attached feed-line tubing.

This chip was made at *ChargeLabs.*

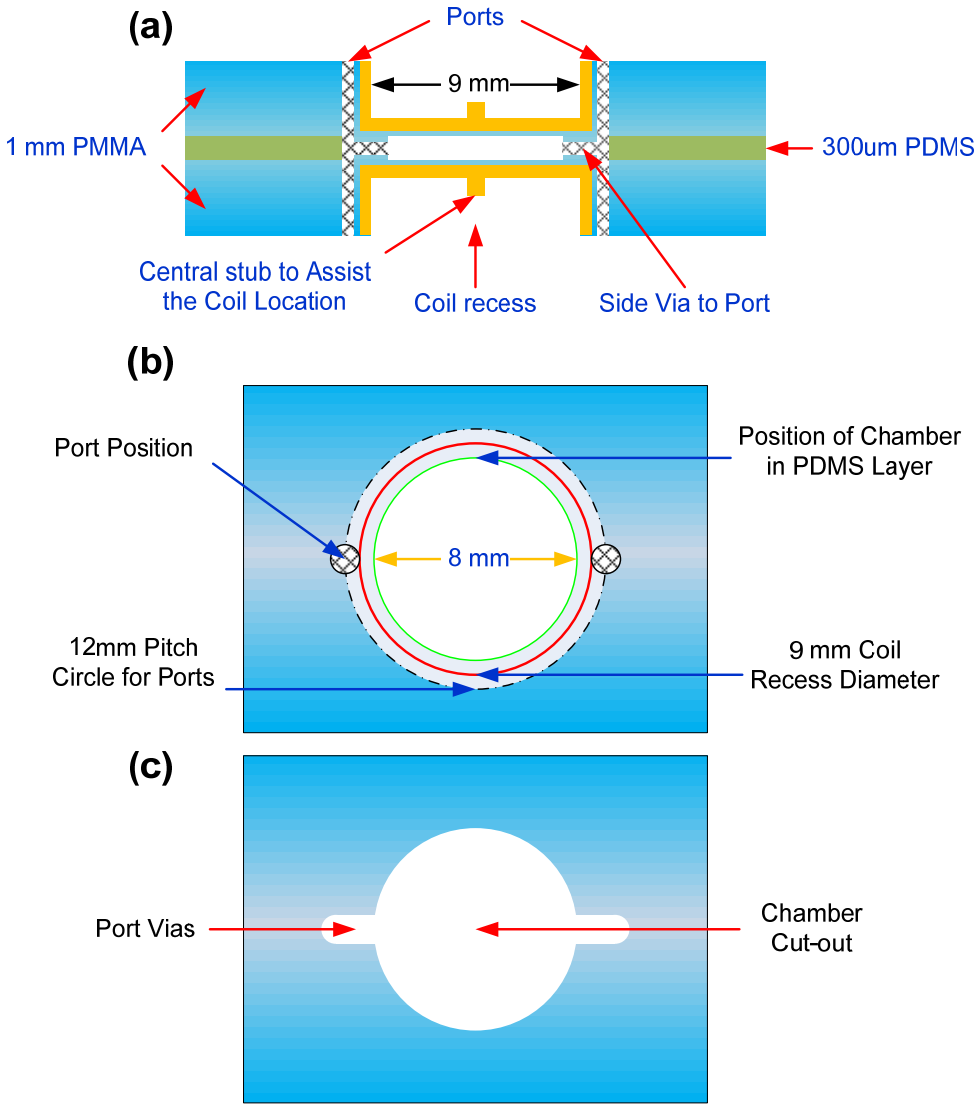

Figure 6.8. Schematic diagram of the microfabricated microchamber. a) Cross-sectional view. b) Plane view. c) Chamber cut-out and position of vias.

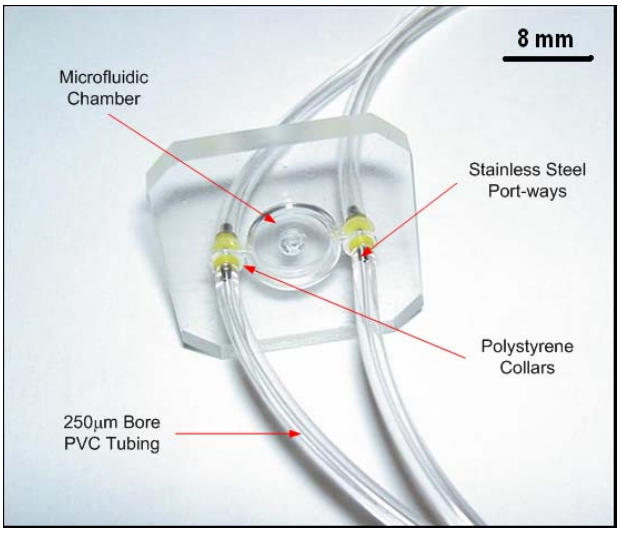

Figure 6.9. A photograph of microfabricated 15µl chamber with PVC tubing.

6.4.2 Microfluidic Chip Docking Station

In order to facilitate use of the device, a chip carrier station was built. This station comprises a heavy wooden base and 20 cm steel column at one end. A bosshead was then fitted to this column, into which the chip carrier proper could fit. The other use of this bosshead is to adjust the height and allow the chip carrier to rotate if necessary during experiment. An 8-port connection block was fitted on the base to provide electrical connections for electromagnets and if necessary, temperature sensors. The chip carrier plate comprises a PMMA plate with a square slot machined through to accommodate the fluidic chip. Two screw-driven pins were place at opposite corners of this slot to secure the microfluidic chip in place. Two brass rods were mounted on this plate to act as coil retainer by using spring-loaded pads.

Valve block was built of two brass blocks on each side of carrier plate with two drilling feed lines on each to accommodate a maximum of four microfluidic tubing. These valves can be activated to pinch off the plastic tubing using a knurled finger-screw. Finally, at one end of carrier plate, four holes were drilled to secure the maximum of two piezoelectric micropumps. These micropumps were used to feed the washing buffer in microfluidic device with controlled flow rate. A photograph of docking station is given in Figure 6.10.

This device was made at *ChargeLabs*.

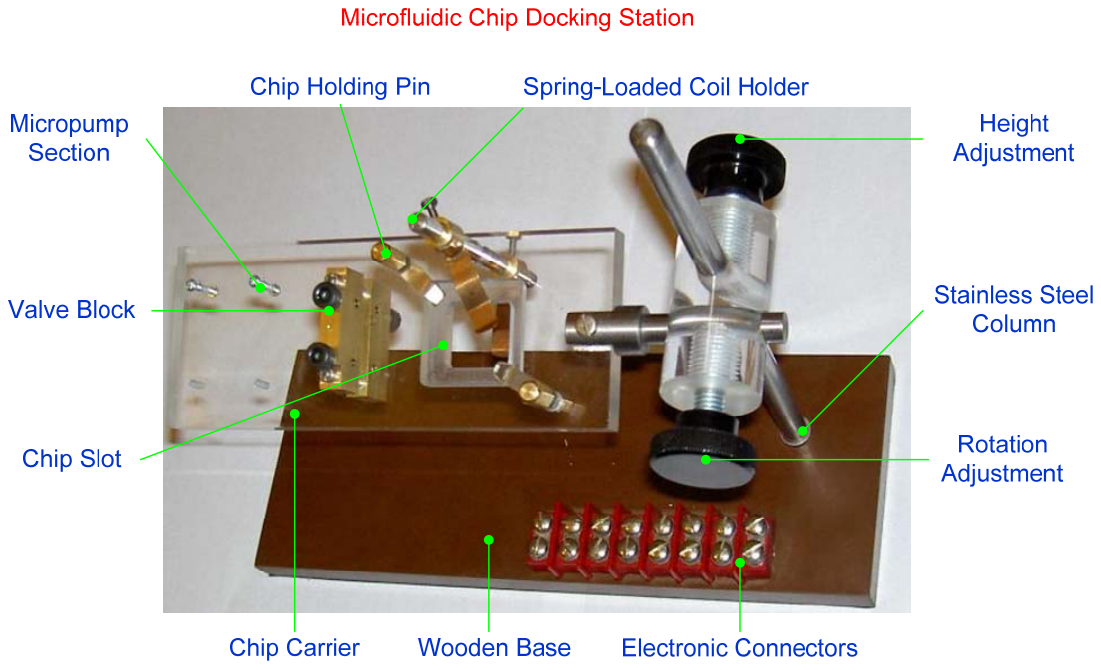

Figure 6.10. A photograph of chip docking station.

6.4.3 Electronic power supply

In order to operate the microfluidic device, a power supply is required to activate magnetic coils with specific switching pattern. This switching pattern cannot be created using a standard laboratory power supply, since they produce DC output. The application of standard function generator is limited by output power, which is not sufficient to activate the magnetic coils designed in this project. Therefore, a custom-designed power unit was designed and constructed. The core of this power unit is a linear voltage-control current-source module.

This unit comprises two output ports to activate two magnetic coils. The range of this current source is limited to 0-999 mA with an accuracy of 1mA. Since the magnets need to be activated in switching and clamping mode, an internal frequency generator was designed to generate switching frequencies between 0.1-10Hz with the ability to switch each output port between AC and DC mode individually. An alphanumeric LCD was added to the unit to display the frequency and two more LCDs were added to display the current in each port. A photograph of the electronic control unit is illustrated in Figure 6.11. The circuit diagram of the power/control unit is shown in Appendix B.

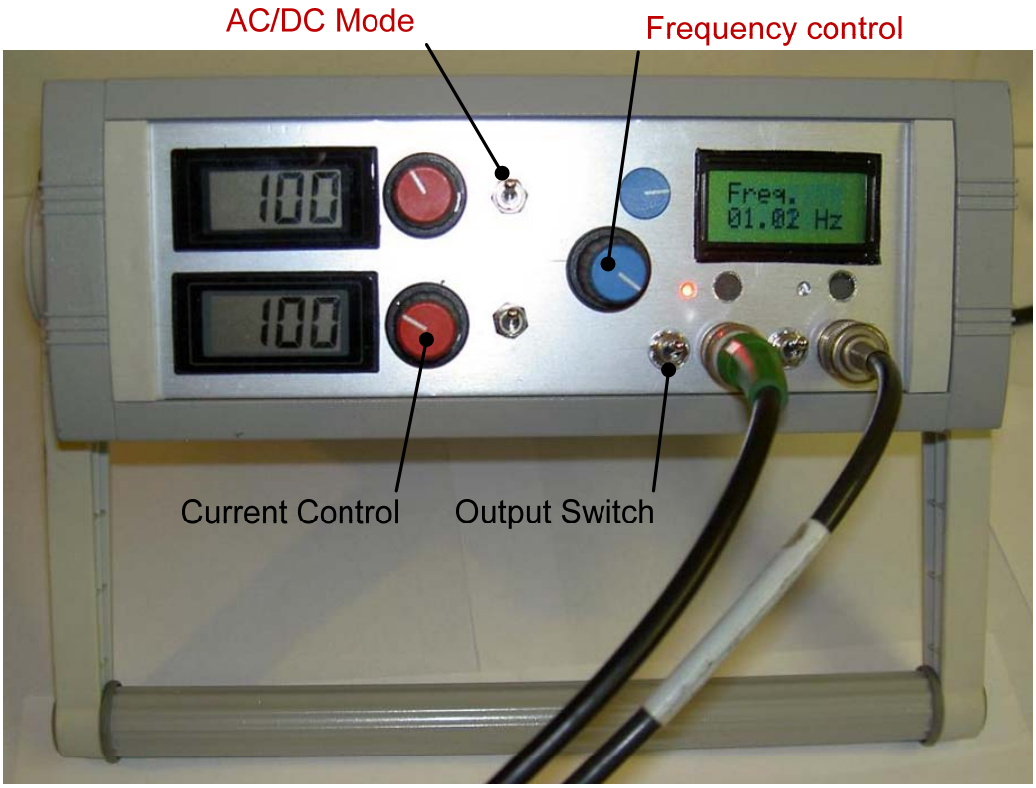

Figure 6.11. A photograph of control/power unit.

6.4.4 Capillary Test-rig

A capillary test-rig was designed and made to facilitate the bead trajectory experimental study. The core of this test-rig comprises a pair of *Martock* single axis micropositioning stages with micrometers. These stages are assembled in opposite directions on a block of PMMA. These micropositioners were used to adjust the distance of coils from the capillary with an accuracy of 1 µm.

Two small PMMA blocks are mounted on micropositioning stage and a central 6 mm diameter circular hole was drilled into which a 50 mm long aluminium rod was fitted. These aluminium rods were secured with two side-wall screws and were used to secure the magnetic coils on central section of the rig next to the capillary.

A capillary carrier was made using PMMA and a middle canal to secure the capillary at the middle of the coils across the central diagonal line. At one corner of the main PMMA plate, a four slot electronic connection block was assembled to ease the connection of magnetic coils to the main control unit. The position of coils was changed to the sides to clear the access point from the top and reduce the effect of gravity of magnetic beads. Figure 6.12 show a photograph of capillary test-rig with assembled coils and a glass capillary tube.

This test-rig was made In *ChargeLabs*

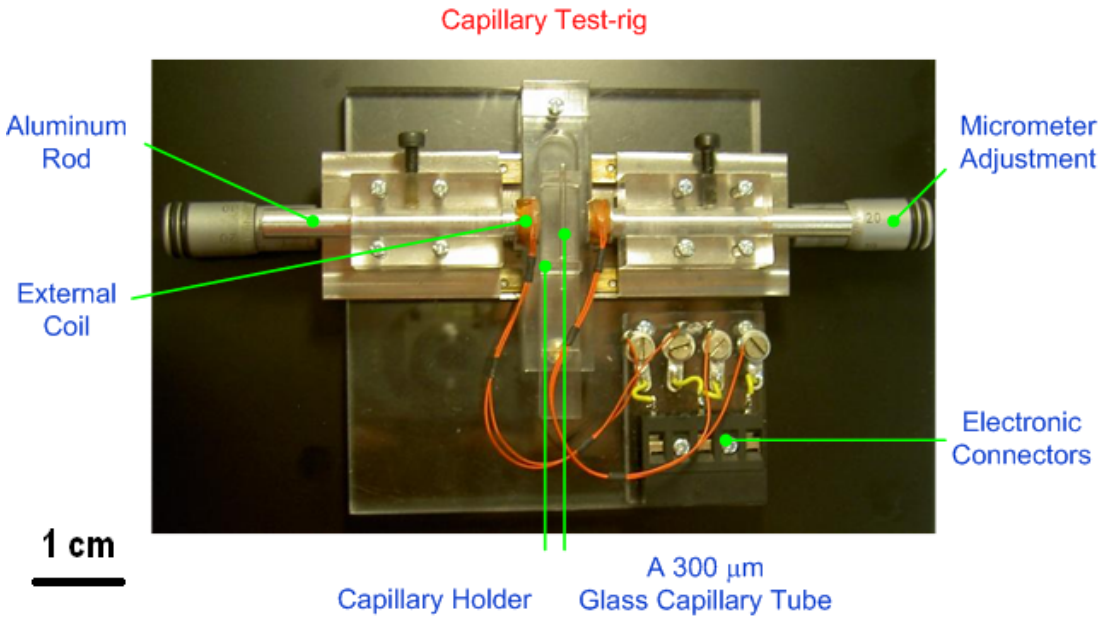

Figure 6.12. A photograph of capillary test-rig used for bead trajectory study.

6.5 Bead Trajectories Using Capillary Test-rig

An experimental study was planned to validate the previous simulation study on magnetic beads trajectories. As mentioned before, due to physical restrictions, a glass capillary test tube was chosen to model a cross-sectional slice of the microchamber. This capillary test tube was used to investigate the efficiency of the magnetic mixing in normal switching mode and dynamic switching mode by using combined quadrupolic and solenoidal field patterns.

6.5.1 Normal Switching Mode

In this section, an experiment was conducted to investigate the efficiency of the magnetic mixing in normal switching mode. In the normal switching mode, each coil was activated individually with no overlap in their activation cycle. Figure 6.13 shows a photograph of the experiment setup using capillary test-rig and power/control unit. A solid-state CCD camera, *DinoLite* USB Digital Microscope, was used to monitor and capture bead trajectories inside the capillary tube. Different bore sizes glass capillary tubes ($300\ \mu m, 500\ \mu m$ and $750\ \mu m$) were made to be used in this experiment. Different magnetic beads were examined in capillary test tube to conclude the effect of bead magnetic permeability and size on mixing efficiency and to extract the optimum mixing frequency.

There are many variables that effectively change the optimised mixing condition. These parameters are bead property, coil current, coil dimension, position of the coils and switching frequency. After a large number of pre-experiments, these conditions were short-listed to minimize complexity of the experiment. These short-listed variables are as follows:

- Heatsink Coil, (2×4) (8 mm in diameter and 4 mm in thickness) was used
- Coils were placed at the distance of 0.4 mm from the capillary (0.9 mm from actual windings to the capillary centre)
- Switching frequency ranging between 0.05 Hz - 10 Hz
- Fixed electric current of 155 mA
- A $300\ \mu m$ in diameter glass capillary was used in this experiment.

Different magnetic beads from four different DNA purification kits were used in this experiment. These kits are *Dynal* DNA universal, *Dynal* SILANE kit, *Promega* Magazorb kit and *LGC* AGOWA Sbeadex kit. Detail of these magnetic beads is given in Table 6.5.

Figure 6.13. The experimental setup using capillary test-rig.

Table 6.5. The property of different magnetic bead used for preliminary experiments.

Parameter	Sbeadex	Magazorb	Dynal MyOne	Dynal 2.8
Colour	Dark Brown	Dark Brown	Brown	Light Brown
Size	80% 5-10 µm, >53 µm	1-5 µm	1.05 µm	2.83 µm
Shape	Irregular	Regular	Uniform-Spherical	Uniform-Spherical
Specific Weight	3.0 – 3.5 g / 10 ml Dry Particles	?	1.4 g/cm^3	1.7 g/cm^3

Based on short-listed conditions an experiment was carried out to investigate the efficiency of the mixing and extract the optimised frequencies for different magnetic beads. The response of different types of magnetic beads was examined at different switching frequencies to extract the maximum response frequencies for each bead. All experiments were carried out at fixed coil position of 0.9 mm from the centre of a 300 µm capillary test tube. The results of this experiment is summarised in Table 6.6 for the maximum switching frequencies and the effective migration time. The effective migration time explains the collection of 90% of beads at the centre of the capillary tube.

Figure 6.14 shows sequential screen-shots of magnetic beads inside the capillary test tube. These screen-shots are given for different times between original positions of beads to the end of mixing, when all beads are collected in the middle section of the coils. Due to the large capillary length to diameter ratio, a bigger bore size capillary

tube (0.75 mm) was used in order to obtain clear image for presentation purpose. This gave the opportunity to fit the whole coil diameter on the capturing screen without restricting visibility. The electric current was increased to 220 mA to compensate the magnetic force. AGOWA Sbeadex was used in this experiment due to their very high magnetic permeability, large sizes and relatively easy to obtain clear images using the CCD camera. A supplementary cooling fan was used to avoid overheating and keep the temperature bellow 56°C. Magnetic beads were suspended in a mixture of water-glycerol to increase the fluid viscosity to ≈2 [cP]. Although these pictures are shown for a bigger bore size capillary tube, it was observed that the overall behaviour of the above different magnetic beads was very similar.

As it is clearly shown in this picture, beads start to chain up very quickly and migrate toward the capillary tube centre, while performing vertical mixing. During the migration time, a clump of beads will be created by increasing the bead concentration toward the centre. After 60 second, majority of bead are collected at the centre. Almost 99% of beads will be collected at the centre after 3 minutes of mixing. If the mixing time increases, the clump of beads will be more compact. It was clearly shown that the overall behaviour of magnetic beads is in close agreement with the simulation results. Beads tend to chain up and migrate toward the centre of the coil. The only different is in the calculation of response-time of magnetic beads to magnetic field (switching frequency).

AGOWA beads have average size of 5-10 μm, which is bigger than the size of beads used in simulation (3 μm). Since all types of magnetic beads responded well to higher frequencies, the bigger size of AGOWA beads is not the main reason for their fast response to the switching field. However, the chain up process in AGOWA beads is faster than the other beads because of their bigger sizes. Before creation of beads chins, the frequency of 0.05 Hz and 0.2 Hz was required to agitate Dynal 2.8 and AGOWA beads respectively. This response of Dynal 2.8 and AGOWA beads is in close agreement with the results of simulations. This response was increased by creation of first set of beads chains (see Figure 6.14, $t = 5\,sec$ & $10\,sec$), and was increased exponentially by creation of multi chains and creation of bulky block of beads (see Figure 6.14, $t = 20\,sec$ & $40\,sec$). This effect can be explained by considering the bulky effect of the magnetic force and viscous drag force on the clump of magnetic beads.

Table 6.6. Summary of different magnetic beads respond time to switching frequency.

Parameter	Sbeadex	Magazorb	Dynal MyOne	Dynal 2.8
Maximum Frequency	10 Hz	6 Hz	4 Hz	2Hz
Effective Migration Time	1 min	1.5 min	2 min	3 min
Coil Current	155 mA	155 mA	155 mA	155 mA

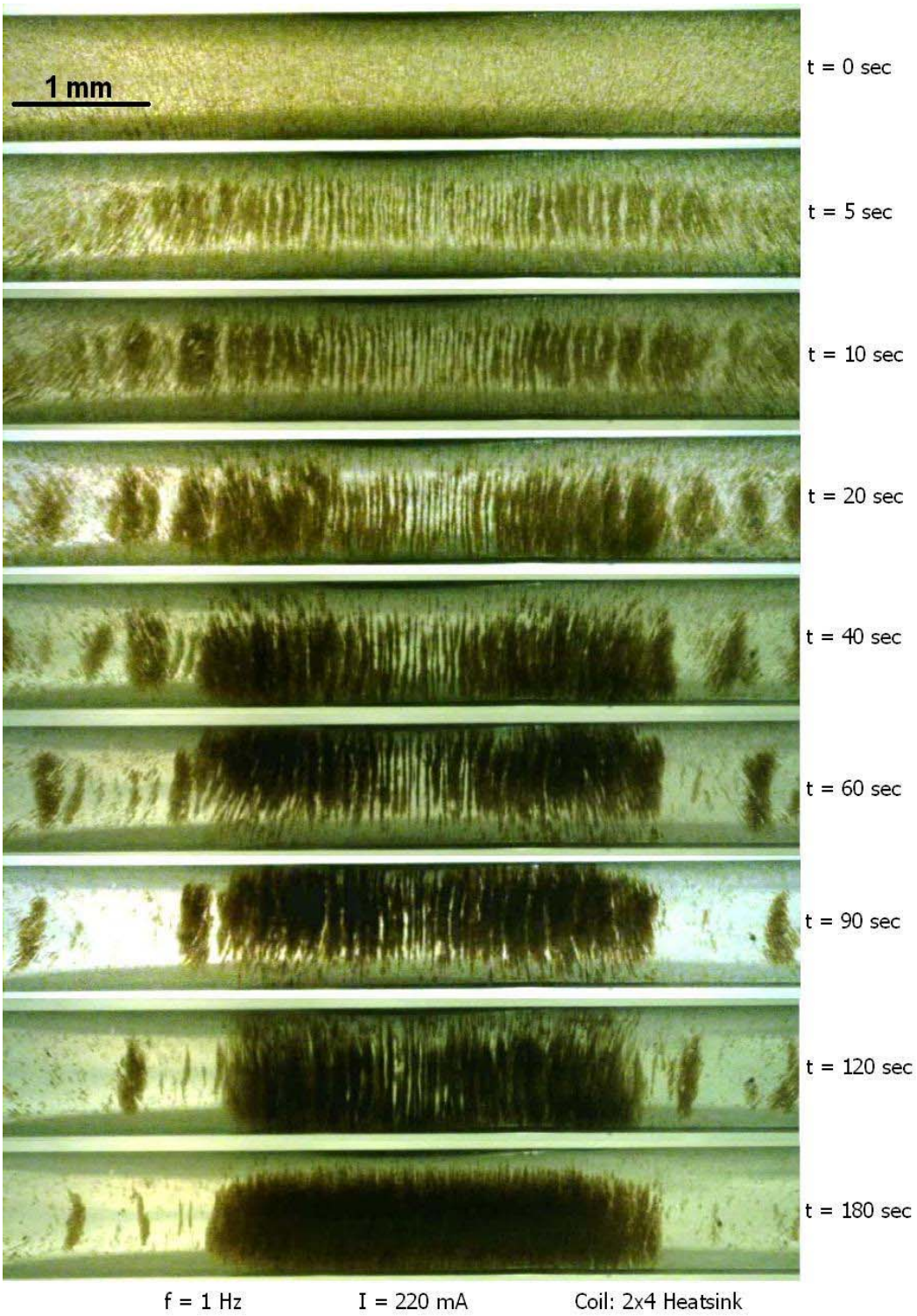

Figure 6.14. Series of screen shots showing the magnetic mixing (AGOWA, Sbeadex) inside a 0.75 mm in diameter capillary tube for a period of 180sec at frequency of 1Hz.

By creation of small bead clumps (multi-chains), magnetic particles will be in physical contact and their induced magnetic field overlaps. In this case of mutual interaction between magnetic particles, the particle-particle mutual effect can be explained in bulk mode.

The majority of commercial magnetic beads are made by doping nano-size magnetic particles inside a polymeric sphere. The resultant magnetic moment of bead is a vector sum of magnetic moments of all nanoparticles. By a similar analogy, the bulky effect of clumped magnetic beads can be explained. By creation of physical contact between beads, after a transient time, their induced magnetic moment will be forced to reorient in the presence of strong external field to create a hybrid magnetic moment. The result is a stronger magnetic moment, which is the sum of individual magnetic moments of beads. By attaching more beads to each other, the resulting magnetic moment will increase relatively. The transient time ($< 1\,\mu s$) for reorientation of magnetic moment is negligible compared to the switching frequency, thus can be ignored. After a specific time, bigger magnetic beads will be created by clump of small magnetic beads. Based on Equation (3.27), the magnitude of magnetic force is proportional to the volume of the bead, and thus their response is faster than each individual bead.

On the other hand, the magnitude of viscous drag force on a magnetic bead inside the clump decreases significantly. This happens because the effective surface of each bead decreases by attaching to the other beads. Therefore, the average of viscous drag force decreases on the clump of beads, which results in faster response of the beads to the external magnetic field.

6.5.2 Application of Quadrupolic and Solenoidal Force Pattern

In normal switching mode, the process of magnetic mixing is limited to migration of bead toward the centre. The mixing will be finished and any further switching will agitate the clump of beads in the central part of the chamber. Therefore, there will be no mixing action and subsequently no DNA collection in other areas. The situation gets worse if the lysis takes place after migration of beads. In most DNA extraction kits, the optimum lysis time is typically 10 min. By considering the migration time in different magnetic beads, the majority of released DNAs will not be captured by beads during their migration time. Since the natural movement of beads in this

magnetic force pattern is towards the centre of the coil, it is important to return the beads to the outer section of the coil/chamber and restart the mixing to increase the chance of DNA capturing. Fortunately, this action can be done using hybrid switching pattern to create quadrupolic force pattern using the same coil arrangement. This force pattern was previously investigated by means of simulation in section 4.9. In this section the efficiency of quadrupolic force pattern is investigated by means of experiment to unpile magnetic beads from the clump. The start time for this experiment is from the end of mixing in previous section, where the beads were collected at the capillary centre. The result of unpiling the beads is shown in Figure 6.15 in a series of screen shot.

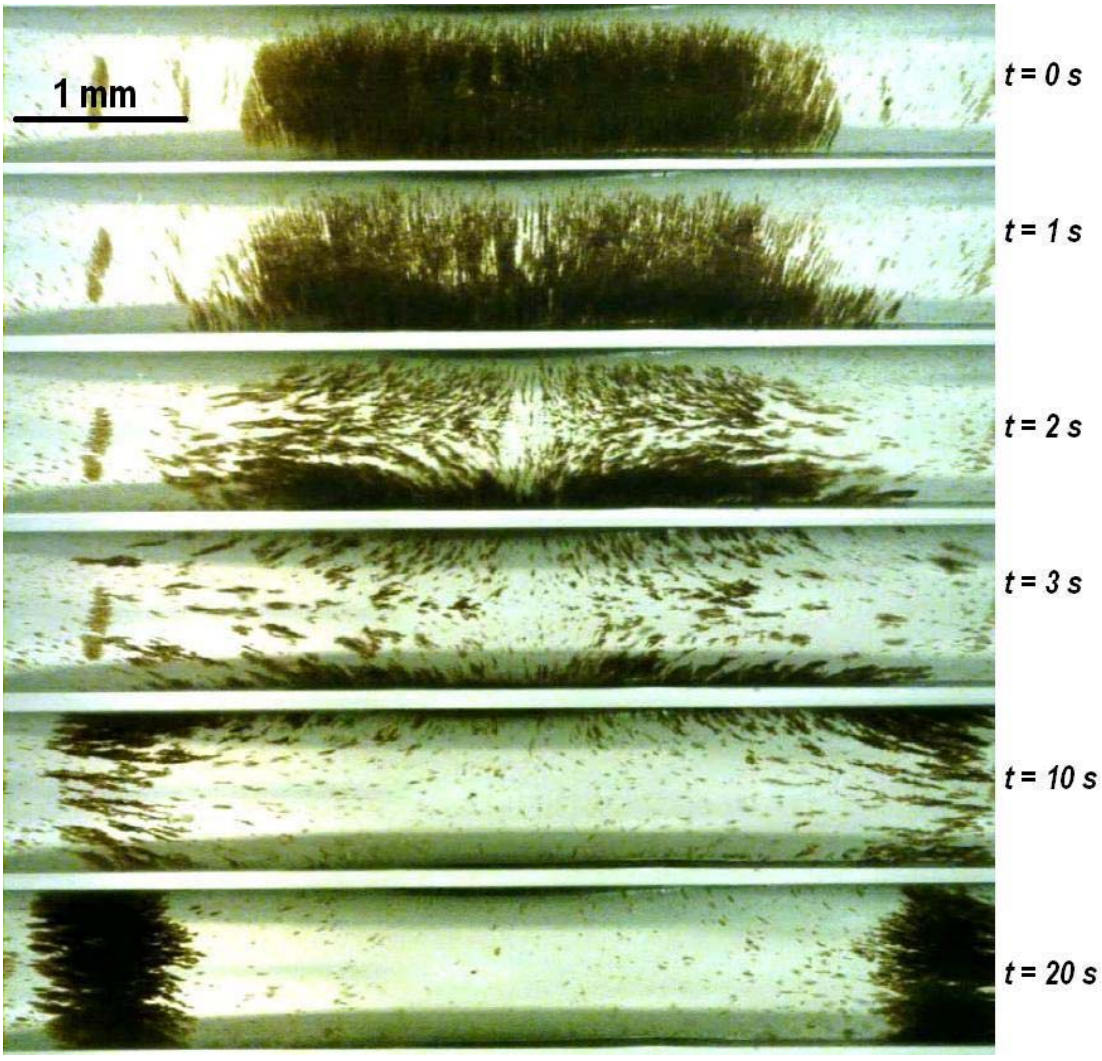

Figure 6.15. Series of screen shots showing the application of quadrupolic coil setup on the bulk of magnetic beads. A combination of quadrupolic and switching field pattern was applied to move the beads out of the centre.

It is clearly shown that the clump of beads easily burst out and will be separated into four groups, based on quadrupolic force pattern. Since the beads tend to stick to the top and bottom of the tube, a mixture of switching-quadrupolic pattern was applied to push them toward the outer section of the coils. The whole process take place in less than 15sec. This is because beads are burst out to smaller piles and still posses' large magnetic moment. Finally, all beads are divided to two piles at two ends of the capillary tube. The process of mixing can be resumed toward the centre using normal switching mode. This process can be repeated continuously to achieve sufficient mixing inside the microchamber.

In addition, this experiment shows that the beads exhibit the superparamagnetic behaviour very well. This behaviour helps to unpile the beads clump very easily by applying inverse quadrupolic force. This behaviour was investigated on other magnetic beads as well and the result is summarised as follow:

- AGOWA beads respond very well to the inverse field and will be separated easily
- Magazorb beads can be separated easily but in larger pieces
- DynaBeads can be separated but in relatively larger pieces compared to other beads

These different results can be explained by considering physical properties of different magnetic beads. AGOWA beads are supplied in different sizes and irregular shapes in the range of 5-10 μm. Magazorb bead have regular shape but in different sizes. Dynabead are supplied in regular shapes and mono-size. The variation in size results in different induced magnetic moment in beads, thus different terminal velocities in response to the magnetic field. This effect describes the response of AGOWA and Magzorb beads. Since Dynabeads have regular shapes and mono-size, their induced magnetic moment and their response is similar to each other. In addition, the surface coating of AGOWA beads represents hydrophilic behaviour in the fluid while, the surface of other magnetic beads show hydrophobic behaviour in fluid. This could be another reason for easy separation of AGOWA beads compared to Dynabeads.

In another experiment, the performance of Solenoidal field pattern was investigated inside the capillary test tube. In this experiment the conditions were kept unchanged

as the previous experiment. The start time for this test was set to the end of application of quadrupolic field pattern. The results of this experiment are shown in Figure 6.16 in a sequence of screen shots.

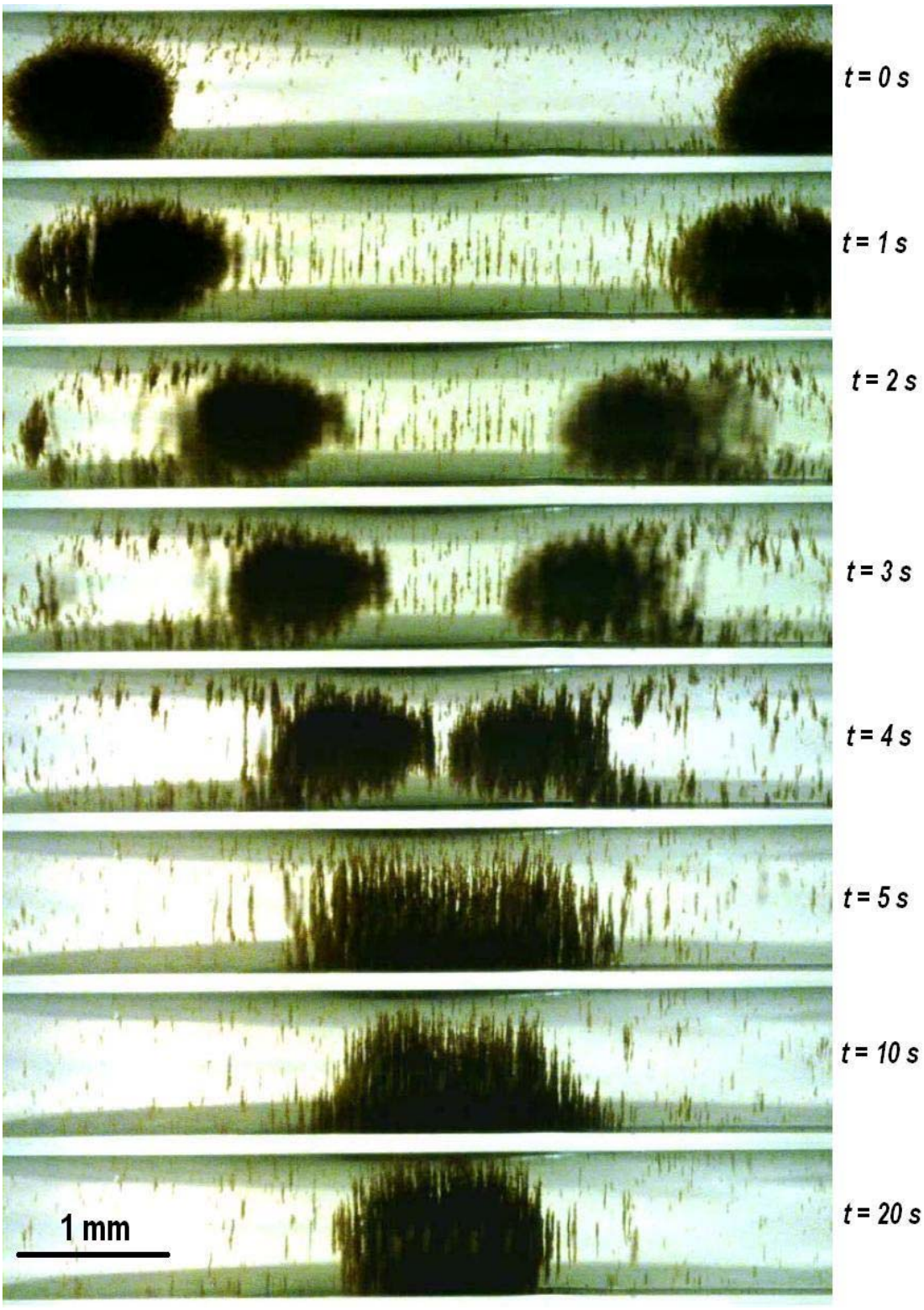

Figure 6.16. Series of screen shots showing the application of solenoidal coil pattern on the bulk of magnetic beads.

By switching to solenoidal mode, the region of higher field strength shifts to the central part of the capillary, thus the clump of magnetic beads is dragged toward this region. Beads move in clump mode and the migration occurs in a couple of seconds. This is because resultant magnetic moment is maxima at clump mode and a lower friction force between beads and capillary walls. Finally beads end up in a more compact clump in the centre of the capillary. This action in a microchamber can be visualised as a toroid, which shrinks toward the centre. The most important application of this field pattern is in the clamping mode, due to the stronger and more concentrated magnetic field pattern generated in this mode.

6.6 Clamping Experiments

The efficiency of bead-based DNA purification process depends on many parameters such as efficient lysing of cells, effective mixing and maintaining the bead/DNA complex inside the microchamber using DC magnetic force during the washing process. This work is not concerned with the efficiency of lysis buffer, since the lysis buffer condition needs to be optimised based on the application. The efficiency of mixing was investigated in *Chapter 5* based on numerical simulations. The focus in this section is thus on magnetic clamping efficiency as the last part of DNA extraction/purification process.

A microfabricated microchamber was fabricated based on the process described earlier in section 6.5 to be used in clamping experiments. A pair of heatsink coil (2×4), 8 mm in diameter and 4 mm in thickness, were used on the microchip installed on chip docking station. A piezo-actuated diaphragm micropump, *Thinxxs* Microtechnology, was used for chip washing process. The flow rate of this piezo-driven micropump can be controlled by supplied controller. The flow rate curves supplied by pump supplier are based on a typical test condition and may vary in different conditions. Therefore, the accurate flow rate was measured at different pumping frequencies in this experimental setup. The minimum and maximum flow rates of 125 µl/min and 1.25 ml/min were measured at the frequencies of 0.5 Hz and 33Hz respectively. Diaphragm-based pumping principle of this micropump indicates that the fluid flow has a pulsing pattern. The strokes created by this pulsing pattern are maximum at the minimum frequency of 0.5Hz. At the maximum possible operating frequency of 200 Hz, the measured flow rate was 0.75 ml/min. at this operating condition, the pulsing effect was observed to be minimal. Therefore, this flow condition was used to perform the washing process.

The experiment was performed using *AGOWA Sbeadex* beads. In order to investigate the clamping at more realistic condition, 3 min magnetic mixing was performed using normal switching pattern with heatsink coils (2 × 4) at 155 mA coil current. Under these operating conditions, all magnetic beads were collected at the centre of the chamber. The bottom coil was used for clamping and the top coil was removed to observe the clamping action. The results obtained for clamping are shown in Figure 6.17 in a series of screen shots. These screen-shots show the position of beads at different times under continuous fluid flow-rate of 0.75 ml/min (the fluid flow is from left to right). Washing process was performed in 3 min until the positions of beads were stabled and no beads were lost.

During the washing process, the clump of beads moves toward the outlet under flow pressure. During this migration, small amount of beads will be released from clamp and washed away. The rest of beads remain clamped under an equilibrium condition between fluid drag force and magnetic clamp force. A manual measurement of washed beads at sump collection tube shows that in this clamping condition 60% of beads will be released from the clamp and 40% stay inside the chamber.

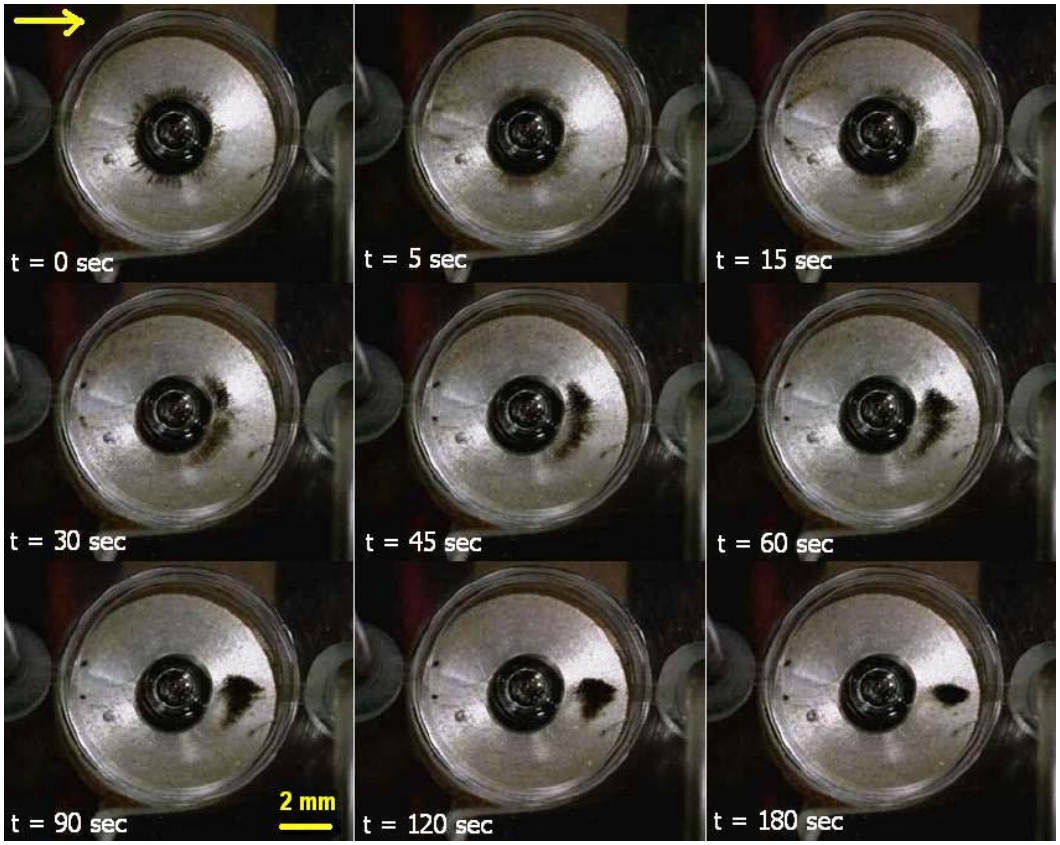

Figure 6.17. The efficiency of magnetic bead clamping inside the microchamber using Sbeadex beads, flow-rate of 0.75 ml/min and clamping current of 150 mA. (The arrow shows flow direction)

To improve the efficiency of clamping, clamping current was increased to 200mA and the result of clamping is shown in Figure 6.18. Fluid flow rate was kept unchanged and the washing process was performed for 3 min. the efficiency of clamping was significantly improved and majority of magnetic beads remained clamped inside the chamber. The ratio of lost beads was measured as 20% to 80% clamped beads. The temperature of clamping coil was monitored using a type *k* thermal sensor. Since the period of clamping was very short (3 min) and the continuous fluid flow acts as a cooling system, the coil temperature was kept below 70°C during clamping.

Therefore it is possible to successfully clamp majority of magnetic beads inside the chamber using 200 mA clamping current under very high flow rate (750 µl/min). This high flow rate was used to show the efficiency of clamping under strong fluid drag force. In addition, by using solenoidal coil arrangement, it is possible to compress the clump of magnetic beads and increase the strength of magnetic clamping force. This was tested on the same experimental condition and the result shows that the ratio of lost beads was below 10%.

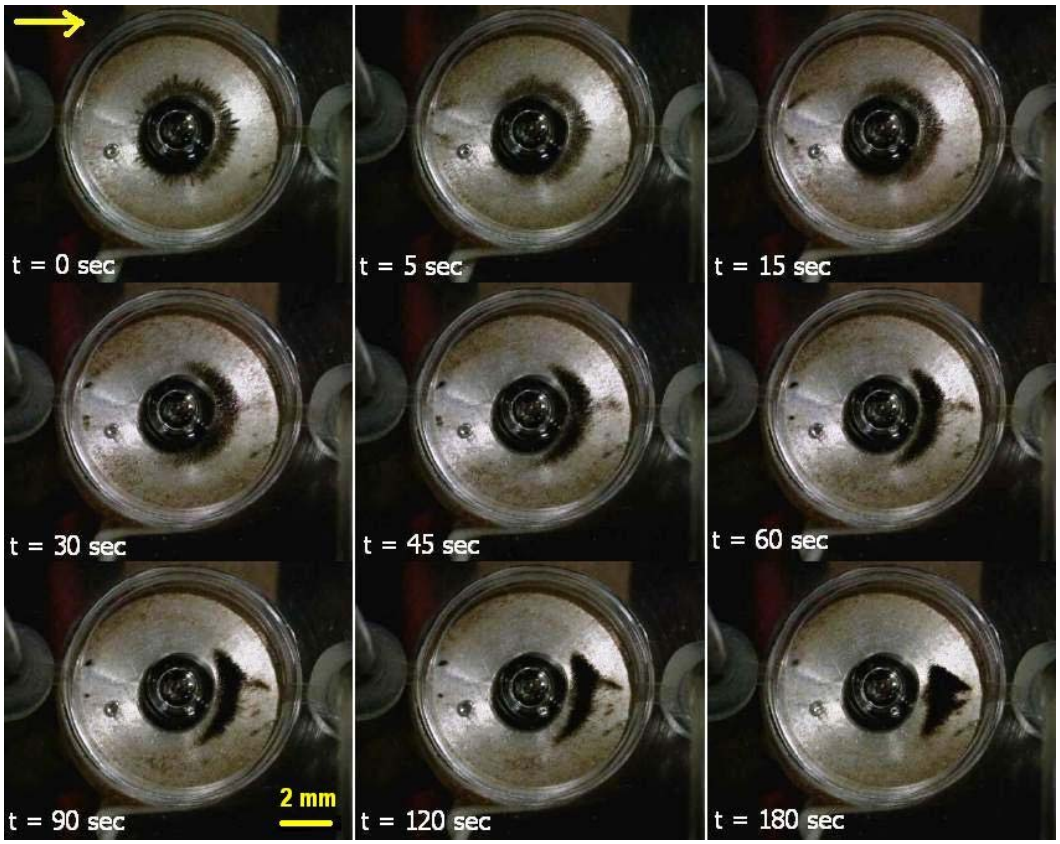

Figure 6.18. The efficiency of magnetic bead clamping inside the microchamber using Sbeadex beads, flow-rate of 0.75 ml/min and clamping current of 200 mA. (The arrow shows flow direction)

While longer washing process improves the purity of DNA sample, 3 min continuous washing consumes large volume of washing buffer (2.25 ml). This volume is much more than recommended volume in commercial kits. This volume was adopted for 15 µl chamber and the required volume was calculated as 34 µl for two washes based on *Promega Magazorb* purification protocol.

A similar clamping experiment was performed using *Promega Magazorb* beads and the results observed are shown in Figure 6.19 and Figure 6.20. The screen shots of Figure 6.19 shows the position of beads before (Figure 6.19a) and after (Figure 6.19b) mixing (both bottom and top magnets are removed to improve the visibility). The mixing was performed with switching current of 155 mA for 3 min.

The screen shots in Figure 6.20 show the position of beads inside the chamber after one minute continuous washing under clamping current of 200 mA and flow-rate of 0.75 ml/min. Similar result as *Sbeadex* beads was extracted with *Magazorb* beads.

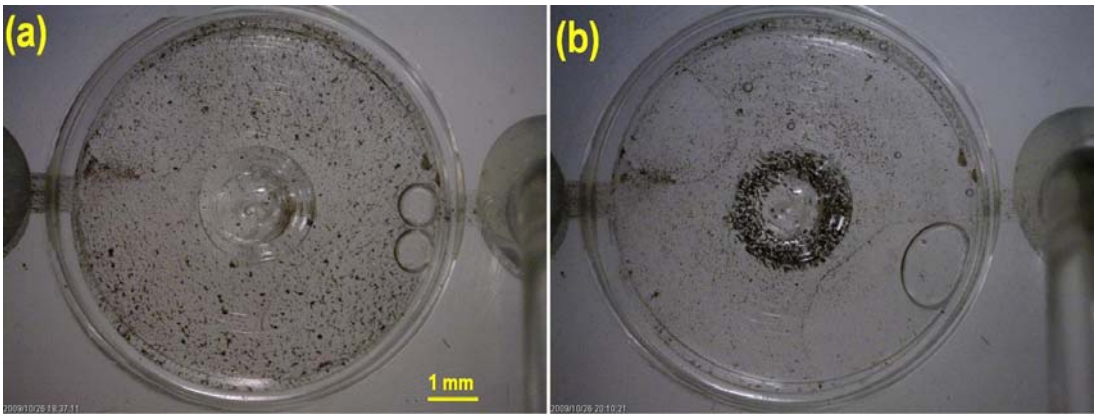

Figure 6.19. Clamping experiment using *Magazorb* beads. Pictures show the position of beads before (a) and after (b) mixing.

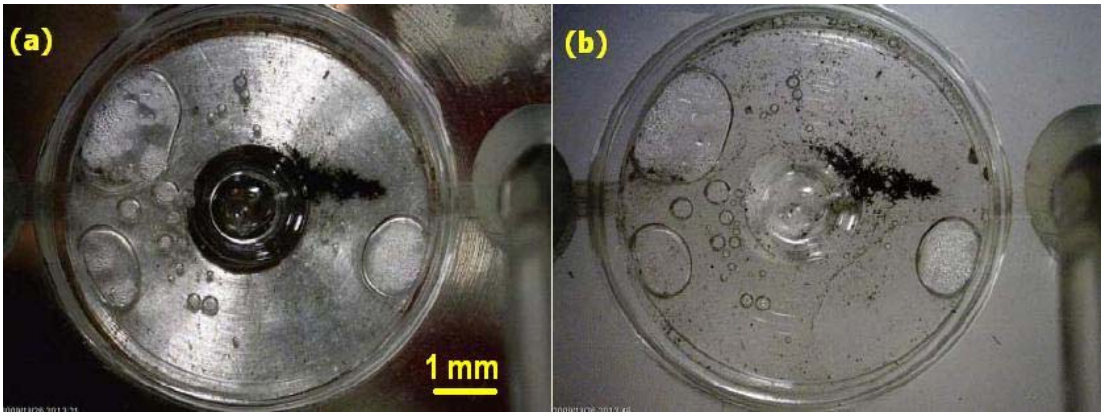

Figure 6.20. a) Position of clamped *Magazorb* beads after 3 min washing process at the flow-rate of 0.75 ml/min. b) The bottom magnet is removed to improve the visibility.

In another experiment, validation of quadrupolic separation of beads clump was investigated inside the microchamber. This result is shown in Figure 6.21. The mixing was performed in 3 min using switching current of 155 mA, until all beads were collected at the centre of the chamber (Figure 6.21a). A quadrupolic field pattern then was applied for the period of 10 sec (Figure 6.21b). This experiment shows the efficiency of unpiling the clump of beads inside the chamber.

By applying a combination of switching field and quadrupolic field it is possible to move the beads further out of the centre, close to the outer section of the chamber. In this experiment, *Magazorb* bead were used for mixing and a pair of (2×4) heatsink magnetic coils were used as magnetic force generators.

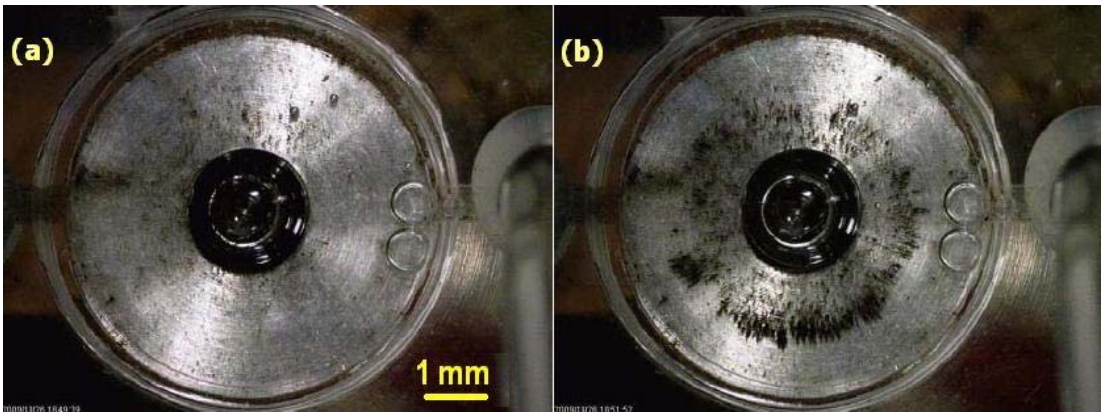

Figure 6.21. A plan view of effect of quadrupolic force pattern applied to *Magazorb* beads inside the chamber.

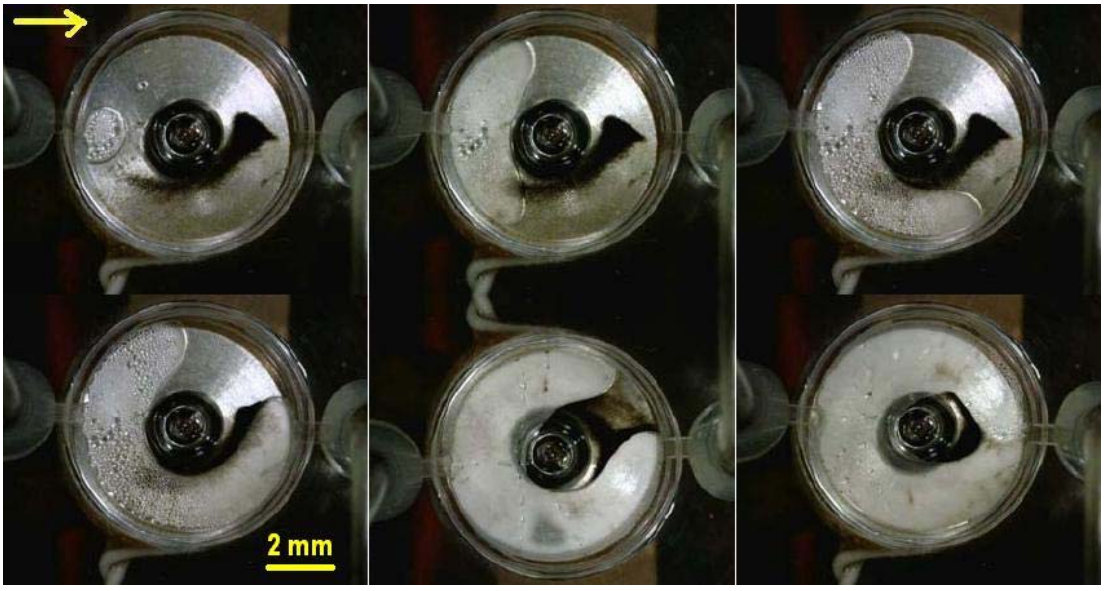

Figure 6.22. Effect of air-washing on clamped magnetic beads inside the chamber in a series of screen-shots (the fluid flow is from left to right).

A different washing experiment was carried out using air-washing. The result of this experiment is shown in Figure 6.22. During this washing process, the clamping was activated at 200 mA current using bottom coil. Pushing the air into the chamber increases the surface tension inside the chamber. Magnetic beads remain clamped but, since the fluid-magnetic force equilibrium is not present anymore, the clamped beads return to their original position at the centre of the chamber. Small volume of fluid remains in the centre of the chamber, trapped between clumps of beads. This air washing method can be used at the end of normal washing process to empty the chamber from washing buffer and introduce the elution buffer if necessary.

6.7 Fluidic Experiments

In this section some microfluidic experiments have been performed to investigate the chamber porting and filling issues. A microfabricated 15 µl chamber was installed on docking station in horizontal plane and filling was performed using 25 µl Hamilton syringes. A syringe pump controller was designed using a DC motor to create very smooth and continuous low flow-rate (Figure 6.23) (The controller was made in *ChargeLabs*).

By introducing the fluid to the chamber, it was observed that in some areas air pockets were trapped. Figure 6.24 shows different screen shots from different unsuccessful filling of the chamber at a flow-rate of *1.0* µl/sec. Since the chamber is empty and dried, surface tension is the dominant force and, if a small air pocket traps inside the chamber, it will be pinned to that area and fluid bypasses this pocket. On average, in 70% of filling attempts, at least one small air pocket was trapped and in 30% of filling attempts, the size of air pocket was bigger than the volume of fluid inside the chamber.

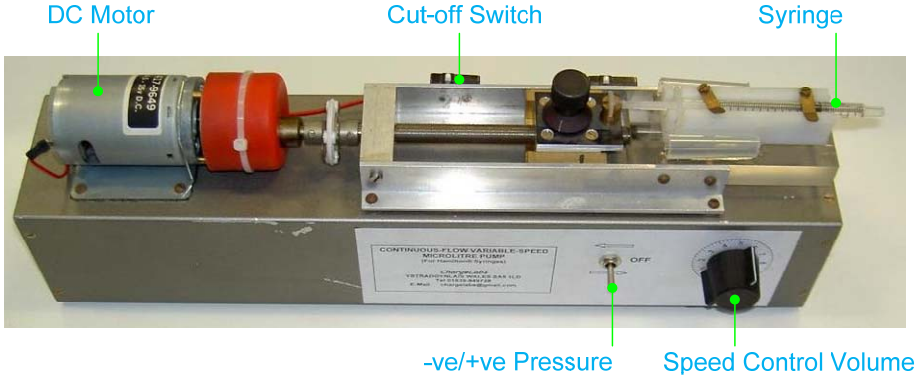

Figure 6.23. A picture of high-precision syringe pump used in fluidic experiments.

To overcome this problem, the chamber was filled in a vertical position. In this position, the chamber was filled from the bottom port. The intension was to investigate the effect of gravity on filling efficiency of the chamber. The result of vertical filling process is given in Figure 6.25 as a series of screen shots. In this filling condition, the fluid velocity was set to 1μ/sec.

As it was expected, the gravity has significantly influenced the filling pattern. Naturally, the fluid level tends to be horizontal under gravity force. This force cancels the surface tension out significantly. This experiment was repeated many times and in 90% of filling attempts, the chamber was filled successfully.

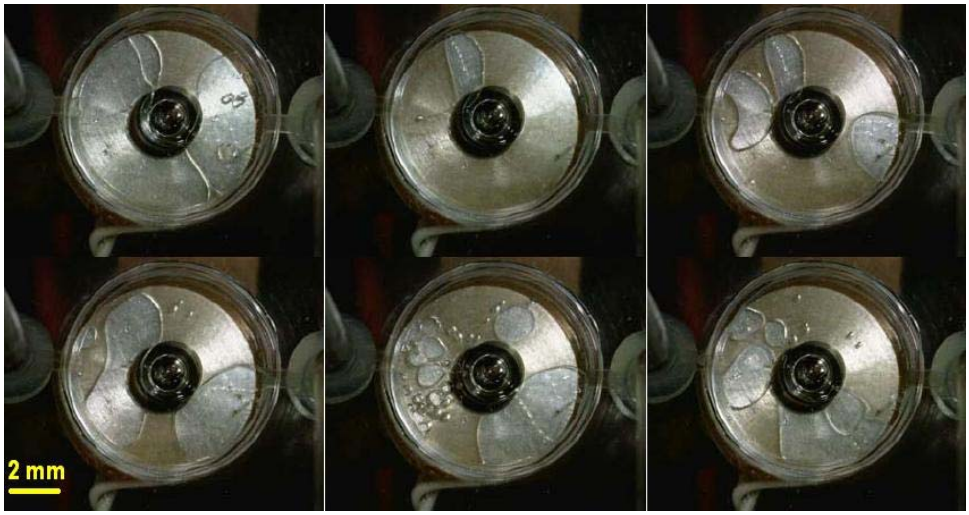

Figure 6.24. Unsuccessful filling of the chamber in horizontal orientation.

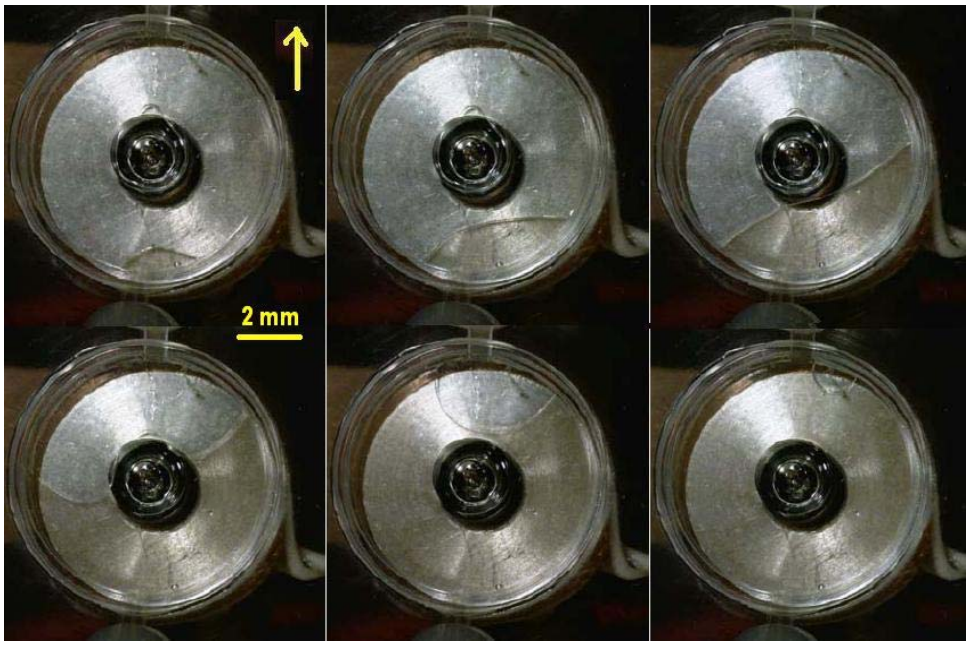

Figure 6.25. Successful filling of the chamber in vertical orientation. (Arrow shows the fluid direction)

This experiment was repeated at different fluid flow-rates and the result was successful at higher flow-rates up to 10µl/sec. in higher flow-rates, usually small air pocket will be trapped close to the outlet. This is because the fluid level increases faster than effect of gravity on the fluid.

In another sets of experiments, the effect of prefilled chamber was investigated at horizontal plane. The result showed that although, introducing the fluid to prefilled chamber eliminates the trapped-air-pocket problem; fluids were partially mixed with at liquid-liquid interface.

The effect of different port position was investigated as well by placing the inlet at the middle of the chamber and outlets at the outer section of the chamber. Surface tension was still the dominant force in dried chamber and air-pocket-trapping was observed again. Therefore, the most effective methods to fill the chamber remain the vertical filling and horizontal filling of pre-filled chamber.

6.8 Summary

In this chapter, a series of experiments were carried out to validate the results of numerical simulations performed in *Chapter 4* and *Chapter 5*. The parameters that were used for validation are the strength of magnetic field, temperature rise in magnetic coils, beads trajectories study, switching frequency, application of different force pattern in manipulation of beads inside the chamber, clamping efficiency and finally some fluidic experiments to establish the best chamber filling method.

The accuracy of simulation was investigated using measuring the strength of magnetic flux density of winded coils. It was noticed that in practice, there will be some dead spaces between windings using circular cross-section of insulated copper wire. The electromagnetic model was modified to take into account the practical limitation of winding. The resulting model showed very close agreement with the experimental result obtained using a precise commercial magnetometer.

In the next section, the validity of thermal analysis was investigated using modified electro-thermal model of magnetic coils with different bobbin sizes and thickness. The steady state temperature was experimentally measured using type *k* thermal sensor and the results obtained were compared with simulation results. The optimum coil current was identified for different coil geometries based on maximum

temperature rise of 56°C for two different scenarios of AC and DC current modes. The aluminium bobbins were used as heatsinks to improve the capacity of heat dissipation in the coils. The validity of this modification was investigated by fabrication of two different bobbin dimensions and their thermal activity was compared with the simulation results. It was shown that by design of specific heatsinks, the heat dissipation ratio increases significantly. However, an optimised design of heatsink depends on the final design of the extraction device.

A capillary test-rig was designed and constructed to investigate the accuracy of numerical simulation model and to determine optimum switching current and frequencies of mixing for different magnetic beads. The results of this experiment show that the behaviour of magnetic beads is in close agreement with the simulation results in predicting their horizontal migration and tendency to form chains. The frequency of mixing was modified as the result of change in magnetic moment of bead chains, and minimum current and maximum frequency of mixing were then obtained for different commercial beads. This experiment showed that the chain effect of magnetic beads improves the efficiency of mixing by increasing the average magnetic moment through formation of beads clump in response to the switching magnetic field.

Application of hybrid field pattern was employed to increase the efficiency of beads manipulation inside the test tube. It was experimentally shown that a combination of quadrupolic and normal switching field pattern can be used to unpile the clump of beads from the centre of the coil and move it to different positions inside the tube. Solenoidal field pattern can be used to collect and compress all beads in the middle of the coil. This effect is desired in magnetic beads harvesting at the end of the DNA extraction/purification process. Nevertheless, a combination of switching field together with solenoidal and quadrupolic filed arrangements can be used for more versatile mixing patterns and manipulation of magnetic beads inside the chamber.

A micromachined microchamber was fabricated to investigate the efficiency of on-chip clamping of magnetic beads. This function is necessary at the end of DNA purification process to separate the DNA-Bead complex from the rest of biological debris. Washing is achieved, while magnetic beads remain clamped in the chamber. Two different clamping currents were used for two types of magnetic beads. It was shown that, to efficiently clamp the beads inside the chamber, a minimum current of

200 mA is necessary. Although, this result was extracted at very high fluid flow-rate and long washing process, lower flow-rates and washing time might be sufficient for real biological sample extraction process.

Finally, the efficiency of filling the chamber was investigated using side-wall porting. In this experiment, it was concluded that horizontal filling of empty chamber is not always successful. This is because of the surface tension effect; as a consequence air pockets are trapped during the filling process. Application of pre-filled chamber reduces the surface tension and improves the filling efficiency at the cost of partial mixing at liquid-liquid interface. Gravity corrected filling was investigated by positioning the chamber in a vertical position and feeding from the bottom port. This method proved to be very successful in order to fill the empty chamber.

CHAPTER 7

BIOLOGICAL VALIDATIONS

7.1 Introduction

A magnetic mixer was introduced and designed in *Chapter 4* and optimised dimensions were extracted based on numerical simulations. The performance of magnetic mixing was further evaluated in *Chapter 5* using beads trajectories study. A preliminary experimental study was conducted in *Chapter 6* to validate the simulation results. In this chapter the focus is to conduct an experimental evaluation to investigate the performance of designed DNA extraction device using real biological samples. To achieve this, different commercial DNA extraction kits were selected to evaluate the extraction efficiency using whole blood sample, which is the main source of genomic DNA molecules. The extraction performance was further evaluated using non-pathogenic bacterial cells, spiked into whole blood sample. This process was performed using different bacterial samples, *E. coli* (Gram negative) and *B. subtilis* (Gram positive). These tests were performed in collaboration with LGC (*Laboratory of Government Chemists, Teddington*).

A problem with commercially available DNA extraction kits is that majority of them are designed for bench-top extraction process, and thus are not suitable for on-chip automation. In these kits, the process of extraction mainly involves separate steps

such as pre-treatment with Proteinase K, cell lysis step and nucleic acid binding step. The volumes of buffers vary in each step in different kits with variable incubation times. Implementation of these standard techniques into microfluidic chip is a very challenging microfluidic problem. On-chip extraction process needs a very simple and fast extraction protocol using minimum processing steps.

Demands for simple and rapid on-chip DNA extraction process has led to design of extraction protocols that are more suitable for on-chip automation. Dynabeads® DNA Direct™ Universal and Dynabeads® DNA Direct™ Blood are the examples of extraction kits with the potential for automation. The extraction process in these kits is very fast (5 minutes total incubation time) in single treatment step using supplied pre-mixed lysis/binding/bead buffer. These protocols are very attractive for on-chip automation process as the microfluidic problem is minimal. However, the problem with this extraction kits is the large volume ratio of extraction buffers to the blood sample (1/20). This large volume ratio requires larger volume microchamber, which is not demanding. For example, to perform the extraction using 25µl of blood, 500µl of lysis/binding buffer is required using these kits. Another problem with this kit is the lower magnetic permeability of these magnetic beads (Dynal 2.8) compared to other magnetic beads. This comparison can be found in *Chapter 6*, Table 6.6. Therefore, in this work a preliminary experimental study was conducted to investigate the efficiency of different volume ratios (Dynabeads buffer to blood) on the performance of extraction. This experiment was carried out manually using bench-top process as well as automated process using microfabricated microfluidic chip. The results were analysed and compared to the standard extraction protocol using *Nanodrop 1000* Spectrophotometer, *Thermo Fisher Scientific*.

Although optimisation of buffer condition is not in the scope of this work, due to the lack of suitable protocol for on-chip extraction, different magnetic-bead-based extraction kits were short-listed to identify the most suitable kit for on-chip extract process. These kits are Magazorb DNA Mini-Prep kit (*Promega, Ltd.*), Dynabeads SILANE genomic DNA kit (*Invitrogen Corporation*) and AGOWA Sbeadex Blood kit (*LGC Limited*). In addition to the above magnetic bead-based extraction kits, a column-based extraction kit (QIAamp DNA Mini Kit, *Qiagen*) was used for bench-marking purpose. These kits were selected based on their outstanding efficiency on DNA extraction from blood sample and their higher permeability magnetic beads.

The optimisation process was aimed at reducing the number of extraction steps and total incubation time. To achieve this, the efficiency of these adapted protocols was first investigated on bench-top process in larger volumes. These results were compared with the manufacturers' standard protocols as well as the column-based extraction protocol. Extracted samples were then analysed using *Nanodrop ND-1000* spectrophotometer.

Identified extraction kit and adapted protocol was selected to perform on-chip extraction process. In this process the efficiency of the designed extraction device was evaluated in two different scenarios. The efficiency of DNA binding to the surface of the magnetic beads was evaluated using spiked free DNA samples (plasmid DNA) into the whole blood. The lysis efficiency was evaluated using a panel of Gram-positive (*B. subtilis*) and Gram-negative (*E. coli*) bacterial cells cultures spiked into the blood sample. The results were analysed using *Nanodrop ND-1000* spectrophotometer, to evaluate the extracted DNA purity. Bacterial DNA extraction recovery was determined by developing a quantitative real-time PCR assay.

7.2 Initial Evaluation of DNA extraction device

Initial evaluation of DNA extraction device was performed using Dynabeads® DNA Direct™ Universal extraction kit. This extraction kit was selected because of its simple and rapid extraction protocol, which is more desirable for on-chip automation process. This experiment aimed to investigate the impact of reducing the ratio of lysis/binding buffer to the blood volume. The standard manufacturers' protocol is as follows:

1. Adding of 200 µl Dynabeads buffer (including lysis buffer and magnetic beads) to the blood sample (the volume of blood sample should not exceed 10µl).
2. Five minutes incubation at room temperature.
3. Magnetic clamping of the beads and removing the supernatant.
4. Two washing steps using 200 µl of washing buffer.
5. Resuspension step to elute off the DNA molecules from the beads using 20-40µl of resuspension buffer. Alternatively, DNA can be eluted off the beads by incubation at 65°C for 5 minutes.

These steps show the simplicity of the standard protocol and its potential to be easily automated using designed extraction chip. However, the major drawback is the ratio of Dynabeads buffer to the blood volume (200µl to 10µl). To overcome this problem, an experiment was conducted to investigate the impact of Dynabeads/blood ratio on the extraction efficiency. Two different Dynabeads buffer/blood ratios (3:1 and 1:1) were initially investigated. The experiment was carried out using a 16 µl microchamber (8 mm in diameter and 300 µm in depth) and two external magnetic coils (heatsink coil (2×4)).

7.2.1 Experimental Setup

Detail of experimental setup is as follows:

- Total volume of blood/lysis buffer was scaled down to the microchamber volume (16µl), 5.3µl blood and 10.6µl Dynabeads lysis buffer.
- Blood and lysis buffer were introduced to the chamber using 25µl Hamilton syringes from two inlets.
- The mixing time was performed in 3 minutes with coil current of 155 mA.
- After mixing, DC magnetic field was used to clamp the magnetic beads inside the chamber. This process was performed using bottom coil with current of 180 mA.
- Chamber content was removed and the magnetic beads-DNA complex was clamped and washed using100 µl wash buffer. A Hamilton syringe was used for washing process.
- After washing process, wash buffer was removed and beads were incubated with 10µl elution buffer. In this step, AC magnetic mixing was performed in 1 minute to release the DNA molecules from the beads.
- DC magnetic field was applied to hold the beads and extract the resuspended DNA molecules in elution buffer.
- Chamber was washed with *Microsol 3+* decontamination reagent (detergent with anti-microbial and nucleic acid degradation properties) to be reused for the next experiments.

The experiment was performed in three replicates and additional negative controls (water). DNA resuspension process was investigated using two different techniques, using elution buffer and thermal elution using incubation at 65°C.

7.2.2 Results and Discussion

The efficiency of extraction was controlled during the incubation step and no obvious cellular lysis was observed. Clamping process found to be particularly problematic due to the build-up of debris within the chip. The long clamping during washing process resulted in temperature rise within the chip, which caused denaturation of unlysed sample. *Microsol 3+* washing process between individual experiments was unable to remove the materials. Therefore, an extensive washing protocol was required to clean the chip. A new harsh chamber wash condition was investigated by incubating/washing using a mixture of 1% SDS detergent/0.2M NaOH (1 hour plus). This washing process appeared to remove the bound materials in the chamber. The result of chip extraction was analysed using Nanodrop 1000 spectrophotometer. The minimum sample required in this device is 1.2µl and the dynamic range is 1-2 ng/µl to 3700 ng/µl. However the output of the spectrophotometer is based on 1µl sample input. The measurement was performed in three replicates for each extracted sample and the average results are given in Table 7.1. This table gives the extracted DNA yield in ng/µl and the quality/purity of the extracted DNA sample was analysed using A260/A280 and A260/A230.

As it is shown in this table, the quantity of the extracted DNA is very low and close to the sensitivity of the spectrophotometer. Therefore, the quantity of the extracted DNA cannot be verified using this method. The quality of the purified sample is also very low, which indicates the presence of the proteins and salts in the extracted sample. This result is not surprising, as the washing process was not efficient due to the presence of bound materials inside the chip after the washing process.

Table 7.1. Nanodrop data given for extracted DNA sample using Dynabeads DNA universal kit.

Sample ID	A260/A280	A260/A230	DNA Yield (ng/µl)
Dynabeads elution Buffer	0.02	0.02	0.01
Blood, Eluted using Elution Buffer	0.69	0.42	1.39
Blood, Eluted using Incubation at 65°C	0.60	0.44	2.47
–ve Extraction Control	0.65	0.49	0.89
–ve Extraction Control (65°C)	0.43	0.42	1.51

A more sensitive plate-based PicoGreen dsDNA quantitation technique was used to quantify the yield of the extracted DNA. The sensitivity of this technique was approximately 0.1 ng/µl detection limit. However, no DNA was detected using this enhanced technique, which indicates very poor DNA recovery of the modified Dynabeads DNA direct universal protocol. Based on the manufacturer's guideline, 20ng – 33ng DNA can be extracted from 1µl of blood sample. The result of this experiment shows that the level of extracted DNA is much below the guideline. The potential recovery issues could be the sub-optimal lysis buffer conditions or loss of DNA-attached beads during the clamping process. Since the result shows very poor DNA yield, the potential problem could be the lysis buffer conditions. This problem can be investigated by comparing the result of the standard protocol, which is the subject of the next section.

7.3 Optimisation of the Bench-top Extraction Protocol

Since the results of Dynabeads DNA direct kit was not satisfactory using modified protocol, a series of experiments were conducted to identify the most efficient extraction protocol. Manufacturer's standard protocols were used under optimal conditions using manual extractions on bench-top. Extraction kits investigated were QIAamp Blood Mini kit (column-based), MagaZorb DNA Mini-prep kit (bead-based), Dynabeads SILANE genomic DNA kit (bead-based) and Dynabeads DNA Direct Universal (bead-based). The experiment aimed to compare the extraction efficiency of the selected kits in order to be used for further optimisation for chip-based DNA extraction.

7.3.1 Experimental Setup

A summary of the standard manufacturer's protocols and volumes of different buffers are given in Table 7.2 for different extraction kits. This table indicates that the ratio of kit reagents to blood sample is lower for QIAamp kit (2.1:1) and very high for Dynabeads DNA Direct Universal kit (20:1). This ratio is important for chip-based extraction, since larger chamber volumes are necessary for larger ratios.

In these experiments, both fresh blood and frozen blood samples (sodium citrate anticoagulated human whole blood, *Sera Laboratories International Ltd., USA*) were used for extraction. Frozen blood contains pre-lysed cells, and therefore acts as a

basic positive extraction control. In addition, the freed DNA molecules inside the frozen blood sample can verify the binding efficiency of the bead-based kits. As it is shown in the Table 7.2, the volumes of the blood samples are not identical in different kits. These ratios were kept as recommended by the manufacturers' in order to compare the efficiency of their extraction at optimal conditions. However, the final yield of DNA can be normalised based on the used sample.

The experiment was carried out in three replicates for each sample (fresh blood, frozen blood and negative control) and was repeated two times. Water sample was used as the extraction negative control.

Table 7.2. A summary of the manufacturer's protocols for the short-listed kits.

	QIAamp Blood Mini Kit	**MagaZorb DNA Mini-Prep Kit**	**Dynabeads SILANE DNA Kit**	**Dynabeads DNA Direct Universal**
Blood Volume	200 µl	200 µl	350 µl	10 µl
Proteinase K Step	20 µl	20 µl	50 µl, 2 min Incubation at Room Temperature	NA
Lysis Step	200 µl Lysis Buffer, 10 min Incubation + 200 µl ethanol	200 µl, 10 min Incubation at 56°C	NA	NA
Binding Step	Centrifuge	500 µl + 20 µl Magnetic beads, 10 min Incubation at Room Temperature	NA	NA
Lysis + Binding Step	NA	NA	350 µl, 10 min Incubation at 55°C + 50 µl Dynabeads + 400 µl Isopropanol, 3 min Incubation at Room Temperature	200 µl, 5 min Incubation at Room Temperature
Washing Step	2 × 500 µl	2 × 1ml	4 × 950 µl + 5 min Drying step	2 × 200 µl
Elution Step	200 µl, 1 min Incubation	200 µl, 10 min Incubation at Room Temperature	100 µl, 2 min Incubation at Room Temperature	100 µl at Room Temperature
Ratios of Kit reagents to Blood Sample	2.1:1	3.7:1	2.43:1	20:1

7.3.3 Results and Discussion

Recovered DNA samples were quantitated using Nanodrop 1000 spectrophotometer and are given in Table 7.3. The spectrophotometer was blanked for elution buffer and the measurements were repeated in three replicates. The results shown in Table 7.3 are given as the average of three measurements. Since recovered DNA samples were eluted in different volumes of the elution buffer, extracted DNA yield is calculated for total elution buffer. To compare the efficiency of the extraction, the recovery of each extraction kit is normalised based on the extracted DNA yield per microliters blood sample.

As it was expected, the Qiagen QIAamp column-based extraction kit gives the highest recovery level at 17 – 21 ng DNA/µl blood. MagaZorb and Dynabeads SILANE kit demonstrating very similar levels at 7 – 15 ng DNA /µl blood. However, the recovery level of Dynabeads SILANE kit is slightly higher than MagaZorb. The quality of DNA samples recovered by these three kits is also very good, as shown by high A260/A280 ratios. The poorest DNA recovery was observed with Dynabeads Universal kit at 2 – 5 ng DNA/µl blood. Since the volume of the used blood in this kit was much less than the volume of recommended elution buffer, a lower elution buffer (40 µl) was used to increase the concentration of DNA. However, the low levels of the recovered DNA sample with this kit approached the detection limit of the UV spectrophotometer. Therefore, this experiment was repeated and recovered DNA sample was eluted in 20 µl elution buffer. The quality of DNA sample extracted with this kit was measured at very low level. This indicates the inefficiency of the lysis process, as it also was observed during the experiment. The yield of recovered DNA sample is higher with frozen blood in all of the kits. This is because the majority of the cells are lysed in frozen blood.

The comparison between these results indicates that Dynabeads Universal kit is not suitable for automated on-chip extraction process, in spite of its simple and rapid extraction protocol. Therefore, MagaZorb and Dynabeads SILANE kits were selected to be used for on-chip extraction process. However these kits are designed for manual bench-top extraction process and their protocols are not suitable for automated extraction process. Therefore, their extraction protocol needs to be optimised for chip-based extraction process.

Table 7.3. Analyzed recovered DNA samples using Nanodrop 1000 spectrophotometer.

	A260/A280	A260/A230	Yield (ng/µl)	Standard Deviation	Corrected Average	Total Yield (ng)	Yield Per µl Blood (ng/µl)
Qiagen, EB	-0.97	-0.18	0.32	-	-	-	-
Qiagen, B	1.90 ± 0.02	1.73 ± 0.40	20.16	1.21	17.05	3410.33	17.05
Qiagen, FB	1.75 ± 0.15	0.99 ± 0.64	23.80	2.75	20.69	4138.67	20.69
Qiagen, –ve	1.49 ± 0.43	-1.55 ± 3.36	3.11	1.19	0.00	0.00	0.00
MagaZorb, EB	0.84	0.91	-1.40	-	-	-	-
MagaZorb, B	2.04 ± 0.11	0.99 ± 0.02	17.82	0.29	7.64	1528.00	7.64
MagaZorb, FB	1.98 ± 0.08	0.82 ± 0.07	22.96	0.59	12.78	2555.67	12.78
MagaZorb, –ve	1.98 ± 0.22	0.74 ± 0.05	10.18	0.03	0.00	0.00	0.00
DS, EB	1.14	-19.65	-0.39	-	-	-	-
DS, B	1.91 ± 0.06	1.78 ± 0.09	28.95	6.88	28.85	2885.43	8.24
DS, FB	1.90 ± 0.03	2.15 ± 0.04	51.86	4.23	51.76	5176.17	14.79
D S, -ve	-0.22 ± 0.59	0.09 ± 0.05	0.10	0.07	0.00	0.00	0.00
DU, EB	-1.23	0.79	0.14	-	-	-	-
DU, B	1.09 ± 0.58	0.30 ± 0.10	0.56	0.17	0.09	3.53	0.35
DU, FB	1.56 ± 0.45	0.60 ± 0.13	1.79	0.69	1.32	52.93	5.29
DU, -ve	0.95 ± 0.13	0.33 ± 0.12	0.47	0.03	0.00	0.00	0.00
DU2, EB	0.81	0.53	0.31	-	-	-	-
DU2, B	0.89 ± 0.22	0.22 ± 0.15	1.78	0.44	1.20	24.03	2.40
DU2, -ve	0.50 ± 0.40	0.25 ± 0.17	0.57	0.42	0.00	0.00	.00

EB: Elution Buffer, **B**: Blood, **FB**: Frozen Blood, **-ve**: Extraction Negative Control
DS: Dynabeads SILANE Genomic DNA Kit, **DU&DU2**: Dynabeads DNA Universal Kit

7.4 Initial Evaluation of *Magazorb* and *Dynabeads SILANE* kits

As discussed in the previous sections, Dynabeads DNA Direct Universal kit generated very low DNA recovery at chip-based extraction process using modified extraction protocol. Further evaluation of this kit indicated a very low recovery level in comparison with other extraction kits, even at optimised conditions using manufacturers' standard protocols. MagaZorb and Dynabeads Universal kits generated higher DNA yields, but their protocol is designed for manual bench-top extraction process. Therefore, a series of experiments were conducted to investigate the impact of different modified standard manufacturers' extraction protocols to a more automation friendly methodology with shorter processing times and higher DNA recovery rates.

7.4.1 Experimental Setup

Three different extraction protocols were initially investigated with different processing times and steps. These modified protocols are defined as follows:

- A – Standard manufacturer's protocol: This protocol was selected for comparison purpose. The standard protocols comprising separate processing steps as proteinase K, lysis and binding steps.
- B – Two step protocol: In this protocol, the proteinase K and lysis steps were combined and the processing time was set to 2 minutes. The second step was binding step with 5 minutes incubation time.
- C – Combined protocol: In this protocol, all of the extraction steps were combined in one step using single proteinase K/lysis/binding step with 5 minutes incubation time.

The washing process and elution step were performed separately as indicated in the manufacturer's protocol. Reagent volumes were scaled relatively for 200 µl blood sample in all protocols. Frozen blood sample, which contains unlysed and lysed cells, was used for the extraction process to evaluate the efficiency of the lysis and binding process. Each experiment was performed with three replicates and two negative extraction controls using water sample. The extracted DNA sample was eluted in 200 µl elution buffer.

7.4.2 Results and Discussion

Recovered DNA samples were quantitated using Nanodrop 1000 spectrophotometer and the measurements were performed using three replicates from each sample. In order to reduce the background noise generated from the elution buffer, the spectrometer was blanked for the elution buffer. The results of this experiment are shown in Table 7.4 as the average of different measurements and replicates for each sample. Both kits produce high quality DNA sample, as shown by A260/A280. Two steps protocol seems to produce higher DNA yields in comparison to the standard extraction protocol in both extraction kits. However, Dynabeads SILANE kit shows higher recovery rate in comparison to MagaZorb kit. A very high peak was observed with Dynabeads extraction control, which could be the result of residual Isopropanol during washing process. Noticeably higher DNA yield was observed with MagaZorb kit with the combined protocol. These results indicate that there is significant room for optimisation of the extraction protocol for on-chip automated extraction process.

Table 7.4. A comparison result of DNA extraction process using Dynabeads SILANE and MagaZorb kits using three different protocols, A: standard manufactures' protocol, B: two-step protocol and C: combined protocol. These results were produced using Nanodrop 1000 spectrophotometer.

	Average A260/A280	Average A260/A230	DNA Yield (ng/µl)	Corrected Average Yield (ng/µl)	Total DNA Yield (ng)
Dynabeads SILANE, Elution Buffer	-0.18	-0.12	0.03	-	-
Dynabeads SILANE, Protocol A	1.74	0.52	39.88	15.74	3148.67
Dynabeads SILANE, Protocol B	1.79	0.52	42.93	18.79	**3758.67**
Dynabeads SILANE, Protocol C	1.78	0.50	36.53	12.40	2479.33
Dynabeads SILANE, Extraction Control	1.64	0.50	24.14	0.00	0.00
MagaZorb, Elution Buffer	-0.07	0.41	0.08	-	-
MagaZorb, Protocol A	1.45	0.56	8.45	8.41	1682.67
MagaZorb, Protocol B	1.54	1.24	10.50	10.47	2093.00
MagaZorb, Protocol C	1.68	1.05	35.05	35.01	**7002.00**
MagaZorb, Extraction Control	0.06	0.38	0.04	0.00	0.00

7.5 Further Optimisation of the *Dynabeads SILANE* kit

As it was shown in the previous section, the modified protocols produced high DNA yields in both Dynabeads SILANE and MagaZorb kits. However, the result was obtained with frozen blood sample, which contains some pre-lysed cells. In order to evaluate the extraction efficiency, further characterisation of these kits is necessary using fresh blood sample and bacterial cells. Therefore, Dynabeads SILANE kit was selected to investigate the efficiency of the modified extraction protocols on the fresh blood sample and bacterial cells.

7.5.1 Manual Characterisation of Dynabeads SILANE Kit

7.5.1.1 Experimental Setup

The efficiency of the adapted extraction protocols was investigated by scaling down the total kit reagent/sample volumes to 100 µl. The scaled protocol volumes are given in Table 7.5. Manual bench-top extraction was performed using adapted two-

steps and combined protocols. Two-steps protocol comprised combined proteinase K/lysis step (2 minutes incubation at 56°C) and with a 5 minutes DNA binding step. Combined protocol comprises a single processing step of proteinase K/lysis/DNA binding with a 5 minutes incubation time at 56°C temperature. In addition to the blood samples, bacterial cell extraction performance was also investigated using *E. coli* culture sample. The approximate concentration of bacterial cells was calculated, which is in the order of $1 \times 10^6\ cells/\mu l$. The total weight of the *E. coil* DNA molecules presented in 29.18 µl used sample was calculated to be approximately 147 ng/µl. In the washing and elution processes, manufacturer's protocol was followed using separate wash and elution steps. Extracted DNA was eluted in 20 µl elution buffer. The extraction process was performed using three replicates for blood and cell samples using separate extraction controls in each protocol.

7.5.1.2 Results and Discussion

Recovered DNA samples were quantitated using Nanodrop 1000 spectrophotometer with 1.2 µl sample volume and replicate measurements. The results of this experiment are shown in Table 7.6. Both extraction protocols produced high quality DNA samples, as shown by A260/A280 index. Despite the previous results using frozen blood sample, Dynabeads SILANE kit produces higher DNA yields with fresh blood sample using combined step extraction method (protocol C). Both protocols produced excellent extracted DNA yield with *E. coli* sample. However, two-steps protocol (protocol B) seems to be more efficient with bacterial cells. These results demonstrate efficient bacterial cells lysis as well as effective DNA binding capabilities using adapted protocols. This finding indicates that these adapted protocols are suitable for use in subsequent automated on-chip extraction process.

Table 7.5. The volumes of Dynabeads SILANE kit reagents scaled down for 100 µl total volume.

Component	Standard Protocol Volumes	Scaled Protocol Volumes
Proteinase K	50 µl	4.14 µl
Blood/sample	350 µl	29.18 µl
Lysis/binding buffer	350 µl	29.18 µl
Dynabeads	50 µl	4.17 µl
Isopropanol	400 µl	33.3 µl

Table 7.6. A comparison between Nanodrop results of Dynabeads SILANE kit DNA extraction process using two adapted protocols. B: two-step protocol and C: combined protocol.

	Average A260/A280	Average A260/A230	Average DNA Yield (ng/µl)	Corrected Average Yield (ng/µl)	Total DNA Yield (ng)
Elution Buffer	0.51	0.82	-0.57		
Protocol B, Blood	2.79	1.49	7.39	6.98	139.50
Protocol B, *E. coli*	1.79	1.55	252.92	252.50	5050.07
Extraction Control	-1.33	0.22	0.41	0.00	0.00
Protocol C, Blood	2.11	1.38	15.59	14.48	289.50
Protocol C, *E. coli*	1.76	1.36	147.82	146.71	2934.13
Extraction Control	2.07	0.27	1.12	0.00	0.00

7.5.2 On-chip Characterisation of Dynabeads SILANE Kit

The results of the manual extractions indicated that simplified adapted protocols can produce high DNA yields, and thus can be used for on-chip extraction process. Combined protocol, with simplified single processing step (combined proteinase K/lysis/binding step), is more suitable for automated on-chip extraction process. Therefore, an experiment was conducted to investigate the performance of the partially optimised Dynabeads SILANE manual protocol on low-volume DNA extraction chip. However, to reduce the impact of different variables, clamping, washing and elution processes were performed manually on the bench-top. The focus was instead given to compare the performance of the on-chip lysis/binding process against the manual process.

7.5.2.1 Experimental Setup

The experiment was performed in low-volume chip (16µl, 8 mm in diameters and 300µm chamber depth, see section 6.4.1) and all reagents were scaled down relatively. Experiment was carried out in three replicates to reduce the variability and parallel bench-top experiments were performed using the same reagents and samples for comparison purpose. To investigate the recovery level (using real-time PCR assay), *B. subtilis* bacterial DNA sample was spiked into blood at approximately 10,000 genomic copy levels. Fresh blood was used as the negative extraction control in addition to the standard negative control. The enzymatic incubation step was

increased to 10 minutes at 55°C for both on-chip and manual extraction process. At the end of chip-based incubation, the sample was extracted from the chip to perform the washing and elution process manually. The extracted DNA sample was eluted in 10 µl elution buffer. On-chip mixing was performed using a pair of external magnetic coils (coil 2×4) at switching frequency of $f = 1\ Hz$ and coil current of 155 mA. The temperature rise required for incubation process (55°C) was generated rapidly using DC current mode and the maintaining the temperature using switching approach. In addition to the standard DNA quantitation technique (UV spectrophotometer), a quantitative real-time PCR assay was developed to determine bacterial DNA extraction recovery level. Standard curves were generated using $10^5 - 10^{-1}$ gDNA copies and were used to calculate approximate concentration of recovered bacterial DNA within the extracted DNA samples (using 1µl sample volumes).

7.5.2.2 Results and Discussion

Recovered DNA samples were quantitated using Nanodrop 1000 spectrophotometer and average values are given in Table 7.7. In comparison to the earlier chip-based extraction (section 7.2), no obvious clogging was observed inside the chip. This is because of lower volume of blood sample and better buffer conditions by keeping the standard ratio of buffers to the blood sample. However, minor material build-up was observed on the chip after washing process, which could not be removed using Microsol 3+ detergent washes. A minor beads trapping was observed inside the chip, which could be due to the coarse surface roughness of the chamber walls (made of PDMS). Therefore, a long washing process (1 hour plus) was performed using 0.2 M NaOH/1% SDS mixture to remove the built-up materials and trapped beads. Stable temperature required for enzymatic incubation step was obtained by magnetic coils with 30 sec temperature rise time.

Chip sealing failed during the experiment and leaking was observed within the chip. After incubation process, it was observed that the majority of the sample and buffers were forced out of the chip into the tubing. This might be because of the evaporation of the Isopropanol (boiling point: 82.4°C) during the incubation step at 55°C temperature. Displaced sample was observed gradually returned to the chamber by cooling off the chamber. Therefore, a portion of the displaced sample was not lysed

efficiently and could be the cause of the minor material built-ups inside the chamber. The impact of partially lysed sample could be the result of lower quality of the extracted DNA (as shown by A260/A280 in Table 7.7). In addition, low DNA recovery levels with chip-based extraction could be the result of partially lysed sample due to the evaporation of the Isopropanol. However, DNA was extracted from chip-based extraction process. The efficiency of the chip-based can be compared to the manual extraction by normalising the yields for used blood samples (as shown in Table 7.7).

To evaluate the recovery level of the spiked *B. subtilis* bacterial DNA into blood sample, a real-time assay was developed against *B. subtilis* microorganism. Real-time PCR analysis was performed using *Applied Biosystems 7900HT* Fast Real-Time PCR system using a 96-well plate. The PCR was performed using 3x replicates from each extracted sample (blood, spiked blood and negatives) as well as the original spiked blood. Figure 7.1 illustrates plots of standard curves and amplification extracted for this experiment. Presence of *B. subtilis* was not observed in the PCR results of blood samples and negative controls. Approximate recovery levels for the spiked *B. subtilis* bacterial DNA copy numbers were calculated for chip-based and manual extraction process as follows:

- Manual extraction: 135 copies/µl = 1350/10k total = 13.5% recovery
- Chip-based extraction: 6 copies/µl = 60/10k copies total = 0.6% recovery

Table 7.7. A comparison between chip-based and manual extraction protocols (protocol C, combined steps) using Dynabeads SILANE kit. The results are shown for fresh blood samples and spiked B. subtilis bacterial DNA into the blood.

	Average A260/A280	Average A260/A230	Average DNA Yield (ng/µl)	Corrected Average Yield (ng/µl)	Yield Per µl Blood (ng/µl)
Elution Buffer	0.38	0.76	0.28	-	-
Chip DNA/Blood	1.07	0.57	1.91	1.27	2.75
Manual DNA/Blood	1.77	1.22	3.64	3.44	7.47
Chip Blood	1.02	0.48	1.11	0.47	1.02
Manual Blood	1.78	1.29	4.25	4.05	8.79
Chip Control	1.14	0.22	0.64	0.00	0.00
Manual Control	0.85	0.05	0.21	0.00	0.00

Low level bacterial DNA recovery was observed with both chip-based and manual extraction. Although the poor recovery levels calculated for the chip-based extraction could be the result of Isopropanol evaporation, the results of the manual extraction suggests that the extraction protocol requires more optimisation. In conclusion, low level DNA recovery and on-chip evaporation of Isopropanol during the incubation step (at 55°C temperature) indicates that Dynabeads SILANE kit is not suitable for automated chip-based extraction process. Since AGOWA Sbeadex kit reagents contain Isopropanol treatment step, therefore, this kit was also eliminated for further processing and optimisation process was further investigated using MagaZorb extraction kit.

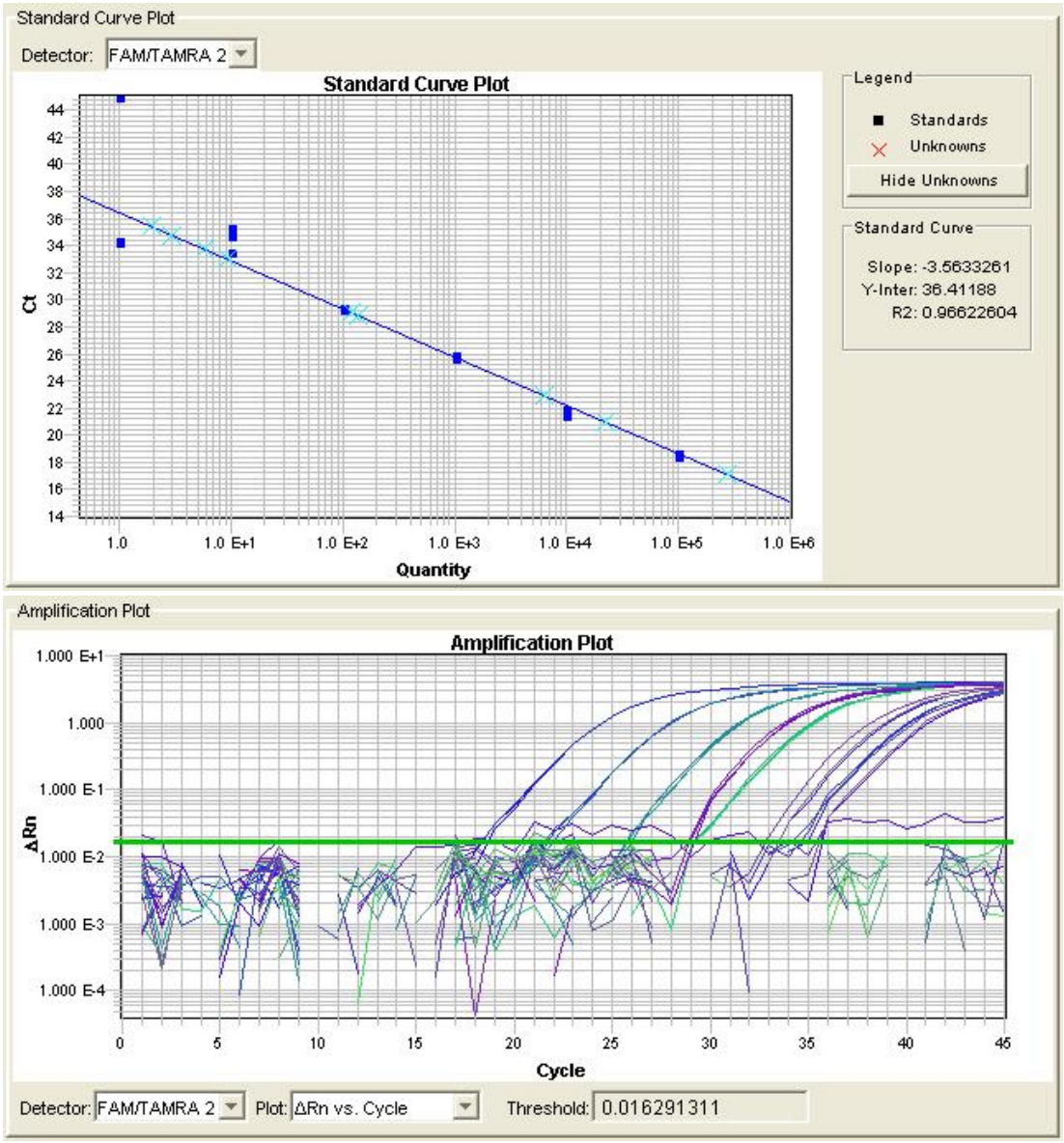

Figure 7.1 Quantitative real-time PCR determination of *B. subtilis* genomic DNA copy levels within extracted DNA samples. a) Standard curve plot. a) Standard amplification plot.

7.6 Characterisation of the Magazorb DNA Mini-prep Kit

The performance of the Dynabeads SILANE kit modified extraction protocol was investigated using chip-based and parallel manual extraction process. Combined protocol was used due to its simplicity and excellent DNA yield on bench-top extraction process. To determine bacterial recovery levels, blood sample was spiked with *B. subtilis* DNA sample and real-time PCR assay was used to calculate the recovery levels. It was observed that the evaporation of Isopropanol during incubation at 55°C temperature forced the sample out of the chip and caused serious damage to the chip sealing and bonding. Therefore, it was decided to stop further optimisation process using this kit and the focus was given to optimisation of MagaZorb kit. Two different experiments were conducted to evaluate on-chip bacterial DNA extraction efficiency of MagaZorb kit using simplified combined protocol. The efficiency of DNA binding and collection was investigated using spiked bacterial sample to the blood and lysis efficiency was determined using spiked bacterial cell sample to the blood.

7.6.1 On-chip Binding Efficiency of MagaZorb Combined Protocol

Efficient binding of released DNA from lysed cells is the most important parameter in the DNA extraction process. This parameter was investigated using spiked DNA sample into the blood. The efficiency of the binding was evaluated by calculation of the recovered DNA levels using quantitative real-time PCR.

7.6.1.1 Experimental Setup

The experiment was performed using low-volume chip (16µl, 8 mm in diameters and 300µm chamber depth, see section 6.4.1) and all reagents were scaled down relatively (as given in Table 7.8). Experiment was carried out in three replicates to reduce the variability and parallel manual bench-top extraction was performed using the same reagents and samples for comparison purpose. Chip decontamination process was performed using long washing process (1 hour plus) using 0.2 M NaOH/1% SDS mixture. Bacterial DNA sample (*B. subtilis*) was spiked into the blood at approximately 10,000 copy levels. Fresh blood was used as the negative extraction control in addition to the standard negative control. The enzymatic

incubation step was performed in 10 minutes at 56°C for both on-chip and manual extraction process. The required temperature was generated and maintained using the external magnetic coils and attached temperature sensor. Chip-based washing and elution steps were performed manually, outside of the chip, by transferring the sample to the eppendorf tubes. The extracted DNA sample was eluted in 10 µl elution buffer. On-chip mixing was performed using a pair of external magnetic coils (coil 2×4) at switching frequency of $f = 1\ Hz$ and coil current of 155 mA. All chip-based fluid handling process was performed manually using Hamilton syringes (25 µl and 100 µl syringes).

7.6.1.2 Results and Discussion

In addition to the standard DNA quantitation technique (UV spectrophotometer), a quantitative real-time PCR assay was developed to determine bacterial DNA extraction recovery levels. Standard curves were generated using $10^5 - 10^{-1}$ gDNA copies and were used to calculate approximate concentration of recovered bacterial DNA within the extracted DNA samples (using 1µl sample volumes).

Table 7.9 shows the results of DNA quantitation using Nanodrop 1000 spectrophotometer for both manual and chip-based extraction process. These results were calculated as the average of the multiple measurements. Both chip-based and manual extractions produced high quality DNA samples, as shown by A260/A280 index. As it was expected, chip-based extractions produced higher yields in comparison to the manual extractions (average of 13.63 ng/µl to 9.49 ng/µl). This is because of higher surface to volume ratio and continuous active mixing process.

Table 7.8. The volumes of MagaZorb kit reagents scaled down for 16 µl total volume of chip.

Component	Standard Protocol Volumes	Scaled Protocol Volumes
Proteinase K	20 µl	0.34 µl
Blood/sample	200 µl	3.4 µl
Lysis Buffer	200 µl	3.4 µl
Binding Buffer	500 µl	8.5 µl
MagaZorb Beads	20 µl	0.34 µl
Wash Buffer	2 × 1 m1	2 × 17 µl
Elution Buffer	200 µl	10 µl

Table 7.9. A comparison between chip-based and manual extraction protocols (protocol C, combined steps) using Dynabeads SILANE kit. The results are shown for fresh blood samples and spiked blood with *B. subtilis* bacterial DNA.

	Average A260/A280	Average A260/A230	Average DNA Yield (ng/µl)	Corrected Average Yield (ng/µl)	Yield Per µl Blood (ng/µl)
Elution Buffer	-0.15	-1.22	-0.05	0.00	0.00
Chip DNA/Blood	1.53	0.24	12.79	6.30	18.54
Chip Blood	1.86	0.33	10.28	3.80	11.18
Average Chip	**1.69**	**0.28**	**11.12**	**4.63**	**13.63**
Chip Control	2.12	0.45	6.48	0.00	0.00
Manual DNA/Blood	2.48	0.32	6.28	3.09	9.09
Manual Blood	2.55	0.45	6.55	3.37	9.90
Average Manual	**2.52**	**0.39**	**6.41**	**3.23**	**9.49**
Manual Control	1.87	0.48	3.19	0.00	0.00

A real-time PCR assay was developed against B. subtilis microorganism to evaluate the recovery level of the spiked *B. subtilis* bacterial DNA into blood sample. Real-time PCR analysis was performed using *Applied Biosystems 7900HT* Fast Real-Time PCR system using a 96-well plate. The PCR plate was seeded using 3x replicates of each extracted sample, the original spiked blood and the standard DNA samples. Figure 7.2 shows plots of standard curves, standard amplification and sample amplification, extracted for this experiment. Presence of *B. subtilis* was not observed in non-spiked blood samples and negative controls. Approximate recovery levels for the spiked *B. subtilis* bacterial DNA copy numbers were calculated for chip-based and manual extraction process and are given in Table 7.10. A very similar recovery levels were obtained with both extractions, 30.19% with chip-based and 38.08% with manual extraction process.

Table 7.10. Quantitative real-time PCR determination of *B. subtilis* genomic DNA copy levels within extracted DNA samples.

	Average Quantity	Standard Deviation	Total DNA in 10 µl Vol.	% DNA Recovery
Chip DNA/Blood	301.91	49.69	3019.10	30.19
Manual DNA/Blood	380.76	23.02	3807.62	38.08

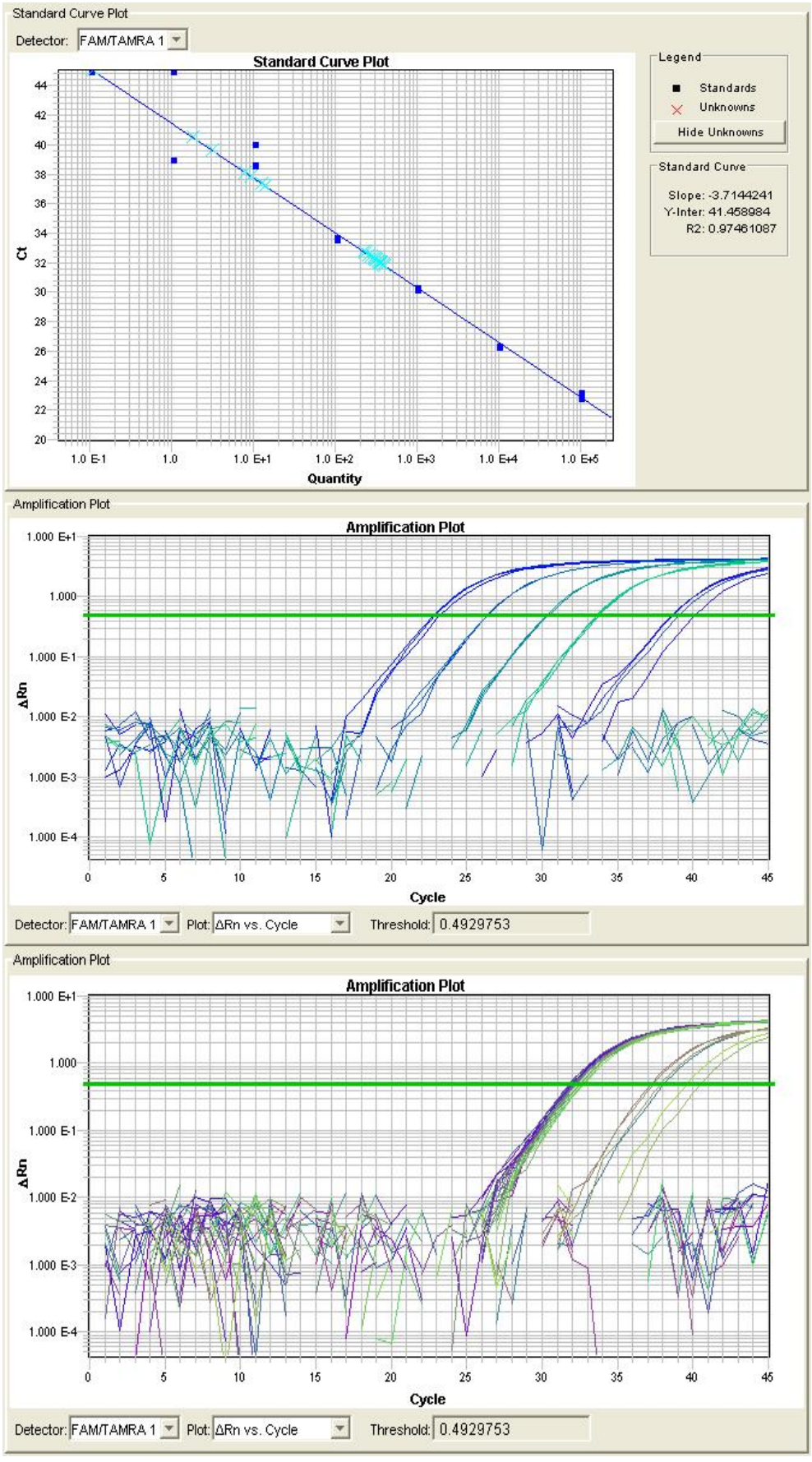

Figure 7.2. Quantitative real-time PCR determination of *B. subtilis* genomic DNA copy levels within extracted DNA samples. a) Standard curve plot. b) Standard amplification plot. c) Sample amplification plot.

By comparing the above results (Table 7.9 and Table 7.10), higher total DNA yield was obtained with chip-based extraction using UV spectrophotometer. While a similar result was expected from quantitative real-time PCR, slightly lower yield was calculated using real-time PCR evaluation. The difference between DNA yield of the chip-based and manual extractions can be explained by two main reasons. The first reason is the higher bead-loss ratio in chip-based extraction due to the bead-trapping inside the chamber and tubing during sample handling. In addition, the lower sample ratio of the chip-based extraction (due to the trapped air-pockets) could be another cause of lower DNA recovery. The lower total yield of manual extraction (38%) indicates that the binding step might not be efficient in sub-optimal buffer conditions of the combined protocol. In addition, the difference between the average number and length of blood genomic DNA molecules to the spiked bacterial DNA sample could be another reason of lower binding efficiency. The average size of human genomic DNA is in the order of 100 M base-pairs, which is 23 times bigger than that of a typical *B. subtilis* bacterial DNA length (4.2 M base-pairs). Since DNA molecules are negatively charged, different DNA sizes indicates that inter-molecular repulsive forces (Coulomb force) can reduce the binding efficiency of the bacterial DNA to the beads.

7.6.2 On-chip Lysis Efficiency of MagaZorb Combined Protocol

In addition to the evaluation of the DNA-bead binding, lysis efficiency was investigated using spiked bacterial cells into the blood sample. The experimental setup was kept similar to the previous experiment (section 7.5.1.1). Approximately 100,000 copy numbers of *B. subtilis* bacterial cells culture were spiked into the blood sample. On-chip and parallel manual extractions were performed in three replicates using blood and negative extraction controls. The ratios of the sample and reagents were used as given in Table 7.8. The recovered DNA samples were analysed using Nanodrop 1000 spectrophotometer and quantitative real-time PCR techniques and the results are shown in Table 7.11 and Table 7.12.

The results of Nanodrop quantitation (Table 7.11) show excellent DNA yields with chip-based extraction and manual extraction. As expected, chip-based extraction seems to be more efficient due to the active continuous magnetic mixing. Both extractions produced high quality DNA sample, as it is shown by A260/A280 index.

Recovered DNA samples were analysed using quantitative real-time PCR and the average results are given in Table 7.12. No trace of bacterial DNA was found in the negatives and blood samples. The actual cell concentration was determined by PCR as 97,664 cells/µl blood, and the DNA recovery calculations were corrected based on this concentration. Plots of standard curves, standard amplifications and sample amplifications are shown in Figure 7.2. Manual extraction process shows higher bacterial DNA recovery in comparison to the chip-based extraction, which is in agreement with the previous experimental results. These results indicate that the combined extraction protocol is not optimised for the Gram positive bacterial extraction process. Although Gram positive cells are more resistant to the lysis buffer, with comparison to DNA binding results (Table 7.10), the main reason for the low recovery rates could be the binding efficiency.

Table 7.11. A comparison between chip-based and manual extraction protocols (protocol C, combined steps) using MagaZorb kit. The results are shown for fresh blood samples and spiked blood with *B. subtilis* bacterial cells.

	Average A260/A280	Average A260/A230	Average DNA Yield (ng/µl)	Corrected Average Yield (ng/µl)	Yield Per µl Blood (ng/µl)
Elution Buffer	-0.87	0.61	0.35	-	-
Manual Blood	1.84	0.54	5.59	3.31	9.74
Manual Cells/Blood	2.22	0.58	7.44	5.16	15.18
Average Manual	**2.03**	**0.56**	**6.52**	**4.24**	**12.46**
Manual Control	2.20	0.36	2.28	0.00	0.00
Chip Blood	1.70	0.39	8.46	6.05	17.79
Chip Cells/Blood	2.17	0.51	8.71	6.30	18.53
Average Chip	**1.93**	**0.45**	**8.58**	**6.18**	**18.16**
Chip Control	1.65	0.34	2.41	0.00	0.00

Table 7.12. Quantitative real-time PCR determination of *B. subtilis* genomic DNA copy levels within extracted DNA samples.

	Average Quantity	Standard Deviation	Total DNA in 10 µl Vol.	% DNA Recovery
Manual Cells/Blood	6936.01	1021.45	69360.08	20.89
Chip Cells/Blood	3267.80	197.56	32677.99	9.84

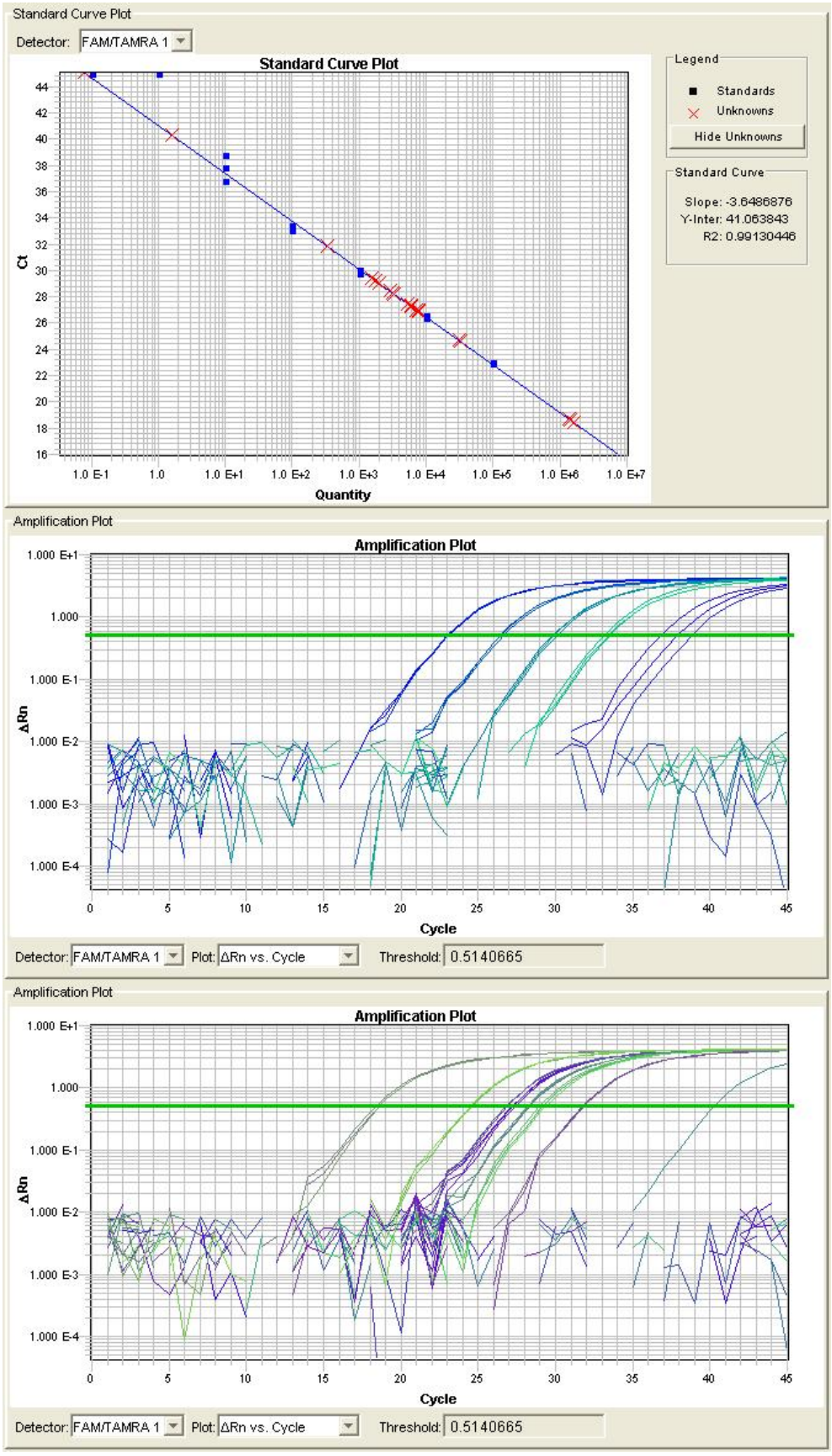

Figure 7.3. Quantitative real-time PCR determination of *B. subtilis* genomic DNA copy levels within extracted DNA samples. a) Standard curve plot. b) Standard amplification plot. c) Sample amplification plot.

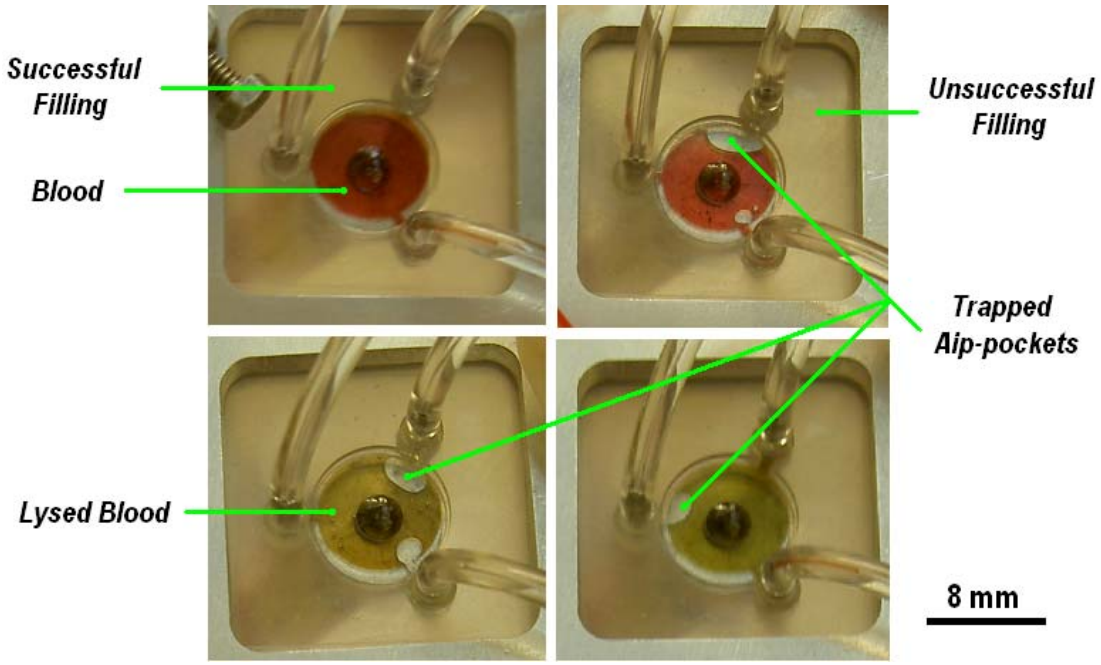

Figure 7.4. A photograph of the microchamber before and after lysis step indication air-pocket trapping issues. The olive green colour indicates blood lysis accomplishment.

In addition to the above problems (low binding efficiency and sub-optimal buffer conditions), the chip-based results were influenced by air-pocket trapping inside the chamber. Figure 7.4 shows a photograph of the filled microchamber before and after lysis step with small tapped air-pockets. On average, occupied volume of air-pockets was measured as large as 10% of the total chamber volume, during the extraction process.

7.7 Optimisation of the Magazorb Kit by On-chip Clamping and Elution steps Using Two-step Protocol

As shown in the above section, combined extraction protocol produced low DNA recovery rates using *B. subtilis* bacterial sample with both chip-based and manual extractions. The main reason for such low recovery rates could be the sub-optimal conditions of the lysis buffer. Therefore, an experiment was conducted to improve the lysis conditions using two-step protocol, which has separate lysis and binding steps. In addition, to fully investigate the efficiency of the extraction chip, the whole extraction process was performed inside the chip including cell lysis, DNA binding, bead clamping/washing and elution steps. The efficiency of lysis step was investigated using two different bacterial cell cultures spiked into the blood sample,

B. subtilis (Gram-positive) and *E.coli* (Gram-negative). Binding efficiency was investigated using spiked DNA (*pSTI* plasmid DNA) into the blood sample.

7.7.1 Experimental Setup

The experiment was performed using low-volume disposable chips (25µl, 8 mm in diameters and 500µm chamber depth, see section 6.4.1) and all reagents were scaled down relatively (as shown in Table 7.13). Two different Bacterial cell cultures (*B. subtilis* and *E. coli*) were spiked into the blood at approximately 100,000 copy levels. Prior to the spiking process, a real-time PCR assay was developed in order to calculate the approximate concentration of the cell cultures. In addition, a bacterial DNA (*pSTI* plasmid DNA) was also spiked into the blood at approximately 10,000 copy levels. Fresh blood was used as the negative extraction control in addition to the standard negative control (water sample). Spiked blood experiment was carried out in five replicates to reduce the variability and a parallel manual bench-top extraction was also performed using the same reagents and samples for comparison purpose. Two-step protocol was used for extraction and the enzymatic incubation steps were performed in two separate steps, 5 minutes lysis step at 56°C and 5 minutes binding step at room temperature. However, due to the temperature rise during magnetic mixing/binding step, the temperature was kept below 45°C. The required temperature was generated and maintained using the external magnetic coils and attached temperature sensor. Chip-based washing and elution steps were performed inside the chip.

Table 7.13. The volumes of MagaZorb kit reagents scaled down for 25 µl total volume of chip.

Component	Standard Protocol Volumes	Scaled Protocol Volumes
Proteinase K	20 µl	0.4 µl
Blood/sample	200 µl	5.4 µl
Lysis Buffer	200 µl	5.4 µl
Binding Buffer	500 µl	13.3 µl
MagaZorb Beads	20 µl	0.5 µl
Wash Buffer	2 × 1 m1	2 × 100 µl
Elution Buffer	200 µl	25 µl

The whole chip-based extraction process is summarised as follows:

- Introduction of the spiked blood sample and lysis buffer into the chip using a 25µl Hamilton syringes.
- 6 minutes incubation of blood/lysis buffer at 56°C.
- Introduction of magnetic beads suspended in binding buffer to the lysed blood sample inside the chip using a 25µl Hamilton syringes.
- 4 minutes incubation of the lysed blood/beads/binding buffer with active magnetic mixing. The mixing was performed using two external heatsink coils (coil 2×4) at switching frequency of $f = 1\ Hz$ and coil current of 200 mA.
- Performing the washing process with on-chip clamping of the magnetic beads using the bottom coil. The clamping current was increased to 250 mA and the washing buffer was introduced to the chip using a 100µl Hamilton syringe. A total of 200µl washing buffer was dispensed in two steps.
- Washing buffer was removed using a 25µl Hamilton syringe, while magnetic beads remained inside the chip under magnetic clamping force.
- 25µl elution buffer was introduced into the chip using a 25µl Hamilton syringe and switching magnetic field was used to mix the DNA-attached beads with the elution buffer. This process was performed in 10 minutes.
- Elution buffer (contained suspended extracted DNA molecules) was removed from the chip using a 25µl Hamilton syringe, while the magnetic beads remained clamped inside the chip.

This experiment was repeated another time on different day with similar extraction conditions.

7.7.2 Results and Discussion

A very successful chamber filling was obtained during adding sample/lysis buffer and beads/binding buffer. However, minor air-pocket trapping was observed during adding binding buffer. This is because of the trapped air-pockets inside the tubing (although inlet tubing was shortened to the length of approximately 2cm to reduce

this problem). A successful temperature control was obtained using the bottom coil, which resulted in a very fast and complete lysis process. As a result of efficient magnetic mixing, a very homogeneous mixture of the binding buffer and lysed blood was also observed. A very efficient chip clamping process was achieved during both washing process and removing the sample after elution step. However, a percentage of the beads were lost (on average <10%) during the clamping and washing process. Figure 7.5 illustrates a series of screen-shots captured from different steps during extraction process describing lysis progress, magnetic mixing progress, beads clamping/washing process and elution step.

Figure 7.6 illustrates a series of captured images describing the air-pocket trapping inside the chamber after adding the binding buffer (Figure 7.6a, 7.6b) and elution buffer (Figure 7.6c). Another problem with chip-based extraction was the trapped elution buffer inside the chip (Figure 7.6d). This problem was observed once during the experiment, and it is believed that this may be due to microchamber surface imperfection. In addition to the above problems, the volume of different microchambers was calculated to be approximately between 20µl to 25µl. This variation in volume is thought to be due to fabrication process.

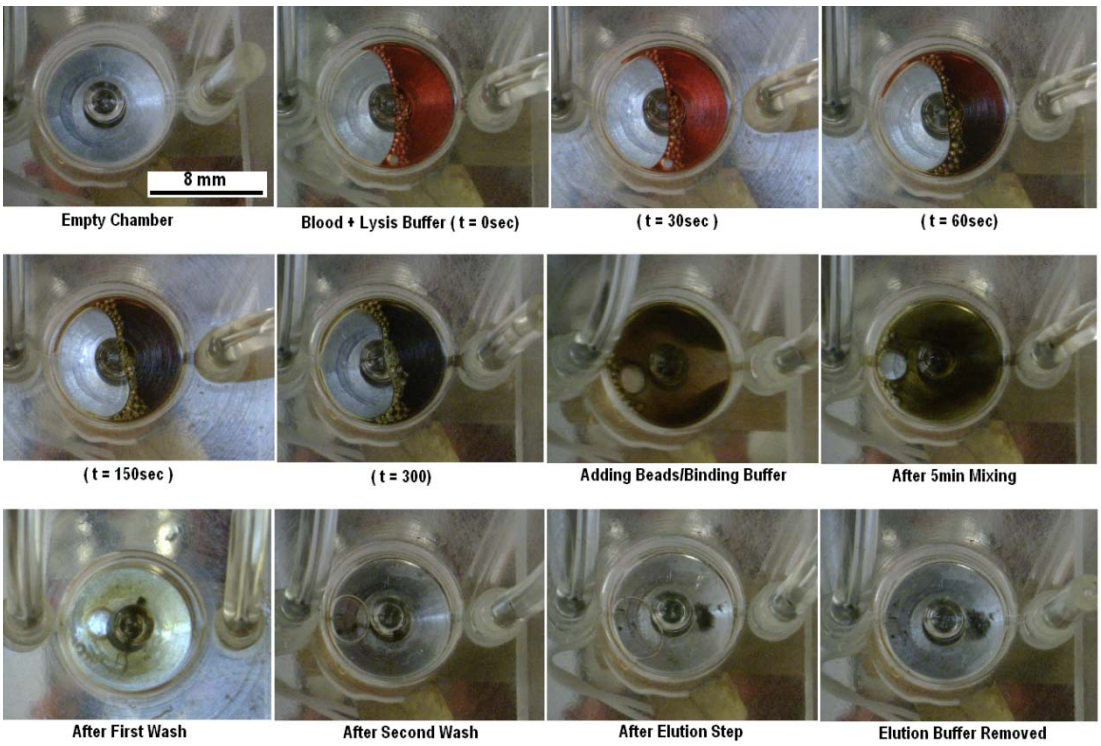

Figure 7.5. A series of screen-shots captured from different steps during chip-based extraction process (describing: lysis progress, magnetic mixing progress, beads clamping/washing process and elution step).

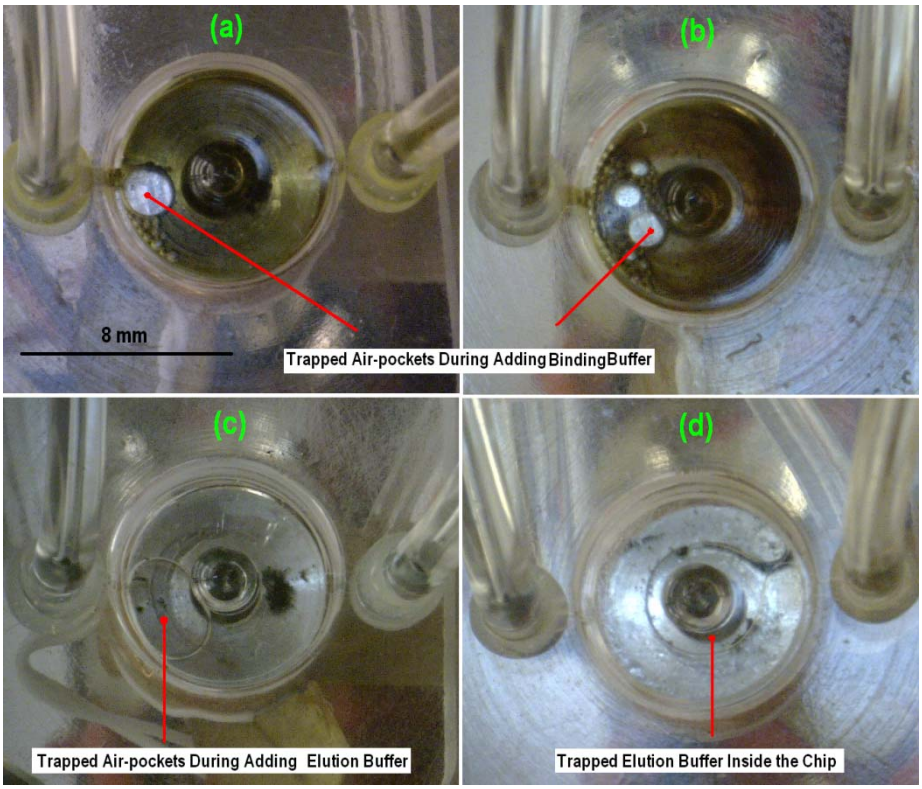

Figure 7.6. A series of screen-shots describing the air-pocket trapping inside the chamber after adding the binding buffer (a, b) and elution buffer (c) as well as the trapped elution buffer inside the chip.

7.7.2.1 Quantitation Using UV Spectrophotometer

Extracted DNA sample was analysed using standard DNA quantitation technique (UV spectrophotometer) to evaluate the total DNA yields and purity factors. The averaged results of Nanodrop analysis are shown in Table 7.14 for both manual and chip-based extractions (data is given for two different extractions). These measurements were performed in three replicates for each sample and the device was blanked with the elution buffer. Both extractions produced good quality DNA, as shown by A260/A280 quality index. However, DNA quality in manual extraction is higher than the chip-based extraction. It was observed that the device is highly sensitive to the residual washing buffer inside the sample during extraction process. This sensitivity can affect the DNA yield measurements significantly (as shown in DNA yield of chip extraction control). Therefore the measurements were corrected based on the extraction controls. Another problem with this quantitation technique was the sensitivity of the device to the presence of magnetic beads inside the sample (it can be seen as high DNA yield in chip/blood (1) sample in Table 7.14). Nevertheless, very high DNA yields were obtained using both extraction methods, which describe the extraction efficiency using two-step protocol.

Table 7.14. A comparison between chip-based and manual extraction protocols (protocol B, Two-step) using MagaZorb kit. The results are shown for fresh blood samples and spiked blood with bacterial cell cultures and free DNA sample.

	Average A260/A280	Average A260/A230	Average DNA Yield (ng/µl)	Corrected Average Yield (ng/µl)	Standard Deviation
Manual Cells/Blood (1)	2.13	0.8	15.63	12.42	6.55
Manual Blood (1)	1.96	0.64	8.43	5.23	0.10
Manual Cells/Blood (2)	2.35	0.66	8.24	5.03	1.23
Manual Blood (2)	2.47	0.59	6.46	3.25	0.12
Manual Control	2.8	0.59	3.20	0.00	0.00
Chip Cells/Blood (1)	1.61	0.57	31.14	8.55	6.74
Chip Blood (1)	1.51	1.09	88.16	65.57	41.43
Chip Cells/Blood (2)	1.68	0.66	29.27	6.68	6.44
Chip Blood (2)	2.10	0.44	24.39	1.80	0.44
Chip Control	1.69	0.90	22.59	0.00	0.00

7.7.2.2 Quantitation Using Real-time PCR Assay

In addition to the standard DNA quantitation technique (UV spectrophotometer), three different quantitative real-time PCR assay were developed to determine bacterial DNA extraction recovery levels using *Applied Biosystems 7900HT* Fast Real-Time PCR system. Determination analysis was performed in separate experiments using three 384-well plates for three microorganisms, *B. subtilis*, *E. coli* and *pSTI*. Standard curves were generated using $10^6 - 10^1$ gDNA copies and were used to calculate approximate concentration of the recovered bacterial DNA within the extracted DNA samples (using 2µl sample volumes).

The PCR plates were setup using 3x replicates of each extracted sample and the standard DNA samples. The regular 1:100 dilution ratios of the original cell cultures (used in the previous qPCR experiments) were replaced with 1:1000 dilution ratios to decrease the effect of PCR inhibitors. In addition, replicates of the cell cultures (1:1000 dilutions) were increased to 9x and pooled averaged results were used to determine the extracted DNA recovery levels of *B. subtilis* and *E. coli* microorganisms. This process can increase the accuracy of DNA recovery

calculations. In a different approach, DNA recovery levels were calculated based on the extracted DNA samples from the original cell cultures used for spiking experiments. The extraction process was performed using the QIAamp DNA mini kit. Pooled averaged results of 9x replicates were used to estimate the extracted DNA recovery levels.

B. subtilis Assay Data:

Figure 7.7 shows plots of the standard and the amplification curves extracted for *B. subtilis* microorganism. Presence of *B. subtilis* was not observed in non-spiked blood samples and negative controls. The approximate genomic equivalent of spiked bacterial cell concentration was calculated using these two above approaches (using original cells culture and extracted DNA from cell cultures). These calculations are shown in Table 7.15, and are given for two different experiments. Estimated recovery levels for the spiked *B. subtilis* bacterial cells were calculated for chip-based and manual extraction process based on the above two approaches and are given in Table 7.16.

Excellent DNA recovery levels were obtained with both chip-based and manual extraction process. Similar DNA recovery levels were obtained with both manual and chip-based extractions, which indicate comparable extraction efficiencies in both techniques. The calculation of the recovery levels based on the extracted DNA approach show higher recovery levels in comparison with the cell-based calculations. These results indicate significant improvement in extraction efficiency using two-step protocol.

Table 7.15. Quantitative real-time PCR determination of approximate *B. subtilis* genome equivalent within blood sample using two different approaches, DNA-based and cell-based.

	Sample	Average genome equivalents	Genome eq. per µl culture stock	Genome eq / 5.4 µl blood sample
Experiment 1	Extracted DNA 1	23866.64	2.39×10^6	1.60×10^5
	Cells 1	8940.78	4.47×10^6	2.99×10^5
Experiment 2	Extracted DNA 2	12857.71	1.29×10^6	6.25×10^4
	Cells 2	10561.26	5.28×10^6	2.57×10^5

Table 7.16. Quantitative real-time PCR determination of the recovery levels for the spiked *B. subtilis* genomic DNA into the blood samples using two different approaches, DNA-based and cell-based.

Spiked Blood Sample	Average	Total quantity (25 µl stock)	% Recovery (DNA-based)	% Recovery (Cell-based)
Chip Cells/Blood (1)	1289.36	64467.81	40.34	21.54
Manual Cells/Blood (1)	1512.26	75613.01	47.31	25.26
Chip Cells/Blood (2)	958.04	47902.15	76.66	18.67
Manual Cells/Blood (2)	897.81	44890.40	71.84	17.49

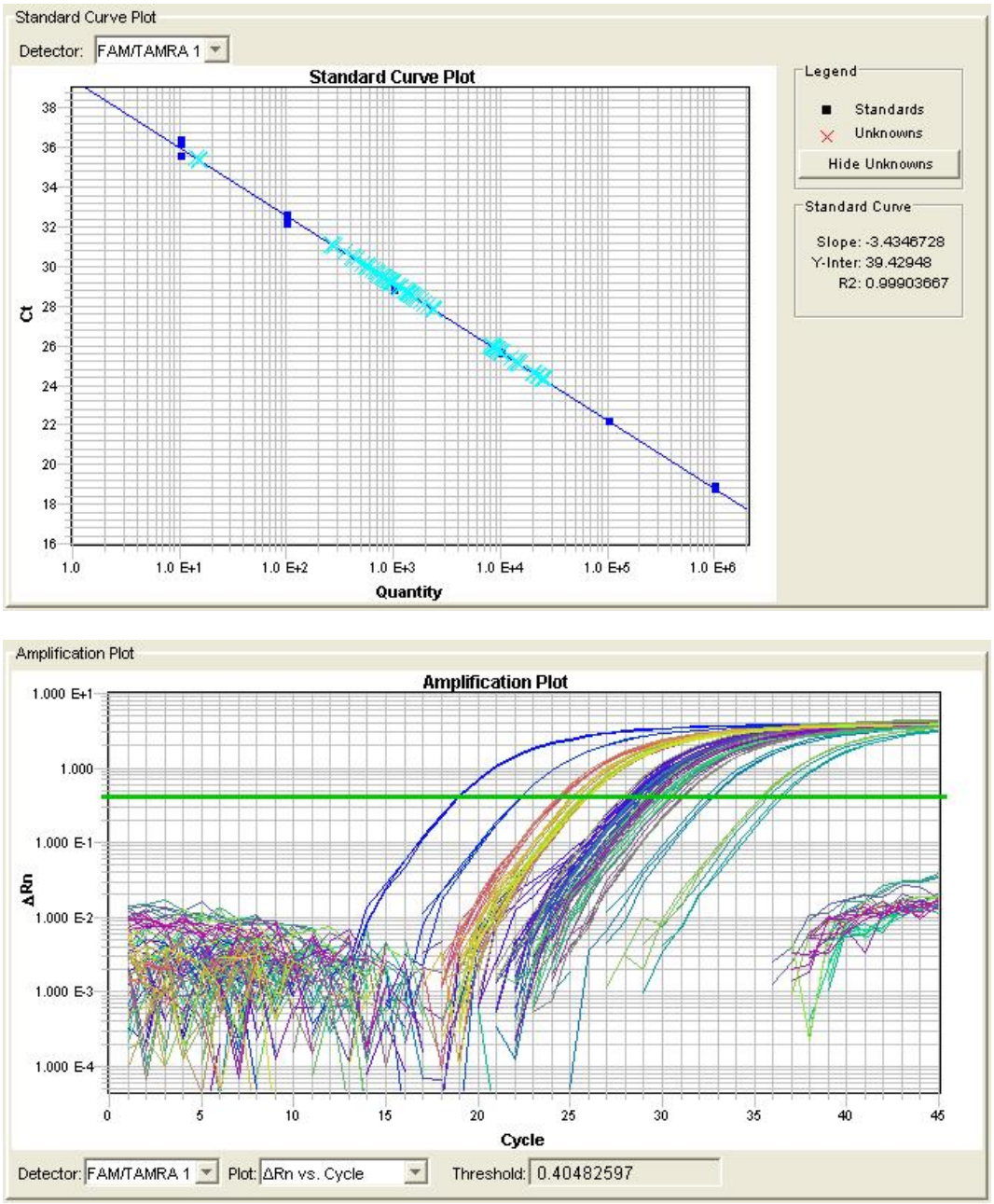

Figure 7.7. Quantitative real-time PCR determination of *B. subtilis* genomic DNA copy levels within extracted DNA samples. a) Standard curve plot. b) Amplification plot.

E.coli Assay Data:

Figure 7.8 shows plots of the standard and the amplification curves extracted for *E. coli* microorganism. Low contaminations (<1%) were observed with non-spiked blood and negative controls due to reagent related issues. The approximate genomic equivalent of spiked bacterial cell concentration was calculated using the above approaches, cell-based and DNA-based. These calculations are shown in Table 7.17, and are given for two different experiments. Estimated recovery levels for the spiked *E. coli* bacterial cells were calculated for chip-based and manual extraction process, and are given in Table 7.18. Calculations show very high DNA recovery levels with both chip-based and manual extraction process. Higher DNA recoveries were obtained using cell-based approach in comparison with the DNA-based approach.

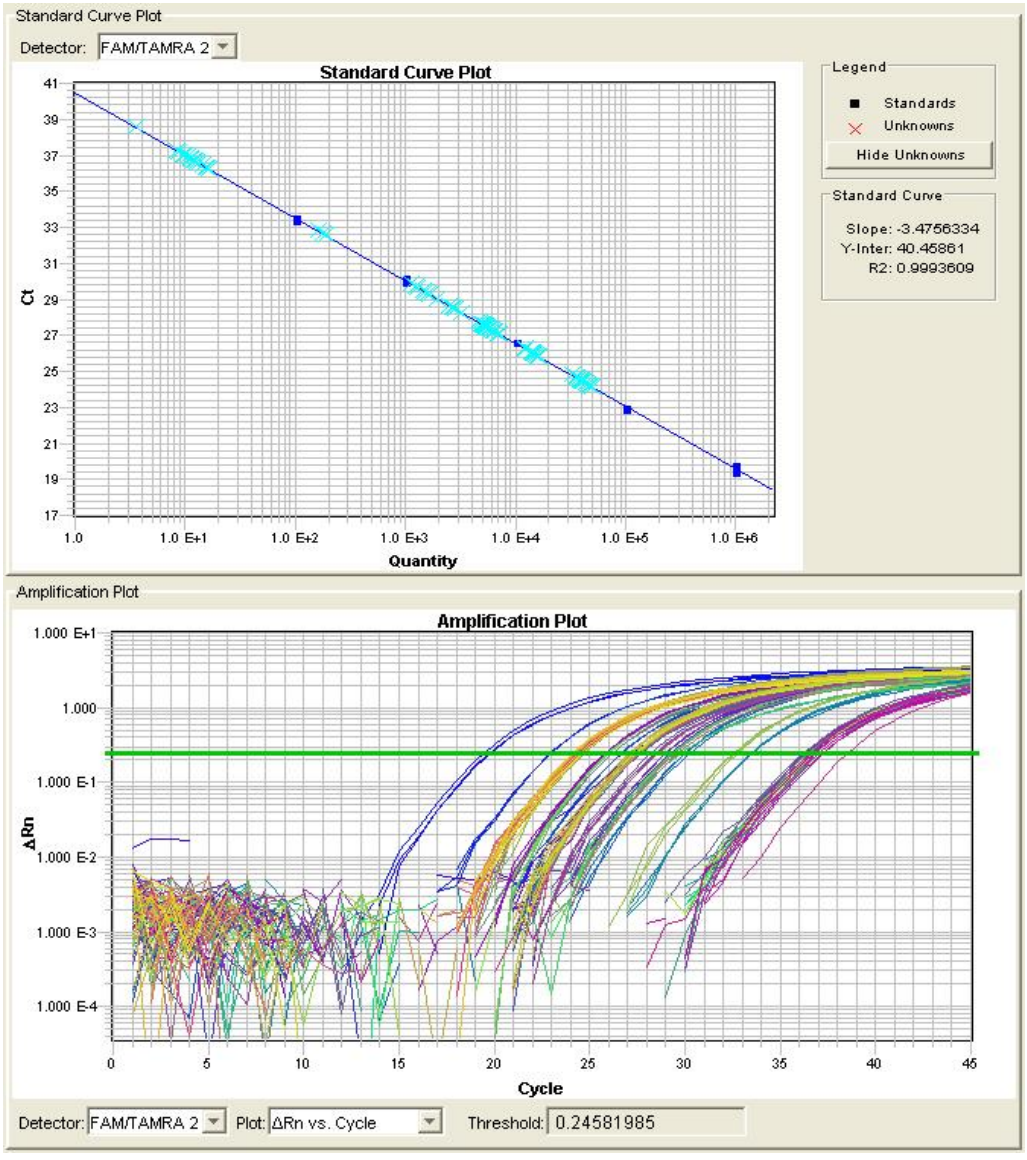

Figure 7.8. Quantitative real-time PCR determination of *E. coli* genomic DNA copy levels within extracted DNA samples. a) Standard curve plot. b) Amplification plot.

Table 7.17. Quantitative real-time PCR determination of approximate *E. coli* genome equivalent within blood sample using two different approaches, DNA-based and cell-based.

	Sample	Average genome equivalents	Genome eq. per µl culture stock	Genome eq / 5.4 µl blood sample
Experiment 1	Spiked Blood 1	43187.04	4.32E+06	4.34E+05
	Cells 1	5641.14	2.82E+06	2.83E+05
Experiment 2	Spiked Blood 2	45160.76	4.52E+06	1.82E+06
	Cells 2	6279.04	3.14E+06	1.27E+06

Table 7.18. Quantitative real-time PCR determination of the recovery levels for the spiked *E. coli* genomic DNA into the blood samples using two different approaches, DNA-based and cell-based.

Spiked Blood Sample	Average	Total quantity (25 µl stock)	% recovery (DNA-based)	% recovery (Cell-based)
Chip Cells/Blood (1)	2583.68624	129184.31	29.78	45.60
Manual Cells/Blood (1)	5469.4323	273471.62	63.05	96.53
Chip Cells/Blood (2)	20339.20643	1016960.32	55.75	80.19
Manual Cells/Blood (2)	14985.8416	749292.08	41.08	59.09

pSTI Assay Data:

Figure 7.9 illustrates plots of the standard and the amplification curves extracted for *pSTI* Plasmid DNA sample. Estimated recovery levels for the spiked *pSTI* plasmid DNA sample were calculated for chip-based and manual extraction process and are given in Table 7.19. Calculations show poor DNA recovery levels with both chip-based and manual extraction process. Higher DNA recoveries were calculated with manual extractions in comparison with the chip-based extraction.

Table 7.19. Quantitative real-time PCR determination of the recovery levels for the spiked *pSTI* plasmid DNA into the blood samples.

Spiked Blood Sample	Average	Total quantity (25 µl stock)	% recovery
Chip Cells/Blood (1)	21.94	1097.11	10.97
Manual Cells/Blood (1)	53.80	2689.94	26.90
Chip Cells/Blood (2)	10.12	505.77	5.06
Manual Cells/Blood (2)	38.49	1924.52	19.25

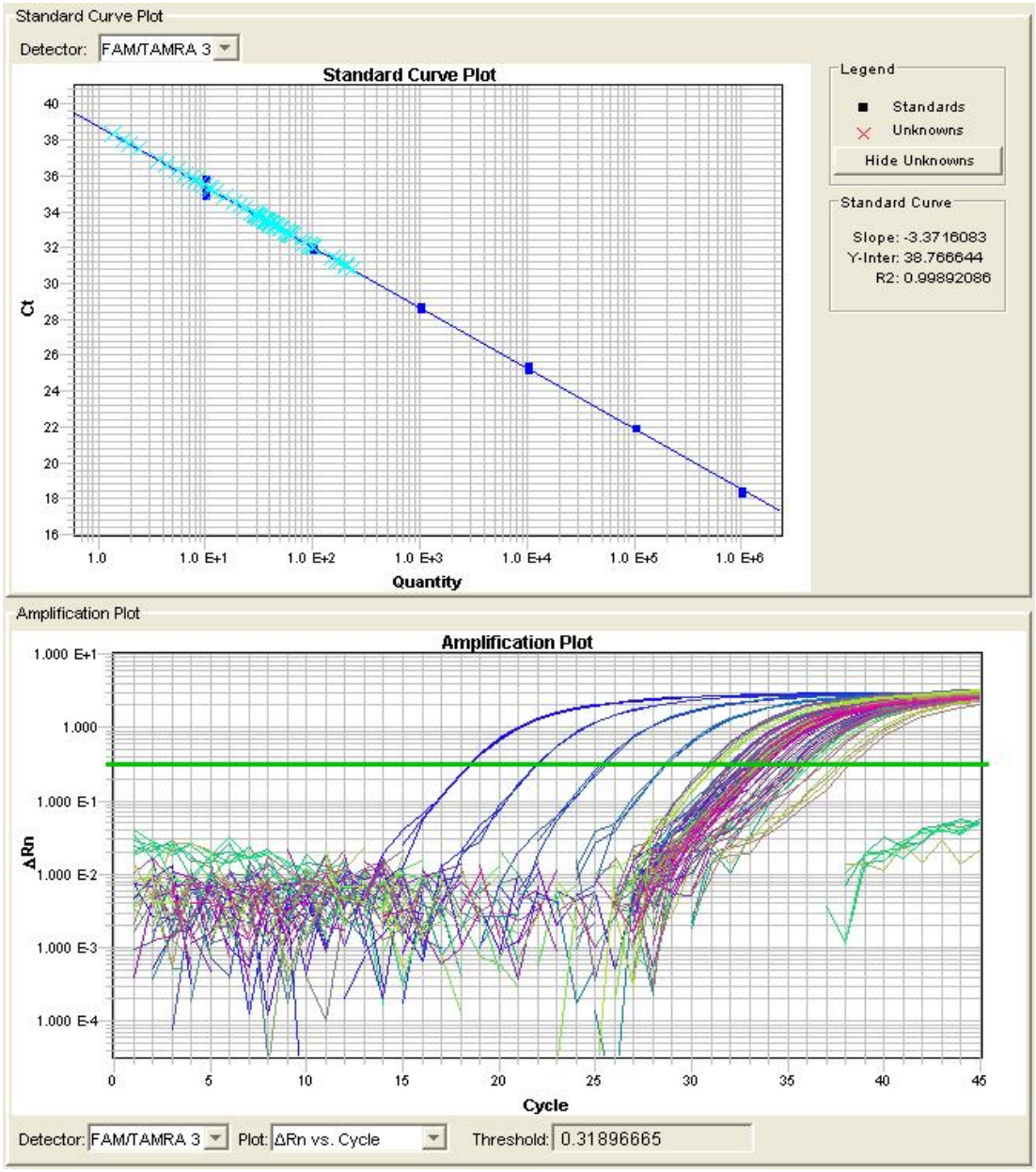

Figure 7.9. Quantitative real-time PCR determination of *pSTI* plasmid DNA copy levels within extracted DNA samples. a) Standard curve plot. b) Amplification plot.

Quantitative results of UV spectrophotometry and real-time PCR assays indicate that the efficiency of the DNA extraction process using two-step protocol has increased significantly in comparison with the combined extraction protocol. The main reason is the optimised buffer conditions of two-step protocol with separate lysis and binding steps. In addition, elution buffer was increased to 25µl, which also improved the DNA resuspension efficiency. The results of DNA recovery levels using real-time PCR indicated comparable results between chip-based and manual extraction process for two different spiked bacterial cell cultures (*B. subtilis*, Gram positive and *E. coli*, Gram negative). Lower recovery rates obtained with *pSTI* plasmid DNA

sample can be explained with respect to its low spiking ratio. A similar low DNA recovery level was previously obtained using combined extraction protocol with spiked *B. subtilis* at concentration of 10,000 copy numbers (Table 7.10, section 7.6.1). This spiking ratio (10,000) is an order of magnitude less than the spiking ratio of the *B. subtilis* and *E. coli* bacterial cell cultures (>100,000 copy numbers), which indicates the less binding probability of the plasmid DNA to the magnetic beads. In conclusion, chip-based extraction seems to be more efficient considering the higher bead loss and lower sample used (due to the smaller chamber volumes) in comparison with the manual extraction process. Therefore, higher efficiency levels can be obtained with the chip-based extraction by improving the beads clamping process and reducing the air-pocket trapping problem.

7.8 Summary

In this chapter, a series of preliminary biological experiments were conducted in order to investigate the efficiency of the designed DNA extraction and purification device. In order to achieve this, a more automation friendly extraction protocol was necessary. An experiment was performed using commercially available magnetic bead-based extraction kit (*Dynabeads DNA Direct Universal*) with simple and rapid extraction protocol. This experiment was aimed to investigate the impact of reducing the ratio of reagents to the blood sample volume. The results of the experiment indicated a very poor DNA yield using modified protocol. Lysis efficiency was very low with major chip washing problem due to the build up of the materials inside the chamber.

Therefore, a series of experiments were performed using two magnetic bead-based DNA extraction kits (Dynabeads SILANE Genomic DNA kit and MagaZorb DNA Mini-prep Kit) in order to adapt a suitable extraction protocol with fewer steps and less processing time. Two modified protocols were investigated, two-step protocol (with combined proteinase k/lysis step and binding step) and combined protocol (with single proteinase k/lysis/binding step). The results of the modified protocols were compared with the standard manufacturer's protocols as well as the result of a column-based extraction kit (QIAamp DNA Mini Kit). Both bead-based extraction kits produced high DNA yields with combined and two step protocols from whole blood samples.

The optimisation process was further investigated using Dynabeads SILANE Kit, which had higher blood sample/reagents volume ratio. Chip-based extraction process was performed using combined protocol with fresh blood samples and spiked *B. subtilis* bacterial DNA samples. The washing process and elution step was performed outside the chip to reduce the complexity of the extraction. The result of this experiment indicated that Dynabeads SILANE kit is not suitable for the chip-based extraction. The main reason was the evaporation of the Isopropanol (included in the binding buffer) during enzymatic incubations at 55°C. The evaporation of the Isopropanol forced the sample out of the chip toward the sump and caused serious damage to the chip.

Therefore, MagaZorb kit was selected to perform the optimisation process. An experiment was conducted to investigate the efficiency of the DNA binding and cell lysis using combined extraction protocol. Spiked bacterial DNA sample (*B. Subtilis,* 10,000 copies) and spiked bacterial cell (*B. Subtilis*, 100,000 copies) into the blood sample were used to investigate the efficiency of the binding and lysis process respectively. High DNA recovery levels were obtained from both manual and chip-based extractions with spiked DNA samples. However, low DNA recovery levels were obtained from both extractions with spiked cells samples. However, the lysis process was not efficient with Gram positive bacterial cells using combined extraction protocol.

Optimisation process was further investigated using two-step protocol and two different bacterial cell cultures (*B. subtilis,* gram positive and *E. coli*, gram negative) spiked into the blood sample. Free DNA sample (*pSTI* plasmid DNA) was also spiked into the blood sample to investigate the binding efficiency at lower level concentration. In order to fully evaluate the efficiency of the chip-based extraction, all extraction steps were performed inside the chip. These steps are: cell lysis, DNA binding/magnetic mixing, beads clamping/chip washing process and finally, the elution step. The results of this experiment indicated excellent DNA yields and recovery with both chip-based and manual extractions from both spiked cell cultures. These results indicated that two-step protocol is more suitable for chip-based extraction. However, chip-based extraction efficiency can be further improved by increasing the efficiency of the magnetic bead clamping, better control of fluidic processes and washing process.

CHAPTER 8

CONCLUSION AND FUTURE WORK

8.1 Conclusion

A DNA extraction and purification chip was designed and developed to be used with whole blood. To achieve this, most of the available literature was reviewed and the focus was given to the magnetic beads-based mixing method. This method was selected based on its outstanding advantages. Magnetic bead-based extraction kits are widely used for DNA extractions and are commercially available from different suppliers. The surface of these magnetic beads is positively charged to attach the negatively charged DNA molecules. Application of non-uniform internal and external magnetic field can be used to efficiently mix the bulk of beads inside the lysed blood in order to collect the released DNA molecules. The non-magnetic property of biological entities indicates that the magnetic force can be applied only on the DNA-attached beads. Therefore, magnetic bead/DNA complex can be clamped inside the chip in order to perform the washing process (removal of cell debris and other blood products).

Different possible geometries were investigated for design of magnetic field source. Among various conductor arrangements, circular spiral coil was shown to produce stronger magnetic force pattern. Two different scenarios were investigated in

parallel, integrated internal electrode design and external coil design. The Numerical simulation techniques were employed to investigate and design using a commercially available finite element simulation package, COMSOL Multiphysics. Both internal and external magnetic coil arrangements were optimised based on the geometrical and physical parameters. It was shown that integrated internal coil arrangement was not suitable for large-scale extraction process due to the fabrication limitations. Magnetic mixing was further developed by introducing more efficient magnetic bead mixing patterns. In this method, solenoidal and quadrupolic field patterns were generated by alternating the current direction and changing the state of magnetic field from switching mode to static mode. More efficient dynamic mixing patterns can be achieved using combined switching, quadrupolic and solenoidal field patterns. Developed magnetic model is a generic model and can be used to design microfluidic nucleic acid extraction chips, which use switching magnetic field for mixing.

A preliminary magnetic bead tracking technique was used to investigate the efficiency of designed magnetic coils. A Matlab code was developed to generate the bead trajectories using COMSOL-Matlab interlink. This generic code can be used to perform the bead trajectory study using different chamber configurations in combination with suitable corresponding magnetic field generating electrodes. The maximum coil currents were calculated based on the electro-thermal equilibrium at the maximum coil temperature of 56°C. This temperature is necessary during incubation step in majority of DNA extraction kits. A target molecule capturing simulation was performed to investigate the efficiency of the designed mixer for capturing the DNA molecules inside the microchamber (chip). It was shown that theoretically, a maximum efficiency of 99% was achievable using the external magnetic coil arrangement. The

A series of experiments were conducted to validate the accuracy of the simulations and extract the optimised parameters. These parameters were the frequency of the mixing, coil current, magnetic field strength, coil temperature and the efficiency of the bead clamping as well as beads trajectories. Various types of coil bobbins were constructed and wound and their magnetic field strength was measured using a magnetometer. Optimised coil current was obtained for different coils and at different operation modes, switching mode and DC mode. Self heatsink bobbins were designed and their performance was tested to increase the heat dissipation ratio.

Another advantage of the heatsink coil was the increased current capacity of the coil, which subsequently increased the strength of magnetic field. However, the main advantage was the increased heat dissipation ratio during bead clamping process using DC current mode.

Bead trajectory study was investigated inside a glass capillary tube using capillary test-rig. Various magnetic beads, coil currents and switching frequencies were investigated. The result of these experiments indicated that the overall behaviour of the beads is in close agreement with the simulation results. However, it was observed that magnetic beads tend to chain up that consequently increased the induced magnetic field and mixing frequency. Different magnetic field patterns were applied and it was shown that application of quadrupolic field pattern can easily unpile the clump of magnetic beads toward the coil outer edges.

A circular microchamber with side-wall porting was fabricated to perform some fluidic experiments and investigate the bead clamping efficiency. It was observed that air-pocket trapping is the main issue of chamber filling process. This is because of dominant capillary forces inside a chamber with large width to depth ratio. However, it was shown that vertical filling method can reduce this problem significantly. The efficiency of bead clamping was investigated using various magnetic beads at different clamping currents and fluid velocities. The results of this experiment indicated that relatively high clamping current is necessary to achieve efficient clamping process. It was observed that injection of air bubbles into the chamber during washing process can disturb the clumped beads and might reduce the clamping efficiency significantly.

A series of biological experiments were conducted to validate the efficiency of the designed chip by extracting released DNA molecules from lysed cells. The investigation was first carried out using more automation friendly extraction kit (Dynabeads DNA Direct Universal, *Invitrogen Corporation*). The main advantage of this extraction kit is the simple and rapid extraction protocol. The main disadvantage of this kit is the very high kit reagents to blood sample volume ratio (20:1). Therefore, an experiment was conducted to investigate the impact of different sample/regents ratios on the extraction efficiency. The experimental results indicated very poor DNA recovery level and yield with both modified protocol and manufacturer’s standard protocol. Obtained results were analysed using UV

spectrophotometer and Picogreen DNA quantitation techniques. Therefore, the extraction performance was further investigated using two different magnetic bead-based extraction kits (MagaZorb DNA Mini-Prep Kit, *Promega Ltd.* and Dynabeads, SILANE Genomic DNA Kit, *Invitrogen Corporation*). Since these kits were designed for manual bench-top extraction process, their protocols were not suitable for automated chip-based process. Therefore, optimisation experiments were conducted to investigate the impact of different modified protocols on the efficiency of the extraction. Two modified protocols were examined and the results were compared to the standard manufacturer's protocol as well as the result of standard column-based extraction kit (QIAamp DNA Mini Kit, *Qiagen*). The preliminary optimisation results indicated excellent DNA yields from both modified protocols and kits using whole blood sample. The results were analysed using quantitative UV spectrophotometry method. Dynabeads SILANE kit was selected for its outstanding DNA yields and higher sample to reagents volume ratio. A chip-based DNA extraction was performed using spiked bacterial DNA sample into the blood. The results indicated very poor DNA recovery from both manual and chip-based extractions. It was observed that evaporation of Isopropanol during incubation step at 55°C forced the sample out of the chip and created serious damage to the chip bonding. Nevertheless, manual extraction also showed a very poor bacterial DNA recovery rate (13.5%). Therefore, further optimisation was carried out using MagaZorb extraction kit.

A chip-based DNA extraction efficiency was investigated using combined protocol of the MagaZorb kit. Binding efficiency was investigated using spiked bacterial DNA sample into the blood and lysis efficiency was investigated using spiked bacterial cell into the blood. The results of binding experiment showed low bacterial DNA recovery levels (30-38%) with both chip-based and manual extractions. Lysis efficiency was also calculated very low using spiked bacterial cells (10-20%). The low bacterial DNA recovery levels can be explained as follows:

- Sub-optimal buffer conditions: Lysis and binding buffers were not optimised in the combined protocol. In the standard protocol, these steps are separated and in different incubation temperatures. However, in the combined protocol these steps were performed simultaneously at 56°C.

- Gram positive bacterial sample: The bacterial cell culture that was used in this experiment (*B. subtilis*) was gram positive, which has hard cell membrane and resist the lysis buffer.
- Bead-loss: A part of low recovery is related to the loss of beads during washing process. However, this ratio was higher in the chip-based extraction as some beads stick to the chip surface and tubing.
- Trapped air-pockets: This problem was observed in the chip-based extraction, which reduced the volume of the sample and consequently reduced the recovery rates.

In addition, low recovery rates from spiked DNA samples indicated that there might be a competition between small-sized bacterial DNA and large-sized human genomic DNA molecules. This might be because of the repelling forces between negatively charged DNA molecules.

Due to the low DNA recovery obtained with both chip-based and manual extractions using combined protocol, extraction efficiency was investigated using two-step protocol. In this experiment, disposable microchips were used and the whole extraction process was performed inside the chip (including cell lysis, DNA binding, beads clamping/washing and elution step). Extraction efficiency was investigated with two bacterial cell cultures (*B. subtilis*, Gram positive and *E. coli*, Gram negative) spiked into the blood sample. Extracted DNA samples were analysed using quantitative UV spectrophotometer and real-time PCR assays. Excellent DNA yields and recovery levels were obtained with both bacterial samples with manual and chip-based extractions. Therefore, it was concluded that two-step protocol is more suitable for extraction of bacterial cell cultures. The efficiency of the chip-based extraction can be further enhanced by improving the efficiency of the magnetic clamping. In this work a rapid and simple DNA extraction method was designed and developed using low cost micromachined microfluidic chip and its performance was successfully tested using non-pathogenic bacterial cell cultures spiked into the blood sample.

8.1 Suggestions for Future Work

This section focuses on making some suggestions to further extend and improve this research. These suggestions are listed as follows:

- As discussed in *Chapter 5*, integrated internal coil arrangements are not suitable for large-volume extraction process. However, a combination of internal and external coil arrangements can be used to improve the magnetic force strength and enhance the mixing efficiency.

- Magnetic clamping was observed to be very critical step in the chip washing process. The temperature rise during this step can release DNA molecules from the beads. More efficient cooling system is suggested to overcome this problem. Further improvement of heat dissipation ratio can be achieved by designing larger heatsinks or using a combination of conductive (heatsink) and convective (i.e. air flow fans) cooling system.

- In this work, a preliminary optimisation process was conducted to modify the extraction protocol. This was because of lack of extraction kit suitable for automated chip-based extraction. Therefore, more optimisations are necessary to obtain a rapid and simple extraction protocol with efficient buffer conditions (lower reagents to sample ratio) suitable for chip-based extraction process.
- The low levels recovery rates of spiked bacterial DNA samples indicated that there might be binding problem regarding repulsive force between blood genomic DNA molecules and small bacterial DNA molecules. More experiments are necessary to investigate this problem. However, this problem may be solved by increasing the number of magnetic beads or by decreasing the repulsive force of the genomic DNA molecules. This might be achieved by cutting the genomic DNA molecules using appropriate restriction enzymes. Shortened DNA molecules possess smaller electric charges, and consequently generate less repulsive forces.

- One of the most important achievements in this work was the stabilisation of the required temperature rise for incubation step using external coils. This temperature control can be used to investigate the efficiency of the on-chip Isothermal Amplifications. Since this process can be performed in the same extraction chamber, it reduces the fluidic problems as well as fabrication complexity. In addition, elution step can be eliminated, as amplification techniques are not sensitive to the presence of magnetic beads.

- One of the problems observed regarding circular microchamber was the creation of trapped air-pockets inside the chamber. The main reason for this problem is the high chamber diameter to depth ratio. Sudden expansion at the interface between inlet tubing and the chamber body was designed to create chaotic pattern to increase the mixing efficiency. However this chaotic pattern might cause the generation of trapped air-pockets. Therefore, different inlet designs needs to be investigated in order to reduce this problem.

- And finally, more biological validation tests need to be done to assess the reliability of the device with different non-pathogenic and pathogenic bacterial and viral DNA samples. More tests can be done using different DNA concentrations to obtain the sensitivity of the device. However, the accuracy of these tests can only be verified using optimised extraction buffer conditions. An automated electronic control system is also necessary to reduce the variability of the results due to the manual controlling during mixing, clamping and washing process.

References

[1]. Kricka, L.J. 2001, "Microchips, microarrays, biochips and nanochips: Personal laboratories for the 21st century", *Clinica Chimica Acta,* vol. 307, no. 1-2, pp. 219-223.

[2]. Figeys, D. & Pinto, D. 2000, "Lab-on-a-chip: A revolution in biological and medical sciences", *Analytical Chemistry,* vol. 72, no. 9, pp. 330A-335A.

[3]. Wang, J. 2000, "From DNA biosensors to gene chips", *Nucleic acids research,* vol. 28, no. 16, pp. 3011-3016.

[4]. Thorsen, T., Maerkl, S.J. & Quake, S.R. 2002, "Microfluidic large-scale integration", *Science,* vol. 298, no. 5593, pp. 580-584.

[5]. Krishnan, M., Namasivayam, V., Lin, R., Pal, R. & Burns, M.A. 2001, "Microfabricated reaction and separation systems", *Current opinion in biotechnology,* vol. 12, no. 1, pp. 92-98.

[6]. Lagally, E.T., Simpson, P.C. & Mathies, R.A. 2000, "Monolithic integrated microfluidic DNA amplification and capillary electrophoresis analysis system", *Sensors and Actuators, B: Chemical,* vol. 63, no. 3, pp. 138-146.

[7]. Anderson, R.C., Su, X., Bogdan, G.J. & Fenton, J. 2000, "A miniature integrated device for automated multistep genetic assays", *Nucleic acids research,* vol. 28, no. 12.

[8]. http://www.osmetech.com/products-esensor-xt8.htm

[9]. http://www.antara-bio.com/

[10]. http://www.dnae.co.uk/platform.htm

[11]. Miller, M.M., Sheehan, P.E., Edelstein, R.L., Tamanaha, C.R., Zhong, L., Bounnak, S., Whitman, L.J. & Colton, R.J. 2001, "A DNA array sensor utilizing magnetic microbeads and magnetoelectronic detection",*Journal of Magnetism and Magnetic Materials,* vol. 225, no. 1-2, pp. 138-144.

[12]. http://www.fluidigm.com/products/chips-kits-digital.html

[13]. http://www.mems.utah.edu/Project_Pages/Integrated_Systems/ContFlowPCR.htm

[14]. Kopp, M.U., De Mello, A.J. & Manz, A. 1998, "Chemical amplification: Continuous-flow PCR on a chip", *Science,* vol. 280, no. 5366, pp. 1046-1048.

[15]. http://www1.qiagen.com/Products/EZ1Advanced.aspx

[16]. https://www.roche-applied-science.com/sis/automated/magna_lc/index.jsp?id=mlcct_010000

[17]. Harrison, D.J., Fluri, K., Seiler, K., Fan, Z., Effenhauser, C.S. & Manz, A. 1993, "Micromachining a miniaturized capillary electrophoresis-based chemical analysis system on a chip", Science, vol. 261, no. 5123, pp. 895-897.

[18]. Burns, M.A., Johnson, B.N., Brahmasandra, S.N., Handique, K., Webster, J.R., Krishnan, M., Sammarco, T.S., Man, P.M., Jones, D., Heldsinger, D., Mastrangelo, C.H. & Burke, D.T. 1998, "An integrated nanoliter DNA analysis device", Science, vol. 282, no. 5388, pp. 484-487.

[19]. Waters, L.C., Jacobson, S.C., Kroutchinina, N., Khandurina, J., Foote, R.S. & Ramsey, J.M. 1998, "Microchip Device for Cell Lysis, Multiplex PCR Amplification, and Electrophoretic Sizing", Analytical Chemistry, vol. 70, no. 1, pp. 158-162.

[20]. Woolley, A.T., Hadley, D., Landre, P., DeMello, A.J., Mathies, R.A. & Northrup, M.A. 1996, "Functional integration of PCR amplification and capillary electrophoresis in a microfabricated DNA analysis device", Analytical Chemistry, vol. 68, no. 23, pp. 4081-4086.

[21]. Fan, Z.H., Ricco, A.J., Tan, W., Zhao, M.-Q. & Koh, C.G. 2003."Integrating Multiplexed PCR with CE for Detecting Microorganisms", 7th Int. Conf. on Miniaturized Chem. and Biochem. Analysis Sys (Oct. 5-9, Squaw Valley, CA, USA), pp. 849-852.

[22]. Pal, R., Yang, M., Lin, R., Johnson, B.N., Srivastava, N., Razzacki, S.Z., Chomistek, K.J., Heldsinger, D.C., Haque, R.M., Ugaz, V.M., Thwar, P.K., Chen, Z., Alfano, K., Yim, M.B., Krishnan, M., Fuller, A.O., Larson, R.G., Burke, D.T. & Burns, M.A. 2005, "An integrated microfluidic device for influenza and other genetic analyses", Lab on a Chip - Miniaturisation for Chemistry and Biology, vol. 5, no. 10, pp. 1024-1032.

[23]. Verpoorte, E. 2002, "Microfluidic chips for clinical and forensic analysis", Electrophoresis, vol. 23, no. 5, pp. 677-712.

[24]. Yuen, P.K., Kricka, L.J., Fortina, P., Panaro, N.J., Sakazume, T. & Wilding, P. 2001, "Microchip module for blood sample preparation and nucleic acid amplification reactions [4]", Genome research, vol. 11, no. 3, pp. 405-412.

[25]. Anderson, R.C., Su, X., Bogdan, G.J. & Fenton, J. 2000, "A miniature integrated device for automated multistep genetic assays", Nucleic acids research, vol. 28, no. 12.

[26]. Yeung, S.W. & Hsing, I.-. 2006, "Manipulation and extraction of genomic DNA from cell lysate by functionalized magnetic particles for lab on a chip applications", Biosensors and Bioelectronics, vol. 21, no. 7, pp. 989-997.

[27]. El-Ali, J., Perch-Nielsen, I.R., Poulsen, C.R., Jensen, M., Telleman, P. & Wolff, A. 2003, "Microfabricated DNA amplification device monolithically integrated with advanced sample pre-treatment", The 12th Int. Conf. on Solid State Sensors, Actuators and Microsystems (June 8-12, Boston, MA, USA), pp. 214-217.

[28]. Hui, W.C., Yobas, L., Samper, V.D., Heng, C.-K., Liw, S., Ji, H., Chen, Y., Cong, L., Li, J. & Lim, T.M. 2007, "Microfluidic systems for extracting nucleic acids for DNA and RNA analysis", Sensors and Actuators, A: Physical, vol. 133, no. 2 SPEC. ISS., pp. 335-339.

[29]. Lee, J.-G., Cheong, K.H., Huh, N., Kim, S., Choi, J.-W. & Ko, C. 2006, "Microchip-based one step DNA extraction and real-time PCR in one chamber for rapid pathogen identification", Lab on a Chip - Miniaturisation for Chemistry and Biology, vol. 6, no. 7, pp. 886-895.

[30]. Cho, Y.-K., Lee, J.-G., Park, J.-M., Lee, B.-S., Lee, Y. & Ko, C. 2007, "One-step pathogen specific DNA extraction from whole blood on a centrifugal microfluidic device", Lab on a Chip - Miniaturisation for Chemistry and Biology, vol. 7, no. 5, pp. 565-573.

[31]. Chung, Y.-C., Jan, M.-S., Lin, Y.-C., Lin, J.-H., Cheng, W.-C. & Fan, C.-Y. 2004, "Microfluidic chip for high efficiency DNA extraction", Lab on a Chip - Miniaturisation for Chemistry and Biology, vol. 4, no. 2, pp. 141-147.

[32]. Melzak, K.A., Sherwood, C.S., Turner, R.F.B. & Haynes, C.A. 1996, "Driving forces for DNA adsorption to silica in perchlorate solutions", Journal of colloid and interface science, vol. 181, no. 2, pp. 635-644.

[33]. Christel, L.A., Petersen, K., McMillan, W. & Northrup, M.A. 1999, “Rapid, automated nucleic acid probe assays using silicon microstructures for nucleic acid concentration”, Journal of Biomechanical Engineering, 121 (1), pp. 22-27.

[34]. Cady, N.C., Stelick, S. & Batt, C.A. 2003, "Nucleic acid purification using microfabricated silicon structures", Biosensors and Bioelectronics, vol. 19, no. 1, pp. 59-66.

[35]. Brinker, C.J. & Scherer, G.W. 1989, “Sol-Gel Science: The Physics and Chemistry of Sol-Gel Processing”, Academic Press: San Diego, CA, pp. 2-10.

[36]. Tian, H., Hühmer, A.F.R. & Landers, J.P. 2000, "Evaluation of silica resins for direct and efficient extraction of dna from complex biological matrices in a miniaturized format", Analytical Biochemistry, vol. 283, no. 2, pp. 175-191.

[37]. Wolfe, K.A., Breadmore, M.C., Ferrance, J.P., Power, M.E., Conroy, J.F., Norris, P.M. & Landers, J.P. 2002, "Toward a microchip-based solid-phase extraction method for isolation of nucleic acids", Electrophoresis, vol. 23, no. 5, pp. 727-733.

[38]. Breadmore, M.C., Wolfe, K.A., Arcibal, I.G., Leung, W.K., Dickson, D., Giordano, B.C., Power, M.E., Ferrance, J.P., Feldman, S.H., Norris, P.M. & Landers, J.P. 2003, "Microchip-based purification of DNA from biological samples", Analytical Chemistry, vol. 75, no. 8, pp. 1880-1886.

[39]. Wu, Q., Bienvenue, J.M., Hassan, B.J., Kwok, Y.C., Giordano, B.C., Norris, P.M., Landers, J.P. & Ferrance, J.P. 2006, "Microchip-based macroporous silica sol-gel monolith for efficient isolation of DNA from clinical samples", Analytical Chemistry, vol. 78, no. 16, pp. 5704-5710.

[40]. Morishima, K., Bennett, B.D., Dulay, M.T., Quirino, J.P. & Zare, R.N. 2002, "Toward sol-gel electrochromatographic separations on a chip", Journal of Separation Science, vol. 25, no. 15-17, pp. 1226-1230.

[41]. Wen, J., Guillo, C., Ferrance, J.P. & Landers, J.P. 2006, "DNA extraction using a tetramethyl orthosilicate-grafted photopolymerized monolithic solid phase", Analytical Chemistry, vol. 78, no. 5, pp. 1673-1681.

[42]. Wen, J., Guillo, C., Ferrance, J.P. & Landers, J.P. 2007, "Microfluidic-based DNA purification in a two-stage, dual-phase microchip containing a reversed-phase and a photopolymerized monolith", Analytical Chemistry, vol. 79, no. 16, pp. 6135-6142.

[43]. Bhattacharyya, A. & Klapperich, C.M. 2008, "Microfluidics-based extraction of viral RNA from infected mammalian cells for disposable molecular diagnostics", Sensors and Actuators, B: Chemical, vol. 129, no. 2, pp. 693-698.

[44]. Bhattacharyya, A. & Klapperich, C.M. 2006, "Thermoplastic microfluidic device for on-chip purification of nucleic acids for disposable diagnostics", Analytical Chemistry, vol. 78, no. 3, pp. 788-792.

[45]. Cao, W., Easley, C.J., Ferrance, J.P. & Landers, J.P. 2006, "Chitosan as a polymer for pH-induced DNA capture in a totally aqueous system", Analytical Chemistry, vol. 78, no. 20, pp. 7222-7228.

[46]. Hagan, K.A., Meier, W.L., Ferrance, J.P. & Landers, J.P. 2009, "Chitosan-coated silica as a solid phase for RNA purification in a microfluidic device", Analytical Chemistry, vol. 81, no. 13, pp. 5249-5256.

[47]. Hong, J.W., Studer, V., Hang, G., Anderson, W.F. & Quake, S.R. 2004, "A nanoliter-scale nucleic acid processor with parallel architecture", Nature biotechnology, vol. 22, no. 4, pp. 435-439.

[48]. Legendre, L.A., Bienvenue, J.M., Roper, M.G., Ferrance, J.P. & Landers, J.P. 2006, "A simple, valveless microfluidic sample preparation device for extraction and amplification of DNA from nanoliter-volume samples", Analytical Chemistry, vol. 78, no. 5, pp. 1444-1451.

[49]. Easley, C.J., Karlinsey, J.M., Bienvenue, J.M., Legendre, L.A., Roper, M.G., Feldman, S.H., Hughes, M.A., Hewlett, E.L., Merkel, T.J., Ferrance, J.P. & Landers, J.P. 2006, "A fully integrated microfluidic genetic analysis system with sample-in-answer-out capability", Proceedings of the National Academy of Sciences of the United States of America, vol. 103, no. 51, pp. 19272-19277.

[50]. Liu, R.H., Yang, J., Lenigk, R., Bonanno, J. & Grodzinski, P. 2004, "Self-Contained, Fully Integrated Biochip for Sample Preparation, Polymerase Chain Reaction Amplification, and DNA Microarray Detection", Analytical Chemistry, vol. 76, no. 7, pp. 1824-1831.

[51]. Liu, R.H. & Lee, A.P. 2007, "Integrated Biochips for DNA Analysis", Springer Science & Lands Bioscience: New York, NY, USA, pp. 47-67.

[52]. Nguyen N. T. and Wereley S. T., 2002, Fundamentals and Applications of Microfluidics, (Boston: Artech House)

[53]. Oosterbroek R. E. and van den Berg A., 2003, Lab-on-a-Chip: Miniaturized System for Bio(Chemical) Analysis and Synthesis, (Amsterdam: Elsevier)

[54]. Geschke O., Klank H. and Telleman P., 2004, Microsystem Engineering of Lab-on-a-Chip Devices, 2nd edn (New York: Wiley)

[55]. Kakuta, M., Bessoth F. G., and Manz A., 2001, Microfabricated devices for fluid mixing and their application for chemical synthesis, Chemical Records 1, no. 5, pp. 395-405.

[56]. Reyes D.R., Iossifidis D., Auroux P. A., Manz A., 2002, Micro total analysis systems: 1. Introduction, theory, and technology, Anal. Chem. 74, pp. 2623–36

[57]. Pierre-Alain Auroux P. A., Iossifidis D., Reyes D. R., Manz A., 2002, Micro total analysis systems: 2. Analytical standard operations and applications, Anal. Chem. 74, pp. 2637–52

[58]. Vilkner T., Janasek D., Manz A., 2004, Micro total analysis systems, Recent developments Anal. Chem. 76, pp. 3373–86

[59]. Erbacher C., Bessoth F. G., Busch M., Verpoorte E., Manz A., 1999, Towards integrated continuous-flow chemical reactors, Mikrochim. Acta 131, pp. 19–24

[60]. Nguyen N. T., Wu Z., 2005, Micromixers-a review, J. Micromech. Microeng. 15, pp. R1–R16

[61]. Hessel V., Lowe H., Schonfeld F., 2005, Micromixers-a review on passive and active mixing principles, Chemical Engineering Science 60, pp. 2479 – 2501

[62]. Hardt S., Drese K. S., Hessel V., Schonfeld F., 2005, Passive micromixers for applications in the microreactor and μTAS fields, Microfluidics and Nanofluidics, 1, pp. 108-118

[63]. Mansur E. A., Ye M., Wang Y., Dai Y., 2008, A State-of-the-Art Review of Mixing in Microfluidic Mixers, Chin. J. Chem. Eng., 16(4), pp. 503-516

[64]. Jen C. P., Wu C. Y., Lin Y. C., Wub C. Y., 2003, Design and simulation of the micromixer with chaotic advection in twisted microchannels, Lab on a Chip, 3, pp. 77–81

[65]. Kamholz A. E., Weigl B. H., Finlayson B. A., Yager P., 1999, Quantitative Analysis of Molecular Interaction in a Microfluidic Channel: The T-Sensor, Analytical Chemistry, 71(23), pp. 5340-5347

[66]. Ismagilov R. F., Stroock A. D., Kenis P. J. A., Whitesides G., 2000, Experimental and theoretical scaling laws for transverse diffusive broadening in two-phase laminar flows in microchannels, Appl. Phys. Lett., 76, pp. 2376–78

[67]. Yi M., Bau H. H., 2003, The kinematics of bend-induced mixing in microconduits, Int. J. Heat Fluid Flow, 24, pp. 645–56

[68]. Wong S. H., Ward M. C. L., Wharton C. W., 2004, Micro T-mixer as a rapid mixing micromixer Sensors Actuators B, 100, pp. 365–85

[69]. Hinsmann P., Frank J., Svasek P., Harasek M., Lendl B., 2001, Design, simulation and application of a new micromixing device for time resolved infrared spectroscopy of chemical reactions in solutions, Lab on a Chip, 1, pp. 16–21

[70]. Wong S. H., Bryant P., Ward M., Wharton C., 2003, Investigation of mixing in a cross-shaped micromixer with static mixing elements for reaction kinetics studies Sensors Actuators B, 95, pp. 414–24

[71]. Gobby D., Angeli P., Gavriilidis A., 2001, Mixing characteristics of T-type microfluidic mixers, J. Micromech. Microeng., 11, pp. 126–32

[72]. Bothe D., Sternich C., Warnecke H. J., 2006, Fluid mixing in a T-shaped micro-mixer, Chem Eng Sci, 61(9), pp. 2950–2958

[73]. Veenstra T. T., 1999, Characterization method for a new diffusion mixer applicable in micro flow injection analysis systems, J. Micromech. Microeng., 9, pp. 199–202

[74]. Jackman R. J., Floyd T. M., Ghodssi R., Schmidt M. A., Jensen K. F., 2001, Microfluidic systems with on-line UV detection fabricated in photo-defineable epoxy, J. Micromech. Microeng., 11, pp. 263–9

[75]. Moebius, H., Ehrfeld, W., Hessel, V. & Richter, T. 1995, "Sensor controlled processes in chemical microreactors", Conf. on Solid-State Sensors and Actuators (Stockholm, Sweden), pp. 775-8.

[76]. Koch, M., Witt, H., Evans, A.G.R. & Brunnschweiler, A. 1999, "Improved characterization technique for micromixers", *Journal of Micromechanics and Microengineering,* vol. 9, no. 2, pp. 156-158.

[77]. Bessoth, F.G., DeMello, A.J. & Manz, A. 1999, "Microstructure for efficient continuous flow mixing", *Analytical Communications,* vol. 36, no. 6, pp. 213-215.

[78]. Haverkamp, V., Ehrfeld, W., Gebauer, K., Hessel, V., Löwe, H., Richter, T. & Wille, C. 1999, "The potential of micromixers for contacting of disperse liquid phases", *Fresenius' journal of analytical chemistry,*vol. 364, no. 7, pp. 617-624.

[79]. Löb, P., Drese, K.S., Hessel, V., Hardt, S., Hofmann, C., Löwe, H., Schenk, R., Schönfeld, F. & Werner, B. 2004, "Steering of liquid mixing speed in interdigital micro mixers - From very fast to deliberately slow mixing", *Chemical Engineering and Technology,* vol. 27, no. 3, pp. 340-345.

[80]. Fluri, K., Fitzpatrick, G., Chiem, N. & Harrison, D.J. 1996, "Integrated Capillary Electrophoresis Devices with an Efficient Postcolumn Reactor in Planar Quartz and Glass Chips", *Analytical Chemistry,* vol. 68, no. 23, pp. 4285-4290.

[81]. Hadd, A.G., Raymond, D.E., Halliwell, J.W., Jacobson, S.C. & Ramsey, J.M. 1997, "Microchip Device for Performing Enzyme Assays", *Analytical Chemistry,* vol. 69, no. 17, pp. 3407-3412.

[82]. Jacobson, S.C., McKnight, T.E. & Ramsey, J.M. 1999, "Microfluidic devices for electrokinetically driven parallel and serial mixing", Analytical Chemistry, vol. 71, no. 20, pp. 4455-4459.

[83]. Bohm S., Greiner K., Schlautmann S., de Vries S., & van den Berg S., “A rapid vortex micromixer for studying high-speed chemical reactions”, Technical Proc. Micro Total Analysis Systems MicroTAS, 2001 (Monterey, CA, USA), pp. 25–7.

[84]. Lin, C-H., Tsai, C-H. & Fu, L-M. 2005, "A rapid three-dimensional vortex micromixer utilizing self-rotation effects under low Reynolds number conditions", Journal of Micromechanics and Microengineering, vol. 15, no. 5, pp. 935-943.

[85]. Hardt S., Dietrich T., Freitag A., Hessel V., Lowe H., Hofmann C., Oroskar A., Schonfeld F. & Vanden B. K., 2002, “Radial and tangential injection of liquid/liquid and gas/liquid streams and focusing thereof in a special cyclone mixer”, Proc. 6th Int. Conf. on Microreaction Technology, pp 329–44

[86]. Knight, J.B., Vishwanath, A., Brody, J.P. & Austin, R.H. 1998, "Hydrodynamic focusing on a silicon chip: Mixing nanoliters in microseconds", Physical Review Letters, vol. 80, no. 17, pp. 3863-3866.

[87]. Jensen, K. 1998, "Chemical kinetics: Smaller, faster chemistry", Nature, vol. 393, no. 6687, pp. 736-737.

[88]. Walker, G.M., Ozers, M.S. & Beebe, D.J. 2004, "Cell infection within a microfluidic device using virus gradients", Sensors and Actuators, B: Chemical, vol. 98, no. 2-3, pp. 347-355.

[89]. Nguyen, N.-. & Huang, X. 2005, "Mixing in microchannels based on hydrodynamic focusing and time-interleaved segmentation: Modelling and experiment", Lab on a Chip - Miniaturisation for Chemistry and Biology, vol. 5, no. 11, pp. 1320-1326.

[90]. Gray, B.L., Jaeggi, D., Mourlas, N.J., Van Drieënhuizen, B.P., Williams, K.R., Maluf, N.I. & Kovacs, G.T.A. 1999, "Novel interconnection technologies for integrated microfluidic systems", Sensors and Actuators, A: Physical, vol. 77, no. 1, pp. 57-65.

[91]. Branebjerg, J., Gravesen, P., Krog, J.P. & Nielsen, C.R. 1996, "Fast mixing by lamination", Proc. MEMS’96, 9th IEEE Int. Workshop Micro Electromechanical System (San Diego, CA), pp. 441.

[92]. Schwesinger, N., Frank, T. & Wurmus, H. 1996, "A modular microfluid system with an integrated micromixer", *Journal of Micromechanics and Microengineering,* vol. 6, no. 1, pp. 99-102.

[93]. Schönfeld, F., Hessel, V. & Hofmann, C. 2004, "An optimised split-and-recombine micro-mixer with uniform 'chaotic' mixing", *Lab on a Chip - Miniaturisation for Chemistry and Biology,* vol. 4, no. 1, pp. 65-69.

[94]. He, B., Burke, B.J., Zhang, X., Zhang, R. & Regnier, F.E. 2001, "A picoliter-volume mixer for microfluidic analytical systems", *Analytical Chemistry,* vol. 73, no. 9, pp. 1942-1947.

[95]. Melin, J., Giménez, G., Roxhed, N., Van Der Wijngaart, W. & Stemme, G. 2004, "A fast passive and planar liquid sample micromixer", *Lab on a Chip - Miniaturisation for Chemistry and Biology,* vol. 4, no. 3, pp. 214-219.

[96]. Sudarsan, A.P. & Ugaz, V.M. 2006, "Multivortex micromixing", *Proceedings of the National Academy of Sciences of the United States of America,* vol. 103, no. 19, pp. 7228-7233.

[97]. Ducrée, J., Haeberle, S., Brenner, T., Glatzel, T. & Zengerle, R. 2006, "Patterning of flow and mixing in rotating radial microchannels", *Microfluidics and Nanofluidics,* vol. 2, no. 2, pp. 97-105.

[98]. Ducrée, J., Brenner, T., Haeberle, S., Glatzel, T. & Zengerle, R. 2006, "Multilamination of flows in planar networks of rotating microchannels", *Microfluidics and Nanofluidics,* vol. 2, no. 1, pp. 78-84.

[99]. Coleman, J.T., McKechnie, J. & Sinton, D. 2006, "High-efficiency electrokinetic micromixing through symmetric sequential injection and expansion", *Lab on a Chip - Miniaturisation for Chemistry and Biology,*vol. 6, no. 8, pp. 1033-1039.

[100]. Miyake, R., Lammerink, T.S.J., Elwenspoek, M. & Fluitman, J.H.J. 1993, "Micro mixer with fast diffusion", Proc. MEMS'93, 6th IEEE Int. Workshop Micro Electromechanical System (San Diego, CA), pp. 248.

[101]. Larsen U. D., Rong W. & Telleman P. 1999, "Design of rapid micromixers using CFD", Proc. Transducers'99, 10th Int. Conf. on Solid-State Sensors and Actuators (Sendai, Japan), pp. 200–203.

[102]. Seidel R. U., Si D. Y., Menz W., Esashi M. 1999, "Capilary force mixing device as sampling module for chemical analysis", Proc. Transducers'99, 10th Int. Conf. on Solid-State Sensors and Actuators (Sendai, Japan), pp. 438–441.

[103]. Voldman, J., Gray, M.L. & Schmidt, M.A. 2000, "Integrated liquid mixer/valve", *Journal of Microelectromechanical Systems,* vol. 9, no. 3, pp. 295-302.

[104]. Hosokawa, K., Fujii, T. & Endo, I. 1999, "Droplet-based nano/picoliter mixer using hydrophobic microcapillary vent", Proc the IEEE International Workshop Micro Electromechanical System (Piscataway, NJ, USA), pp. 388.

[105]. Handique, K. & Burns, M.A. 2001, "Mathematical modeling of drop mixing in a slit-type microchannel", *Journal of Micromechanics and Microengineering,* vol. 11, no. 5, pp. 548-554.

[106]. Paik, P., Pamula, V.K. & Fair, R.B. 2003, "Rapid droplet mixers for digital microfluidic systems", *Lab on a Chip - Miniaturisation for Chemistry and Biology,* vol. 3, no. 4, pp. 253-259.

[107]. Song, H., Bringer, M.R., Tice, J.D., Gerdts, C.J. & Ismagilov, R.F. 2003, "Experimental test of scaling of mixing by chaotic advection in droplets moving through microfluidic channels", *Applied Physics Letters,*vol. 83, no. 22, pp. 4664-4666.

[108]. Tice, J.D., Lyon, A.D. & Ismagilov, R.F. 2004, "Effects of viscosity on droplet formation and mixing in microfluidic channels", *Analytica Chimica Acta,* vol. 507, no. 1, pp. 73-77.

[109]. Hessel, V., Hardt, S., Löwe, H. & Schönfeld, F. 2003, "Laminar mixing in different interdigital micromixers: I. Experimental characterization", *AICHE Journal,* vol. 49, no. 3, pp. 566-577.

[110]. Hardt, S. & Schönfeld, F. 2003, "Laminar mixing in different interdigital micromixers: II. Numerical simulations", *AICHE Journal,* vol. 49, no. 3, pp. 578-584.

[111]. Lin, Y., Gerfen, G.J., Rousseau, D.L. & Yeh, S.-. 2003, "Ultrafast Microfluidic Mixer and Freeze-Quenching Device", *Analytical Chemistry,* vol. 75, no. 20, pp. 5381-5386.

[112]. Wang, H., Iovenitti, P., Harvey, E. & Masood, S. 2002, "Optimizing layout of obstacles for enhanced mixing in microchannels", *Smart Materials and Structures,* vol. 11, no. 5, pp. 662-667.

[113]. Bhagat, A.A.S., Peterson, E.T.K. & Papautsky, I. 2007, "A passive planar micromixer with obstructions for mixing at low Reynolds numbers", *Journal of Micromechanics and Microengineering,* vol. 17, no. 5, pp. 1017-1024.

[114]. Jiang, F., Drese, K.S., Hardt, S., Küpper, M. & Schönfeld, F. 2004, "Helical flows and chaotic mixing in curved micro channels", *AICHE Journal,* vol. 50, no. 9, pp. 2297-2305.

[115]. Nichols, K.P., Ferullo, J.R. & Baeumner, A.J. 2006, "Recirculating, passive micromixer with a novel sawtooth structure", *Lab on a Chip - Miniaturisation for Chemistry and Biology,* vol. 6, no. 2, pp. 242-246.

[116]. Mengeaud, V., Josserand, J. & Girault, H.H. 2002, "Mixing processes in a zigzag microchannel: Finite element simulations and optical study", *Analytical Chemistry,* vol. 74, no. 16, pp. 4279-4286.

[117]. Kockmann, N., Kiefer, T., Engler, M. & Woias, P. 2006, "Convective mixing and chemical reactions in microchannels with high flow rates", *Sensors and Actuators, B: Chemical,* vol. 117, no. 2, pp. 495-508.

[118]. Kockmann, N., Kiefer, T., Engler, M. & Woias, P. 2006, "Silicon microstructures for high throughput mixing devices", *Microfluidics and Nanofluidics,* vol. 2, no. 4, pp. 327-335.

[119]. Hong, C.-C., Choi, J.-. & Ahn, C.H. 2004, "A novel in-plane passive microfluidic mixer with modified Tesla structures", *Lab on a Chip - Miniaturisation for Chemistry and Biology,* vol. 4, no. 2, pp. 109-113.

[120]. Liu, R.H., Stremler, M.A., Sharp, K.V., Olsen, M.G., Santiago, J.G., Adrian, R.J., Aref, H. & Beebe, D.J. 2000, "Passive mixing in a three-dimensional serpentine microchannel", *Journal of Microelectromechanical Systems,* vol. 9, no. 2, pp. 190-197.

[121]. Vijayendran, R.A., Motsegood, K.M., Beebe, D.J. & Leckband, D.E. 2003, "Evaluation of a three-dimensional micromixer in a surface-based biosensor", *Langmuir,* vol. 19, no. 5, pp. 1824-1828.

[122]. Chen, H. & Meiners, J.-. 2004, "Topologic mixing on a microfluidic chip", *Applied Physics Letters,* vol. 84, no. 12, pp. 2193-2195.

[123]. Park, S.-J., Kim, J.K., Park, J., Chung, S., Chung, C. & Chang, J.K. 2004, "Rapid three-dimensional passive rotation micromixer using the breakup process", *Journal of Micromechanics and Microengineering,* vol. 14, no. 1, pp. 6-14.

[124]. Ottino, J.M. 1989, "The kinematics of mixing: stretching, chaos, and transport", Cambridge, New York: Cambridge University Press.

[125]. Chang, S. & Cho, Y.-. 2005, "Static micromixers using alternating whirls and lamination", *Journal of Micromechanics and Microengineering,* vol. 15, no. 8, pp. 1397-1405.

[126]. Sudarsan, A.P. & Ugaz, V.M. 2006, "Fluid mixing in planar spiral microchannels", *Lab on a Chip - Miniaturisation for Chemistry and Biology,* vol. 6, no. 1, pp. 74-82.

[127]. Johnson, T.J., Ross, D. & Locascio, L.E. 2002, "Rapid microfluidic mixing", *Analytical Chemistry,* vol. 74, no. 1, pp. 45-51.

[128]. Stroock, A.D., Dertinger, S.K.W., Ajdari, A., Mezić, I., Stone, H.A. & Whitesides, G.M. 2002, "Chaotic mixer for microchannels", *Science,* vol. 295, no. 5555, pp. 647-651.

[129]. Stroock, A.D. & Whitesides, G.M. 2003, "Controlling flows in microchannels with patterned surface charge and topography", *Accounts of Chemical Research,* vol. 36, no. 8, pp. 597-604.

[130]. Stroock, A.D., Dertinger, S.K., Whitesides, G.M. & Ajdari, A. 2002, "Patterning flows using grooved surfaces", *Analytical Chemistry,* vol. 74, no. 20, pp. 5306-5312.

[131]. Wang, H., Iovenitti, P., Harvey, E. & Masood, S. 2003, "Numerical investigation of mixing in microchannels with patterned grooves", *Journal of Micromechanics and Microengineering,* vol. 13, no. 6, pp. 801-808.

[132]. Schönfeld, F. & Hardt, S. 2004, "Simulation of Helical Flows in Microchannels", *AICHE Journal,* vol. 50, no. 4, pp. 771-778.

[133]. Aubin, J., Fletcher, D.F., Bertrand, J. & Xuereb, C. 2003, "Characterization of the mixing quality in micromixers", *Chemical Engineering and Technology,* vol. 26, no. 12, pp. 1262-1270.

[134]. Lim, D., Kamotani, Y., Cho, B., Mazumder, J. & Takayama, S. 2003, "Fabrication of microfluidic mixers and artificial vasculatures using a high-brightness diode-pumped Nd:YAG laser direct write method",*Lab*

on a Chip - Miniaturisation for Chemistry and Biology, vol. 3, no. 4, pp. 318-323.

[135]. Biddiss, E., Erickson, D. & Li, D. 2004, "Heterogeneous surface charge enhanced micromixing for electrokinetic flows", *Analytical Chemistry,* vol. 76, no. 11, pp. 3208-3213.

[136]. Kim, D.S., Lee, S.W., Kwon, T.H. & Lee, S.S. 2004, "A barrier embedded chaotic micromixer", *Journal of Micromechanics and Microengineering,* vol. 14, no. 6, pp. 798-805.

[137]. Kang, T.G., Singh, M.K., Kwon, T.H. & Anderson, P.D. 2008, "Chaotic mixing using periodic and aperiodic sequences of mixing protocols in a micromixer", *Microfluidics and Nanofluidics,* vol. 4, no. 6, pp. 589-599.

[138]. Bertsch, A., Heimgartner, S., Cousseau, P. & Renaud, P. 2001, "Static micromixers based on large-scale industrial mixer geometry", *Lab on a Chip - Minituarization for Chemistry and Biology,* vol. 1, no. 1, pp. 56-60.

[139]. Lu, L.-H., Ryu, K.S. & Liu, C. 2002, "A magnetic microstirrer and array for microfluidic mixing", *Journal of Microelectromechanical Systems,* vol. 11, no. 5, pp. 462-469.

[140]. Ryu, K.S., Shaikh, K., Goluch, E., Fan, Z. & Liu, C. 2004, "Micro magnetic stir-bar mixer integrated with parylene microfluidic channels", *Lab on a Chip - Miniaturisation for Chemistry and Biology,* vol. 4, no. 6, pp. 608-613.

[141]. Mensing, G.A., Pearce, T.M., Graham, M.D. & Beebe, D.J. 2004, "An externally driven magnetic microstirrer", *Philosophical Transactions of the Royal Society A: Mathematical, Physical and Engineering Sciences,*vol. 362, no. 1818, pp. 1059-1068.

[142]. Deshmukh, A. A., Liepmann, D., & Pisano, A. P., 2000, "Continuous micromixer with pulsatile micropumps", *Technical Digest of the IEEE Solid State Sensor and Actuator Workshop (Hilton Head Island, SC)*, pp. 73–76.

[143]. Deshmukh, A. A., Liepmann, D., & Pisano, A. P., 2000, 2001, "Characterization of a micro-mixing, pumping, and valving system", *Proc. Transducers'01, 11th Int. Conf. on Solid-State Sensors and Actuators (Munich, Germany)*, pp. 779–782.

[144]. Fujii, T., Sando, Y., Higashino, K. & Fujii, Y. 2003, "A plug and play microfluidic device", *Lab on a Chip - Miniaturisation for Chemistry and Biology,* vol. 3, no. 3, pp. 193-197.

[145]. Glasgow, I. & Aubry, N. 2003, "Enhancement of microfluidic mixing using time pulsing", *Lab on a Chip - Miniaturisation for Chemistry and Biology,* vol. 3, no. 2, pp. 114-120.

[146]. Niu, X. & Lee, Y.-K. 2003, "Efficient spatial-temporal chaotic mixing in microchannels", *Journal of Micromechanics and Microengineering,* vol. 13, no. 3, pp. 454-462.

[147]. Okkels, F. & Tabeling, P. 2004, "Spatiotemporal Resonances in Mixing of Open Viscous Fluids", *Physical Review Letters,* vol. 92, no. 3, pp. 383011-383014.

[148]. Moroney, R.M., White, R.M. & Howe, R.T. 1991, "Ultrasonically induced microtransport", Proc. MEMS'91, 3th IEEE Int. Workshop Micro Electromechanical System (Nara, Japan), pp. 277.

[149]. Rife, J.C., Bell, M.I., Horwitz, J.S., Kabler, M.N., Auyeung, R.C.Y. & Kim, W.J. 2000, "Miniature valveless ultrasonic pumps and mixers", *Sensors and Actuators, A: Physical,* vol. 86, no. 1-2, pp. 135-140.

[150]. Vivek, V., Zeng, Y. & Kim, E.S. 2000, "Novel acoustic-wave micromixer", *Proceedings of the IEEE Micro Electro Mechanical Systems (MEMS),* , pp. 668-673.

[151]. Yasuda, K. 2000, "Non-destructive, non-contact handling method for biomaterials in micro-chamber by ultrasound", *Sensors and Actuators, B: Chemical,* vol. 64, no. 1-3, pp. 128-135.

[152]. Yang, Z., Goto, H., Matsumoto, M. & Maeda, R. 2000, "Active micromixer for microfluidic systems using lead-zirconate- titanate(PZT)-generated ultrasonic vibration", *Electrophoresis,* vol. 21, no. 1, pp. 116-119.

[153]. Yang, Z., Matsumoto, S., Goto, H., Matsumoto, M. & Maeda, R. 2001, "Ultrasonic micromixer for microfluidic systems", *Sensors and Actuators, A: Physical,* vol. 93, no. 3, pp. 266-272.

[154]. Liu, R.H., Yang, J., Pindera, M.Z., Athavale, M. & Grodzinski, P. 2002, "Bubble-induced acoustic micromixing", *Lab on a Chip - Miniaturisation for Chemistry and Biology,* vol. 2, no. 3, pp. 151-157.

[155]. Liu, R.H., Lenigk, R., Druyor-Sanchez, R.L., Yang, J. & Grodzinski, P. 2003, "Hybridization enhancement using cavitation microstreaming", *Analytical Chemistry,* vol. 75, no. 8, pp. 1911-1917.

[156]. Yaralioglu, G.G., Wygant, I.O., Marentis, T.C. & Khuri-Yakub, B.T. 2004, "Ultrasonic mixing in microfluidic channels using integrated transducers", *Analytical Chemistry,* vol. 76, no. 13, pp. 3694-3698.

[157]. Tseng, W.-., Lin, J.-., Sung, W.-., Chen, S.-. & Lee, G.-. 2006, "Active micro-mixers using surface acoustic waves on Y-cut 128° LiNbO3", *Journal of Micromechanics and Microengineering,* vol. 16, no. 3, pp. 539-548.

[158]. Shilton, R., Tan, M.K., Yeo, L.Y. & Friend, J.R. 2008, "Particle concentration and mixing in microdrops driven by focused surface acoustic waves", *Journal of Applied Physics,* vol. 104, no. 1.

[159]. Johansson, L., Johansson, S., Nikolajeff, F. & Thorslund, S. 2009, "Effective mixing of laminar flows at a density interface by an integrated ultrasonic transducer", *Lab on a Chip - Miniaturisation for Chemistry and Biology,* vol. 9, no. 2, pp. 297-304.

[160]. Mao, H., Yang, T. & Cremer, P.S. 2002, "A microfluidic device with a linear temperature gradient for parallel and combinatorial measurements", *Journal of the American Chemical Society,* vol. 124, no. 16, pp. 4432-4435.

[161]. Tsai, J.-H. & Lin, L. 2002, "Active microfluidic mixer and gas bubble filter driven by thermal bubble micropump", *Sensors and Actuators, A: Physical,* vol. 97-98, pp. 665-671.

[162]. Ould El Moctar, A., Aubry, N. & Batton, J. 2003, "Electro-hydrodynamic micro-fluidic mixer", *Lab on a Chip - Miniaturisation for Chemistry and Biology,* vol. 3, no. 4, pp. 273-280.

[163]. Tsouris, C., Culbertson, C.T., DePaoli, D.W., Jacobson, S.C., De Almeida, V.F. & Ramsey, J.M. 2003, "Electrohydrodynamic mixing in microchannels", *AICHE Journal,* vol. 49, no. 8, pp. 2181-2186.

[164]. Lin, C.-H., Fu, L.-M. & Chien, Y.-S. 2004, "Microfluidic T-form mixer utilizing switching electroosmotic flow", *Analytical Chemistry,* vol. 76, no. 18, pp. 5265-5272.

[165]. Fu, L.-M., Yang, R.-J., Lin, C.-H. & Chien, Y.-S. 2005, "A novel microfluidic mixer utilizing electrokinetic driving forces under low switching frequency", *Electrophoresis,* vol. 26, no. 9, pp. 1814-1824.

[166]. Sasaki, N., Kitamori, T. & Kim, H.-. 2006, "AC electroosmotic micromixer for chemical processing in a microchannel", *Lab on a Chip - Miniaturisation for Chemistry and Biology,* vol. 6, no. 4, pp. 550-554.

[167]. Tang, Z., Hong, S., Djukic, D., Modi, V., West, A.C., Yardley, J. & Osgood, R.M. 2002, "Electrokinetic flow control for composition modulation in a microchannel", *Journal of Micromechanics and Microengineering,* vol. 12, no. 6, pp. 870-877.

[168]. Wu, H.-Y. & Liu, C.-H. 2005, "A novel electrokinetic micromixer", *Sensors and Actuators, A: Physical,* vol. 118, no. 1, pp. 107-115.

[169]. Qian, S. & Bau, H.H. 2002, "A chaotic electroosmotic stirrer", *Analytical Chemistry,* vol. 74, no. 15, pp. 3616-3625.

[170]. Oddy, M.H., Santiago, J.G. & Mikkelsen, J.C. 2001, "Electrokinetic instability micromixing", *Analytical Chemistry,* vol. 73, no. 24, pp. 5822-5832.

[171]. Wong, P.K., Wang, T.-H., Deval, J.H. & Ho, C.-M. 2004, "Electrokinetics in micro devices for biotechnology applications", *IEEE/ASME Transactions on Mechatronics,* vol. 9, no. 2, pp. 366-376.

[172]. Deval, J., Tabeling, P. & Ho, C.-. 2002, "A dielectrophoretic chaotic mixer", *Proc. MEMS'02, 15th IEEE Int. Workshop Micro Electromechanical System (Las Vegas, Nevada)*, pp. 36.

[173]. Lee, Y.-K., Deval, J., Tabeling, P. & Ho, C.-M. 2001, "Chaotic mixing in electrokinetically and pressure driven micro flows", *Proc. MEMS'01, 14th IEEE Int. Workshop Micro Electromechanical System (Interlaken, Switzerland)*, pp. 483.

[174]. Bau, H.H., Zhong, J. & Yi, M. 2001, "A minute magneto hydro dynamic (MHD) mixer", *Sensors and Actuators, B: Chemical,* vol. 79, no. 2-3, pp. 207-215.

[175]. Solomon, T.H. & Mezic, I. 2003, "Uniform resonant chaotic mixing in fluid flows", *Nature,* vol. 425, no. 6956, pp. 376-380.

[176]. Gijs, M.A.M. 2004, "Magnetic bead handling on-chip: New opportunities for analytical applications", *Microfluidics and Nanofluidics,* vol. 1, no. 1, pp. 22-40.

[177]. Suzuki, H. & Ho, C.-M. 2002, "A magnetic force driven chaotic micro-mixer", *Proc. MEMS'02, 15th IEEE Int. Workshop Micro Electromechanical System (Las Vegas, Nevada)*, pp. 40.

[178]. Suzuki, H., Kasagi, N., & Ho, C.-H. 2003, " Chaotic Mixing of magnetic beads in micro cell separator", *Proc. 3rd Int. Symp. Turbulence and Shear Flow Phenomena Sendai, Japan, June 24-27*, pp. 817-822.

[179]. Suzuki, H., Nakano, M., Kasagi, N., & Ho, C.-M. 2003, "Particle tracking velocimetry measurement of chaotic mixing in a micro mixer", *Int. Symp. Micro-Mechanical Engineering (ISMME2003), Tsuchiura, 1-3 December*, pp. 397-402.

[180]. Suzuki, H., Ho, C.-M. & Kasagi, N. 2004, "A chaotic mixer for magnetic bead-based micro cell sorter", *Journal of Microelectromechanical Systems,* vol. 13, no. 5, pp. 779-790.

[181]. Rong, R., Choi, J.W., & Ahn, C.H. 2003, "A novel magnetic chaotic mixer for in-flow mixing of magnetic beads", *7th International Conference on Miniaturized Chemical and Biochemical Analysts Systems October 5-9, Squaw Valley, California USA*, pp. 335-338.

[182]. Rida, A., Lehnert, T., & Gijs, M.A.M. 2003, “Microfluidic mixer using magnetic beads”, *7th International Conference on Miniaturized Chemical and Biochemical Analysts Systems October 5-9, Squaw Valley, California USA,* pp. 579-582.

[183]. Rida, A. & Gijs, M.A.M. 2004, "Manipulation of self-assembled structures of magnetic beads for microfluidic mixing and assaying", *Analytical Chemistry,* vol. 76, no. 21, pp. 6239-6246.

[184]. Shikida, M., Koyama, M., Nagao, N., Imai, R., Honda, H., Okochi, M., Tsuchiya, H. & Sato, K. 2009, "Agitation of magnetic beads by multi-layered flat coils", *Sensors and Actuators, B: Chemical,* vol. 137, no. 2, pp. 774-780.

[185]. Shikida, M., Takayanagi, K., Honda, H., Ito, H. & Sato, K. 2006, "Development of an enzymatic reaction device using magnetic bead-cluster handling", *Journal of Micromechanics and Microengineering,* vol. 16, no. 9, pp. 1875-1883.

[186]. Wang, Y., Zhe, J., Chung, B.T.F. & Dutta, P. 2008, "A rapid magnetic particle driven micromixer", *Microfluidics and Nanofluidics,* vol. 4, no. 5, pp. 375-389.

[187]. Lin, Y., Wong, T.-S., Bhardwaj, U., Chen, J.-M., McCabe, E. & Ho, C.-M. 2007, "Formation of high electromagnetic gradients through a particle-based microfluidic approach", *Journal of Micromechanics and Microengineering,* vol. 17, no. 7, pp. 1299-1306.

[188]. Azimi, S.M., Balachandran, W., Ahern, J., Slijepcevic, P. & Newton, C. 2008, "DNA extraction chip using key-type planar electrodes", *NSTI Nanotech 2008, Technical Proceedings (June 1-5,Boston, MA, USA)*, vol. 3, , pp. 249.

[189]. Zolgharni, M., Azimi, S.M., Ayers, H. & Balachandran, W., "Labelling of biological cells with magnetic particles in a chaotic microfluidic mixer", *Proc. of the 2nd IEEE Int. Conf. on Nano/Micro Engineered and Molecular Systems (Jan. 16 - 19, 2007, Bangkok, Thailand)*, pp. 55.

[190]. Zolgharni, M., Azimi, S.M., Bahmanyar, M.R. & Balachandran, W., "A microfluidic mixer for chaotic mixing of magnetic particles", *NSTI Nanotech 2007, Technical Proceedings (May 20-24, Santa Clara, CA, USA)*, vol. 3, pp. 336.

[191]. Zolgharni, M., Azimi, S.M., Bahmanyar, M.R. & Balachandran, W. 2007, "A numerical design study of chaotic mixing of magnetic particles in a microfluidic bio-separator", *Microfluidics and Nanofluidics,* vol. 3, no. 6, pp. 677-687.

[192]. Hayt, W.H., Buck, J.A., 2001, "Engineering Electromagnetics", *McGraw Hill*, 6th edition, pp. 288-297.

[193]. Schmitt, R., 2002, "Electromagnetics Explained", *Newnes-Elsevier science*, USA, pp. 51-73.

[194]. Sorensen, C.M., "Nanoscale Materials in Chemistry", *John Wiley and Sons, Inc.*, New York, 2001, pp. 169.

[195]. Harris, L.A., "Polymer Stabilized Magnetite Nanoparticles and Poly(propylene oxide) Modified Styrene-Dimethacrylate Networks", Ph.D. thesis, *Virginia Polytechnic Institute and State University*, 2002.

[196]. Jones, T.B., 1995, "Electromechanics of Particles", *Cambridge University Press*, New York, USA.

[197]. Mikkelsen, C.I., 2005, "Magnetic Separation and Hydrodynamic Interactions in Microfluidic Systems. Ph.D. Thesis, *Technical University of Denmark*.

[198]. Jackson, J.D., 1998, "Classical Electrodynamics, *John Wiley & Sons Ltd*, 3rd Ed., New York, USA.

[199]. Choi, J.-W., Ahn, C.H., Bhansali, S. & Henderson, H.T. 2000, "New magnetic bead-based, filterless bio-separator with planar electromagnet surfaces for integrated bio-detection systems", *Sensors and Actuators, B: Chemical*, vol. 68, no. 1, pp. 34-39.

[200]. Smistrup, K., Tang, P.T., Hansen, O. & Hansen, M.F. 2006, "Microelectromagnet for magnetic manipulation in lab-on-a-chip systems", *Journal of Magnetism and Magnetic Materials*, vol. 300, no. 2, pp. 418-426.

[201]. Clayton T. Crowe, 2006, "Multiphase Flow Handbook", *CRC Press*, Boca Raton.

[202]. Mikkelsen, C. & Bruus, H. 2005, "Microfluidic capturing-dynamics of paramagnetic bead suspensions", *Lab on a Chip* - Miniaturisation for Chemistry and Biology, vol. 5, no. 11, pp. 1293-1297.

[203]. Stokes, G. G., 1851, "On the effect of the internal friction of fluids on the motion of pendulums", *Trans. Cam. Phil. Soc*., vol. 9.

[204]. Coulson J.M., Richardson, J.F., Backhurst, J.R. & Harker, J.H. 1991, "Chemical Engineering: Particle Technology and Separation Processes. Volume 2", *Pergammon Press* Ltd, Oxford.

Appendix A

LIST OF PUBLICATIONS

Patent

Balachandran, W., **Azimi, S.M.,** Ahern, J., Zolgharni, M., Bahmanyar, M.R. & Slijepcevic, P., 2008, "Microfluidic Device", WO 2008/084245 A2.

Preprint

Azimi, S.M., Nixon, G., Ahern, J. & Balachandran, W., "A Magnetic Bead-based DNA Extraction and Purification Microfluidic Device"

Published

1. **Azimi, S.M.,** Nixon, G., Ahern, J. & Balachandran, W. 2010, "DNA Extraction, Purification and Quantification Using Micromachined Microfluidic Chip", *NSTI Nanotech 2010, Technical Proceedings (June 21-25, Anaheim, CA, USA)*, in press.

2. **Azimi, S.M.,** Balachandran, W. & Ahern, J. 2010, "A Novel Microfluidic Magnetic Mixer Using Dynamic Switching Field", *NSTI Nanotech 2010, Technical Proceedings (June 21-25, Anaheim, CA, USA)*, in press.

3. **Azimi, S.M.,** Balachandran, W., Ahern, J., Slijepcevic, P. & Newton, C. 2008, "DNA extraction chip using key-type planar electrodes", *NSTI Nanotech 2008, Technical Proceedings (June 1-5,Boston, MA, USA)*, vol. 3, , pp. 249.

4. **Azimi, S.M.,** Bahmanyar, M.R., Zolgharni, M. & Balachandran, W., 2007, "Numerical investigation of magnetic sensor for DNA hybridization detection using planar transformer", *Int. J. of Multiphysics*, vol. 1, no. 4, pp. 367-376.

5. **Azimi, S.M.,** Zolgharni, M., Bahmanyar, M.R. & Balachandran, W., 2007 " Using Spiral Inductors for Detecting Hybridization of DNAs Labeled with

Magnetic Beads", *NSTI Nanotech 2007, Technical Proceedings (May 20-24, Santa Clara, CA, USA)*, vol. 2, pp. 567-570.

6. **Azimi, S.M.,** Bahmanyar, M.R., Zolgharni, M. & Balachandran, W. 2007, "An Inductance-based Sensor for DNA Hybridization Detection", *Proc. of the 2nd IEEE Int. Conf. on Nano/Micro Engineered and Molecular Systems (Jan. 16 - 19, Bangkok, Thailand)*, pp. 524-527.

7. Zolgharni, M., **Azimi, S.M.,** Bahmanyar, M.R. & Balachandran, W. 2007, "A numerical design study of chaotic mixing of magnetic particles in a microfluidic bio-separator", *Microfluidics and Nanofluidics*, vol. 3, no. 6, pp. 677-687.

8. Zolgharni, M., **Azimi, S.M.,** Bahmanyar, M.R. & Balachandran, W., 2007 "A microfluidic mixer for chaotic mixing of magnetic particles", *NSTI Nanotech 2007, Technical Proceedings (May 20-24, Santa Clara, CA, USA)*, vol. 3, pp. 336-339.

9. Zolgharni, M., **Azimi, S.M.,** Ayers, H. & Balachandran, W. 2007 "Labelling of biological cells with magnetic particles in a chaotic microfluidic mixer", *Proc. of the 2nd IEEE Int. Conf. on Nano/Micro Engineered and Molecular Systems (Jan. 16 - 19, Bangkok, Thailand)*, pp. 55-58.

Appendix B

Schematic Diagram of the Designed Power Supply

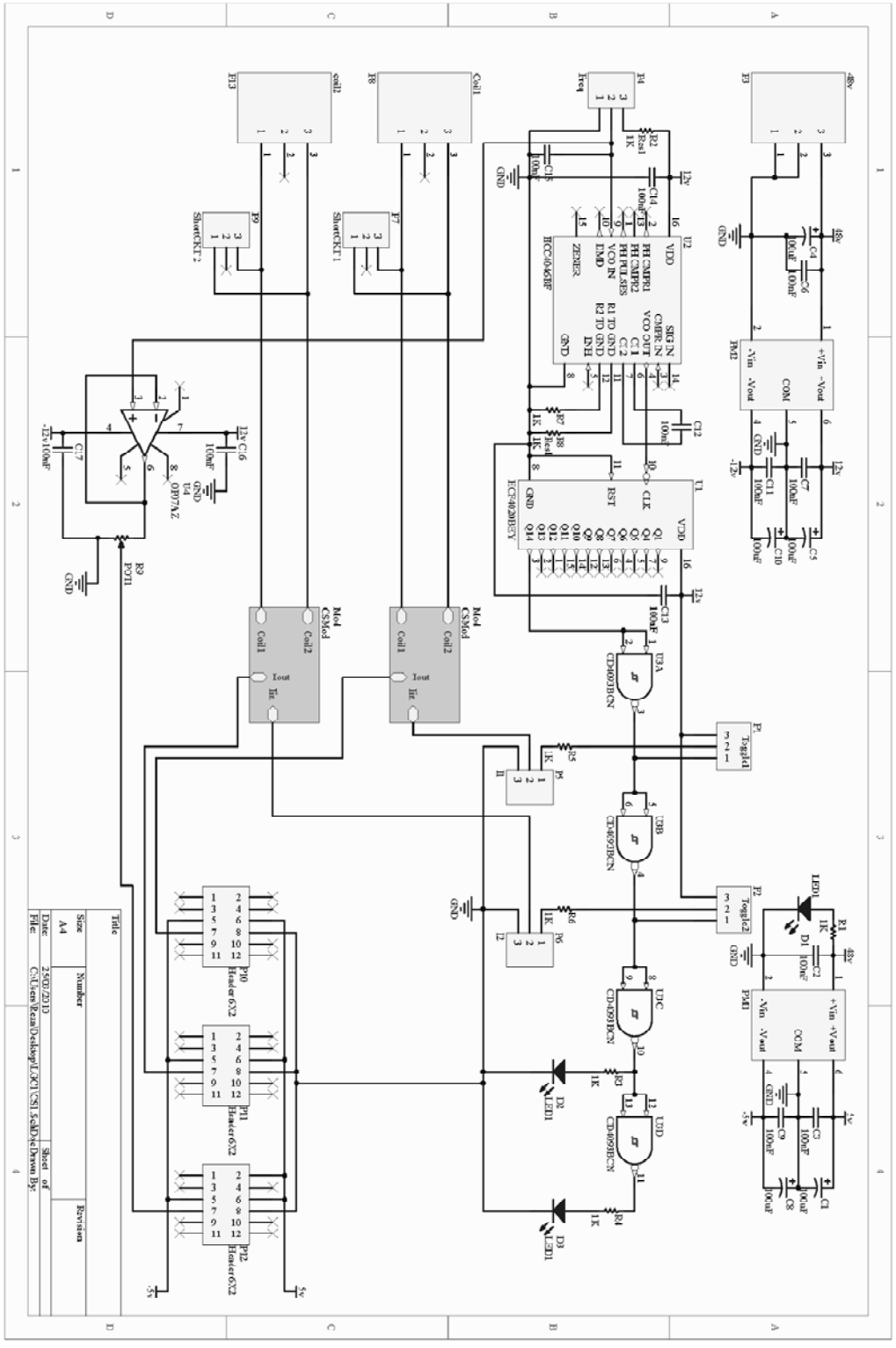

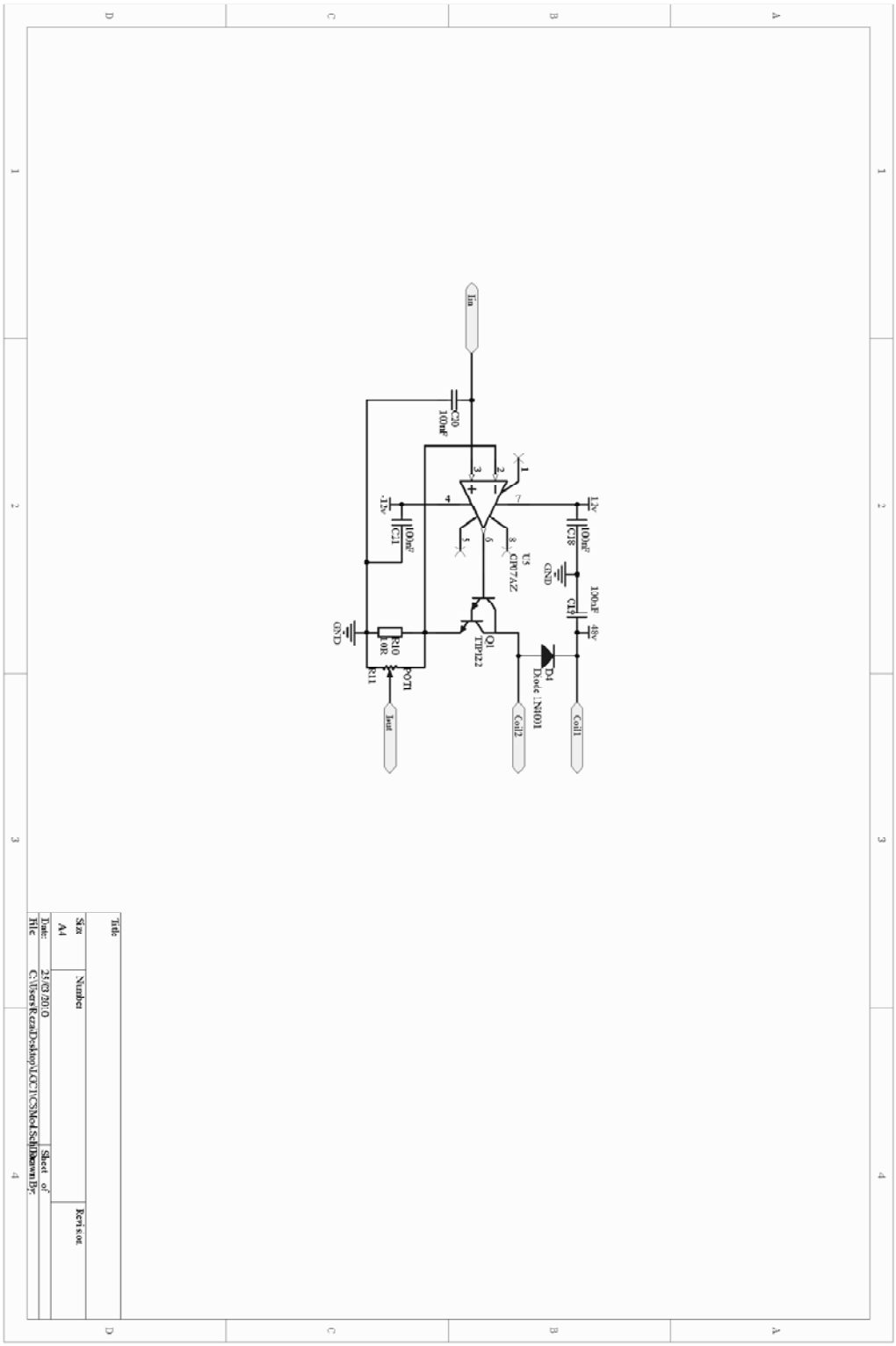
Iin
C20
100nF
12v
C21
100nF
-12v
U5
CA0741Z
GND
12v
C18
100nF
GND
C19
100nF
48v
Q1
TIP122
R10
1.0R
POT1
R11
D4
Diode 1N4001
Iout
Coil2
Coil1
Title
Size
A4
Number
Revision
Date:
21/03/2010
Sheet of
File
C:\Users\Reza\Desktop\LGC1\GSM\sch\Sch1.SchDoc
Drawn By: